Linking cellular tensional force dynamics with actin architecture

Tomas Andersen

Communauté
UNIVERSITÉ Grenoble Alpes

THÈSE

Pour obtenir le grade de

DOCTEUR DE LA COMMUNAUTE UNIVERSITE GRENOBLE ALPES

Spécialité : **Physique pour les sciences du vivant**

Arrêté ministériel : 25 mai 2016

Présentée par

Tomas Andersen

Thèse dirigée par **Dr Martial Balland, Liphy, MOTIV group**

préparée au sein du **Laboratoire Interdisciplinaire de Physique** dans **l'École Doctorale de Physique**

Relier la dynamique de la force de tension cellulaire avec l'architecture de l'actine

Thèse soutenue publiquement le **22 Octobre 2018**, devant le jury composé de :

Hans Geiselmann
Professeur, Université Grenoble Alpes, Président
Cecile Gauthier-Rouviere
Directeur de recherche, INSERM, Rapportrice
Atef Asnacios
Professeur, Université Paris Diderot, Rapporteur
Manuel Thery
Directeur de recherche, CEA Paris, Membre
Mathieu Coppey
CR1, Curie Institute, Paris, Membre
Emmanuelle Planus
Maître de Conférences Biologie, IAB, Membre

Para mi Tia Ñata
Por apoyarme sin siquiera dudarlo

Acknowledgements

Looking back after three years of being a PhD student I can safely and happily say that they were three amazingly and properly spent years. To begin with, I would like to thank Martial, my supervisor, for welcoming me to his research group. Somehow, and I am very grateful for it, he knew I had to be part of his team even before I had any idea about what to do with my future. His complete trust in me and both his life philosophies and great heart made for a stupendous mentor both inside and outside the office. Thank you Martial for all the knowledge shared, the discussions and for being an awesome person. During the project I realized how important the working environment is and how fortunate I was with the group I had joined. Elisa, Katha and Vanni were, hands down, the best office crew I could have asked for. Huge thanks to those three who became great friends aside from helpful and supportive colleagues. Sorry for all the singing though. From random and fun lunch conversations to heated scientific discussions, MOTIV team proved to be a truly awesome and encouraging group. I would like to thank you all, and namely Philippe and Irene for your enormous help and contagious happiness, and Thomas and Aurelian for conversations of every sort.

Inside the lab it was fun, but outside was even better. I want to thank my awesome group of friends without whom this period would not have been the same. Those friends that are the very definition of feeling at home, the feeling of belonging. Friends that I will not get rid of, in the good sense of the phrase, if there is one. Those in the group that were here from the beginning, making my PhD choice easier, as well as those I made along the way and who enriched my life so much more. Thank you so much, and again, sorry for all the singing though.

To my parents, the ones mainly responsible for me being here since they made me who I am, I will keep thanking them every day. Next in line my three best allies, my sisters, and my whole family, my most valuable 'possession'. An endless source of love, support and joy, they are my true north.

To those friends back in Argentina that understood and grudgingly accepted my restless desire for travelling (also applies to my family). Friends that after all these years are still 'by my side' through emails, messages and video calls as if no time had passed wielding at the same time that yet unanswered question: when will you be back?

Last but almost ahead of all the rest, I would like to thank one particular friend, Martina, whose personal decision opened for me the doors to this amazing three-year adventure.

Table of contents

Abstract

The structural stability and mechanical integrity are key elements for the proper functioning and preservation of complex living systems. Being in constant interaction with their surroundings and subjected to external inputs, such systems need to be able to face changes in order to thrive. These inputs can affect the system both in a localized way or disturb it as a whole. Any perturbations that cannot be mechanically withstand by the living system will result in a crucial malfunctioning or, ultimately, in its death. The general mechanism responsible for maintaining the system's physiological conditions at the proper state, despite environmental variations, is identified as homeostasis. More specifically, one of the processes known in mechanobiology to preserve the appropriate mechanical equilibrium of a living system is called tensional homeostasis.

It is important to note that all of the above stated holds true both at the scale of collective behaviour of complex organisms, and all the way down to the single cell level. In fact, it is actually this last small scale which draws our interest. Cells face constant mechanical perturbations from their surrounding and are able to respond accordingly maintaining a relatively stable internal mechanical state. The existence of this internal tensional equilibrium relies on a very dynamic process with constant feedback loops between the internal biochemical contractile machinery and the external active generated forces.

Our interest is to understand better this active mechanism by dynamically perturbing the tensional homeostatic system while studying its return to equilibrium.

CHAPTER 1 - Background and research environment

1.1 Mechanical integrity

As a general term, mechanical integrity can be defined as the condition of a system where its parts are properly arranged and in optimum conditions, in order to ensure both the correct functioning of such system and the prevention of any possible failure that might affect it [1]. In nature, this condition can be seen at every level of hierarchy. From the collective behaviour of independent organisms, as is the case of fire ants, through organs and tissues, all the way down to the cell.

Over the last few decades, the emerging field of mechanobiology has identified the cell not only as a widely known complex biochemical sensor, first described as such by Pfeffer in 1884, but also as a sophisticated biomechanical structure were mechanical signals, both internal and external, affect the cellular decision-making in complex environments. Physical environmental and intracellular factors significantly influence vital cellular processes such as migration, differentiation and fate [2]–[6].

It is essential for the cell, and the tissue of which it is part, to ensure mechanical integrity, sustaining optimum tensional values and mechanical equilibrium. Collapse of this integrity and abnormal interpretation of mechanical cues may lead to physiological dysfunctions or pathologies such as fibrosis, atherosclerosis and even cancer [7], [8]. A dysregulation of cell and tissue forces can disturb the mechanical integrity of the system and its mechanotransduction, thus promoting disease progression [9]–[11].

Among the mechanisms used by the cell to preserve this mechanical integrity, one of the most important, and the one we will be focused on henceforth, is what is known as tensional homeostasis.

1.2 Tensional homeostasis

1.2.1 The concept of homeostasis

The process of cellular tensional homeostasis started to be defined after the work done by Brown and colleagues in 1998. However, the general mechanism of homeostasis has been around since the 19th century and I would like to spare a few lines to bring this concept into context, before diving into the more specific tensional one.

In 1865, French physiologist Claude Bernard (Fig. 1A left) elaborated the concept of 'milieu interieur' (internal environment), stating that it is the stability of this environment what gives an organism freedom and independence from the external environment.

Quoting one of Bernard's arguments:

"The stability of the internal environment implies an organism so perfect that it can continually compensate for and counterbalance external variations. Consequently, far from the higher animals being indifferent to their surroundings, they are on the contrary in close and intimate relation to them, so that their equilibrium is the result of compensation established as continually and as exactly as if by a very sensitive balance.'' [12].

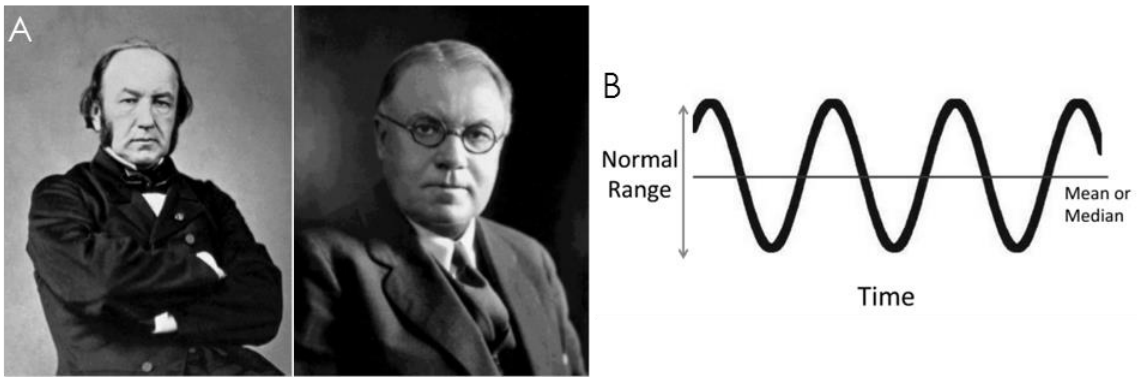

Figure 1 A) Claude Bernard (left) and Walter Cannon (right). B) Graphic simplified representation of the homeostatic process where the system fluctuates, within an accepted range, around an 'ideal'

physiological state. Adapted from 'An Introduction to the History of Medicine' by Fielding Hudson Garrison. [13].

Almost 70 years later, the American physiologist Walter Cannon (Fig. 1A right) reformulated Bernard's idea of the constancy of the milieu interieur by coining the, now widely known, concept of homeostasis (*The Wisdom of the Body*, 1932). This new term conveyed the idea that biological organisms, being in constant interaction with the outer environment, would be able to maintain and adjust internal conditions within 'narrow limits' when faced with external disturbances. It is important to note that the choice of the word was not arbitrary. Cannon decided to use the prefix "homeo" (Greek meaning 'like' or 'similar') instead of "homo" ('same' or 'fixed'), to transmit the notion that the constancy of this internal physiological state is more relative than absolute [12], [13] (Fig. 1B).

Following this same line, Bornstein and colleagues coined the term of dynamic reciprocity in 1982, which was further elaborated by Mina Bissell et al during that same year (Fig. 2). This concept derived from the homeostasis ideas of Cannon but also introduced the notion that cells actively react to the extracellular matrix (ECM) influences, responding accordingly and altering the composition and structure of the ECM, hence creating a feedback loop in between both sides. Bissell's work would emphasize the idea of the important role that the ECM played on the cell's fate by stating that "the influence of ECM on the cell, both during the developmental process and in established tissues, appears to evolve continually." [14]. This idea of a bidirectional interaction between cells and their microenvironment proved to be right, enhancing the understanding of the cellular homeostasis and expanding the approaches needed to study such a dynamic phenomenon.

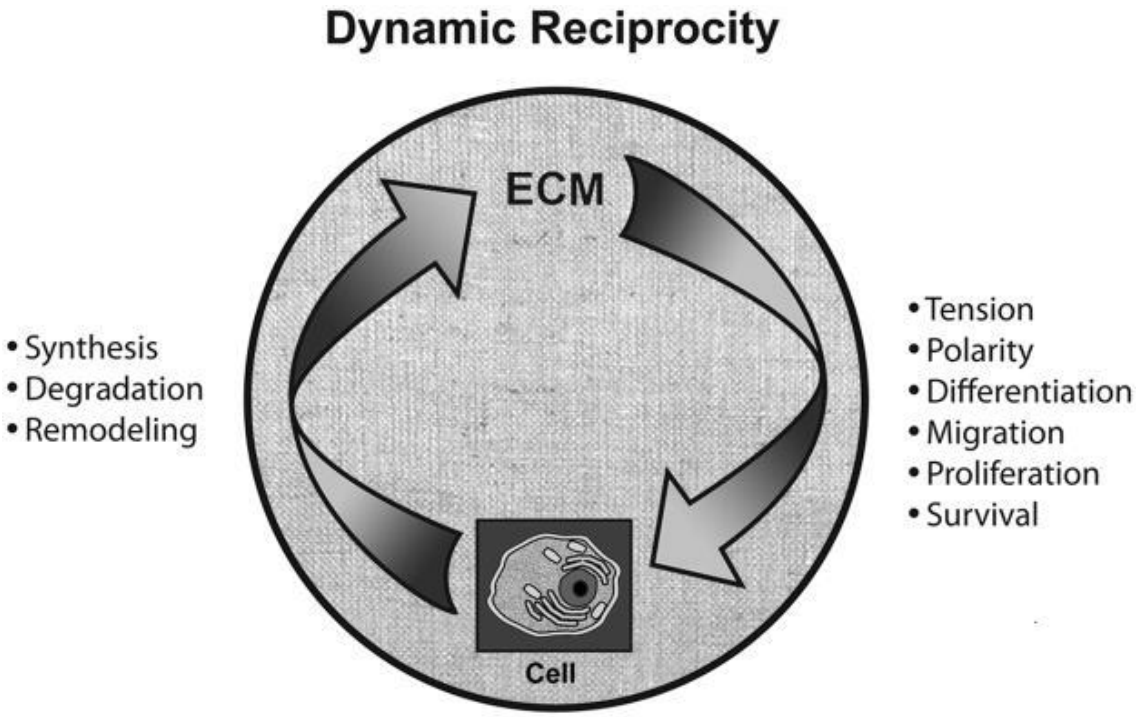

Figure 2 ***A graphic depiction of the principle of Dynamic Reciprocity.*** *The ECM impacts on the cell's functions and behaviour, and the cell responds accordingly modifying the environment. Adapted from* [15].

1.2.2 Tensional homeostasis at the single cell level

The term homeostasis has been kept until today and used in many different fields and at different hierarchies. As a consequence, it was in 1998 that Brown et al presented tensional homeostasis as "the control mechanism by which fibroblasts establish a tension within their extracellular collagenous matrix and maintain its level against opposing influences of external loading" [16]. Since then, tensional homeostasis has had slightly diverse definitions in the literature but it roughly relates to the ability of cells to maintain or attempt to maintain a constant level of tension when faced with perturbations from the extracellular matrix.

Such control mechanism is of utmost importance for the cellular integrity. Attempts at properly understanding the processes involved in this phenomenon have rapidly increased over the last few years and I will talk about them throughout this chapter.

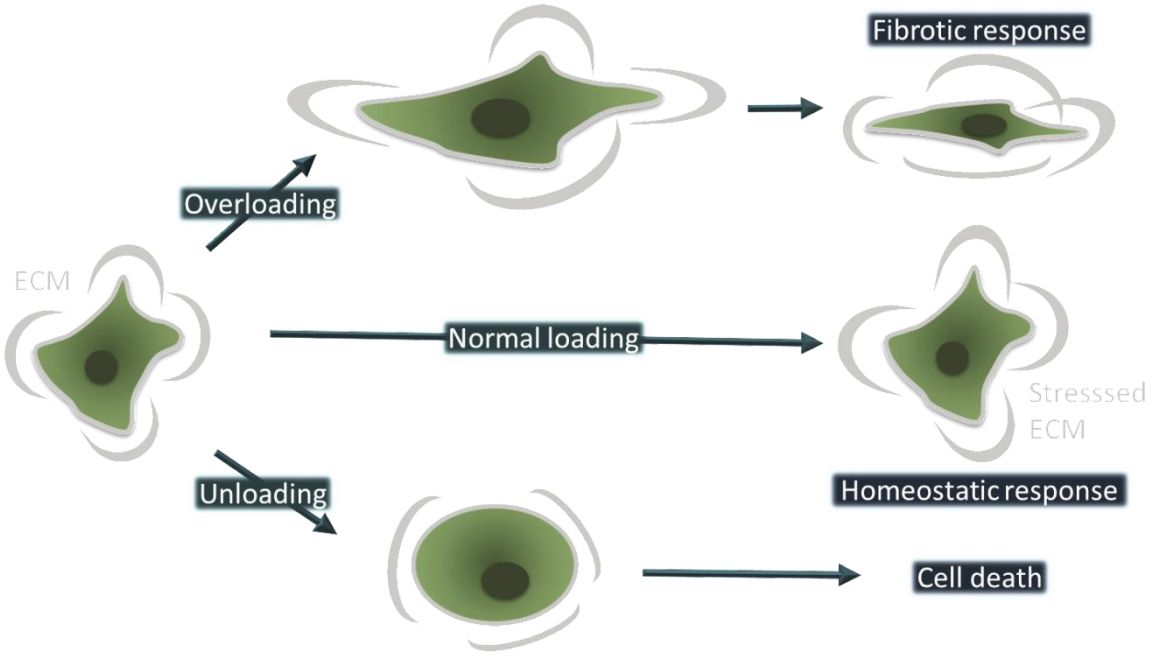

Figure 3 ***Extracellular matrix influences in cellular mechanic responses****. Mechanical interactions between the cell and its environment can be divided into three main categories. A normal loading situation is where forces applied by the ECM are correctly countered by the cell resulting in the maintenance of a physiological tensional state. An overloading, such as an abnormal remodelling of the ECM, can exceed the limits of tensional response of the cell, resulting in a pathological response such as fibrosis. A degradation or loss in the mechanical properties of the ECM can induce the cell into apoptosis. Adapted from* [17].

Nowadays, it has been well reported that the process of tensional homeostasis is regulated in the cell through mechanotransduction; the cellular machinery senses internal and external mechanical cues and transforms them into biochemical signalling [18].

1.2.3 Cellular mechanosensing tools

The mechanosensing machinery (Fig. 4) of the cell comprises both intracellular and extracellular ingredients, among which the most important structural ones are the membrane and its cell surface adhesive protein complexes, the nucleus, and the cytoskeleton. The cell surface adhesive protein complexes that mediate the attachment to the surrounding extracellular matrix are known as focal adhesions, and the ones involved in attaching to neighbouring cells are identified as cell-cell junctions. Focal adhesions are macromolecular assemblies consisting of

transmembrane proteins, integrins, which mediate the cell interaction with extracellular ligands, and intracellular proteins connected to the actomyosin cytoskeleton [19]–[22]. Cell-cell junctions, on the other hand, consist mainly of Cadherins, transmembrane proteins that form adherent junctions binding cells to each other [23], [24]. On the non-adhesive side of the cell surface there are mechanosensitive ion channels (or stretch-gated ion channels) involved in sensing mechanical forces coming from variations in the flow of fluids, such as blood, or pressure differences, as is the case of sound. They are vital for processes such as touch and hearing, as well as feeling and memory formation [25], [26], and when opened by physical forces and deformation they can induce electrical signals and ion exchange.

Looking at the inner part of the cell, the cell nucleus and the nuclear lamina have been found to possess its own mechanical machinery that can respond to and transduce mechanical stimuli coming both from the cell (through the actomyosin cytoskeleton) and from inside the nucleus (through altered gene expression and transcriptional profiles) [27]–[31].

The cytoskeleton, consisting mainly of actin filaments, microtubules and intermediate filaments, is a network which spans the whole cell body preserving its shape and mechanical integrity. It is connected to each of the previously mentioned components, allowing for force transmission in between cells and in between the cell and the extracellular matrix. This network, in collaboration with motor proteins, such as myosins, modulates crucial cellular processes such as migration [32], division [33], differentiation [34] and cell shape [35]. By provoking actomyosin contraction it balances intracellular and extracellular forces [7], [36]–[38]. Moreover, the variations of its length, density, cross-linking and arrangement, together with its kinetics and dynamics, directly regulate cell's mechanical properties such as contractility, rigidity and motility [7], [37], [39]. Finally, the membrane as a whole has been seen to act as a global tensional sensor which, through the combination of cortical, substrate and

membrane tension, regulates cellular processes and parameters such as shape, polarity and motility [40]. Moreover, recent results suggest that the overall shape of the cellular membrane is a separate signal source which can modulate mechanical signalling and 'store' information coming from both chemical and physical sources [41].

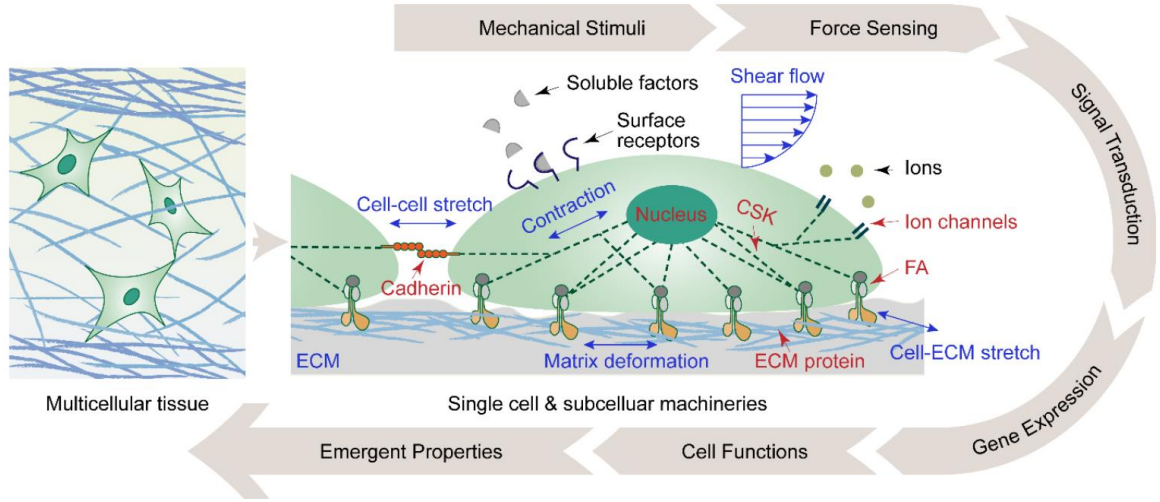

Figure 4 ***A representative scheme showing the processes and structures involved in cellular mechanosensing.*** *An initial external mechanical stimulus (such as shear flow, ECM remodelling or cell-cell contact) is sensed by the cell surface proteins which trigger a signalling cascade inside the cell. This cascade may lead to a modulation of gene expression at the nucleus that will impact on cell functions such as polarity, migration and fate. Adapted from* [42].

Signalling elements, which work in tight interaction with focal adhesion proteins, are the second set of important ingredients that contribute to the cellular tensional homeostasis and mediate cellular force responses and contractility (Fig. 5). Among the main players that can be activated at the onset of a physical stimuli, we found the Rho-family GTPases, such as RhoA, responsible for inducing actin cross-linking and remodelling, protein phosphorylation and ultimately mediating gene expression by affecting the activity of transcriptional factors [7], [43]–[45]. Another signalling pathway which can be activated through integrin sensing and has been recorded to regulate cell differentiation and proliferation, is the mitogen-activated protein kinase-extracellular signal-regulated kinase (MAPK-ERK) pathway [8], [17], [46].

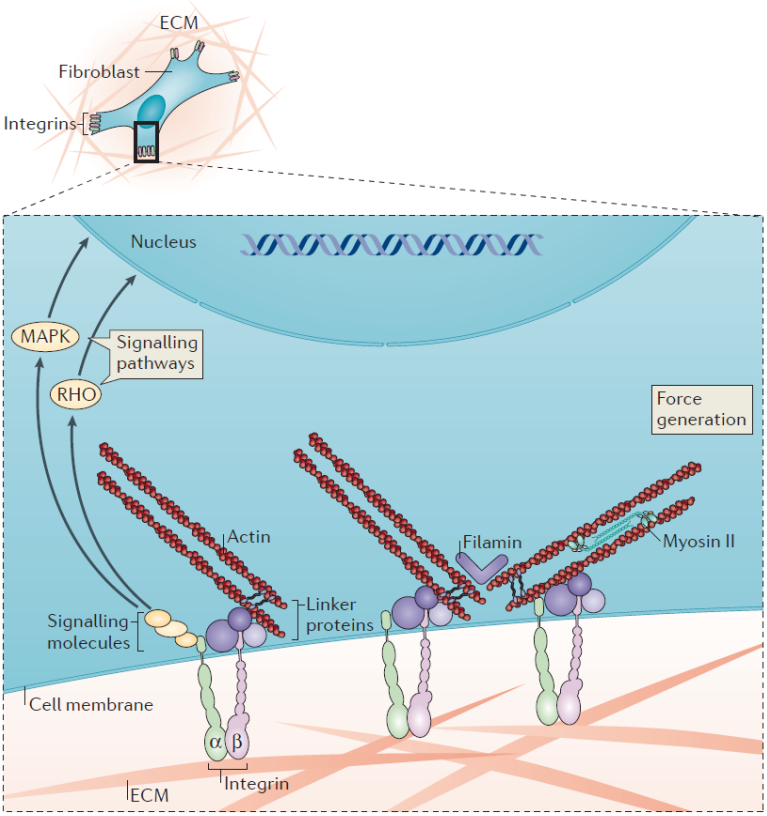

Figure 5 ***Simplified graphic depiction of the key signalling pathways connected to integrin activation in the cellular mechanosensing processes.*** *Transmembrane receptors known as integrins mediate the external mechanical interaction between the cell and the ECM while at the same time being in direct contact with the internal signalling molecules that also make up the focal adhesion complexes. Upon mechanical stimulation (communicated by the integrins) these signalling molecules will trigger the signalling cascades MAPK and Rho that will lead to gene regulation at the nucleus, and mechanical responses from the actomyosin network, ultimately affecting posterior cellular response and adaptation. Adapted from* [17].

All the sensing machinery aforementioned safeguards the mechanical integrity of the cell against an environment that subjects it to a variety of exogenous forces such as shear stress, gravity, and compressive and tensile forces [47]. The proper understanding of how mechanical signals are assimilated and transduced into biochemical responses is of paramount importance. Dysregulation or malfunction of any of these sensing elements can affect the cell and the whole tissue, leading to apoptosis or progress into pathological conditions. Moore and collaborators have reported that the inhibition of the RhoA pathway affects the developing lungs by preventing branching angiogenesis and epithelial budding [48]. Other authors have

found that erroneous mechanical response from endothelial cells to turbulent blood flows can lead to a pro-inflammatory state which can develop into atherosclerosis [49], [50]. A higher uncontrolled cytoskeletal tension as a result of abnormal stromal interaction increases the risk of expression of malignant genes leading to tumours [18], [51].

1.2.4 Extracellular matrix contribution to the cell mechanical state

Even though I have focused so far on explaining why it is so important that the cell protects itself against extracellular modifications, we are missing the other half of the story. As it was hinted by the concept of dynamical reciprocity in the opening paragraphs, the cell not only relies on external cues and physical stimuli to thrive and develop (Fig. 6), but it also exerts forces and plays an active role in modifying the mechanical properties of its surrounding. As a matter of fact, tissue rigidity and exogenous and cell-cell forces play an important role on cellular activities [47].

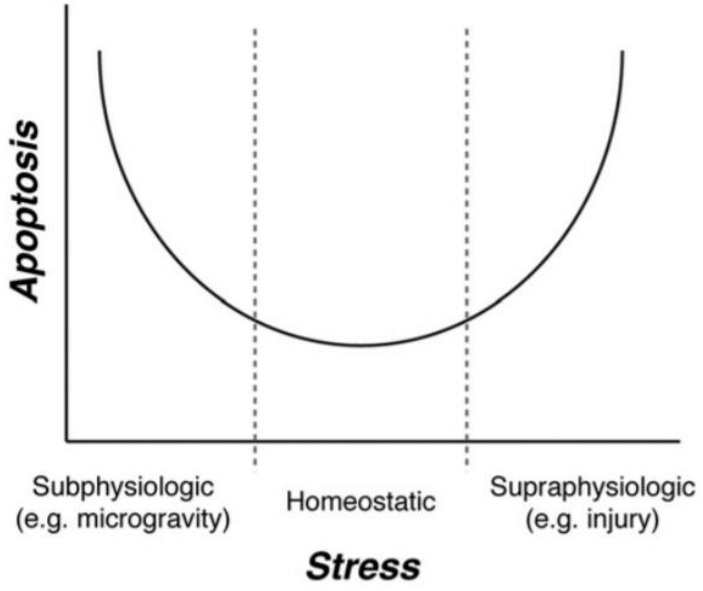

Figure 6 ***Graphic depiction of how the stress and physical stimuli from the cellular environment impact on the physiological state of the cell.*** *Similar to what it was depicted on Figure 3, this condensed graph shows a minimum of cellular apoptosis when the stress that the cell senses is within the homeostatic range, and an increase in cell death outside this range. Adapted from* [52].

Indeed, this concept of the cell relying on mechanical stimuli from the environment was also posed by Grinnell in 1994: "As long as the tissue is under mechanical stress, cell proliferation and biosynthetic activity will persist. Once mechanical stress is relieved ... cells will switch to a non-proliferative phenotype and begin to regress even in the continued presence of growth factors.'' [53].

The role of the ECM in mechanically regulating the cellular behaviour and development has been thoroughly researched in the field of mechanobiology [47], [52], [54]. Kilian et al found that geometric features which increased actomyosin contractility promoted osteogenesis while reduced actomyosin contractility drove the stem cells towards adipocytes [55] (Fig.7). Geometrical cues have been also shown to control the positioning of branching during morphogenesis of mammary epithelial cells and primary organoids [56].

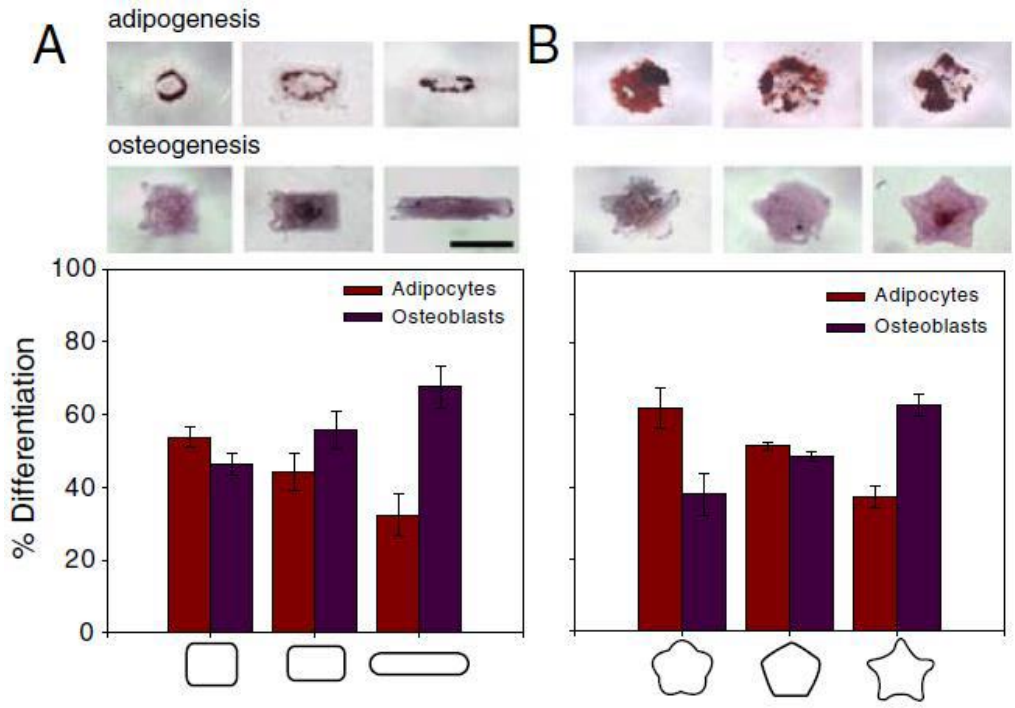

Figure 7 ***Stem cells differentiation towards adipocytes or osteoblasts based on geometrical constraints.*** *(A) Quantification of cells captured on rectangles of varying aspect ratio differentiating to adipocytes or osteoblast lineage. (B) Quantification of cells differentiating to either lineage when captured on fivefold symmetric shape. Adapted from* [55].

In the case of tissues used to high loading, such as bones and cartilage, it has been reported that reduced mechanical stimulation results in a reduction of proteoglycan content and bone mineral density [47]. Moreover, further studies have shown an enhancement in the expression on bone-transcription factors, induced by MAPK/ERK pathways, on stiff matrixes in contrast with softer matrixes [46]. Bissell and Radisky have even claimed that an effective regulation or 'normalization' of the tumour mechanical environment can help in the prevention of cancer progression [57]. The rearrangement of the ECM physical properties inflicted by cell forces and protein deposition can also lead to pathologies in case of exacerbated or altered modifications. Fibrotic diseases appear as a consequence of abnormal or elevated ECM deposition by the cell [58], and increased matrix stiffness as a result of ECM remodelling can play a crucial role in tumour progression [59].

1.2.5 Interrogating the homeostatic system

From all of what it has been presented previously, it would seem to derive that understanding the mechanical interplay between the cell and its surrounding is vital for the treatment and prevention of a variety of diseases [47]. Unmistakably, we can talk about a dynamic feedback between the internal biochemical contractile machinery and the external active generated forces, as well as a reciprocal force interaction or force feedback loop in between the cell and its environment [47]. A better characterization of the mechanical properties of cells and cellular force dynamics can improve the diagnosis of their biological state and the understanding of the pathogenic basis of diseases [60].

1.2.5.1 *Biochemical and genetic perturbations*

Several pharmacologic reagents have become a standard approach at the moment of characterizing the mechanical properties of the cell and its contractility. They consist mainly of small-molecule inhibitors, which are membrane permeable, that target different mechanosensing mechanisms and structures of the cell and are normally supplemented to cell growth medium during experiments. To recover the targeted cellular mechanism, the reagents have to be washed out from the medium. Blebbistatin has been well-established as a modulator of cell contractility by inhibiting molecular motor myosin II and thus the actomyosin network tension [61]. Polymerization processes of actin can be blocked using latrunculin or cytochalasin D [62] or enhanced by using jasplakinolide [63], a reagent known to bind strongly to filamentous actin. Nocodazole is an agent known to depolymerize microtubules and prevent FA disassembly [64]. The RhoA signalling pathway can be modulated through the use of rho kinase inhibitors such as Y27639 [65] or fasudil [66]. Upstream regulators of myosin phosphorylation such as ML-6 and ML-9 can also be used to modulate cellular contractility [67].

The molecular-genetic methods intended at disrupting the mechanical properties of the cell can target both signalling pathways and structural proteins. This tool uses two main approaches: knockdown, the expression of one or more genes is reduced (with the use of siRNA), and knockout, genetic modification that inactivates an existing gene by replacing it or disrupting it. Therefore, a perturbation can be done in the cellular mechanosensing mechanism by targeting the gene or the mRNA responsible for the studied protein enabling the regulation or inactivation of it [68]–[70]. The first method is generally reversible, unlike the second one where the targeted gene is disrupted and therefore the cell cannot express it anymore, unless exogenously added.

1.2.5.2 *Physical perturbations*

Applying controlled external mechanical stresses to cells in order to study their mechanical properties has been done in many ways for the last forty years. Techniques have ranged from the conventional micropipette aspiration [71], [72] and cell poking [73], to deformable culture substrates [74] and fluid shear stresses [75], [76]. More localized and subcellular mechanical perturbations and force measuring techniques have been made with the use of optical [77] and magnetic [78] tweezers. These methods consist on manipulating surface-bound microbeads through the use of optical traps or magnetic fields, allowing the application of mechanical inputs specifically to integrin receptors in the membrane and their linked cytoskeletal counterparts [79].

I would like, however, to focus on the attempts aimed at specifically probing and interrogating the cell tensional homeostatic system that have slowly increased in the recent years. Brown and collaborators presented tissue mechanical response against mechanical loading by using a culture force monitor where precise tensional loads were applied across a fibroblast populated collagen lattice, through a computer-controlled microdrive motor [16]. A few years later, Mizutani et al used an elastic deformable substrate to probe single fibroblast stiffness responses and concluded that the cellular mechanical response to deformations was due to actomyosin contractile tension [80]. This backed up the idea that dynamical tensional homeostasis was regulated by the tensile forces that phosphorylated myosin would generate on already existing stress fibres, and not on the reorganization of the actin network. In parallel, many studies supported the importance of motor proteins in cell mechanosensitivity and identified myosin II as a main regulator of cytoskeletal tension and, hence a mayor responsible of maintaining tensional homeostasis in dynamic mechanical environment [81]–[83].

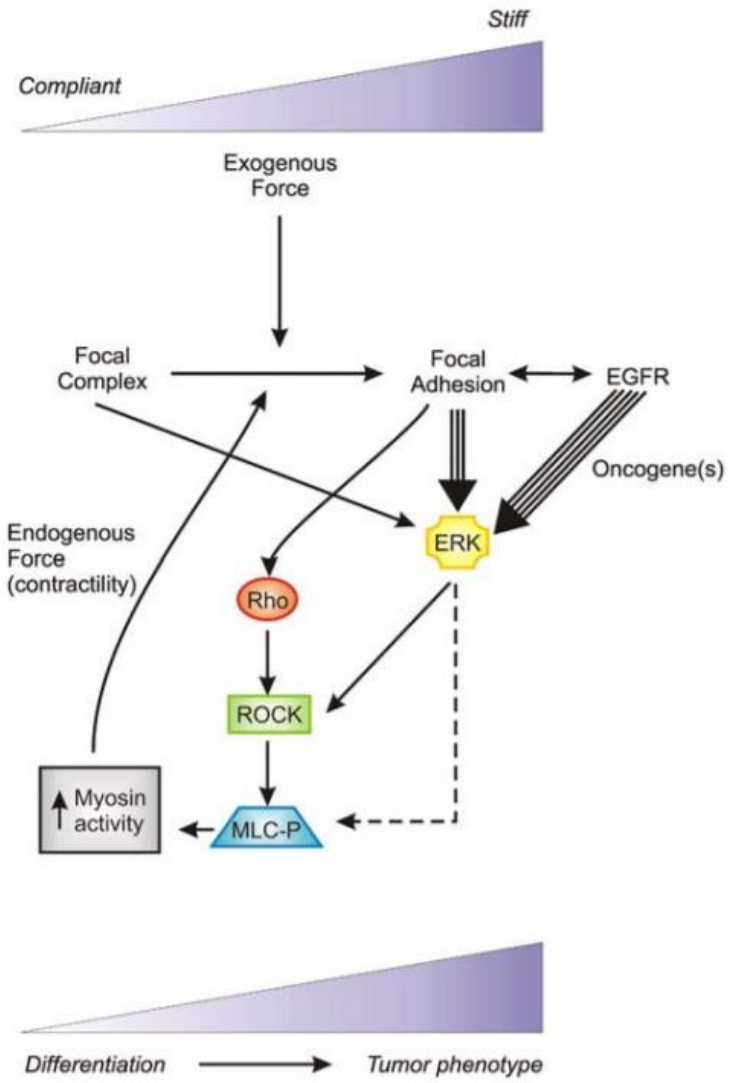

Figure 8 ***Scheme showing the dependence of the tumour-malignant transformation with the exogenous stiffness evidencing the ERK- and RHO- mechanoregulatory circuits.*** *An increase in the extracellular matrix stiffness prompts focal adhesion formation and subsequent activation of both Rho and ERK, ultimately resulting in inner cellular tension. Major matrix stiffening enhances the probabilities of oncogene activation, which may lead to "tumorigenesis". Adapted from* [84].

With the intention of probing the role of integrins and the signalling pathways known to be involved in cellular contractility (Rho and ERK), Paszek et al subjected tumour cells to a wide range of matrix rigidities (Fig. 8). Their results showed that both signalling molecules are mayor players in the cellular mechanoregulatory system which connects the physical external cues sensed by the integrins, with signalling pathways that mediate cell proliferation and tissue phenotype [84]. From these observations they concluded that the cellular tensional homeostasis is favoured

in soft matrix but in the event of an abnormal rigidity increase that persists through time, this tensional regulation can be lost leading to malignant transformations in the cells favouring the apparition of a tumour.

Although it had been demonstrated that a cell can respond to mechanical stimuli, little data had been presented to prove that there is a basal internal equilibrium stress state at the single cell level [85]. One of the first ones to do so was Fletcher and collaborators using Atomic Force Microscopy (AFM) as a direct force measurement technique, isolating the cell between a patterned substrate and the AFM tip (Fig. 9). They recorded steady-state cellular forces in time even after imposing mechanical displacement perturbations through controlled movements of the AFM cantilever [86].

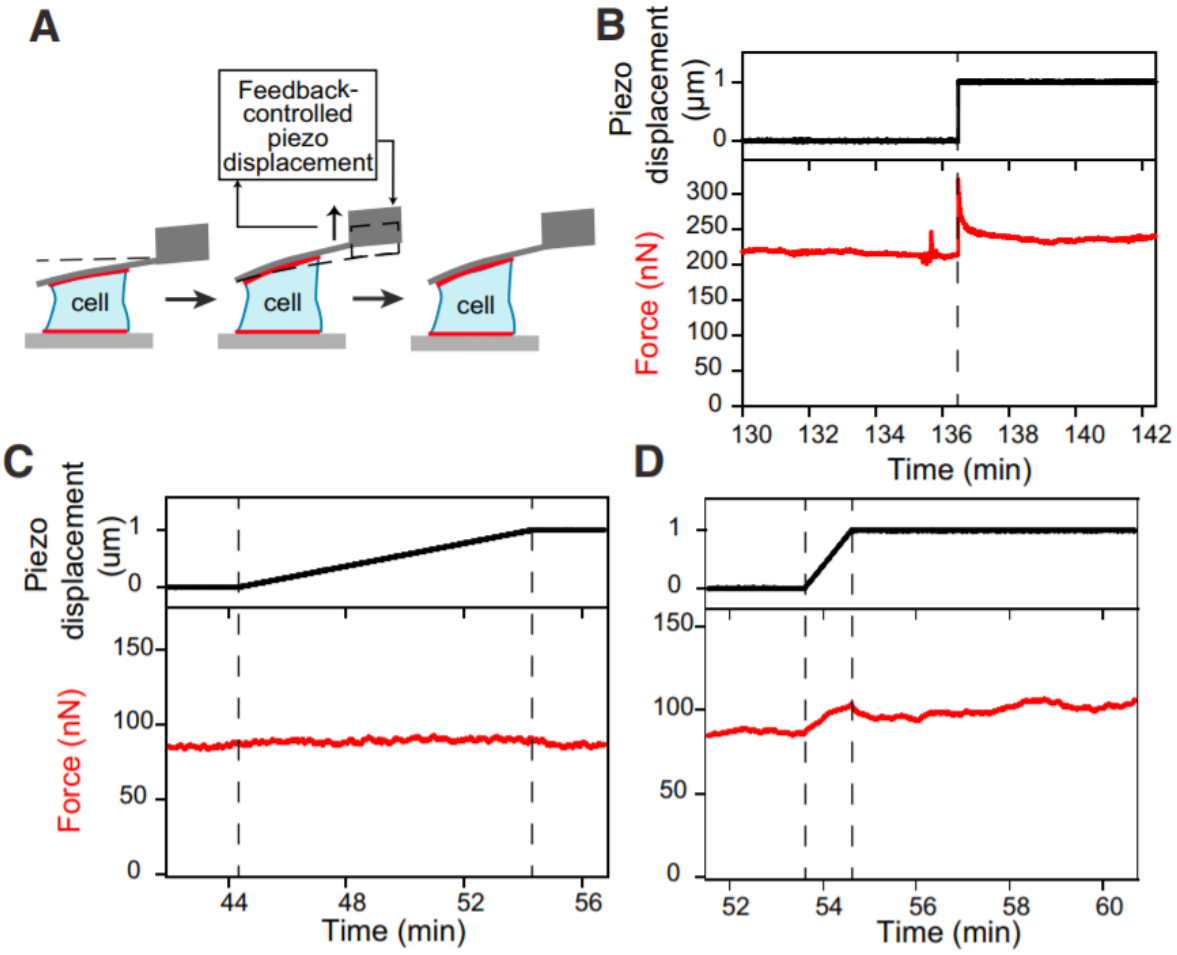

Figure 9 ***Stable tensional state and response to displacement perturbations in isolated fibroblasts.*** *(A) Depiction of the probing device. Isolating the cells between a micropatterned*

substrate and an AFM tip enables both measuring and modulating forces while also imposing displacements, as mechanical perturbations, to individual contracting cells. (B-D) Application of a 1 μm displacement in different time windows shows a force response followed by a tensional stabilization. Adapted from [86].

Very recently, Zollinger and collaborators also studied the tensional basal state both of single cells and cell clusters through the use of Traction Force Microscopy (Fig. 10). Measuring the traction forces of cells in a continuous manner, they concluded that the cellular force steady-state is in fact a cell-type dependent phenomenon [87].

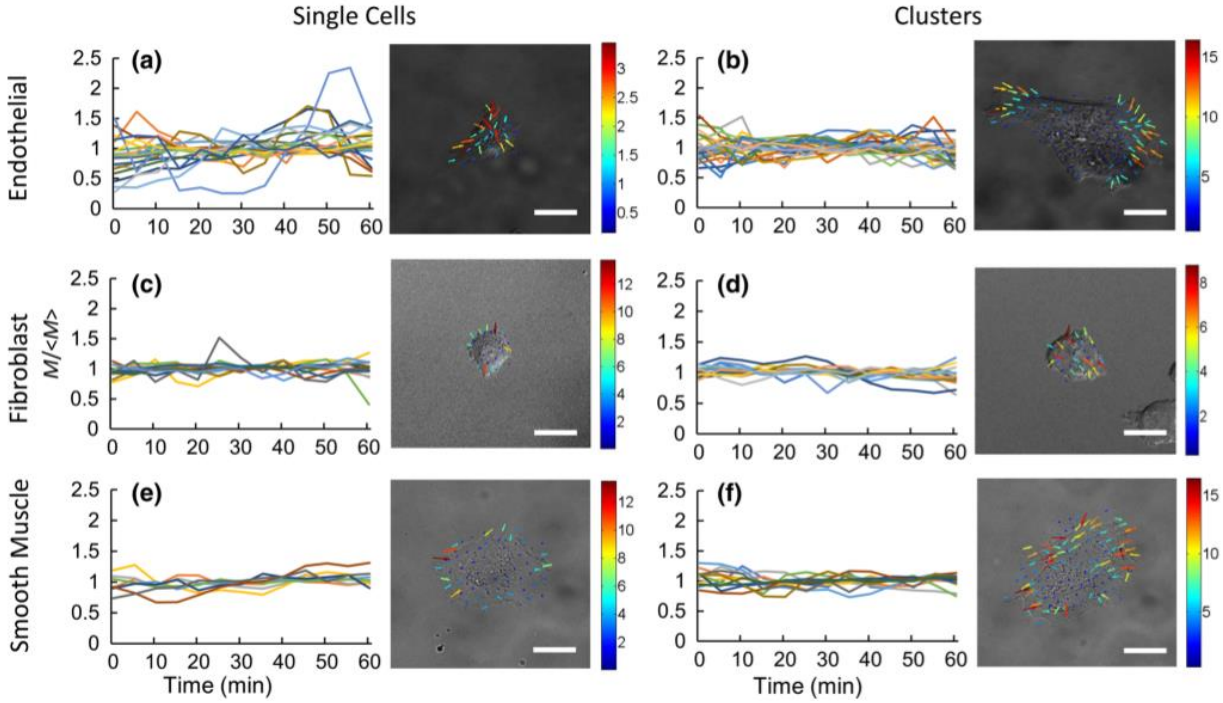

Figure 10 ***Temporal fluctuations of traction forces in isolated and clustered cells of different types.*** *(a-b) The normalized contractile moment of isolated endothelial cells presents significantly higher fluctuations than for the case of clusters. (c-f) Both fibroblasts and vascular smooth cells present steady state contractility at the single cell and multicellular scale. Forces were obtained using Force Traction Microscopy and each colour represents a different cell. The results obtained implied that the phenomenon of tensional homeostasis is cell-type dependent. Scale bars, 25 μm. Adapted from* [87].

Finally, a recent and very interesting study done by Weng et al analysed the subcellular rheostasis of the cellular mechanosensing mechanism (Fig. 11). Using stretchable micropost array cytometry and pharmacological perturbations of the contractile cellular machinery, they arrived to a biophysical model which provided a

quantitative characterization of single cell mechanical homeostasis [88]. Their results supported and re-vindicated tensional homeostasis, referred by them as mechanical homeostasis, as a single-cell phenomenon regulated mainly by the actomyosin network tension and the focal adhesions.

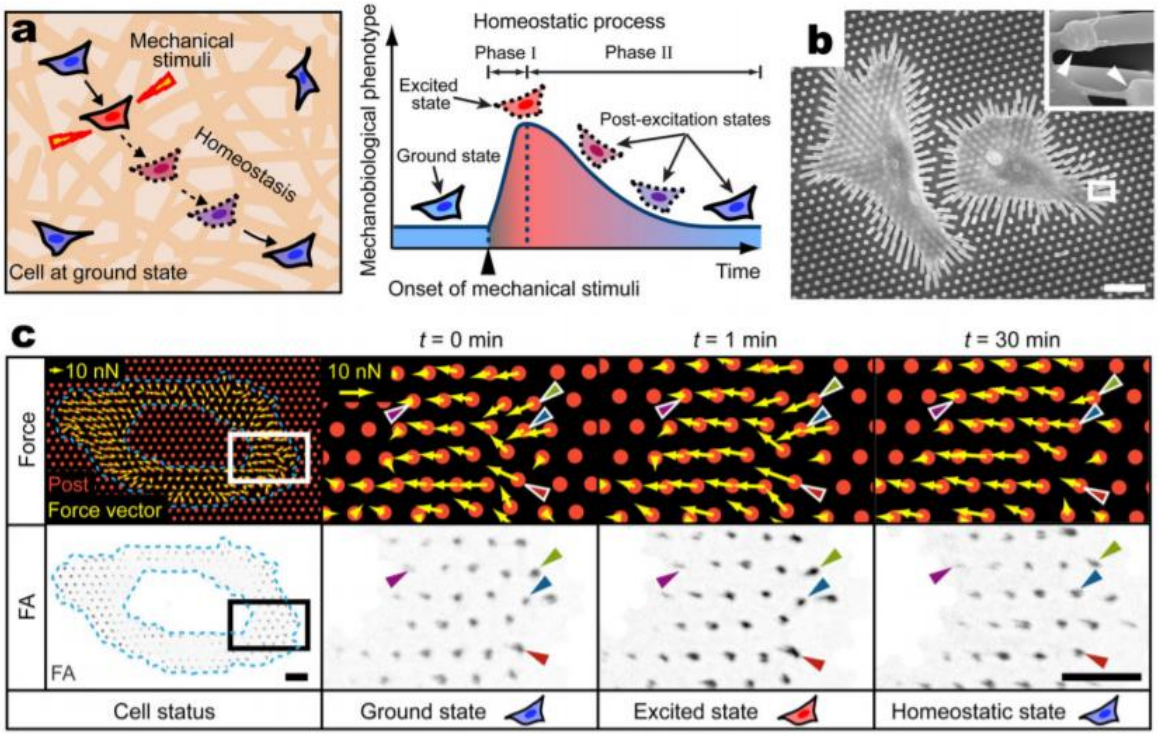

Figure 11 ***Single cell mechanical homeostasis dynamics at the subcellular level.*** *(a) Depiction of a single cell suffering a mechanical perturbation followed by the homeostatic process of regaining mechanical equilibrium. (b) Fibroblasts spread on the microposts and SEM image of the cell-micropost attachment corresponding to the white rectangle. Scale bar, 20 μm. (c) Upper row shows subcellular forces (yellow arrows) exerted on the microposts (red dots) before, during and after the mechanical stimuli. Lower row shows the fluorescently stained focal adhesions corresponding to the upper row images during the same states. The colour-coded arrowheads identify the changes in force and focal adhesions variations during mechanical stimulation. Scale bar, 10 μm. Adapted from* [88].

1.3 Summary

The evidence showing the relevance of mechanical homeostasis in crucial processes across tissue, cellular and subcellular levels is varied and irrefutable. Tensional homeostatic balance is of great importance for the cell and mechanical forces are one of the main factors controlling it. A better understanding of the major mechanisms involved in modulating cell mechanical responses when faced with external physical stimuli is needed. Much work has been done addressing this issue. However, most of the methods lack molecular specificity in their manner of stress application; they either distort whole cells or large areas of cell membrane. Moreover, many experimental approaches seeking to probe tensional homeostasis at the single cell level have coupled external mechanical perturbations to cell mechanical readouts in a unidirectional manner. But tensional homeostasis relies on the bidirectional coupling between external mechanical cues and internal biochemistry circuits. The overall process implying dynamic feedback loops.

We find that there is still work to be done and there is still a need for much better quantification so that functional interactions can be isolated and established. For this reason we decided to design a novel approach where the perturbation could be made internally, rather than externally, and with very high spatiotemporal resolution under controlled and reproducible conditions. In the following chapter I will present and describe our approach in which we coupled a dynamic input, making use of the emergent and powerful technique of optogenetics, to a dynamic output measuring tool that will record the live cellular mechanical responses, patterned traction cytometry.

CHAPTER 2 – Our approach to interrogate the cellular tensional homeostasis

2.1 Introduction

Since our aim was to study the mechanical response of a cell to dynamical and transient tensional perturbations with high-temporal and spatial resolution, we needed a better method than the traditional ones. Physical external probes such as sharp tips or stretchable substrates can provide useful information about the dynamic general cell response to physical stimuli. However, they do not allow the possibility of pulling apart the internal cell tensional mechanism and connecting a perturbation with a specific internal response. Pharmacological perturbations have proven to be very effective at controlling internal nodes but they lack spatial control and temporal flexibility, particularly when considering their reversibility speed and the possibility of using them in multiple off-on cycles [89], [90]. Similar limitations are present when using genetic perturbation techniques, such as mutations, knockdowns and siRNAs [91], [92]. These are highly specific but relatively slow and broad in their effects with very little to none modulation possibilities causing generally permanent perturbations.

Therefore, we turned our focus towards a more recent and powerful method that offers precise spatio-temporal perturbations and live-cell signalling activity readouts: optogenetics. In the following section I will briefly review how this approach was developed and the impact it has had in the scientific community. Afterwards, I will describe it in the context of my project.

2.2 Optogenetics

It could be argued that using light to interfere in biological structures and processes is not a novelty. Biologists had already been using a few light-based methods to probe biological systems before the appearance of optogenetics. Such is the case of laser ablation and laser inactivation. These techniques enable high spatiotemporal resolution at the moment of inhibiting proteins, by destroying them [93], or understanding the role of cellular structures by simply ablating them [94].

However, not only these approaches can entail unwanted cytotoxic effects, but they also lack modular and reversible characteristics. Not to mention the fact that with these tools, biological signals or structures can be disrupted or destroyed but not triggered or induced.

Optogenetics, on the other hand, brought about the possibility of intervening in biological processes in a highly precise, robust, reliable and reversible manner, hence revolutionizing science.

Figure 12 ***Optogenetic system plugged to the head of a mouse****. By selectively inserting opsins—which react to light—into them, neurons can be activated or inactivated for research purposes Then, when light shines on the brain through optic fibres, only those neurons will respond and induce a certain behaviour in the studied animal. Early behavioural applications of the technique induced mice to act in certain, easily observable ways (left). A simplified graphical representation of a light-gated ion channel activated by light (right). (Source: Optogenetic methods Julich, John B. Carnett/GETTY).*

Everything started when the Rhodopsins came into play back in the 70s. Rhodopsins are biological light-energy transducers and abundant phototropic mechanisms. They were first found in the early 1970s in the archaeal halophiles where their main function was as proton pumps used to generate a light-driven proton gradient as a source of energy for the cell. However, it was not until the year 2000 when, thanks to metagenomics, they were found in green algae Chlamydomonas reinhardtii [95]. This allowed for better isolation and characterization of their function. As a result, in the following years Nagel and collaborators described two membrane channel proteins responsive to blue light which when hit by blue photons, would suffer a conformational change, regulating the flow of positively charged ions [96], [97]. Having the genetic code for this membrane channel proteins there was no need any more for injecting light-sensitive reagents into cells as they would be the ones expressing them. From then onwards, the bioengineers took the lead. In 2005, Boyden and Deisseroth were the first ones to publish their achievement of using channel rhodopsin II for light-induced firing neurons with unprecedented time and spatial resolution, opening officially a new field: optogenetics [98] (Fig. 13). Allowing precise neural activity control, this tool revolutionized neurobiology, consequently being chosen method of the year in 2010 by Nature methods.

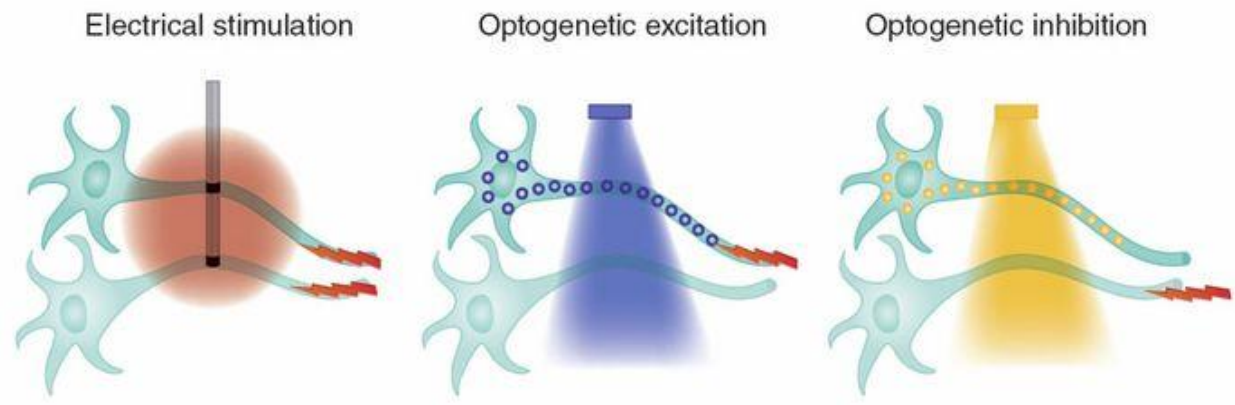

Figure 13 ***Working principles of optogenetics.*** *Electrical stimulation would induce a generalized action potential in the neuron axons that are in the vicinity of the electrode. Optogenetic allows for a selective excitation or inhibition of neurons action potential happening only on photosensitive cells. Adapted from* [99].

Although neuroscience was the first field to exploit and make use of this technique, the versatility and efficiency of the method attracted the rest of the scientific community [99]. Further tools and approaches where discovered and developed since then, turning optogenetics into a technique that enables real-time precise control of cellular processes, cells, networks and animal behaviour by using light-activated proteins that affect membrane voltage or intracellular signals [100].

Several optogenetic systems have been designed to control spatio-temporally the activity distribution of a protein with such accuracy and specificity that activation is possible even at the subcellular scale. Moreover, these light-based perturbative tools fulfil the following properties: reversibility, are rapid and modular, and they allow for a direct readout of light-induced activity. The potential cytotoxicity of this method is almost negligible due to the fact that the light energies and wavelengths used to activate the photo-sensitive systems share the same range as the ones used for optical imaging [92].

The working principle of these systems when subjected to light is based either on the significant conformational change of its main protein or on the high affinity in between two components (Fig. 14). The first case refers to a light-switchable allostery, meaning that the presence of light causes a conformational change on the photosensitive protein that can switch it to its active mode, a membrane channel for example. The second case exploits the association capabilities of two components. Being one of the two sensitive to light, it will suffer a conformational change when subjected to light that will strongly increase its affinity towards the other component. Both components by themselves have no signalling or triggering capabilities but can be easily coupled to other proteins or to specific parts of the cell. As a result, a target protein can be localized to a precise part of a cell or two separate components can be brought together to trigger a response through the use of the photosensitive system. Each of these systems has their practical considerations and has been used based on their advantages and adaptability.

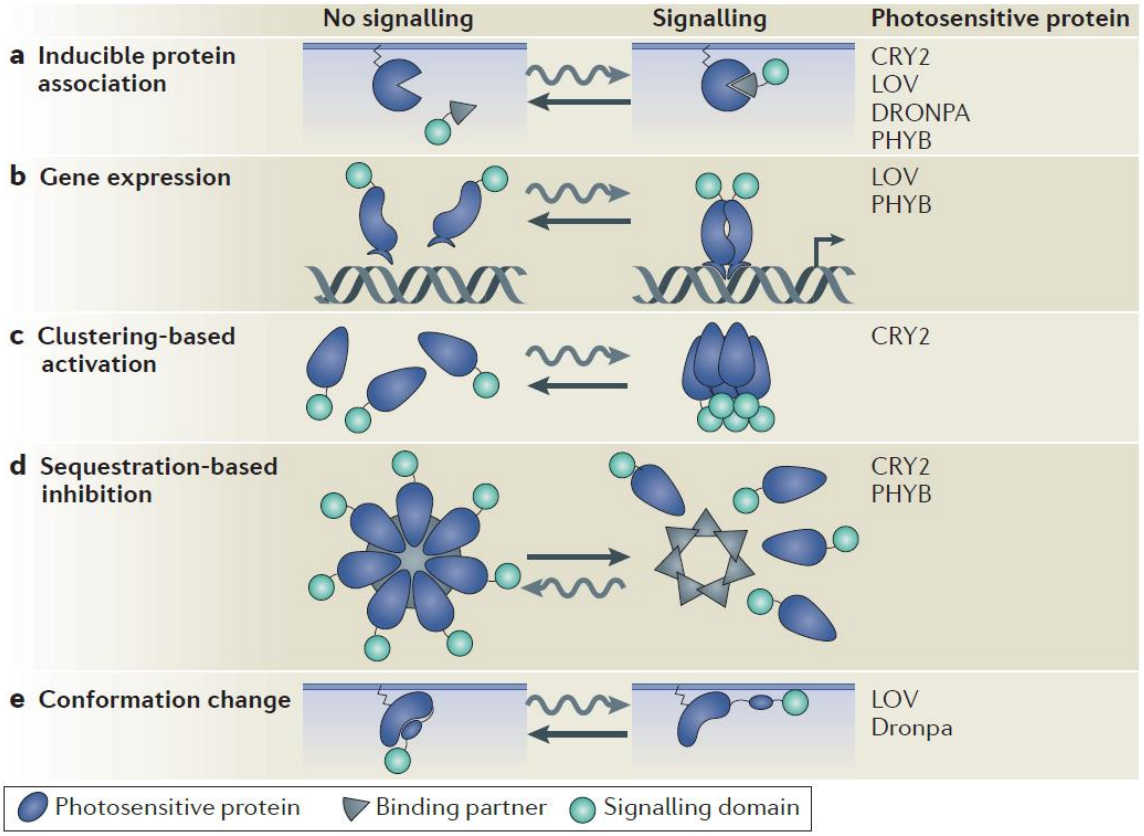

Figure 14 Different optogenetic approaches depending on the process studied and the photosensitive protein. Adapted from [101].

2.2.1 The PHYTOCHROME B (PHYB) protein and PID6.

First one to be used to enable light-controlled protein translocation, described by Levskaya et al [102], is an optogenetic system obtained from the Arabidopsis thaliana phytochrome signalling network. Upon red light (650 nm) illumination PHYB binds to its natural interaction partner, phytochrome interaction factor 3 (PIF3), and it dissociates when subjected to infrared light (750 nm). Depending on the biological process under study, the fact that a direct inactivation is needed gives higher control and temporal resolution to the experimentalist. The main issue with this system is the requirement of a chromophore only present in photosynthetic organisms, thus the need to be exogenously added when studying non-photosynthetic systems.

2.2.2 The CRYPTOCHROME 2 protein (CRY2) and CIB1/CIBN.

Cryptochromes (Crys) are photoreceptors found almost in every living being. They require a ubiquitously expressed endogenous flavin adenine dinucleotide (FAD) chromophore that is characterized by blue light-induced reduction. CRY2, the most widely used cryptochrome, has been found in A. thaliana and upon blue-light exposure (405-488 nm) it homo-oligomerizes and binds to its partner, CIB1 (cryptochrome-interacting basic helix–loop–helix 1), within seconds. Dissociation and return to initial state of both previously activated components happens spontaneously after ~5 minutes in the dark. In 2010, Kennedy et al described an enhanced Cry2-CIB dimerization system where only the N-terminal photolyase homology region (PHR) of the CRY2 was used and a shorter N-terminal version of CIB1 (CIBN) was tested. This modification rendered a smaller and more versatile dimerization system. In that same work they presented what is known as the split protein approach, where the protein under study is expressed as two inactive fragments that upon light absorption reconstitute into a functional protein [103].

2.2.3 The LOV (Light-oxygen-voltage-sensing) domains.

This optogenetic system consists mainly on the LOV sensory domains which have been described in several different organisms and which also use the ubiquitously expressed endogenous flavin as a chromophore. Hence, these domains are all sensitive to blue light (440-473nm). As a first strategy it can be used allosterically by changing conformation upon blue light and allowing, as a result, the activation of a protein of interest bound to it [104]. The second strategy was described by Yazawa et al in 2009 using the blue light-activated dimerization between the LOV protein FKF1 and GIGANTEA, an interacting protein obtained from A. thaliana, to direct the localization of a signalling protein to the membrane in order to trigger a specific

signalling cascade [105]. A third strategy consists on using the light-induced homodimerization of a LOV domain bound to DNA, thereby regulating gene expression [102][101].

The pursuit of a smaller system, with enhanced capabilities and tunable properties led, three years later, to the appearance of what Strickland et al decided to call TULIPs. Tunable, light-controlled interacting proteins (TULIPs) derived from the LOV2 domain of Avena sativa phototropin 1 (AsLOV2) and its synthetic interaction with an engineered PDZ domain (ePDZ). Through bioengineering and mutation, TULIPs offer a tunable range of binding and kinetic parameters which makes them easily adaptable to signalling pathways with diverse sensitivity and response times [106].

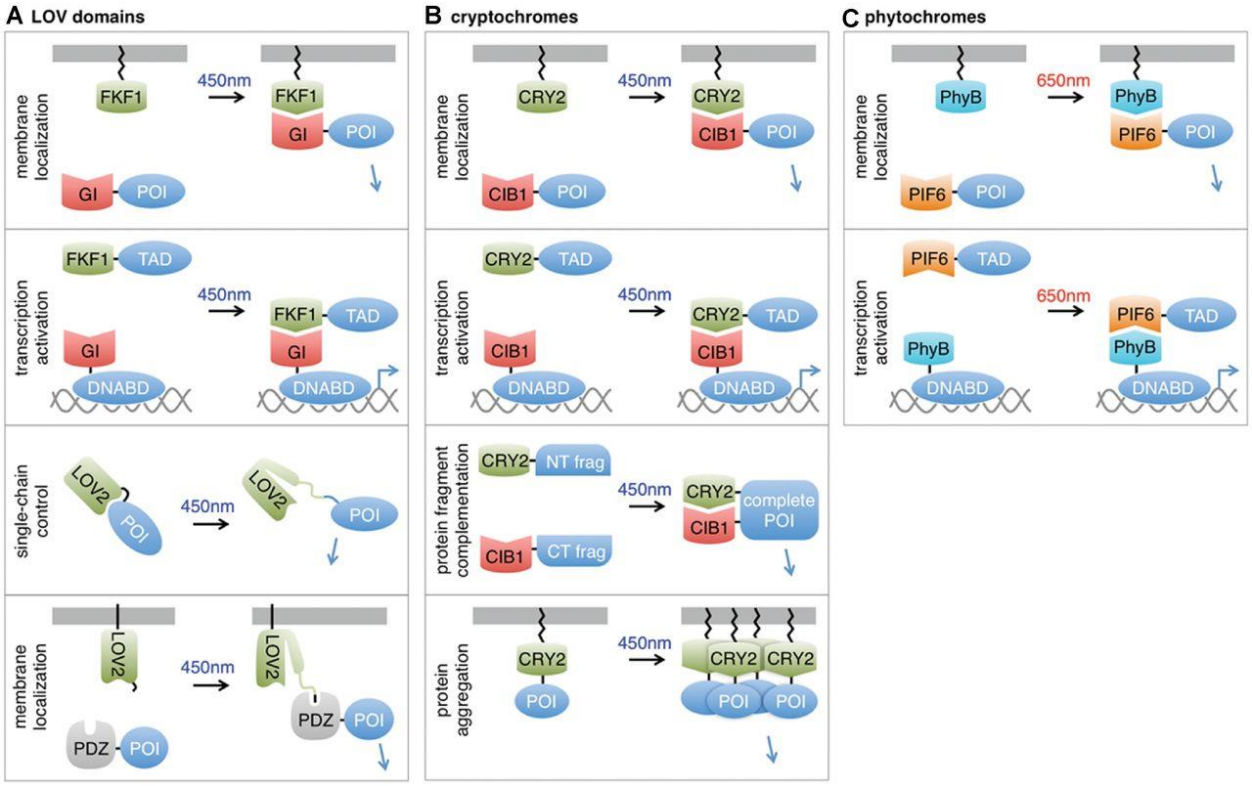

Figure 15 Proposed applications for three most widely used photosensory proteins: LOV domains, cryptochromes and phytochromes. Adapted from [107].

2.2.4 *The Dronpa protein.*

This tool is based on fluorescent protein-based interactions that do not need small-molecule chromophore. Upon light activation (390 nm) the quaternary structure of the Dronpa protein monomer changes inducing a dimerization of the system. The activity of a protein of interest can be modulated by fusing it to a Dronpa monomer and inducing dimerization with light, flanking it and thus inhibiting its function. Shining light at a wavelength of 490 nm reverses the system to the monomer state reactivating, at the same time, the protein of interest [108]. In contrast with the previously discussed approaches, Dronpa can be used to target proteins that cannot be controlled by relocalization. Moreover, the inherent fluorescence of this protein anticipates the need for an exogenous reporter or biological endpoints, reducing potential variability or delay in measurements [109].

Table 1. Optogenetic Tools for Controlling Protein-Protein Interactions and Protein Oligomerization

Optogenetic Interaction System, Chromophore and Color of Activation	Advantages (+) and Disadvantages (−) of the Tools
Phytochrome	
→ PhyB-PIF3/PIF6	+ bimodal switchable
Bilin chromophore	+ deep tissue penetration of red/far-red light
Activation by red light (660 nm), far-red inactivation (730 nm)	+ color tuning possible using different bilin variants
	− chromophore not ubiquitously available
LOV domain	
→ FKF1 and GIGANTEA	+ ubiquitous chromophore availability
→ AsLOV2-peptides	+ tuned variants with different time constants and affinities
→ TULIPs	+ high dynamic range of improved variants
→ Magnets	+ small size of LOV domain
FMN chromophore	− no color tuning
Activation by blue light (470 nm)	
Cryptochrome	
→ Cry2 and CIB(N)	+ ubiquitous chromophore availability
FAD chromophore	+ tuned variants with different time constants and affinities
Activation by blue light (470 nm)	+ high dynamic range of improved variants
	− large protein size
	− no color tuning
Fluorescent proteins	
→ Dronpa K145N	+ bimodal switchable
Cys-Trp-Gly as chromophore	+ GFP-based: small protein, tunable
UV/cyan (variable)	− UV light for activation
	− low dynamic range
	− only homodimerization

Figure 16 Contrasting the different optogenetic systems described. Adapted from [110].

2.3 State of the art of optogenetics in mechanobiology

Recapitulating, the optogenetic technique allows for a reliable, robust probing of the system, at the subcellular scale, with precise doses and repetitions, highly modular and reversible, and capable of targeting varying steps in a signalling cascade (Fig. 17). In other words, it enables the opening of the biochemical circuit's black box to study each part of it with precise resolution and in a time-controlled manner.

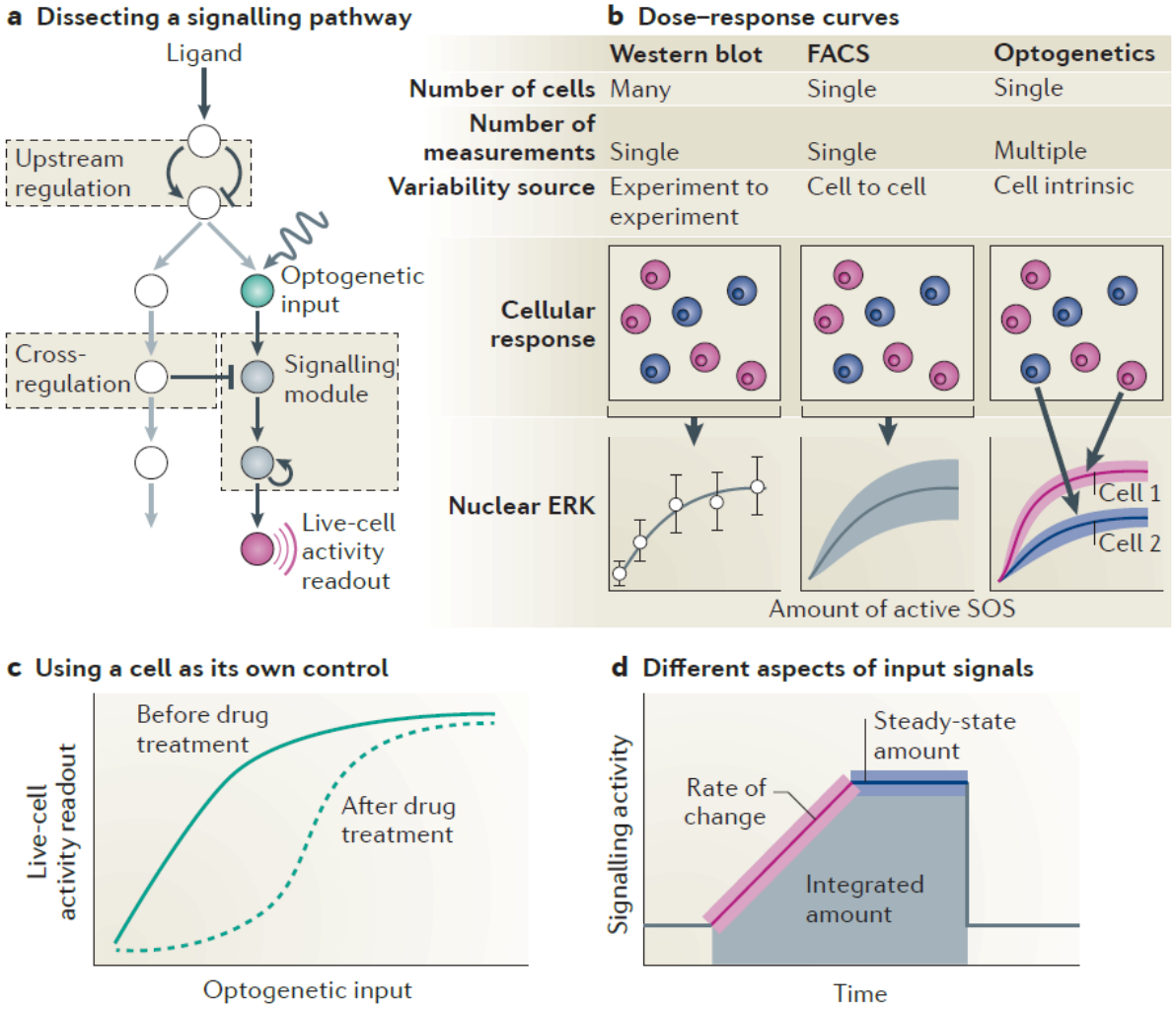

Figure 17 ***Benefits of optogenetic approaches in cell signalling and biochemistry.*** *(a) Targeting a specific node in a signalling pathway to better understand the intermediates involved in it. (b) Possibility of studying single cell response avoiding distortion of data from multiple heterogeneous cells. (c) Being a reproducible and non-toxic method, the same cell can be probed in different conditions and be used as its own control. (d) The intensity of light stimulation can be modulated, hence obtaining a modulated activity or response in the cell. Adapted from* [101].

Since its discovery it has been given a diverse range of applications such as, controlling the firing of neurons [98], modulating protein activity [111], gene expression regulation [112], [113], inducing signalling cascades [102], and even for metabolic engineering processes [114], among others.

It is not surprising then that the field of mechanobiology decided to make use of optogenetic approaches. As it has been discussed in the first chapter, the mechanosensing machinery of the cells consists of both structural components and signalling pathways. With the aim to better understand these intracellular pathways and the interaction of the proteins involved in the cellular mechanical responses, recent work has been done to couple them to optogenetic probes.

At the multicellular scale, a CRY2-CIB1 protein dimerization system was used to better understand the role of cell contractility during embryonic development by inducing cortical actin polymerization and cell contractility through the activation of a phosphoinositide PI(4,5)P2, a regulator of actomyosin contraction [115]. This approach enabled the analysis of the spatial range of force integration necessary to drive collective contractions and tissue invagination in a drosophila embryo with high spatio-temporal resolution [116].

Moving to the single cell level, in 2009, Yi Wu and colleagues designed a photoactivatable Rac1 protein to study its activity in cells by sterically blocking its interaction capabilities with a photosensitive LOV domain. Rac1 is one of the main members of the Rho-family GTPases, involved in the regulation of actin cytoskeletal dynamics, ultimately inducing the formation of protrusions rich in actin at the cellular edges [117]. By reversibly and repeatedly activating Rac1 to drive localized cell protrusions and ruffling, they could better understand the role of Rac activity in the generation of polarized cell movement [104].

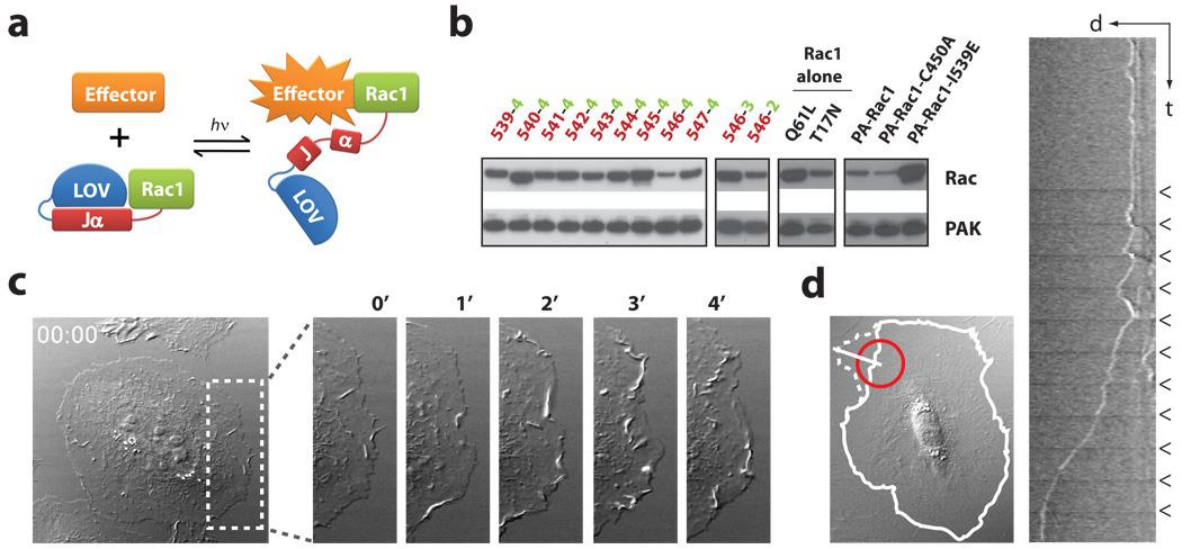

Figure 18 ***Working principle and cellular response to the activation of the photosensitive Rac1 construct.*** *(a) Graphic depiction of the optogenetic set-up used. Upon irradiation the LOV domain detaches from Rac1 triggering its activity. (b) Mutant Rac1 was obtained to diminish unwanted interactions with growth factors. (c) Light activation of a HeLa cell. (d) Localized photoactivation (red circle) evidencing the formation of ruffles and protrusions after repeated light pulses. Adapted from* [104].

The scope was extended shortly after to the other two important Rho-family GTPases Cdc42 and RhoA. Cdc42 drives, as well as Rac, the polymerization of branched actin via the activation of Arp2/3, inducing in this case the formation of filopodes and focal adhesion there where the filopodes contact the substrate (Fig. 18). RhoA, on the other hand, regulates the myosin activation, its crosslinking with the actin fibres, the presence of stress fibres enriched in actin and the formation of focal adhesions. Levskaya et al presented a light-switchable system based on the Phy-PIF interaction to induce translocation of the guanine nucleotide exchange factors (GEFs) responsible for the activation of the Rho- and Ras-family small G-proteins under study. Results demonstrated a global cell body contraction when triggering the recruitment of RhoGEF with light, and the possibility of inducing localized lamellipodia and actin assembly through the high spatiotemporal regulation in the activity of Rac and Cdc42, respectively [102].

Having proven to be an important modulator of cell contractility and stress fibre formation, RhoA and its signalling pathway have been in the spotlight these last few

years. Taking advantage of the precision and high specificity of the optogenetic approach, Rao et al used a LOV2 domain to photoactivate a downstream effector of the RhoA signalling pathway, a diaphanous related formin mDia1. This enabled a better characterization of this signalling domain showing its role in inducing filopodia, lamellipodia and F-actin formation, and uncoupling it from the cell contractile response [118].

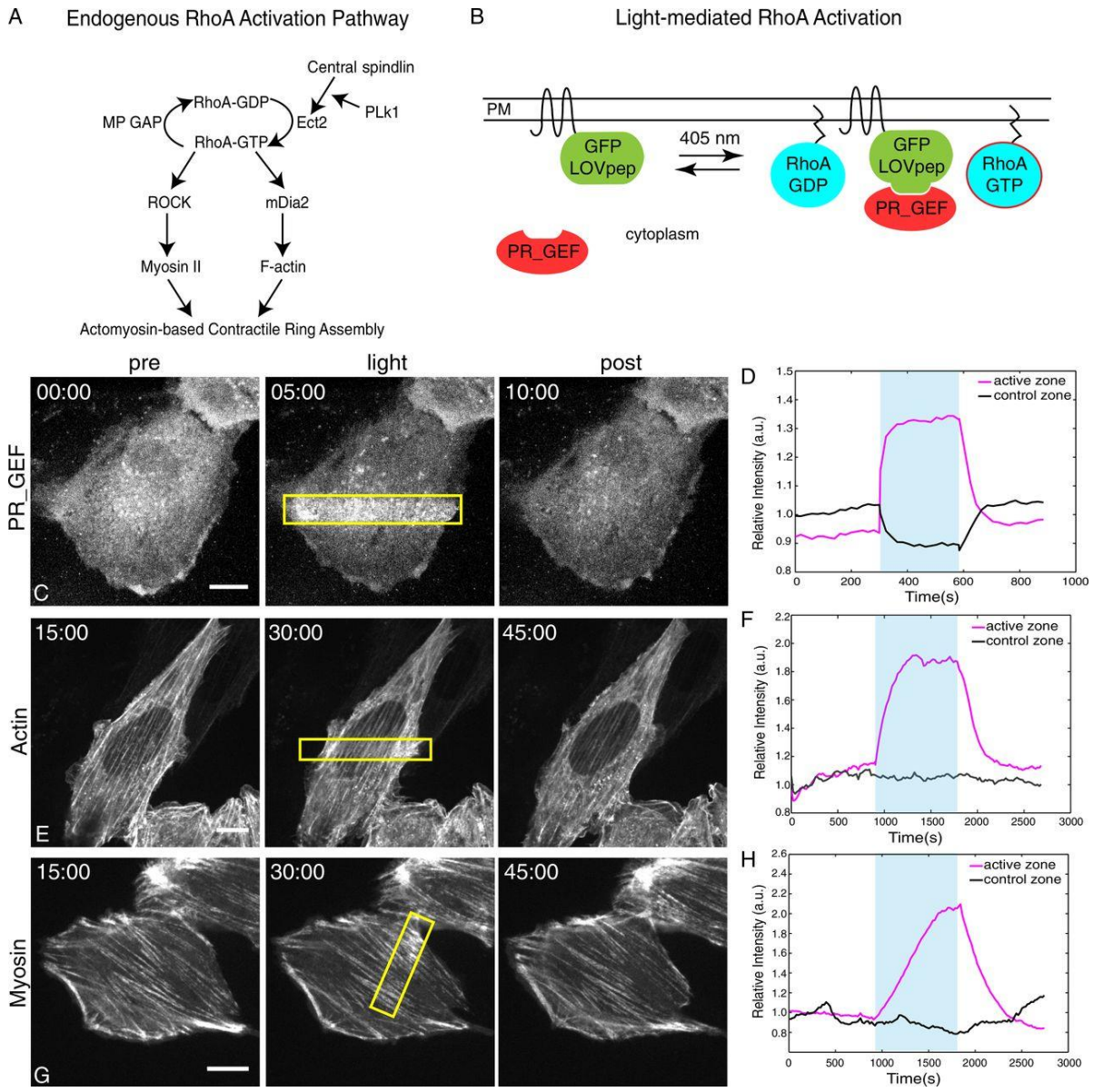

Figure 19 ***Working principle and cellular response to RhoA light activation.*** *(A) Scheme showing the RhoA signalling cascade. (B) Cartoon depicting the activation of RhoA through the recruitment of GEF to the membrane using a TULIP optogenetic set-up. Images and quantification of the relative fluorescence intensity increase upon activation of GEF recruitment to the membrane (C-D), F-actin polymerization and reinforcement (E-F) and myosin accumulation (G-H). Scale bar, 10 µm. Adapted from* [119].

As RhoA has also been shown to be involved in cytokinesis, TULIPs were used to gain precise and tight control of RhoA activity, through the photoactivation of RhoGEF, in order to better define the spatiotemporal regulatory logic of the contractile ring assembly at the final stage of cell division [119] (Fig. 19).

All the work previously described had managed to expand our knowledge on how mechanotransductory signalling pathways work and can be regulated. However, not much had been done in understanding the dynamics of cellular force production and the force interaction with the extracellular matrix. To start addressing this, Valon and collaborators designed a system similar to that of Levskaya et al where the GEF catalytic domain responsible for the activation of Cdc42 (Intersectin) [120], or RhoA (RhoGEF) [121], was recruited to the cellular membrane or the mitochondria membrane. They introduced the CRY2/CIBN optogenetic system in MDCK cells and claimed to obtain a higher recruitment yield compared to PHYB/PIF6 or TULIPs [120] in a reproducible and easy to set up way. Through single and repetitive photoactivations of the RhoA pathways they could measure cellular traction force changes in a non-toxic and highly versatile manner, thus establishing an efficient and reliable tool for interrogating and controlling cell contractility and tissue deformation with a large dynamic range and a temporal control of a few tens of seconds [121] (Fig. 20).

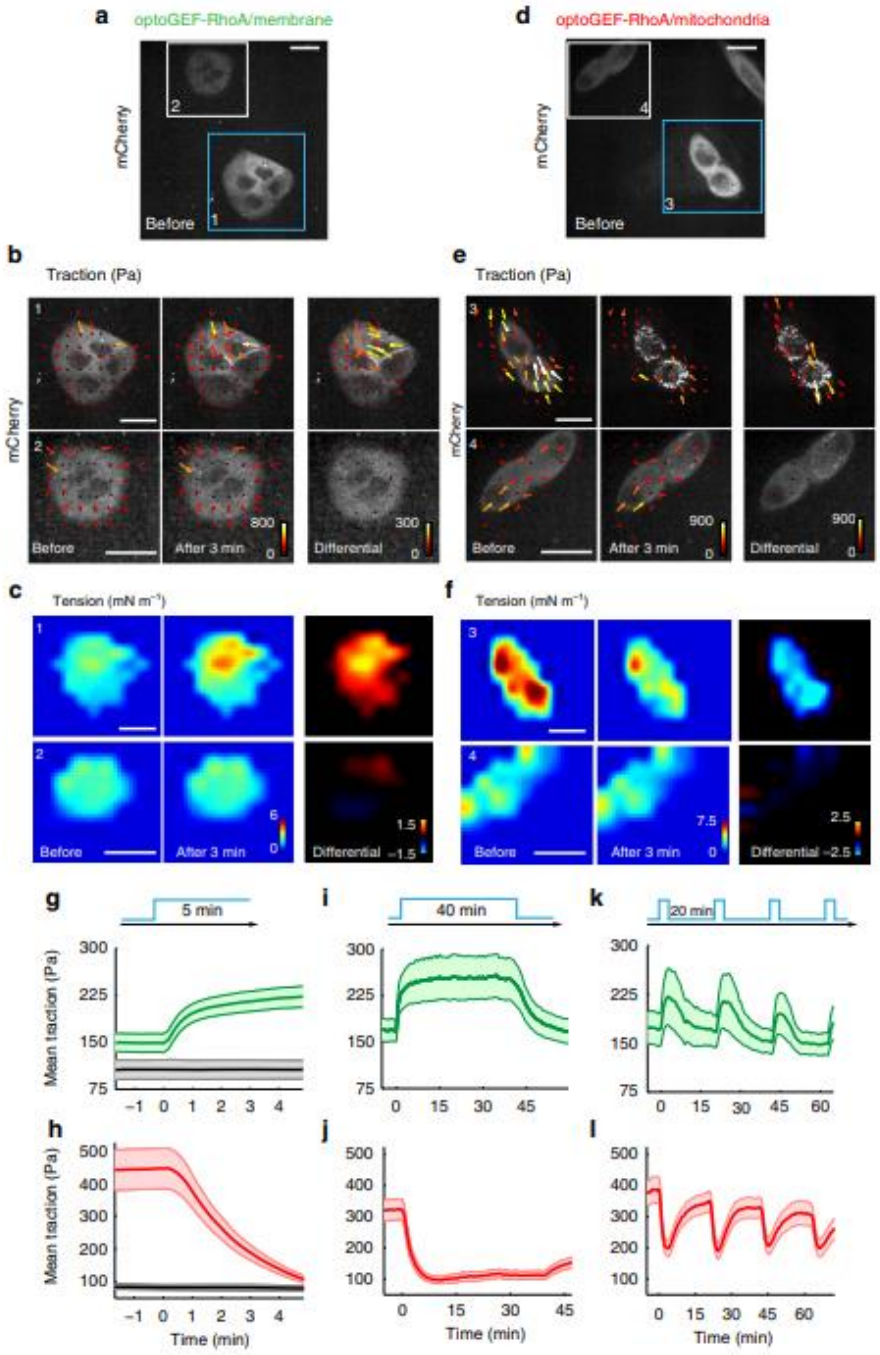

Figure 20 ***Modulation of cell contractility by optoGEF-RhoA translocation.*** *(a-f) Clusters of cells expressing the optoGEF-RhoA construct and their response before and after photo-activation. (g, I, k) Mean traction profile of cells expressing optoGEF-RhoA that will translocate to the cell membrane upon light stimulation. Force peaks can be observed during light exposure. (h, j, l) Mean traction profile of cells expressing optoGEF-RhoA that will translocate to the mitochondria membrane upon light stimulation. Decrease of force can be observed during light exposure. Scale bar, 20 μm. Adapted from* [121].

In parallel, Oakes and collaborators used a similar approach but based on the LOV/PDZ interaction, in order to subcellularly activate the RhoA pathway and delve into the dynamics of actomyosin-based force generation [43] (Fig. 21). Their

experimental result, along with a molecular model presented in their work, demonstrated the elastic behaviour of stress fibres and identified zyxin, an established mechanosensitive protein [122], as a regulator of stress fibre mechanics.

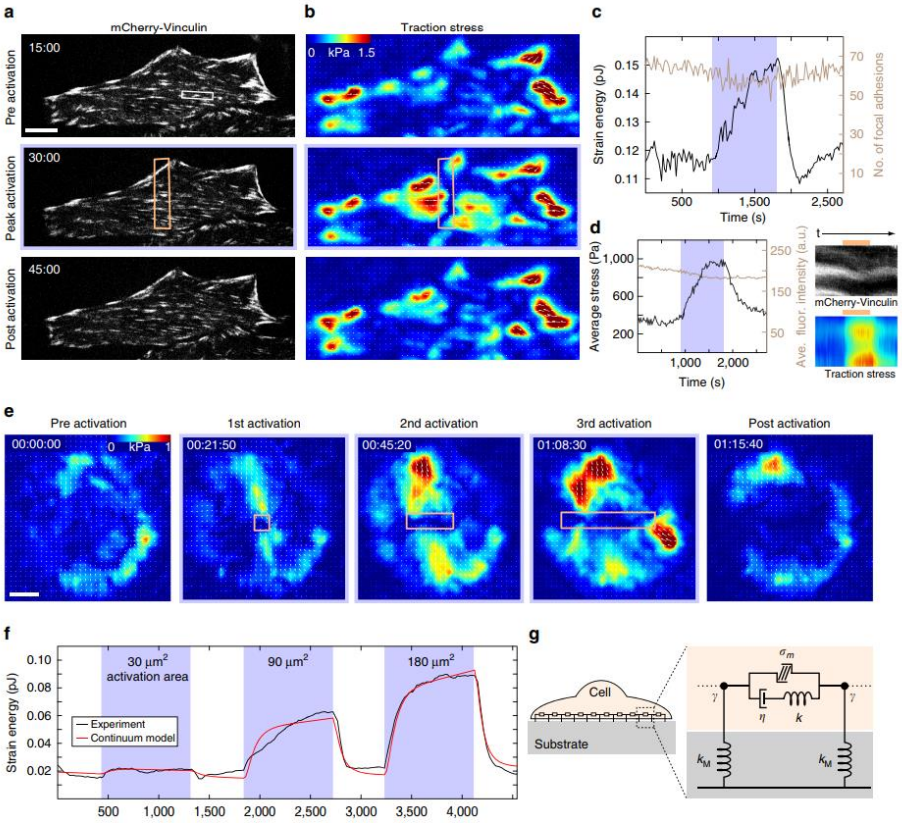

Figure 21 ***Cell contractile responses to increasing sub-cellular RhoA activation areas.*** *(a-b) Evolution of stained vinculin and traction forces in a cell before, during and after photo-activation. The orange box indicates the stimulated region. (c) Quantification of the strain energy and average number of focal adhesions in time before, during and after a period of light stimulation. (e) Traction force images showing the force increase with sequential number of photo-activations and augmenting light illuminated region (orange box). (f) Time plot of the experimental (black line) and theoretical (red line) contractile response to photo-stimulation in activation areas with increasing size. (g) Schematic of the biophysical model used to describe the cell behaviour. Scale bar, 10 µm. Adapted from* [43].

The work done by both last authors addressed and restated the tensional homeostatic mechanism present in the cell, while at the same time presented optogenetics as an ideal tool to interrogate such dynamic mechanism.

The optogenetic approach presented in this work is the one developed by Valon et al to characterise RhoA signalling and induce cell contractility and traction forces. I will talk about it in the following section.

2.4 Our probing system

2.4.1 The optogenetic set-up: CRY2/CIBN RhoA activation

Briefly recapping, RhoA is a major regulator of cell contractility through the promotion of actin polymerisation via the downstream effector Diaphanous-related formins (Dia) and the phosphorylation of myosins via Rho-associated kinase (ROCK). In addition, the activity of RhoA regulates the enrichment of stress fibres and focal adhesion formation [45]. Being a clear modulator of the cellular mechanosensing mechanisms, and following the lead of the previously presented works, we decided to focus on the RhoA pathway as a way to interrogate the cellular tensional homeostasis.

To do so we obtained the fibroblast cell line engineered by Leo Valon during his PhD thesis at Dr. Coppey's lab, Curie Institute, Paris. We decided to use fibroblasts as a model cell system based on their normal exposition to tensional inputs in their natural microenvironment, and also due to their previous use in tensional homeostasis experiments. This NIH 3T3 optoARHGEF11 fibroblast cell line has a plasma membrane CRY2/CIBN optogenetic system composed of two proteins expressed by the cell: CIBN-GFP-CAAX (CIBN) localized at the cell membrane with a CAAX anchor and CRY2PHR-mCherry-ARHGEF11 (CRY2), which is initially cytoplasmic. This CRY2/CIBN optogenetic construction to activate RhoA was developed during Dr. Valon's PhD project [123] and used in a scientific publication to activate Cdc42 [120]. Such a system does not require the addition of any exogenous chromophore. When the cell is subjected to blue light (460 nm), CRY2 is recruited to the plasma membrane with a time window of a few seconds (Fig. 22). Recruitment to the membrane of the nucleotide exchange factor ARHGEF11 triggers

the activation of RhoA, which is naturally anchored to the cell membrane by its C-terminus. Taking into consideration the fact that most intracellular signalling pathways are slower than the time of recruitment, the light-induced perturbation can be assumed to be instantaneous [120].

The advantages of using this approach are manifold. In the first place, having a cell transfected with a RhoA activator instead of RhoA itself ensures that, upon blue light, the cell contractile response will be triggered by endogenous levels of RhoA. Respecting these endogenous levels guarantees that the cell's tensional homeostatic response is the closest to the physiological one [121]. Secondly, the specificity of the tool ensures no other pathway or secondary protein to be activated apart from RhoA. Moreover, the amount of activated RhoA is directly proportional to the amount of blue light used, thus allowing for a modulated perturbation and an accordingly modulated homeostatic response. The versatility and reproducibility of the method allows for different activation cycles done on a same single cell without affecting its viability.

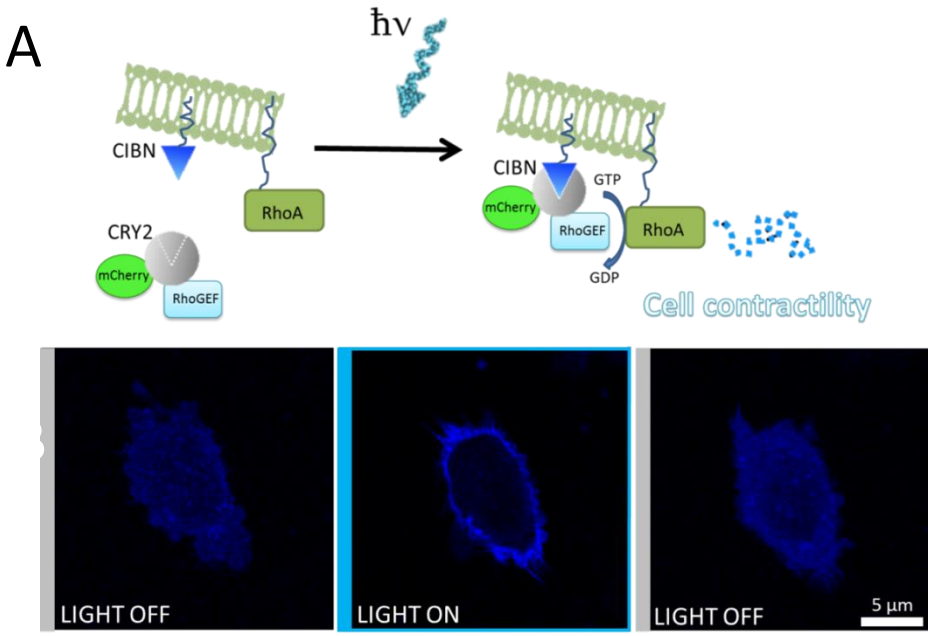

Figure 22 ***The optogenetic system – CRY2/CIBN RhoA activation.*** *(A) Scheme of the optogenetic system to trigger cell contractility. The system is based on overexpressing a RhoA activator (DHPH domain of ARHGEF11) fused to the light-sensitive protein CRY2-mcherry. The resulting protein is called optoGEF-RhoA. Upon illumination, CRY2 changes conformation and binds to its optogenetic partner*

CIBN. To increase contractility, the translocation of optoGEF-RhoA is forced to the cell surface, where RhoA is located, by targeting CIBN-GFP to the plasma membrane. The system dissociates to its initial state spontaneously. (B) Confocal fluorescence images of a cell with the opto-construct before, during and after light activation. The time scale of maximum membrane recruitment after photo-activation is 20~30 seconds while the dissociation time is 3~5 minutes.

As it was already stated, single cells balance internal and external mechanical stimuli through adhesion and cytoskeletal related forces following a process called tensional homeostasis. In other words, for the cell to maintain a mechanical equilibrium against external perturbations, there has to exist a constant mechanical feedback loop between the cell and the surrounding matrix. This implies that, if we are to interrogate such a system, a dynamic and rapid approach is required, both to induce a perturbation and to record and measure the cellular response. The optogenetic system of choice presents itself as an ideal probing tool, allowing rapid light-mediated perturbations, with low toxicity and fast reversibility. In the following section I will present and describe the method in charge of dynamically measuring the cellular output: time resolved traction force imaging.

2.4.2 Time resolved traction force imaging

Techniques to study and quantify the force interaction between the cell and the extracellular matrix have been under development for the last 40 years. The main readout on which traction force imaging approaches are based is the deformation imposed by the cell onto the substrate to which it is attached. First observations of this were done by the pioneer Harris and co-workers in 1980 (Fig. 23A), where they attempted to quantitatively measure the elastic distortion and wrinkling phenomena occurring when a cell spread over a flexible silicone substrate [124]. Unfortunately, quantitative analysis was very complex due to the non-linearity between the wrinkling and magnitude of the applied cellular traction force. Therefore, suppressing the wrinkles was crucial for a proper analysis. This was finally achieved 4 years later by Lee et al who introduced a stretchable non-wrinkling film that

incorporated beads as fiduciary markers of the film's reaction to cell traction forces (Fig. , giving birth to the technique known as Traction Force Microscopy (TFM) [125].

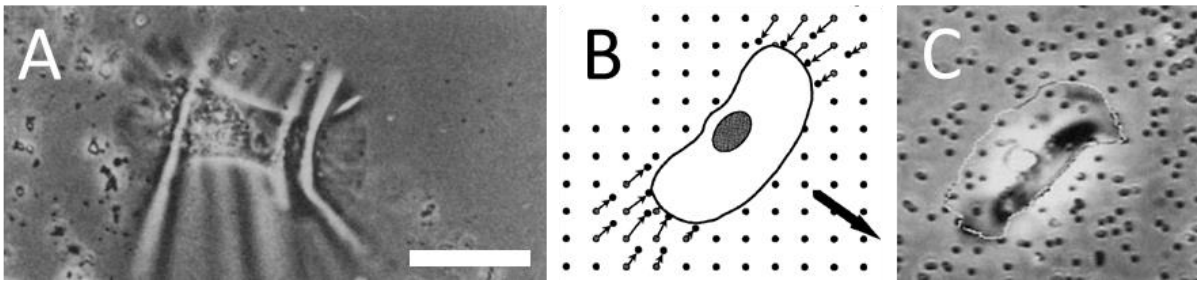

Figure 23 ***Pioneer traction force microscopy experiments.*** *(A) A fibroblast attached to a silicon rubber substrate that wrinkles under the exerted cellular force. (B) Graphic depiction of the non-wrinkling substrate. Small arrows represent the pulling forces exerted by the cell on the substrate and the long big arrow represents the direction of migration. (C) Phase contrast image showing a cell spread over the silicon substrate with latex beads embedded. Scale bar, 50 μm. Adapted from* [124], [125].

2.4.3 Traction force microscopy

Since the seminal work of Lee et al, traction force microscopy became the standard method to study the cellular traction forces produced by stationary or migrating cells on elastic substrates [126]. The transition from glass substrates to elastic substrates was a tipping point in mechanobiology since in their natural environment the most common attachment site for a mammalian cell is another similar cell or the extracellular matrix. Such materials have elastic moduli on the order of 10 to 10.000 Pa against petri dishes which have elastic moduli of 1 GPa [127], [128] (Fig. 24). Usually consisting of polyacrylamide (PAA) or polydimethylsiloxane (PDMS), these elastic substrates can be tuned to a specific physiologically relevant stiffness and coated with extracellular matrix proteins such as fibronectin or collagen.

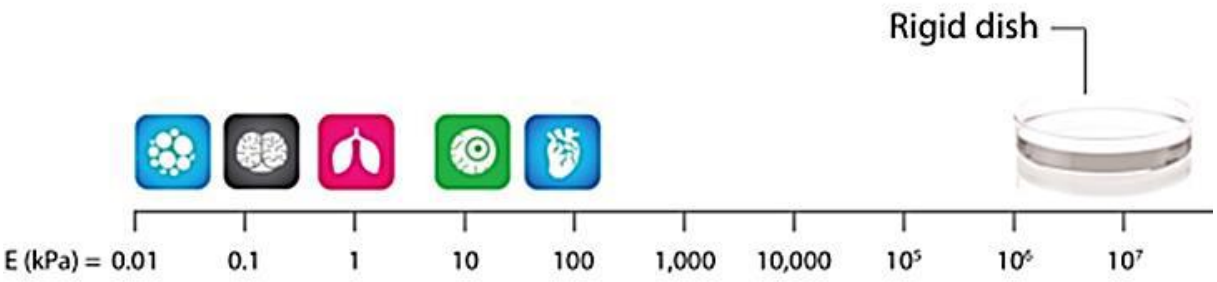

Figure 24 Scheme of physiological tissue rigidity, from fat to cardiac muscle, compared to a rigid dish. Adapted from [129].

Fluorescent microbeads are embedded close to the surface of the polymer gel and are the markers which will aid the quantitative traction force measurement. When a cell is adhering to the soft substrate it will exert forces through its adhesion sites provoking a deformation. Consequently, as the gel is deformed the microbeads will suffer a displacement from their initial position. Knowing the mechanical properties of the substrate and calculating the microbeads displacement, the cellular traction forces can be reconstructed. In order to achieve this, two images are needed: the image of the beads when the cell is adhering and deforming the substrate and the beads image when the cell has been removed and the gel has elastically returned to its original configuration. The displacement field of the substrate's top surface is obtained when comparing both images. To estimate the traction field, one of the most widely used analytical method is known as the Boussinesq formulation [130], first adopted by Dembo and Wang [131]. Calculation of the Bousinessq formulation was significantly improved later on by Butler et al by solving the equation using Fourier transform, coining the new term of traction field calculation as Fourier transform traction cytometry (FTTC) [132], [133].

2.4.4 TFM theoretical description

The aim of the traction force microscopy technique is to calculate the forces (F) exerted by a cell on a continuous substrate using the deformation measurements. To do that experimentalists need to solve an inverse problem that is ill-posed due to the

presence of noise. From this inverse problem solution, it is possible to calculate traction forces at each adhesion site by using linear elasticity theory. Here linear theory of elasticity has been used to calculate the cellular stress field [134]. For FTTC calculation the substrate is considered to be homogeneous and a linear elastic semi-infinite half space. The prepared polyacrylamide gel has to be thick enough for this assumption. Both the lateral distance over which displacement is measured, and the lateral dimension of force or deformed area should be small with respect to the substrate thickness in order to approximate semi-infinite elastic continuum to finite one. Thickness of our gels is 70 - 80 μm as considered for all experiments. The displacement vector induced by cellular forces at any point can be written as u_i on the elastic substrate as convolution form:

$$u_i(\mathbf{x}) = \int G_{ij}(\mathbf{x}-\mathbf{x}')f_j(x')d\mathbf{x}' \qquad (1.1)$$

Where u_i represents the experimental displacement and f_j the desired traction field. The force field includes forces from all other points x apart from the applied point of force. $G_{ij}(x)$ is the Green function which includes the mechanical properties of the substrate used and can be written in index notation as

$$G_{ij}(r) = \frac{1+\nu}{\pi E}\left[(1-\nu)\frac{\delta_{ij}}{r} + \nu\frac{x_i x_j}{r^3}\right] \qquad (1.2)$$

or in full form as

$$G_{ij}(r) = \frac{1+\nu}{\pi E r^3}\begin{bmatrix} (1-\nu)r^2+\nu x^2 & \nu xy \\ \nu xy & (1-\nu)r^2+\nu y^2 \end{bmatrix} \qquad (1.3)$$

Where

$$r = \sqrt{\mathbf{r}.\mathbf{r}} = \sqrt{x^2+y^2}$$

E is the young modulus and ν is the Poisson ratio of the substrate under consideration.

The Green function for the system under consideration has the following properties:

1. It has singularity at the origin.
2. It varies as 1/r.

This makes the inverse problem of extracting the force more complicated since the 1/r factor has long range effect. Mathematically three standard methods have been established to calculate the force from the displacement field:

1. Boundary element method (BEM) [135].
2. Fourier transform traction cytometry (FTTC) [132].
3. Traction reconstruction with point forces (TRPF) [136].

BEM technique is based on inverting a large number of linear equations in real space. Hence it requires long computational time and in exchange a very high resolution can be reached. FTTC method solves the inverse problem in Fourier space which turns out to change the previous convolution (1.1) in a simple matrix multiplication making the computation easy and considerably less time consuming. Some recent advances in the technique called TRPF have been shown by Schwarz et al [137]. TRPF gives a better accuracy in point force measurement, but it requires a prior knowledge of focal adhesion placements that turns out to add microfabrication steps in the experimental set-up. Comparative study conducted by Sabass et al demonstrated that FTTC, when combined with a proper regularization parameter and filtering, is comparable with results obtained by using BEM0 [136].

As one of our goals is to provide statistical measurements, we have chosen to implement a home-made FTTC algorithm for our cell traction calculation. A MATLAB expert in our group, Irene Wang, developed a Fourier Transform Traction

Cytometry software which combines Particle Image Velocimetry (PIV) and Particle tracking for displacement field measurements.

2.4.4.1 Displacement field extraction

To determine cell-induced displacement field, the very first step of the analysis is global correction of stage drift using images of beads before (stressed) and after (relaxed) killing the cell. Drift correction is achieved by cross correlating the two images. Position of the maximum peak of cross-correlation corresponds to the global translation. After determining this maximum cross-correlation in between stressed and non-stressed bead images, translation is corrected and bead images are resized to the same dimension. On the first step of displacement field analysis, we perform PIV calculation, where stressed and relaxed bead images are overlapped and subdivided into small windows. Here all the small window sizes are kept constant, typical size of 64 or 128 pixels. Cross-correlation is obtained between the corresponding pair (stressed and relaxed) of bead images [131], [136]. Mean displacement is calculated from the peak of the maximum cross-correlated image[132], [138], [139], then each bead displacement is mapped using particle tracking in each sub-window. A schematic diagram (Fig. 25) shows the displacement field calculation. The new displacement for each bead turns out to be:

$$[U'x']_i = U_i(x) + X_i \qquad (1.4)$$

where i corresponds to each PIV window. Xi gives the average displacement in each case and the value of Xi is constant for the all beads on the same PIV window. This calculation needs to determine the bead identity as the displacement can be measured when initial and final position of the beads are known. PIV requires a large enough window to yield accurate values. Therefore, there is a compromise between resolution and accuracy.

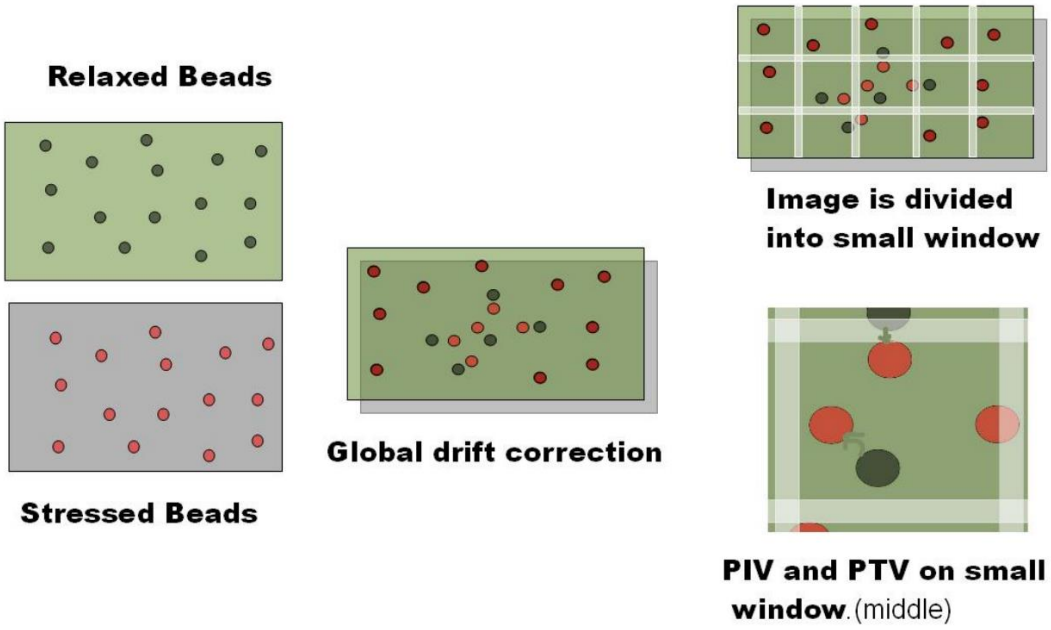

Figure 25 Schematic diagram showing the displacement field determination by Particle Image Velocimetry and particle tracking. Adapted from [140].

During particle tracking there will be no ambiguity between a bead and its neighbour in the radius of bead displacement, as large displacements have already been corrected. The accuracy of the measurement will depend on the bead density which translates into a good spatial resolution. These two step processes (PIV and Particle tracking) help to track the beads more accurately. A grid is designed on the displacement field with regular intervals. By interpolation we obtain a field vector on each node of the grid as shown in figure 26.

2.4.4.2 *Traction field determination*

As previously described by Butler et al 2002 [132] we used Fourier transform (FT) to solve the inverse problem. Thus, matrix convolution equation becomes a simple matrix multiplication. $\check{G}(k)$ becomes diagonal in Fourier space. After Fourier transform eq (1.1) becomes:

$$\tilde{u}(k) = \tilde{G}(k) * \tilde{f}(k) \tag{1.5}$$

Where $\tilde{u}(k)$, $\breve{G}(k)$ and ~f(k) are the displacement field, Green's tensor, and force field, respectively, in Fourier space. And k is the wave vector in the Fourier space.

$$\tilde{f}(k) = \tilde{G}^{-1}(k) * \tilde{u}(k) \tag{1.6}$$

$$\tilde{G}_{ijk} = \frac{2(1+\nu)}{E}\left[\frac{\delta_{ij}}{k} - \frac{\nu_{ij}k_ik_j}{k^3}\right]$$

$$= \frac{2(1+\nu)}{Ek^3}\begin{bmatrix} (1-\nu)k^2 + \nu k_y^2 & \nu k_x k_y \\ \nu k_x k_y & (1-\nu)k^2 + \nu k_x^2 \end{bmatrix} \tag{1.7}$$

Where

$$k^2 = k^2{}_x + k^2{}_y$$

It is easy to calculate $\breve{G}^{-1}(k)$ since it is diagonal in Fourier space. The displacement field $\tilde{u}(k)$ is calculated by Fourier transform. Since we have obtained the displacement field in regular mesh, it fulfils the requirement of the Fast Fourier transform. Force field is calculated in Fourier space by multiplying the displacement with the inverse of the Boussinesq Green function. It has been shown before that inverse problem is "ill-posed" in the presence of noise and spatial resolution of force can be achieved by adapting a regularization scheme [136], [137]. With the regularization Fourier transform equation becomes:

$$\tilde{f}(ik) = \left[\sum_{lj}\left\{\sum_{m}\tilde{G}_{ml}\tilde{G}_{mi} + \lambda^2\tilde{H}_{il}\right\}^{-1}\tilde{G}_{jl}\tilde{u}_{(j)}\right]_k \tag{1.8}$$

For the regularization kernel Ĥij (x-x′) 0th order regularization has been chosen. Finally, force is mapped into real space by inverse fast Fourier transform. After calculation it is then transformed back to the real space by inverse Fourier transform to map the traction force.

In the following figure we present an example of classical traction force calculation with NIH 3T3 cells cultured on non-patterned polyacrylamide gel substrate by using the technique as described before (Fig. 26).

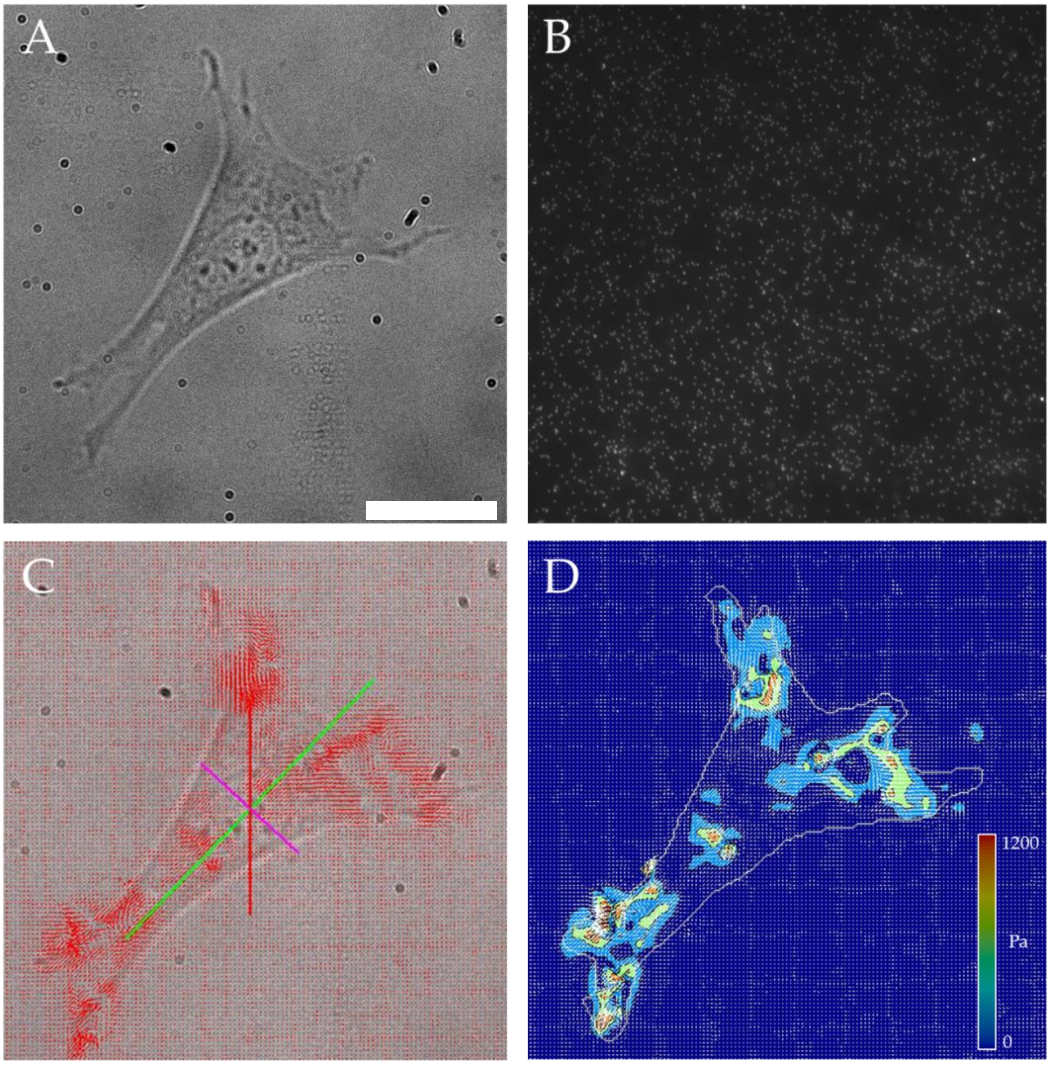

Figure 26 ***Classical traction force calculation on a single cell.*** *(A) Brightfield image of a cell cultured on 5 kPa soft substrate (B) Image of the fluorescent beads embedded on the soft gel (C) Cell force map showing the calculated force arrow at each point plus the two main force axes (green and violet) and a reference line (red) (D) Cell stress map with colour bar showing the intensity of stress exerted by the cell (in Pa). Scale bar, 20 µm.*

To understand more about cell-substrate interaction, contractile or strain energy is also calculated by integrating the traction force times the displacement over the whole area of an individual cell. The strain energy or contractile energy U is equal to the net force applied by the cell on the substrate integrated over the whole projected surface area of the cell. The element of the shear moment matrix can be written as:

$$U = (1/2) \int \vec{f}(\vec{r}).\vec{u}(\vec{r})dxdy \qquad (1.9)$$

In other words, the strain energy represents the energy used by the cell to deform the substrate while the total force represents the non-vectorial sum of each point force exerted by the cell without considering the gel displacement or the cell area. The FFTC technique we have implemented has the advantage to be computationally not intensive. It requires a few seconds to analyse the force field. Making use of PIV and PTV coupled to FTTC technique results in a highly accurate displacement field determination.

2.5 Proof of concept – Testing our approach

Having coupled optogenetics as a dynamical input with traction force microscopy as a dynamical output we were ready to interrogate the tensional homeostasis of fibroblasts. Unlike Valon and Oakes, who mainly probed the mechanical responses of either multicellular assemblies or at the subcellular scale, our interest was to focus on the single cell global homeostatic response.

If we consider the mechanosensing machinery of the cell as a closed pre-stressed structure, it follows that an accurate way of studying it is to measure its global response instead of a localized one. In other words, to understand the tensional cellular behaviour as an integrated, hierarchical system rather than as isolated parts.

In figure 27 we present a graph showing the time course of the total force of single cells with a 100 ms photoactivation at t=10 minutes. The cells analysed were freely spreading on a homogenous layer of fibronectin, deposited over a polyacrylamide layer with a Young modulus of 4.47 kPa . Observing the colour code, which identifies different cells with increasing total cell area from blue to red, we could conclude that there is a positive correlation between the basal traction force level and the cell size. Moreover, when quantifying the relative force increase upon photoactivation of every cell, we found a tendency that would also indicate a positive correlation between cell size and force response.

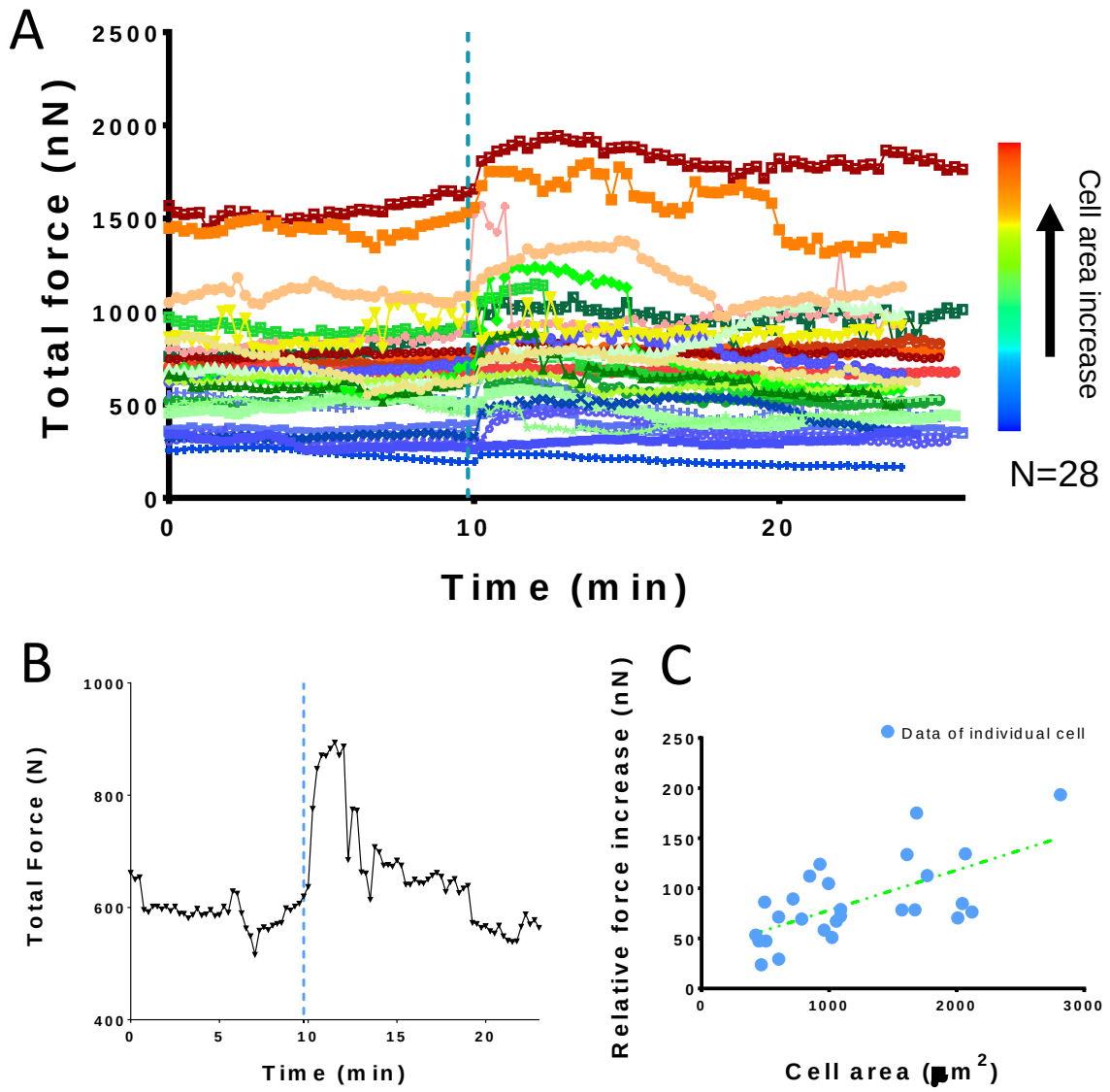

Figure 27 ***Freely spread cells force dynamics upon photo-activation.*** *(A) Quantification of the total force in time for cells expressing the optoGEF-RhoA construct. The light-blue discontinuous vertical line represents a light pulse of 100 ms exposure time at time=9.75 minutes. Each coloured curve*

represents one cell and the colour code used is related with an increase in cell size from blue to red. (B) Time plot of the total force for a single cell subjected to a light pulse of 100 ms exposure time. (C) Quantification of the relative force increase upon photo-activation. Each blue dot represents a single cell and its value was obtained by subtracting the basal tension to the highest point of the force peak after photo-stimulation.

At this point, it is worth rising three arguments that will narrow down our study and support the addition of another ingredient to our experimental approach:

1) It has been recorded in the work of both Valon and Oakes that the cellular contractility increase, as a result of photoactivation, does not induce changes in focal adhesion morphology or distribution, at least for the conditions used in those experiments [43], [121].
2) The work done by Mizutani and collaborators concluded that the mechanical cellular responses to the induced physical perturbations originated with the contractile tension generated by the stress fibres. This would imply that the dynamical tensional homeostasis is carried out mainly by the actomyosin network [80].
3) The findings of Valon and Oakes also showed that light stimulation does not induce de novo stress fibre formation, hence implying that the dynamic mechanical homeostatic response could mainly be modulated by the already existent actomyosin network, and not by a reorganization or reassembly of it [43], [121].

As a matter of fact, the cellular actomyosin skeleton is not a randomly arranged network. Work done on cell shape and actin organization [35], [141], along with results obtained during this project, show that depending on the cell geometry, size and matrix rigidity, actin filaments and stress fibres present a certain level of order and organization (Fig. 28). The geometry and mechanics of the cellular environment impact on cell architecture and play a notable role by modulating the forces produced by cells.

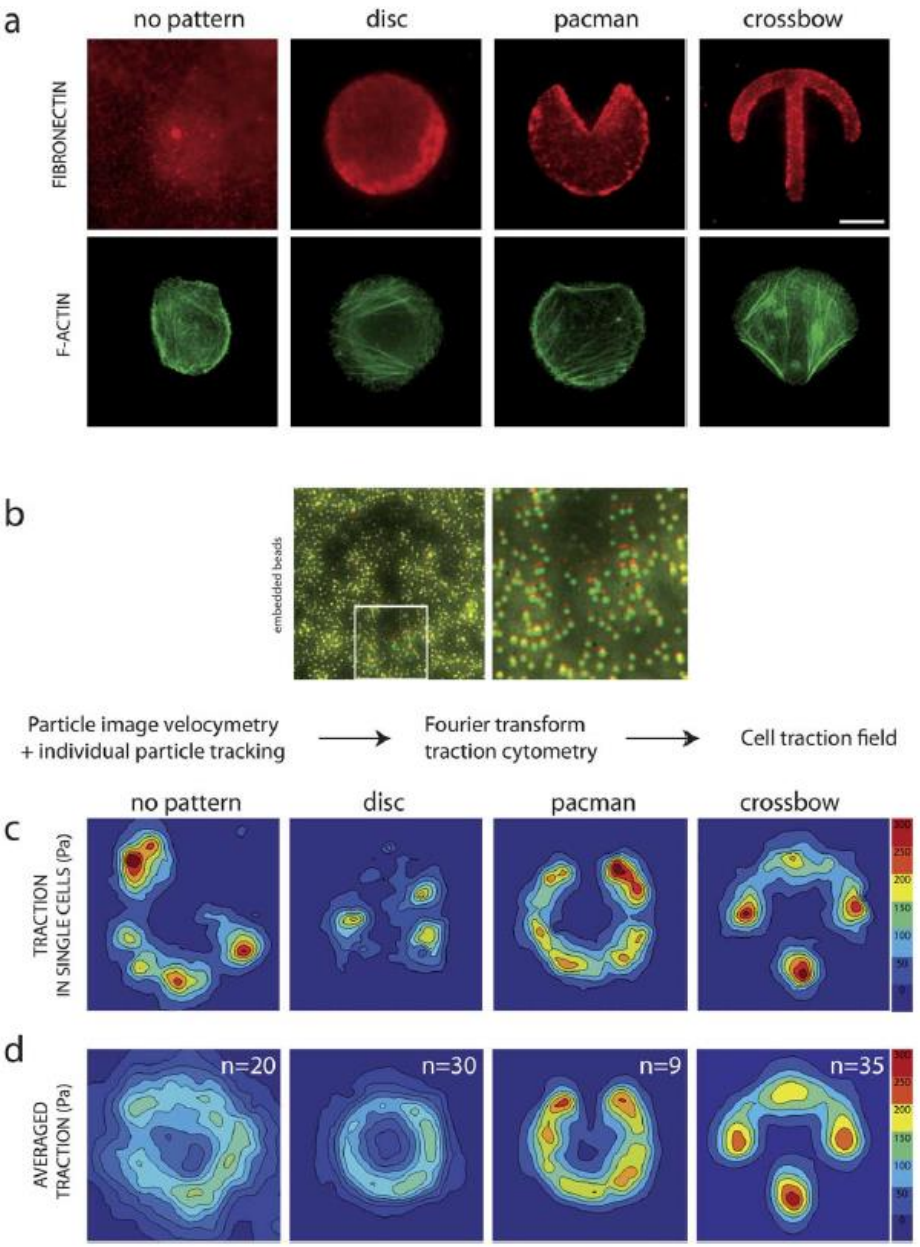

Figure 28 ***Impact of different micropatterned geometries in the cellular actin skeleton and stress maps.*** *(a) Top row: fluorescence fibronectin images of a non-patterned substrate and 3 different adhesive geometries. Bottom row: actin stained cells spread on the 4 different substrates (non-patterned, Disk, Pac-man and bow). Scale bar, 10 μm. (b) Representative image showing the overlap between the bead image before and after detaching the cell, evidencing the gel deformation. (c-d) Experimental and theoretical force traction fields, evidencing how the geometry of the adhesive fibronectin patterns induces a particular stress distribution. Adapted from* [141].

The aim of this project is to study the spatio-temporal tensional homeostatic response of a cell to dynamic perturbations of its internal signaling pathway. It has been shown that a main regulator of this mechanical response is the actomyosin network. However, considering that this network depends on factors such as size, geometry

and rigidity, and that tensional homeostasis intrinsically relates tensional balance to cell shape regulation, the interplay between internal machinery perturbations and external forces generations would appear to be best studied in situations where cell shape can be controlled. In this way we can actually manage to narrow down possible variables, being able then to examine effects of single parameters that are often coupled. As a result of this we can better understand the link between cellular force and stress energy dynamics with the actomyosin network arrangement. For that purpose and through the use of micropatterning techniques, we introduced a new component to our experimental approach that would impose specific geometrical constraints: patterned traction cytometry.

2.6 Patterned traction cytometry

This approach couples microfabrication techniques with force imaging. Using a combination of cell micropatterning and traction force microscopy on soft elastic substrates it is possible to systematically probe the existing relation in between cell shape and cell force generation in response to ECM physical properties.

2.6.1 Micropatterning

Microfabrication is a very useful approach in cell mechanics as well as in fluid mechanics. The main interest for researchers relies on the possibility to design model environments with fixed boundary conditions (micropatterns, microwells, micropillars etc.). By designing the artificial environment, cell internal organization and multi-cellular assemblies can then be modulated enabling at the same time a statistical analysis of cell morphological behavior.

The geometry and architecture of the external matrix surrounding the cell can be mimicked and tailored using surface micropatterning. This technique is based on the fabrication of extracellular matrix (ECM) protein patches of controlled size and shape, called micropatterns, surrounded by antifouling polymers which prevent the cell or other proteins from nonspecific adhesion (Fig. 29). It has been widely shown that the cell adhesive microenvironment geometry regulates many vital physiological processes such as cell shape, internal cell organization, cell fate, differentiation, etc. [35], [142]. Studies have proven that cell shape plays a role in various cellular processes, such as focal adhesion assembly [143] or stem cell lineage commitment [144].

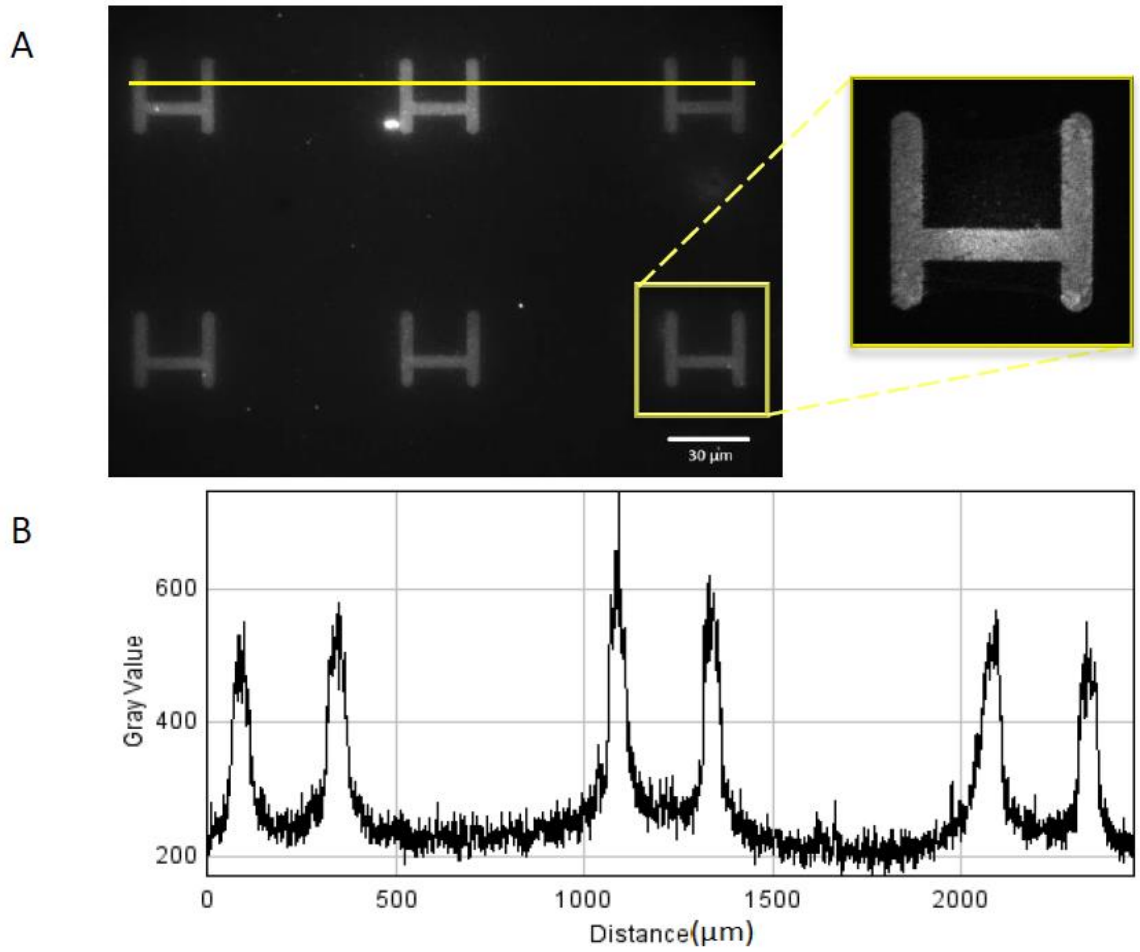

Figure 29 (A) Micropatterns on acrylamide gel after detachment from the initially patterned surface. (B) Plot profile of ECM protein fluorescence measured along three micropatterns confirms the specificity of the coating, showing reproducible spacing between patterns and robust fluorescence intensity.

The micropatterning technique used is based on the one already described by Vignaud et al [142]. During the procedure the patterned soft substrate is obtained directly from the photomask, ensuring in this way a very high spatial resolution. The patterning process is efficient at large scales. The great interest of this technique is thus to fabricate tens of thousands of patterns at a time on the same coverslip. The patterning substrate of choice is polyacrylamide hydrogel (PAA), the rigidity of which can be modulated to very low Young modulus, around 0.5 Pa and higher up to 40 kPa, by controlling the concentration of the acrylamide and bis-acrylamide used for polymerization.

The interest of working with polyacrylamide gels is manifold:

1. Polyacrylamide (PAA) is a soft elastic material that allows experimentalists to measure cellular tractions forces.
2. PAA is very transparent enabling imaging through the gel.
3. PAA is very easy to prepare.
4. PAA is mechanically very stable and its mechanical properties can be easily tuned.
5. PAA material is biocompatible.

In recent years, micropatterning on soft substrates [145], [146] has enabled the study of traction forces associated with a given cell shape. Consequently, traction forces were found to increase with the cell spreading area [147], [148] and cellular force distribution was shown to be strongly affected by the cell aspect ratio [149], [150]. All of these studies where done on soft substrates using adhesive patterns with convex shapes, such as full disks, squares or rectangles [55], [151]. Such patterns made it possible to control the overall shape and area of cell envelope. Considering that both the spatial organization of the ECM protein and the substrate stiffness have consequences for cell physiology it is logical to combine both in order to faithfully reproduce and control cell microenvironment [142].

2.7 Summary

Pulling together the techniques described in this Chapter, we developed a unique tool coupling a CRY2/CIBN optogenetic system with patterned traction cytometry. Such a set-up would enable us to apply global internal perturbations to living single cells via reproducible and highly controlled pulses of blue light (460 nm), while acquiring traction force cellular responses with a subcellular resolution in real time. Leveraging the unique capability of systematically activating the endogenous level of RhoA, we can successfully characterize the dynamic cell contractile response by triggering the RhoA signaling pathway in a controlled manner with high spatiotemporal resolution. Moreover, the addition of geometrical constraints, through the use of micropatterns, enables the control of actomyosin organization, enabling a deeper understanding of its role in dynamical tensional homeostasis.

Chapter 3 – Results and model

3.1 Tuning the set-up

The starting point of our experimental quest was to corroborate some of the statements done during the introduction. In the first place, we needed to confirm the existence of a basal tensional level in a cell constrained to a micropattern. As far as we knew, the main record of this had been presented by Webster and colleagues when studying the tensional homeostasis in single fibroblast, by constraining the cell in between an AFM cantilever tip and a fibronectin coated micropatterned substrate [86]. The following step would be to tune and characterize the optogenetic system, verifying the onset of contractile episodes upon light activation and testing the reproducibility and modularity of the approach. The confirmation of the previous steps would then enable us to start the tensional homeostasis interrogation and its connection with the actomyosin network.

3.2 Choosing the micro-pattern geometry

We fabricated soft substrate micropatterns with high spatial resolution to constrain the cell under study to a specific adhesive geometry which would remain virtually unaffected. The geometry of choice was a full circle or disk-shaped micropattern with a projected area of 1000 um^2. The choice of geometry was not arbitrary. Studies have shown that micropatterns that present corners or asymmetric geometries can modulate the polarity and organization of the cellular actomyosin network [151]–[153] (Fig. 30), hence imposing a bias on the cytoskeletal tension. It is in our interest to study the cells dynamic tensional homeostasis and its actomyosin network with the least number of pre-imposed mechanical stresses. For this reason, we designed a circular micropattern where we expected the cell to present a more unbiased behavior [152].

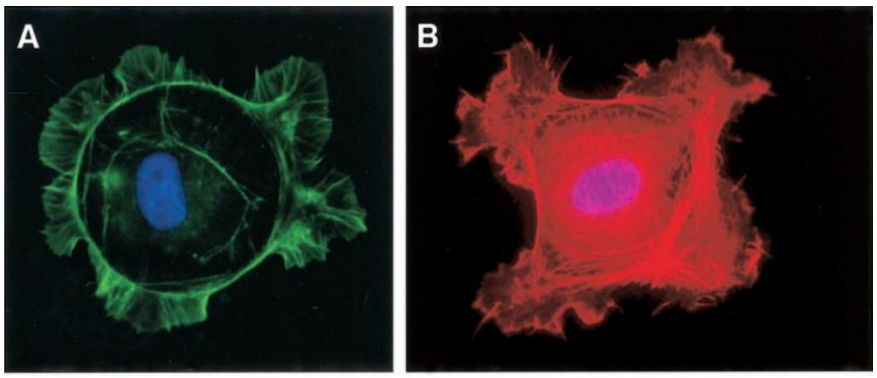

Figure 30 ***Lamellipodia behaviour on micropatterned endothelial cells.*** *Actin Fluorescence microscopy image of cells spread on 50 µm diameter circular micropattern (A) and on a 40µm x 40µm square adhesive geometry (B). DAPI stain in blue enables the visualization of the nuclei. Comparison in between both cases show that cell processes start preferentially from the corners. Adapted from* [152].

Studying only cells which covered the full extension of the disk-shaped micropattern, we used live traction force microscopy to record the tensional state of a cell throughout time and static traction force microscopy to obtain higher statistical data. In parallel, we used phalloidin to stain the actin cytoskeleton and study the stress fibres organization. Observing the cellular force and stress maps together with the actin staining (Fig. 31) we encountered our first striking result. Being in a completely symmetric shape, we had expected the cell to present isotropic force behavior and a random actin distribution. From the force and stress images obtained we could see a polarized cell with what it seemed a bipolar force pattern. This was further supported by the fact that the stress fibres presented a clear direction of alignment instead of a random disorganized one.

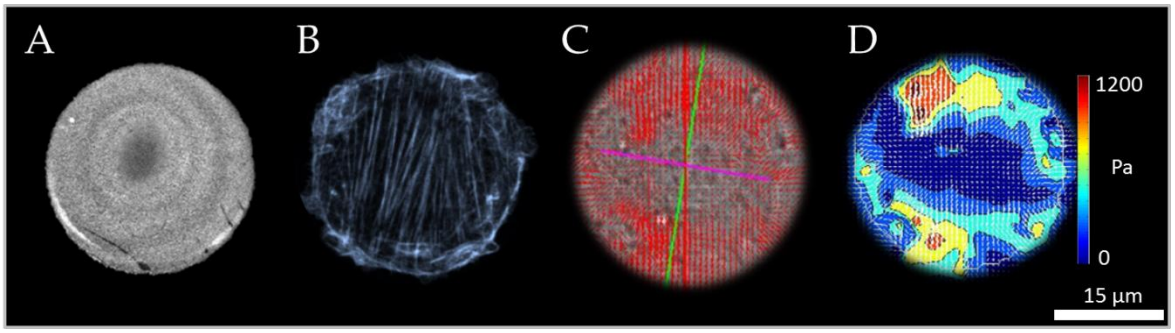

Figure 31 ***Fibroblast constrained to a circular micropattern of 1000 um^2 adhesive area.*** *(A) Disk shaped fibronectin micropattern on polyacrylamide hydrogels with 1000 um^2 surface area. (B) Individual actin-labelled cell. (C) Bright-field image merged with respective force maps and two main force cell axes. (D) Individual stress map calculated by Fourier Transform Traction Cytometry shows that traction forces are localized at cell contour. Both (C) and (D) show a bipolar force pattern.*

In order to better quantify and characterize this potential polarized behavior of the constrained cell we decided to calculate the first order moment of the force distribution [132], also known as force dipole. This is defined as a 2x2 tensor M_{ij}, which has energy dimensions and describes the contraction/dilation forces as well as the torque applied by the cell. The elements M_{ij} are obtained by integrating the coordinate r_i times the traction stress T_j over the cell envelope:

$$M_{ij} = \int r_i T_j(\boldsymbol{r}) d\boldsymbol{r}$$

Since the net torque exerted by the cell is expected to be zero, the matrix M is symmetrical in theory. Hence, it is possible to find the principal contractile axes by applying a rotation operator to obtain a diagonal matrix. In this description, the force distribution is reduced to two contractile dipoles along the two principal directions (Fig. 32).

Practically, the first order moment tensor M is calculated from the experimental traction map for individual cells and the dominant orientation is determined from the direction of the eigenvector corresponding to the largest eigenvalue. This direction should indicate the cell orientation in the case of a polarized force pattern (for further information please see [151]).

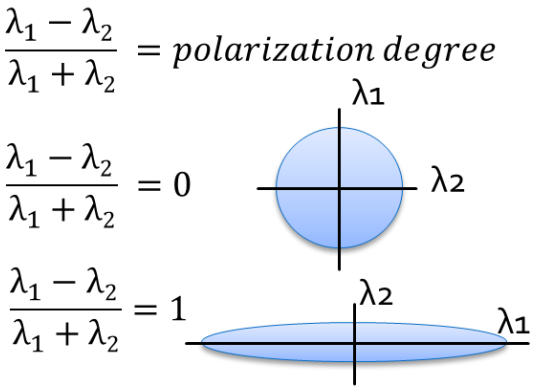

Figure 32 ***Graphic depiction of the polarization degree.*** *Values vary in between 0, where both main force axes are equal and isotropic, and 1, where all the cellular force is directed towards one axes implying maximum cell polarization.*

The division of the main contractile dipole (λ_1) by the second one (λ_2) yields what we consider as the cellular force polarity degree. Figure 33 explains it graphically.

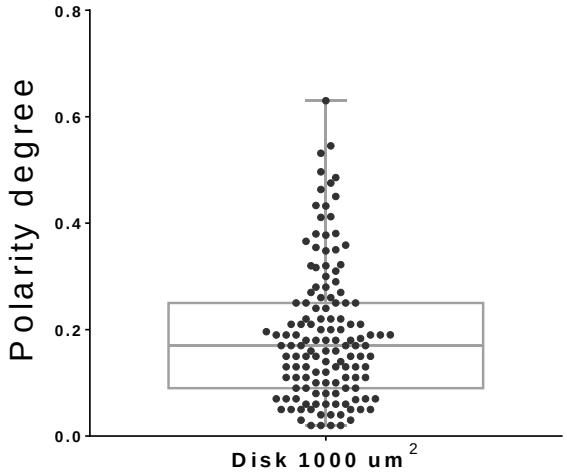

Figure 33 Quantification of the polarity degree of fibroblasts cultured on a disk-shaped micropattern of 1000 um2 adhesive area. Each blue dot represents a cell and 135 cells were analysed.

From a population of 135 cells we found a mean value for the polarization degree of 0.1928. This result is not strong enough to consider that cells on the studied micropattern present a high polarization. However, it showed that even when constrained to a completely symmetric geometry the cell will still attempt to polarize and align in a specific direction.

3.3 Tensional homeostasis in a constrained cell

To record the live tensional state of cells on the circular micropattern we used live traction force microscopy. Pictures of the cell and the microbeads embedded on the soft gel were taken every 20 seconds during a period of 52 minutes. The stack of images obtained from that experiment was used to reconstruct the traction forces exerted by the cell on the substrate during that time window. A total of 23 cells were studied and their tensional profile was obtained and graphed. Both the non-vectorial sum of all the forces exerted by the cell (Total force) and the strain energy are shown. In the graphs of figure 34 we can see an average of the studied cell population

showing a steady-state in the cellular forces with time, thus confirming the concept of a stable tensional homeostasis. The averaged strain energy showed a mean value of **2.086e-13** ± 7.996e-015 J and a variation coefficient of 3.83%, and the averaged total force showed a mean value of **434.1** ± 9.150 nN and a variation coefficient of 2.11%. Both force and stress values were consistent with previous observations [35], [139], [141], [151]. The coefficient of variation shows the extent of variability in relation to the mean of the population and it's a good measure of how much the tensional level fluctuates.

It is important to point out that this stability was studied in the course of 52 minutes were none of the cells suffered cell division or detachment from the micropattern. Vianay et al have very recently shown that traction forces vary as the cell goes through its natural cycle of division [154].

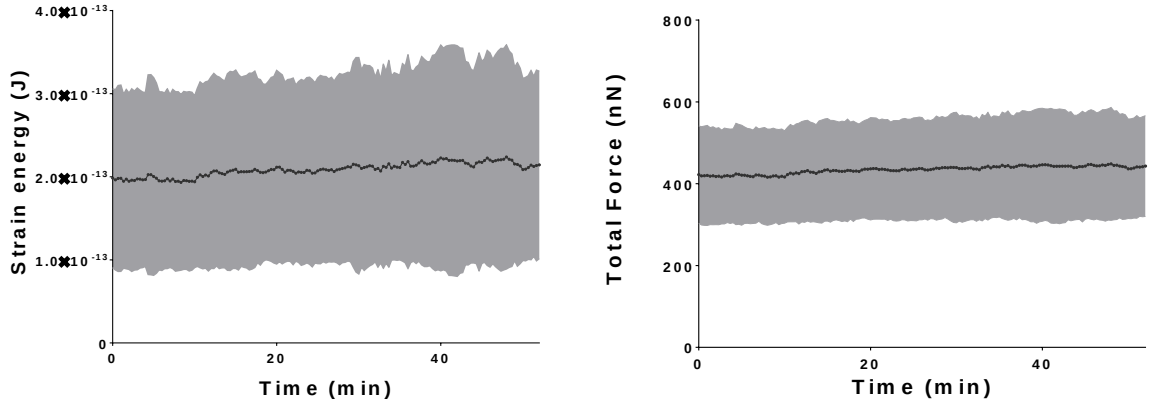

Figure 34 ***Time course of the strain energy and total force for cells spread on the disk-shaped micropattern.*** *Full lines show mean values, shaded regions correspond to standard deviations. The curves represent averages of the reduced set of 23 circle-patterned cells and the duration of the experiment was of 52 minutes.*

We can corroborate, from the discussed results and for non-dividing cells in the time window studied, the existence of a stable cell tensional state that is not affected or hampered by constraining the cell to a micropattern. We can now carry on with the photo-perturbations.

3.4 Tuning the optogenetic system

As it was described on Chapter 2, the experimental approach used involves a CRY2/CIBN optogenetic system, developed originally by Dr. Valon at the Curie Institute in Paris [120]. Upon blue light activation, this system relocalizes the nucleotide exchange factor ARHGEF11 to the cell membrane bringing it closer to RhoA and, consequently, triggering the activation of the RhoA signaling cascade.

However, there is an extra feature in this optogenetic construction which consists of a mCherry reporter linked to the CRY2 molecule. It gives the advantage of testing the system to confirm the interaction of the CRY2/CIBN couple before tackling the analysis of the RhoA activation. An increase of mCherry fluorescence in the membrane and a depletion of it in the cytoplasm right after photo-activation, confirms the well-functioning of the optogenetic system (Fig. 35). Failure to see such recruitment would imply that the cell has lost the optogenetic construct and further analysis is futile.

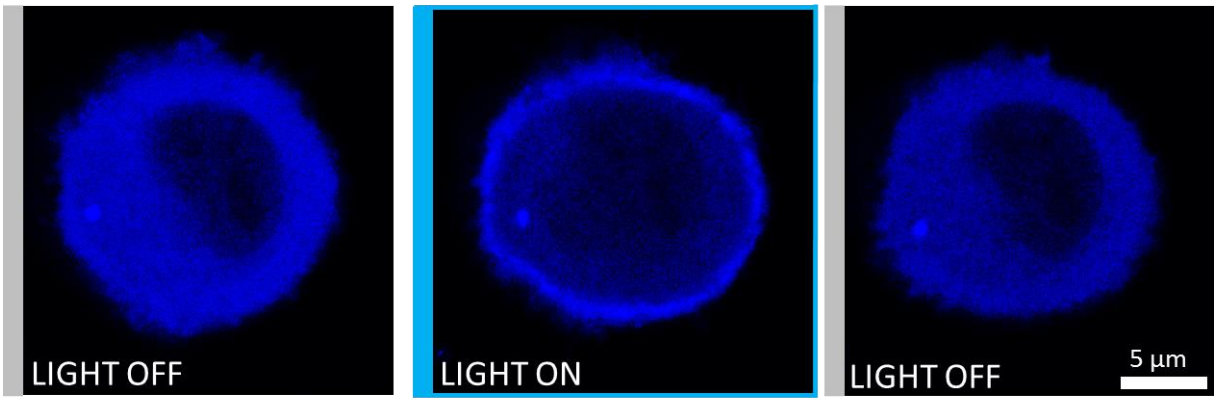

Figure 35 ***CRY2 membrane recruitment upon blue light (480 nm) activation.*** *Fluorescence confocal microscopy images of a cell cultured on a disk-shaped adhesive island. During the "light-off" periods the CRY2-mCherry construct is cytoplasmic and this can be confirmed by an homogenous intensity with exception of the nucleus. When the blue light is switched on CRY2 translocates to the cell membrane where CIBN is anchored and this can be confirmed by an intensity increase at the cell edges.*

Once the CRY2 recruitment to the membrane upon light activation was confirmed, we could address the contractile response of the cell to the photo-perturbation.

In the following two graphs on figure 36, we present the two main experiments aiming at tuning and characterizing the optogenetic system. In the first graph we can see the averaged strain energy profile of 7 individual cells being subjected to a 50 ms pulse of blue light followed by another one of the same exposure time 15 minutes later. Not only there is a clear response to the perturbation and a return to the tensional homeostatic level, but there is also an evident reproducibility and robustness in the method.

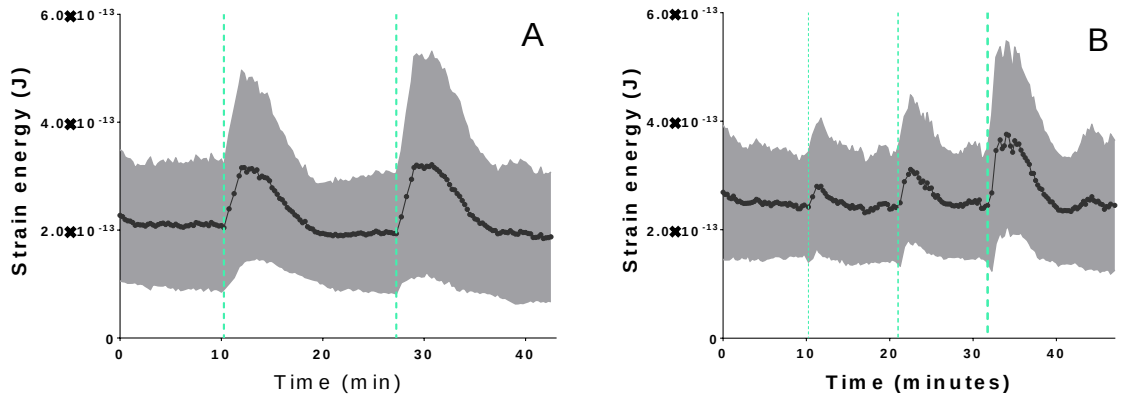

Figure 36 ***Cell tensional response to repetitive or modulated light perturbations.*** *Full lines show mean values, shaded regions correspond to standard deviations. The curves represent averages of the reduced set cells. Light blue dotted lines represent light activation events. (A) Quantification of the mean strain energy over 42 minutes for 7 cells on disk-shaped micropattern subjected to one 50 ms pulse of blue light followed by another one of the same exposure time 15 minutes later. (B) Quantification of the mean strain energy over 47 minutes for 12 cells on disk-shaped micropattern subjected to three pulses of increasing exposure time (10 ms, 20 ms , 50 ms) separated by a period of 10 minutes every time. Both graphs show clear tensional response upon light activation with a successive return to basal state.*

These last two characteristics are also supported in the second graph with 12 cells analysed, where we also find the possibility of a modulated response dependent on the amount of light used for the perturbations. The light pulses on the second experiment were of 10, 20 and 50 ms of exposure time. Consistent with what is shown in Dr. Valon's work [123], where the recruitment intensity increases with the

light exposure time (Fig. 37), we find the same positive correlation between the light exposure and the cellular contractile response.

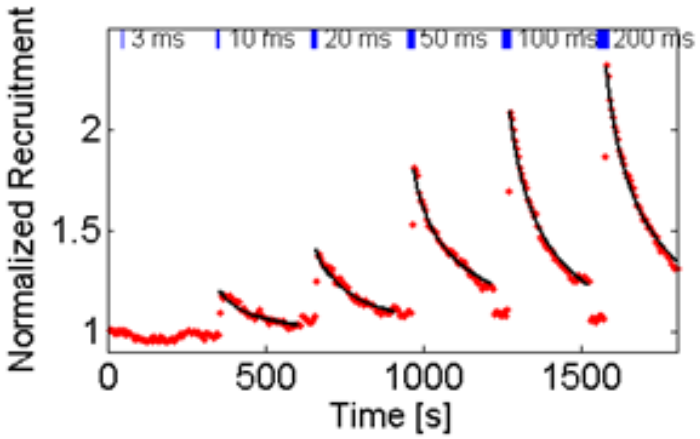

Figure 37 ***Membrane recruitment of the CRY2/CIBN system upon increasing time exposure light activations.*** *Quantification of fluorescence increase in the same cell, with a light exposure variation from 3 to 200 ms, and constant laser power. Adapted from* [123].

In a more detailed analysis of the graphs in figure 36, it can be seen that a light pulse of 50 ms time exposure induced an averaged cellular contractile energy maximum increase of **3.20456E-13** ± 1.34598E-13 J in **2.025** ± 0.56 minutes. The relaxation time of the system to the basal tensional state was **8.61** ± 1.82 minutes. For 20 ms light pulse the maximum stress amplitude **1.28448E-13** ± 9.10807E-14 J was achieved in **1.73** ± 0.41 minutes with a return to equilibrium in **3.44** ± 0.74 minutes. Finally, a light pulse of 10 ms exposure time induced a contractile maximum increase of **4.51817E-14** ± 4.01348E-14 J in **1.42** ± 0.42 minutes with a time relaxation of **2.54** ± 1.15 min. This results seem to imply a correlation in between the amount of light used and the cell's tensional response, both in amplitude and time.

Having confirmed the tensional homeostatic behavior in constrained single cells and characterized the probing system we can move on to the more detailed analysis and interrogation of the cellular dynamical contractile responses.

3.5 Mechanical adaptation to area changes and perturbations

As presented at the end of Chapter 2, during the analysis of the tensional dynamic response on freely spread cells, we found a positive correlation between the basal traction force level and the cell size. Moreover, when quantifying the relative force increase upon photoactivation of every cell, we found also a tendency that would indicate a positive correlation between cell size and force dynamic response to perturbation.

Following the concept that tensional homeostasis intrinsically relates tensional balance to cell shape regulation, these findings led us to include the micropatterning technique as part of the experimental approach with the aim to better quantify the cellular contractile behavior and narrow down the variables. Constraining the cell to a specific geometry would enable us to better regulate both the size ranges and parameters involved in the cellular mechanical response of the actomyosin network, such as cellular size and shape. With the aim to repeat the experiment done on freely spread cells with varying spread areas in a more controlled manner, we decided to use 3 disk-shaped micropatterns of increasing surface area: 500 um^2, 1000 um^2 and 1500 um^2.

In Figure 38 the 3 representative sizes can be observed along with the respective properly spread cell stained for actin. A plug-in from the image software Fiji, called OrientationJ, was used to qualitatively show the actin orientation of cells on the 3 sizes. A more detailed and quantified study of this orientation will be addressed further on. Stress maps of the 3 representative cells show qualitatively an increasing stress range. To characterize this trend in a more accurate way we performed live traction force measurements.

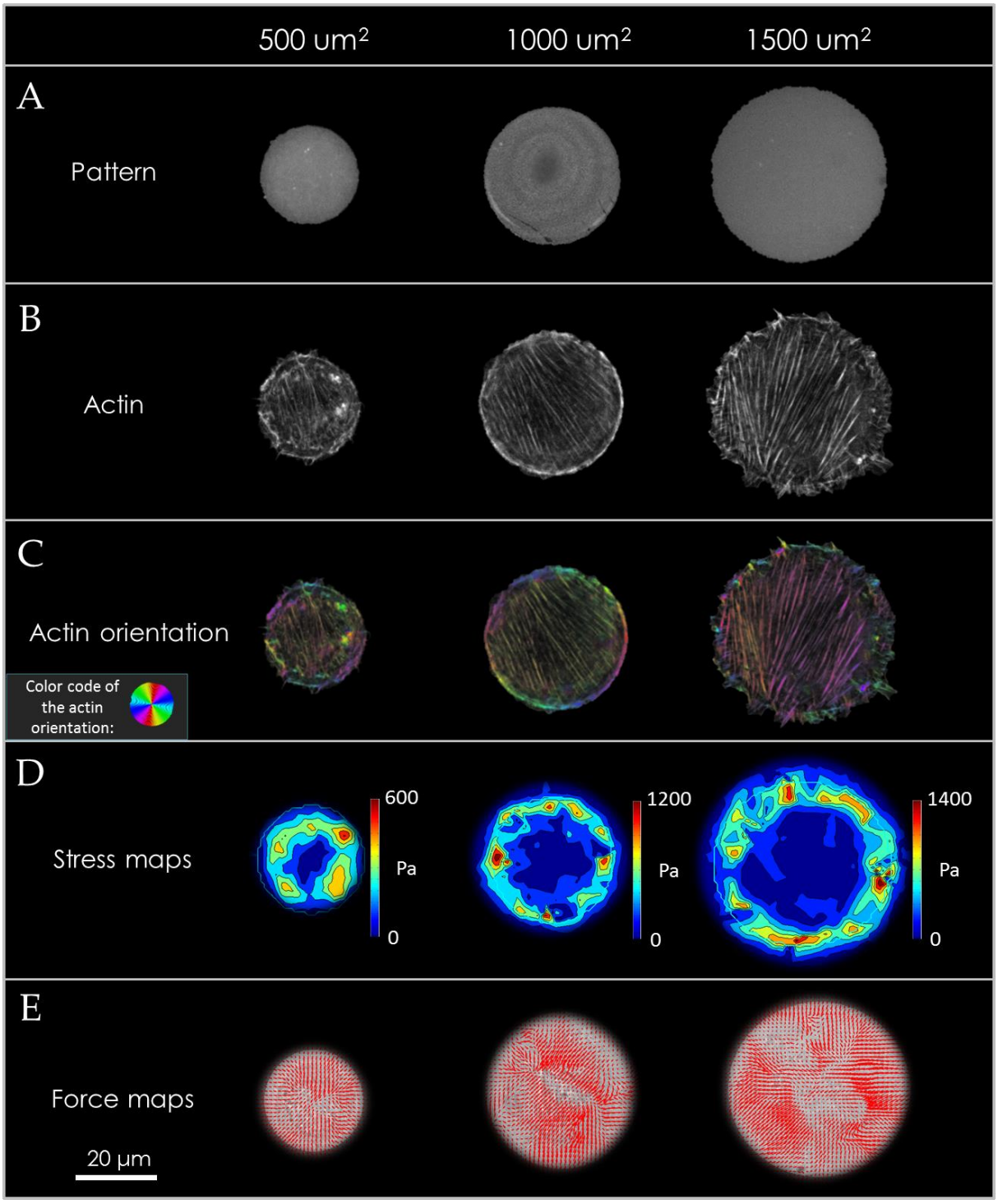

Figure 38 (A) Disk shaped fibronectin micropatterns on polyacrylamide hydrogels with increasing surface area. The patterns cover an area of 500-1000-1500 µm^2. (B) Fluorescence confocal microscopy images of individual actin-labelled cells. (C) Colour-coded map obtained with OrientationJ (plugin from Fiji) showing the orientation of actin fibres in the respective cells. (D) Individual stress maps calculated by Fourier Transform Traction Cytometry show that traction forces are localized at cell contour. (E) Bright-field images merged with respective force maps show that NIH 3T3 cells fully spread on all three patterns.

The first result when studying the live basal contractile state of individual cells spread on each of the 3 sizes showed 3 defined strain energy levels in a time window of 56 minutes (Fig. 39 A). It could already be concluded that changing the size did not affect the force regulation and tensional homeostasis of the cell. It did, however, change the basal level values for each size. We observed a strain energy mean value of **7.121e-014** ± 5.638e-015 J for cells on 500 um^2 disk with a coefficient of variation of 7.92%. Cells on 1500 um^2 presented average strain energy of **5.139e-013** ± 9.977e-015 J with coefficient of variation of 1.94%.

When analyzing a larger set of cells through static force microscopy (Fig. 39 B) we obtained higher variability but we still found 3 significantly different strain energy levels. The mean contractile level was **3.422e-014** ± 2.039e-014 J, **2.446e-013** ± 1.513e-013 J and **3.198e-013** ± 1.575e-013 J for 500 μm2, 1000 μm2 and 1500 μm2 disk-shaped patterns, respectively. Regarding the coefficient of variation we calculated the values 59.58%, 61.87% and 49.26% for 500 um2, 1000 um2 and 1500 um2 disk-shaped patterns, respectively.

The increase in cellular basal tension associated with size increase has been interestingly discussed by Wang and collaborators who described the cell as an active mechanical structure with a certain level of pre-stress [155]. This active stress is exerted by the actomyosin network even in the absence of an externally applied force and, in other words, could be considered as none other than the cellular tensional homeostasis. However, this pre-stress is directly related to the cell's shape and size and thus whenever the active structure, in this case the cell, suffers an increase in shape, it will necessarily suffer an increase in internal pre-stress. What we see in our results would appear to be consistent with this statement.

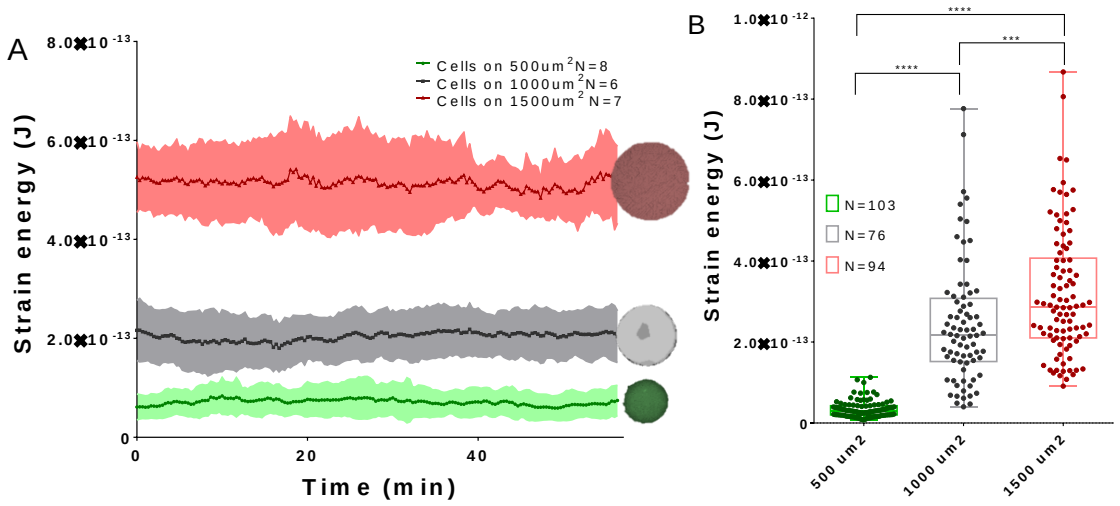

Figure 39 ***Stable tensional levels displayed on cells of different sizes.*** *(A) Time course of the strain energy for cells on the different disk sizes. Full lines show mean values, shaded regions correspond to standard deviations. Each curve represents averages of the reduced set of 8, 6 and 7 cells on 500, 1000, 1500 µm² respectively. Duration of the experiment was 56 minutes. (B) Static strain energy for cells spread on the three different disk sizes. A 1-way ANOVA test showed significant difference in between the three data groups.*

Now, our aim was to interrogate this internal pre-stress in order to understand its dynamics. We did so by photoactivating the cells spread on each of the 3 different disk-shaped patterns with only one pulse of light of 100 ms (Fig 40).

This photoperturbation induced an averaged cellular contractile energy maximum increase of **9.068e-014** ± 4.883e-014 J, **3.005e-013** ± 1.659e-013 J and **4.262e-013** ± 3.251e-013 J for cells on 500 µm², 1000 µm² and 1500 µm² respectively. The time to peak was of **2.56** ± 0.67 min, **3.61** ± 0.72 min and **3.25** ± 1.35 min with a relaxation time of **4.47** ± 1.2 min, **5.71** ± 1.45 min and **5.97** ± 0.72 min for cells on 500 um², 1000 um² and 1500 um² respectively. It could be confirmed that the change in cell size did not affect its potential of recovering the basal tensional state. Interestingly, it could also be observed that the higher pre-stressed state of cells on larger patterns did not prevent or diminished its force response capabilities. As it had been seen with the freely spread cells, the cell's contractile response was higher for cells on larger disk-shaped micropatterns.

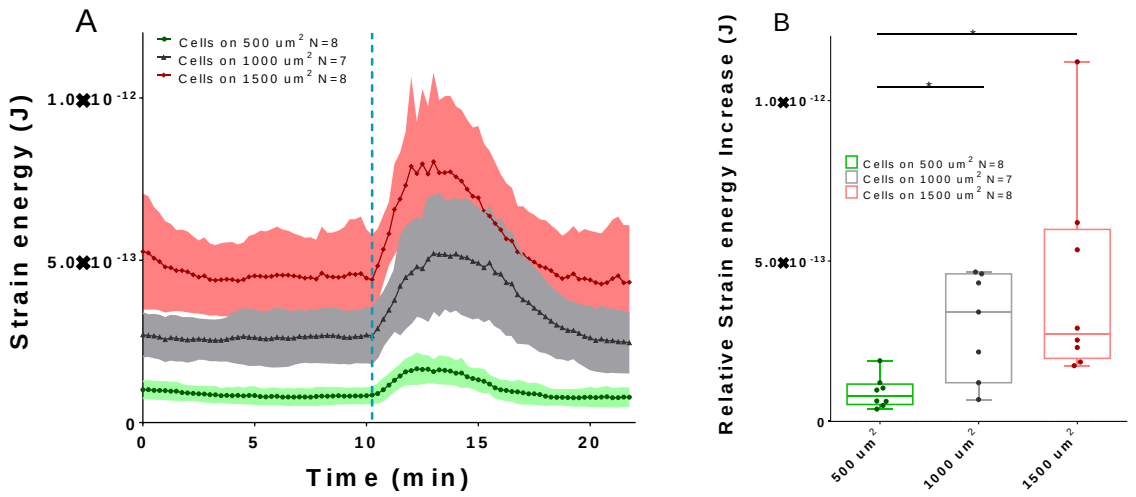

Figure 40 ***Larger cells produce higher strain energy both before and during activation.*** *(A) Time course of the mean strain energy for cells on the different disk sizes subjected to one light pulse of 100 ms. Full lines show mean values, shaded regions correspond to standard deviations. Light blue dotted vertical light represents the photo-activation event. (B) Strain energy increase for every activated cell on the three different disks. A 1-way ANOVA test shows significant difference between the strain energy increase of cells on 500 μm^2 and the two bigger sizes. Each dot represents one cell.*

The question that we had to pose ourselves after obtaining these results was whether the spreading size was the only explanation to the differences in the force levels and responses or if there was any variation in the internal tensional mechanism being also involved.

Since it had been mentioned many times that there is a direct link between the active cellular internal stress and the actomyosin network, a better way to understand the obtained force dynamic readouts was to study what was happening with the cellular contractile machinery.

A statistical analysis of the actin network organization in phalloidin inmunostained cells gave an interesting outcome. To study the arrangement of stress fibers in the cells we implemented a software that calculates the local orientation of actin stress fibres and renders an 'order parameter'. This parameter represents how parallel the local orientation of each actin stress fibre is to the average orientation. The closer to 1 means the more aligned the fibres are with each other (a more detailed description of

this parameter can be found in the Materials and Methods Appendix). When analyzing the cells on the 3 disk-shaped patterns we found a trend that implied a positive correlation between the size and the internal actin alignment (Fig. 41). This trend had been seen in the cases were the micropattern changed, elongating the cell [35]. However, this finding meant that even when the geometry and shape envelope of the cell was preserved, the size increase was altering the internal actin alignment, hence possibly modifying the actomyosin contractile network dynamics.

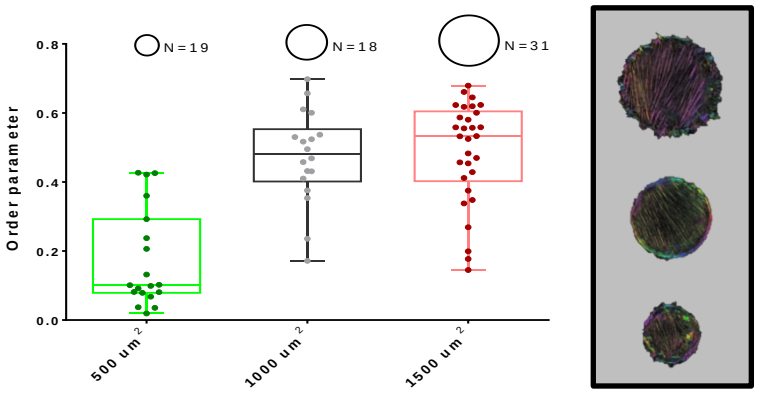

Figure 41 ***Larger cells display a higher actin arrangement.*** *Quantification of the global cellular actin fibre alignment for cells spread on each disk size. Each dot represents one cell.*

In order to go one step deeper in the actomyosin network analysis we decided to record its behavior in live mode and verify if the photo-activations where inducing actin rearrangements. To track the stress fibers throughout the photo-perturbation protocol we incubated the cells under study with SiR-actin. Based on the fluorophore silicon rhodamine and the actin binding natural product jasplakinolide, Sir-actin allows the labelling of filamentous actin in live cells with high specificity and low background [156]. Videos done recording the cellular stress fibres while the cell was being photo-activated supported the data presented by Valon et al and Oakes et al. While photo-activation induced an increase in the intensity of labeled stress fibres (not so evident when doing global photo-activation), implying a reinforcement of these structures, it did not prompt the rearrangement of the actomyosin network (Fig. 42).

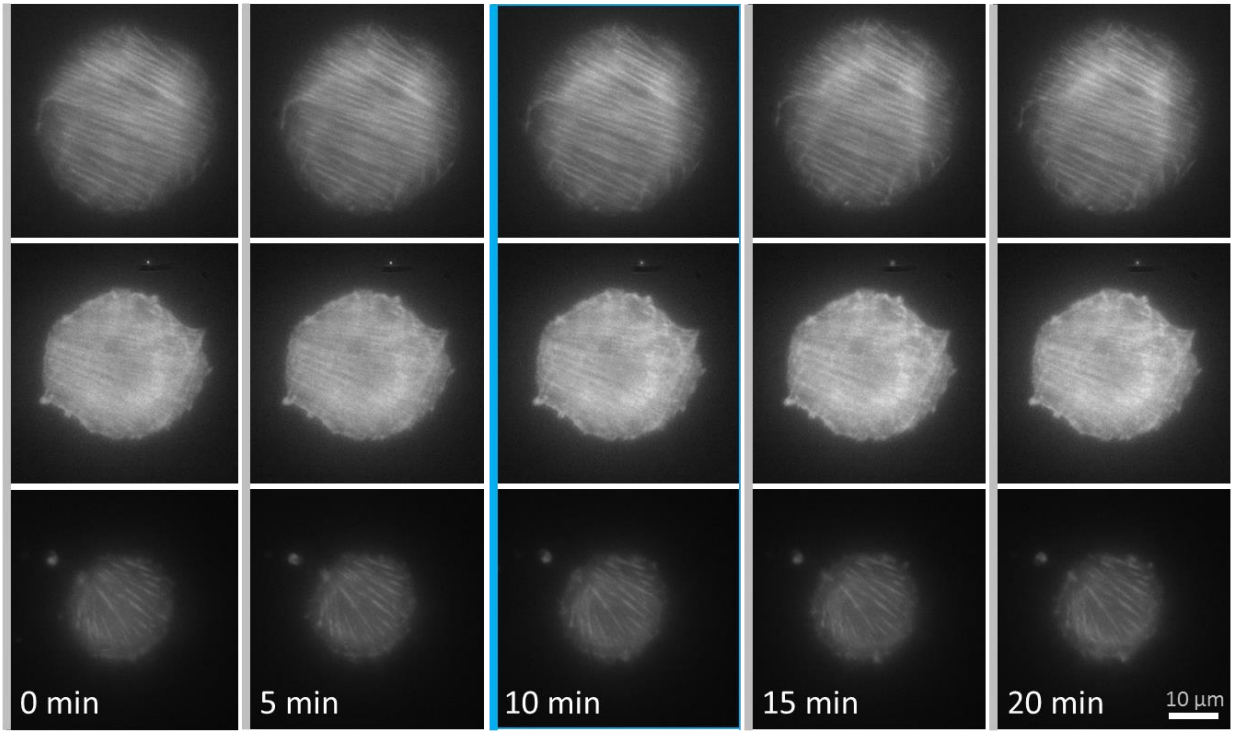

Figure 42 ***Photo-activation does not induce actin re-arrangement.*** *Time sequence of fluorescent microscope images of SiR actin stained cells on the three different disk adhesive geometries. At t=10 minutes cells were photo-activated with a pulse of blue light of 100 ms time exposure. Live actin images post-light activation, at t=15 minutes and t=20 minutes, do not show a change in the actin arrangement in any of the three sizes.*

Our main goal was to interrogate the dynamic tensional homeostasis to better understand the response of the actomyosin network to the internal perturbations induced by photoactivation. In order to do so, we had to narrow down possible variables that would be linked to that response such as shape, migration potential and rigidity. However, as it could be concluded from the order parameter, there also seemed to exist a link between the actomyosin network dynamics and the cell size. This led us to pose ourselves a new question: Can we uncouple those parameters inducing a different actin alignment independently from the cell spread area? If we could achieve that then the dynamic tensional interrogation would be directly addressed to the actomyosin network arrangement.

3.6 Decoupling area from actin organization in cellular response to photoperturbation

It has been shown that cells with similar shape maintain the same contractile state regardless of the adhesive geometry [151], [157]. Nevertheless, as far as we are concerned the dynamics of this global state and its response against a mechanical perturbation have not been addressed. We would like to probe that contractile state in single cells with the same shape but modifying their actomyosin alignment. In other words, we want to keep the same adhesion area and cell envelope while affecting the actin architecture and understand how that could impact on the tensional homeostasis dynamics.

As we found for the case of the 1000 μm^2 disk-shaped micropatterns (hereinafter referred as Disk), the actin and stress fibers alignment is considerable. Basing our conclusion strictly on the order parameter, cells spread on Disk present high actin alignment. What would happen with the cellular mechanical response if we could keep the shape and size of the cell while reducing the internal actin alignment? At what level does the actomyosin network arrangement affects the cell's contractile response to perturbations?

3.7 Searching for the actin troublemaker

Taking advantage of the versatility of microfabrication and micropatterning we designed different potential candidates (Fig. 43). We had seen through own experience and scientific publications [141], [151], [158], [159], that subcellular geometries and non-adhesive borders can induce particular actin arrangements. Based on this knowledge we designed 10 different micropatterns which imposed the

same projected area (1000 μm²) and shape (circular) on spread cells but offered different sub-cellular geometries or boundary adhesiveness.

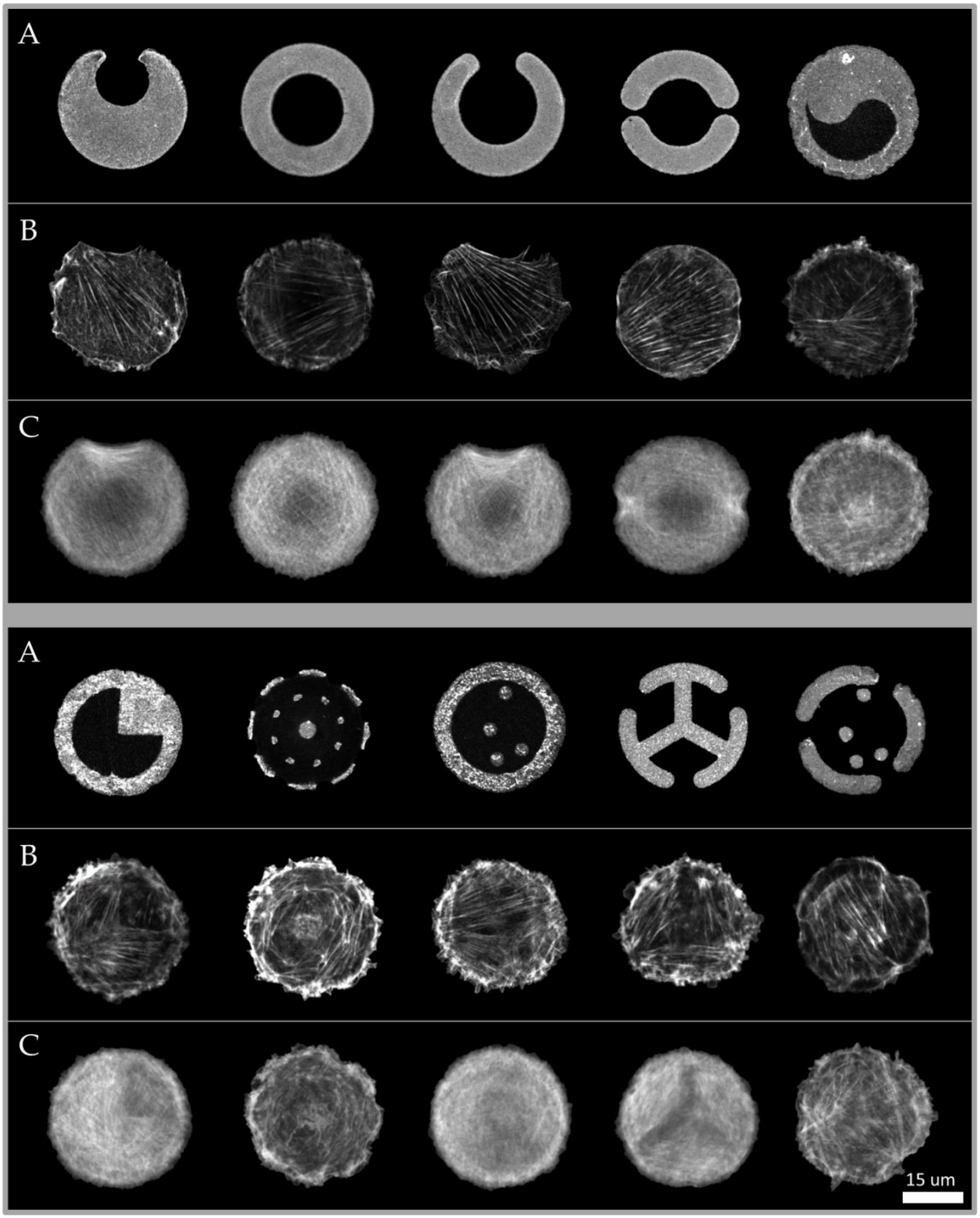

Figure 43 ***A study of actin arrangement on different micropatterned geometries.*** *(A) Circular fibronectin patterns on polyacrylamide hydrogels, with similar projected area but different contours and internal geometries. All the patterns cover an area of 1000 μm². (B) Fluorescence confocal microscopy images of individual actin-labelled cells. All cells fully cover the adhesive patterns. (C) Averaged fluorescence confocal microscopy images of actin-labelled cells.*

On 4 of those patterns we decided to maintain the same adhesive contour while including different internal potential anchoring points that would affect the actin networking, the idea being that those points would add branching points in the network and also decrease the number of long and aligned stress fibers. For the rest we also modified the adhesive boundary to modulate and modify the available anchoring points (focal adhesions) of stress fibers that span the whole cell body.

Studying the actin network of the cells on each of these patterns led us to a promising result. Even though a few of the geometries would induce cellular actin misalignment, only one of them would do it in a stable, reproducible, repetitive and significant way. The need for reproducible and stable misalignment was not a minor issue considering the fact that having most of the fluorescence spectra dedicated to photo-activation, micropatterns and microbeads, the possibility of tracking the cellular actin while coupling light stimulations with traction force measurements was not experimentally achievable. As it can be observed on figure 43, the micropattern that resembles a 3-spoked wheel with a discontinuous contour (hereinafter referred as Wheel) imposed what could be lightly called a triangular actin arrangement with 3 main stress fiber orientations. A qualitative idea of this can be obtained by observing the averaged actin stained images, where the internal geometry is still visible, implying that most of the stress fibers adopt the mentioned triangular arrangement instead of going over the “spokes”.

A more quantitative approach was done by comparing the order parameter obtained for cells spread on all the shapes designed. In the graph of Figure 44 we plotted the order parameter of cells spread on each of the 10 micropatterns. With an averaged order parameter of 0.1724, calculated over a sample number of 46 cells, the Wheel pattern induced the lowest actin alignment on cells.

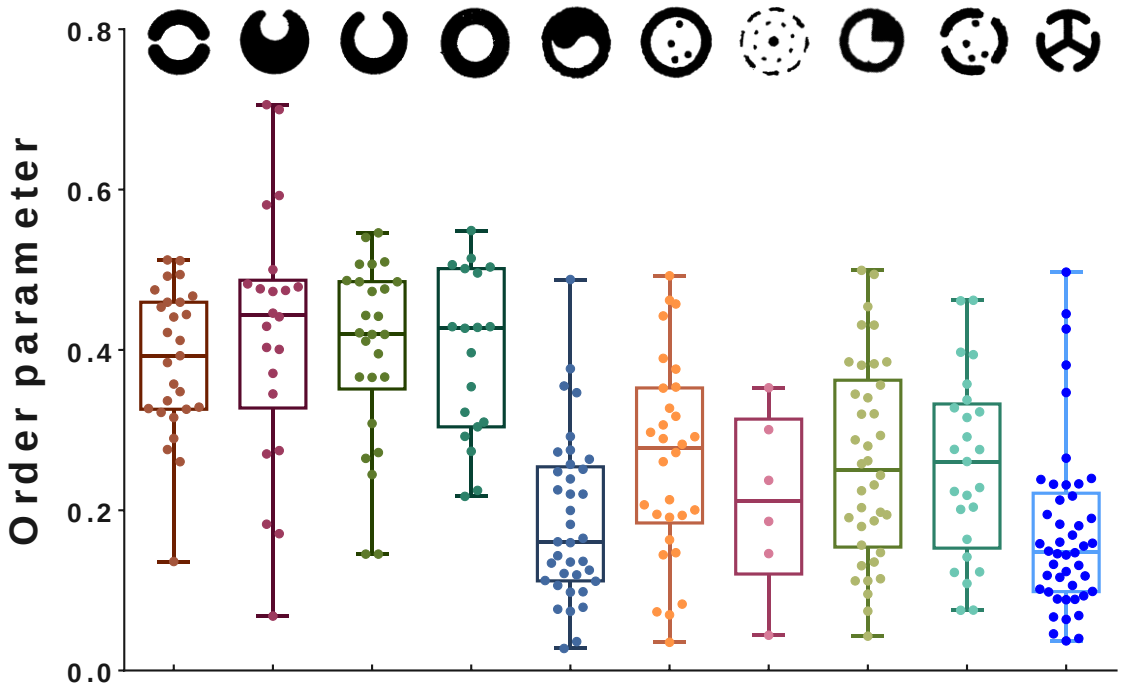

Figure 44 ***Quantification of the order parameter of cells on 10 different micropatterns.*** *Each dot represents one cell and each data set corresponds to cells cultured on the micropattern depicted directly above, at the top of the graph.*

The 'stability' of the actin disarrangement imposed on the cell by the wheel shape was followed and corroborated with the use of live SiR-actin stained cells. As it can be observed for a representative cell in Figure 45, it maintained the 'triangular actin arrangement' aforementioned throughout a period of 10 hours.

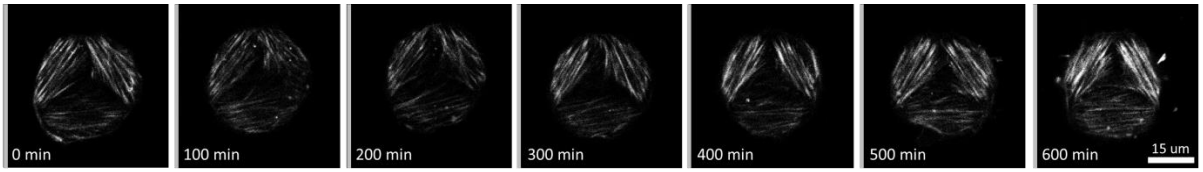

Figure 45 ***Time course actin organization for cells on wheel.*** *Fluorescence confocal images of a SiR-actin stained cell spread on a Wheel pattern. Pictures were taken every 10 minutes for a total experimental time of 10 hours.*

Finally, the comparison of the order parameter between the Disk and the Wheel showed a significantly lower global actin alignment for cells spread on the second micropattern (Fig. 46). Having found the desired actin troublemaker we moved to the following step of characterizing its tensional behaviour.

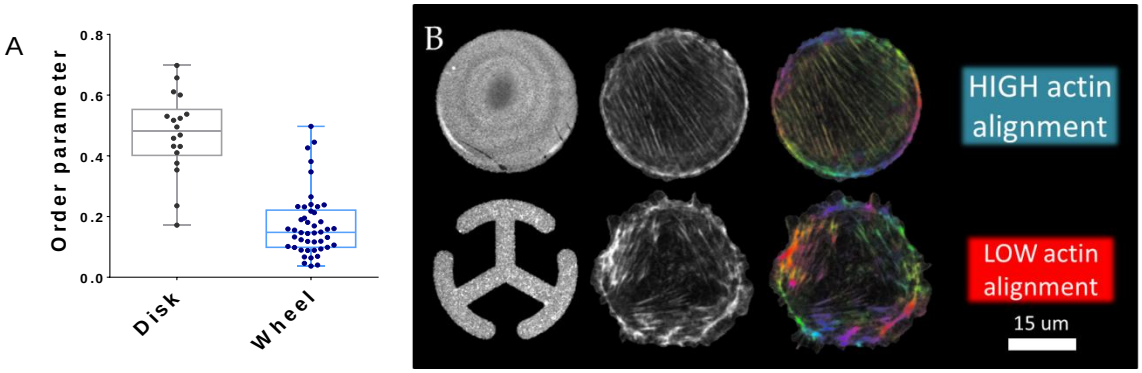

Figure 46 ***Cells on Wheel present a lower actin alignment than those on Disk.*** *(A) Order parameter quantification for cells spread on Disk (blue) and Wheel (red). Each dot represents one cell. (B) Qualitative comparative analysis between cells on both shapes showing the fibronectin patterns on polyacrylamide gels, fluorescence confocal images of individual actin-labelled cells and actin images analysed with OrientationJ (Fiji plugin).*

3.8 Force and tensional characterization of the confronted patterns

Using live and static traction force microscopy we analyzed the tensional homeostasis of cells spread on the Wheel and contrasted it afterwards with the data obtained for cells on the Disk. Consistent with what had been discussed regarding cells with same shape and size, the unperturbed tensional state of cells on the Wheel was similar to the ones on the Disk with no significant differences (Fig. 47). Averaging the basal strain energy of 23 cells spread on the Wheel shape we obtained a mean value of **2.289e-013** ± 5.686e-015 J with a coefficient of variation of 2.48% (for the disk we had measured an average strain energy of **2.086e-13** ± 7.996e-015 J). The static traction force analysis showed a mean contractile level of **2,341e-013** ± 1,046e-013 J and **2,199e-013** ± 9,662e-014 J for cells on Wheel and Disk, respectively.

This result not only supported the claim that cell's with similar projected area presented the same tensional baseline, but also proved that the degree of order of the cellular actomyosin network doesn't appear to affect such baseline. On the other

hand, a clear tripolar force pattern could be appreciated on cells spread on Wheel in contrast to the more dipolar force pattern seen already on the Disk.

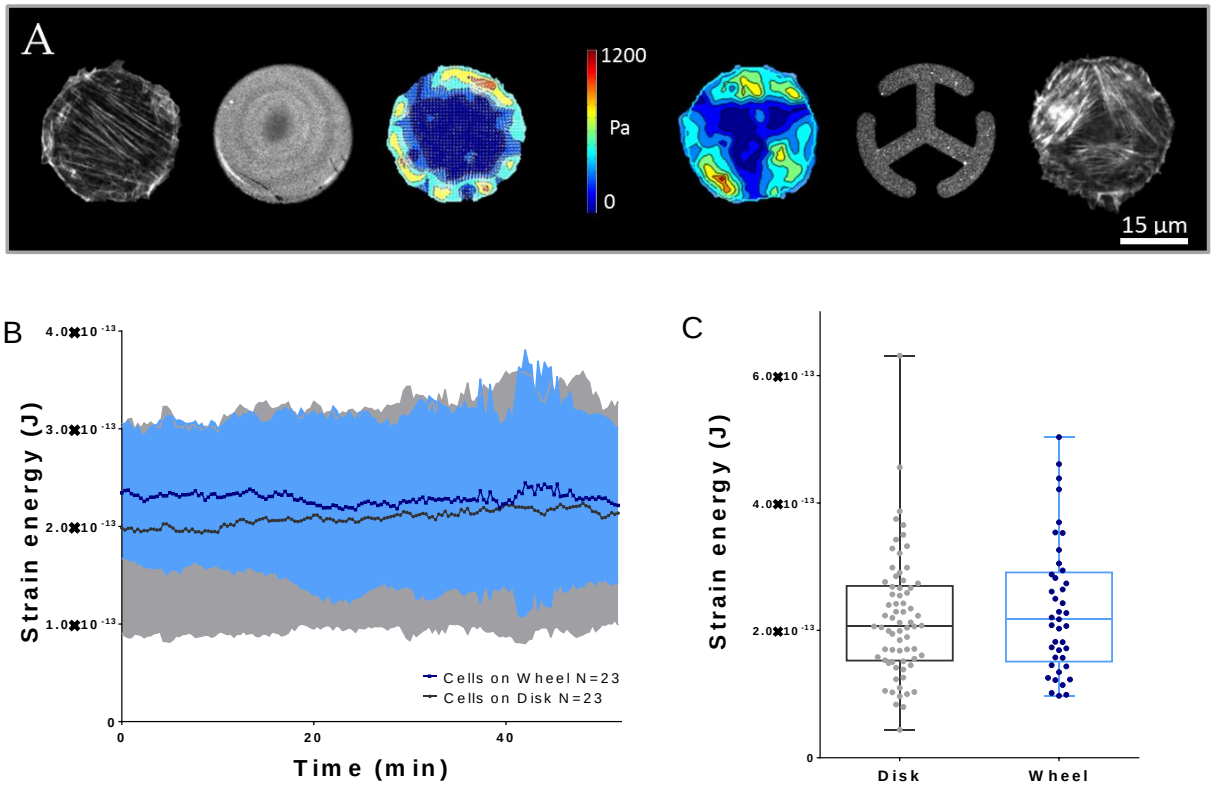

Figure 47 ***Similar tensional level for cells on Disk vs cells on Wheel.*** *(A) Qualitative comparison between a representative cell on Disk and another on Wheel. From left to right and then inverted: Fluorescence confocal microscopy images of individual actin-labelled cells. Disk/Wheel shaped fibronectin micropatterns on polyacrylamide hydrogels. Both patterns cover an area of 1000 µm^2. Individual stress maps calculated by Fourier Transform Traction Cytometry show a tripolar force pattern for the Wheel and a more bipolar one for the Disk. (B) Time course of the strain energy for cells on the two different patterns. Full lines show mean values, shaded regions correspond to standard deviations. Each curve represents averages of the reduced set of 23 cells. Duration of the experiment was 52 minutes. (C) Static strain energy for cells spread on the Disk and the Wheel shape. Using a non-parametric t-test, significant difference is not found between the two cases.*

Indeed, even when this result was expected, based on what was discussed regarding cells with same size and envelope, it was paramount for our intentions of decoupling the cellular size and shape variables from the actomyosin network arrangement. Now, this last parameter could be linked to the cellular response against perturbation in a more clear and straightforward way.

3.9 Actomyosin alignment response to perturbation

Having a confirmed and significant difference between the stress fibres alignment on cells on Disk against those on Wheel, we performed photo-activation pulses on both cases. Results obtained after photo-perturbation with 100 ms time exposure light pulse revealed a difference in the magnitude of tensional response in between the two cases (Fig. 48). Cells spread both on the Disk and on the Wheel presented a force increase upon light activation and a subsequent return to tensional equilibrium. The average time to peak after photo-activation of 7 cells on Wheel was of **2.27** ± 0.54 minutes with a subsequent relaxation time of **4.70** ± 1.40 minutes. Both times were lower than for the case of cells on the Disk: time to peak of **3.61** ± 0.72 min and relaxation time of **5.71** ± 1.45 min. This time difference had to be linked with the tensional response difference. Cells on Wheel didn't achieve the same force level of response as the ones on the Disk. With an averaged contractile maximum response of **1.853e-013** ± 8.601e-014 J against **3.536e-013** ± 2.284e-013 J, cells on Wheel exerted a lower contractile response to photo-activation than cells on Disk.

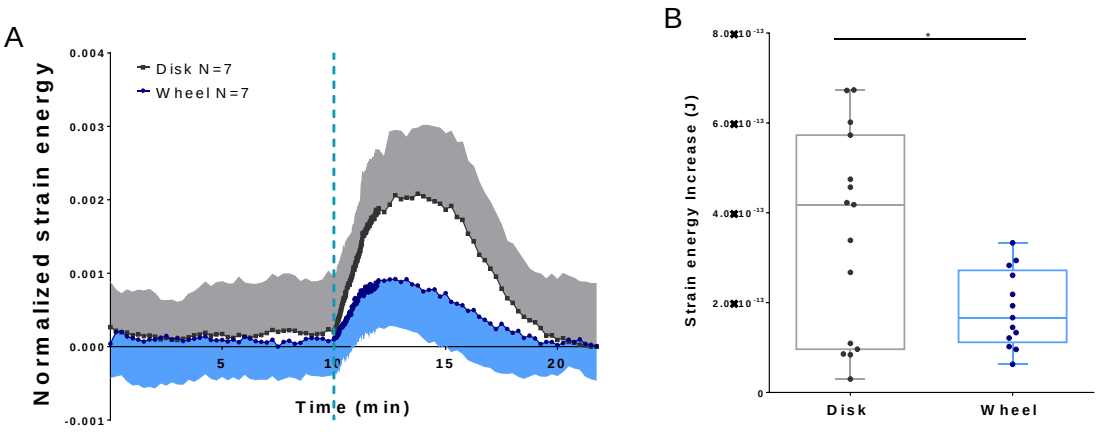

Figure 48 ***Higher contractile response obtained for cells on Disk against Wheel.*** *(A) Normalized quantification of the mean strain energy over time for cells on both shapes subjected to one light pulse of 100 ms. Full lines show mean values, shaded regions correspond to standard deviations. Each curve represents averages of the reduced set of 7 cells. Duration of the experiment was 22 minutes. (B) Strain energy increase for every activated cell on the two different shapes. Calculation is made by subtracting the strain energy value before activation to the highest strain energy value obtained after light activation. A non-parametric t-test showed significant difference in between both data sets.*

This was a remarkable result considering the fact that we had shown that cells on both shapes had a similar basal tensional state. On top of that, such steady-state value had neither been modified by the available subcellular spreading area nor by the internal actin global alignment. The difference appeared when disrupting the cellular mechanical equilibrium, forcing the cell to contract. In the event of a photo-perturbation, the actin arrangement would be controlling the efficiency of force production in terms of the amplitude of the induced perturbation.

Our observations led us to the realization that the concept of tensional homeostasis needs to be characterized both in an unperturbed state as well as during a perturbed one. While the system parameters may not modify the steady-state, they could determine the out-of-equilibrium dynamics.

The conclusion that we could draw from our specific findings is that the cell's contractile machinery performance is susceptible to the internal actin order in a clear significant way. The arrangement of stress fibers and the actin organization strongly modulates the dynamic cellular force response.

3.10 Modelling the experimental data

In order to obtain a quantitative experimental recapitulation and a better understanding of the cell's tensional responses, a mechano-biophysical model was constructed by the theoreticians Dr. Ulrich Schwarz and Dimitri Probst from the Institute for Theoretical Physics in Heidelberg, Germany.

Briefly stated, the model considers the cell as a Kelvin-Voigt viscoelastic system with an elastic component, represented by E_c, and a viscous component, represented by η (Fig. 49). Both components are parallel to each other giving the material a damped response behavior against any instantaneous signal. An active stress component σ is included in the system. This stress tensor represents the "background stress" (σ_{back}) that the cell exerts on the substrate, i.e. the homeostatic cellular tensional state, plus the stress contribution that occurs upon photoactivation (σ_{ph}). The substrate to which the cell is attached is represented as springs of constant density Y and is non-zero at any place of the pattern where the cell can actually create anchoring points.

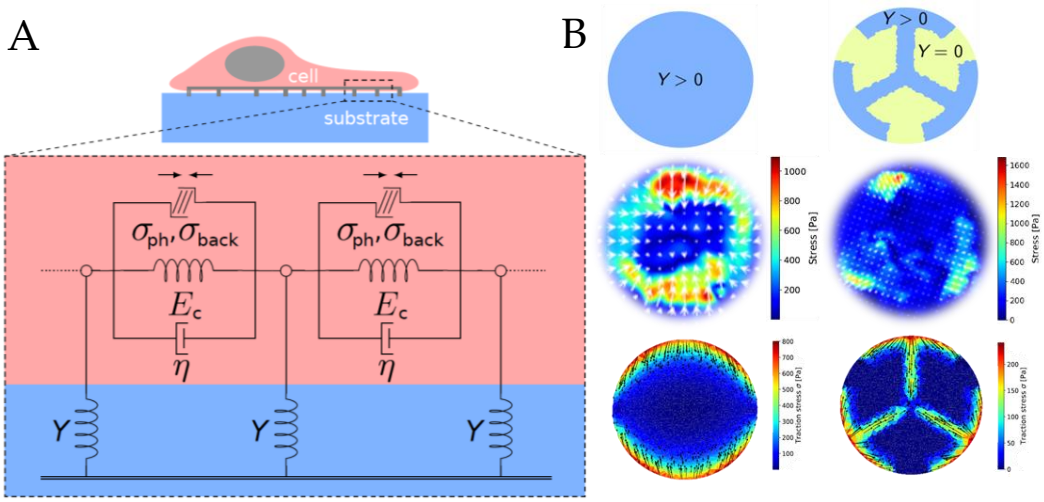

Figure 49 ***Effective physical representation of the cell and the elastic substrate on different fibronectin patterns and qualitative distribution of simulated traction stresses contrasted with experimental ones.*** *(A) A Kelvin-Voigt model with active contractility and coupling to an elastic foundation is used to reconstruct the dynamic energy response of cells upon global optogenetic activation (side view). (B) From top to bottom: Distribution of the spring stiffness, experimental stress maps obtained during photo-activation and a typical qualitative stress map during the simulated photo-activation of Disk-patterned and Wheel-patterned cells, respectively.*

This active Kelvin-Voigt model as a mechanical representation of the cell was used to fit the experimental curves obtained for both the disks of varying sizes (500 μm², 1000 μm² and 1500 μm²) and the Wheel, and also to characterize times of activation and relaxation. A full description of the model and the data obtained can be found in the Appendix C.

3.11 Supporting our findings

3.11.1 Decoupling adhesive area from actomyosin organization

The main feedback obtained when presenting this work to the scientific community was the question whether there was an actual correlation between the contractile response and the available spreading area. Was it safe to claim that the responsible for the lower force production was mainly the actin alignment? An available spreading area disparity of 570 μm² in the Wheel against the 1000 μm² offered by the Disk could very possibly be another reason for this force response difference, as this could be having a significant impact on focal adhesion distribution and stress fiber anchoring points.

3.11.2 One ring to rule them all (the findings)

To tackle this matter and put our findings to the test we went back to our previously designed micropatterns to see if we could find the proper compromise that would decouple the adhesive area from the actomyosin organization. We were looking for a shape that would maintain a high actin alignment as the Disk while having a similar adhesive area as the Wheel. Observing the results obtained for the previous shapes

we considered that the best candidate for the control experiments would be the Ring (Fig. 50), an 'empty' circular micropattern with an available spreading area of 630.75 μm^2, a closer area value to that one of the Wheel: 570 μm^2.

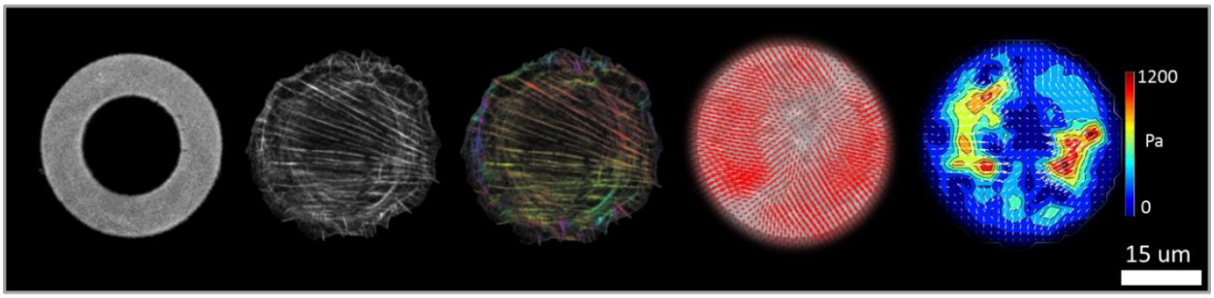

Figure 50 ***A representative cell spread on the Ring shape.*** *From left to right: 1000 μm^2 ring shaped fibronectin micropattern on polyacrylamide hydrogels. Individual actin-labelled cell. Colour-coded map obtained with OrientationJ (plugin for Fiji) showing the orientation of actin fibres in the cell. Bright-field image merged with respective force map. Individual stress map calculated by Fourier Transform Traction Cytometry, showing dipolar force traction similar to that one seen for cells on the Disk.*

The stress map obtained for cells on the Ring showed a similar dipolar pattern to that one seen for cells on the Disk. In the same manner, we found the actin alignment to be comparable in cells on both shapes. The graph of Figure 51 shows no significant difference in the order parameter of cells on Disk and Ring, and a clear difference with the Wheel.

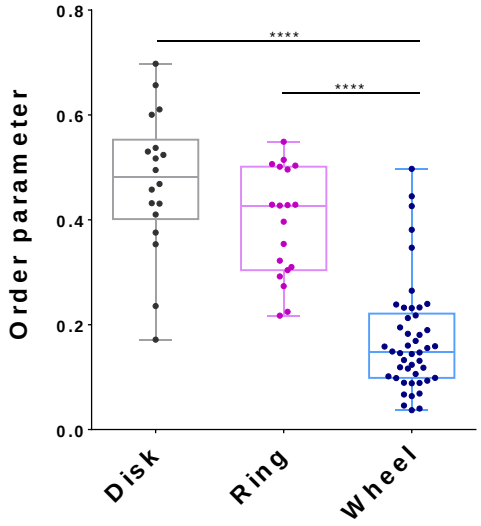

Figure 51 ***Cells on the Ring display a similar order parameter than that of the Disk.*** *Order parameter quantification for cells spread on Disk (blue), Ring (Pink) and Wheel (red). Each dot represents one cell. A 1-way ANOVA test showed significant difference in between cells spread on Wheel and those on Disk and Ring, but no significant difference between Ring and Disk.*

3.11.3 Response to photo-perturbation for cells on Ring and focal adhesions comparison

Using a light pulse of 100 ms exposure time we probed the response of 10 cells on Ring to contrast it with the already obtained data for cells on Disk and Wheel (Fig. 52). With a mean strain energy increase of **3.741e-013** ± 1.869e-013 J, cells on the Ring presented a significant higher contractile response against photo-stimulation than those on the Wheel but no significant difference with those on the Disk.

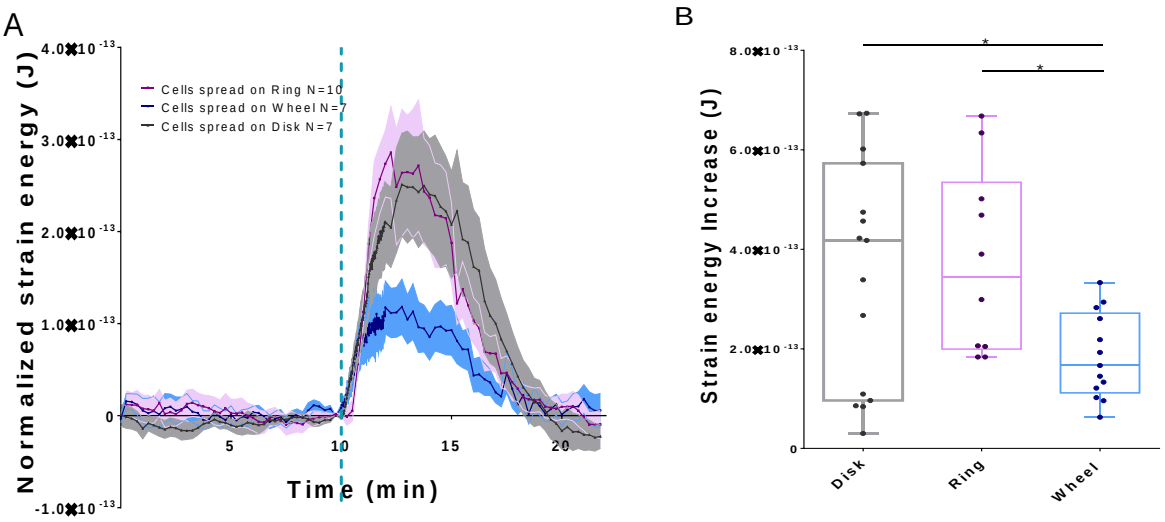

Figure 52 ***Similar contractile response obtained for cells on Disk and Ring.*** *(A) Normalized quantification of the mean strain energy over time for cells on the three shapes subjected to one light pulse of 100 ms time exposure. Full lines show mean values, shaded regions correspond to standard error of the mean. Duration of the experiment was 22 minutes. Light-blue dashed vertical light marks the photo-activation event. (B) Strain energy increase for every activated cell on the three different shapes. Calculation is made by subtracting the strain energy value before activation to the highest strain energy value obtained after light activation. A 1-way ANOVA test showed a significant difference in between the Wheel and both the Ring and the Disk. No significant difference was seen between Ring and Disk.*

This result would seem to support our previous statement linking actin alignment to force response. However, another variable that had to be looked at was how the focal adhesions were being affected by the shape and available spreading area differences. Was there any variation in the focal adhesions size or quantity that could account for the contractile response differences observed?

To answer this we performed vinculin staining assays on cells spread on the 3 patterns (Fig. 53). Vinculin is a cytoskeletal protein present in the focal adhesion complex involved in the link between integrins and filamentous actin [160]. Staining of this protein has been a standard way of focal adhesion characterization.

The analysis gave some interesting results. Observing the vinculin stained cells individually showed a similar trend in the morphology and orientation of the focal adhesion to that one seen on the actin stained cells. Elongated focal adhesions in cells on Ring and Disk showed high alignment in one preferred direction while those in cells on Wheel seemed to follow the already mentioned 'triangular arrangement'.

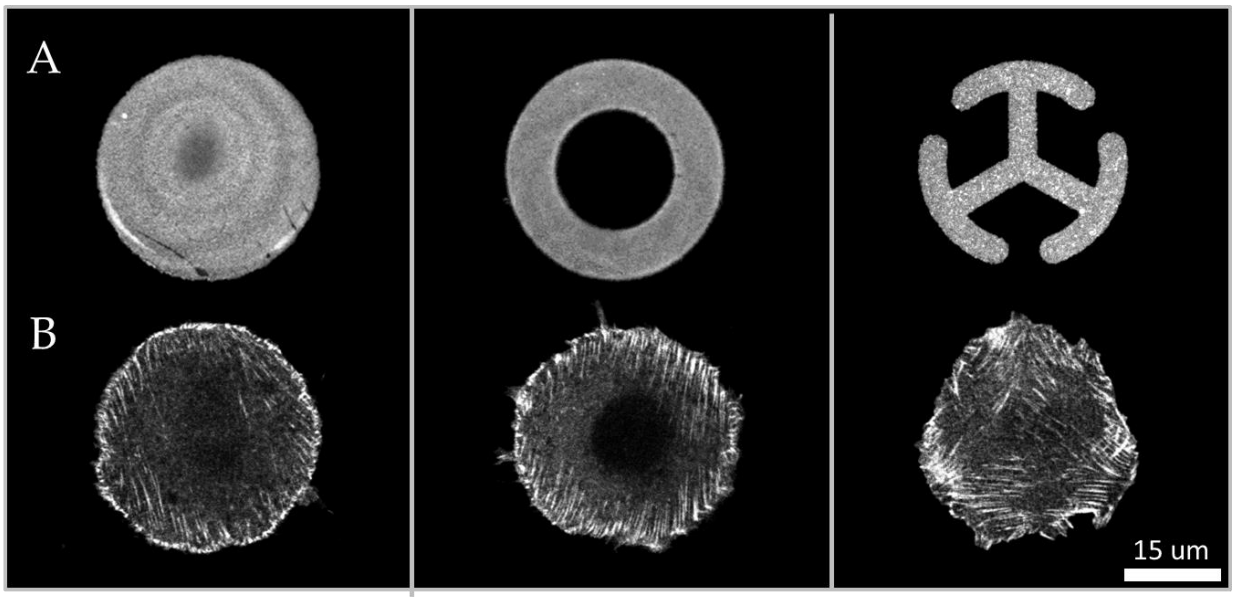

Figure 53 ***Similar focal adhesion characteristics for cells spread on Ring, Disk and Wheel.*** *(A) Disk, Ring and Wheel fibronectin patterns on polyacrylamide hydrogels. (B) Individual vinculin- stained cells.*

On the other hand, the statistical analysis proved that with a mean total area of **64.07** ± 20.84 um^2, **69.09** ± 16.20 um^2 and **56.10** ± 14.71 um^2 for Disk, Ring and Wheel respectively, there was **no significant difference in the overall cell focal adhesion coverage.** Similar results were obtained for the case of the mean average area of single focal adhesions in Disk, Ring and Wheel with mean values of **0.7060** ± 0.2069 um^2**, 0.7859** ± 1553 um^2 and **0.7721** ± 0.1842 um^2, respectively.

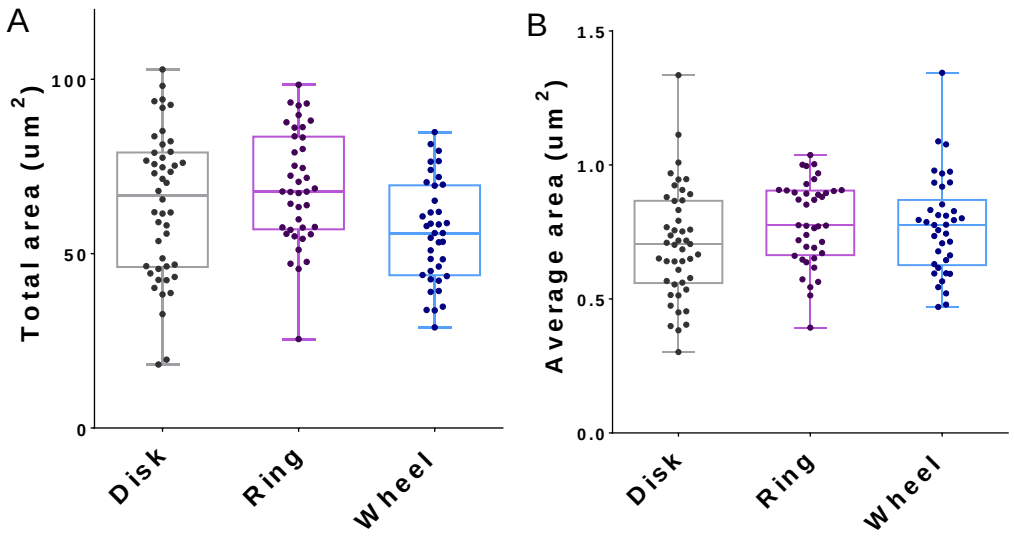

Figure 54 ***Plot showing focal adhesion characteristics for cells spread on Ring, Disk and Wheel.*** *(A-B) Quantification of the total area covered by the focal adhesions, and average area of individual focal adhesions on each pattern. Each dot represents a cell. Disk (N=69), Ring (N=43) and Wheel (N=41).*

Taken together, results obtained from graphs A and B of Figure 54 showed that there was no significant difference in the size and amount of focal adhesions present in cells spread on any of the 3 shapes. This would be confirming the major role of the actin organization in the force production response.

3.11.4 Saturation phenomena after multiple photo-activations of increasing intensity

In order to further characterize the optogenetic system and the cell contractile responses to varying photo-activations, we tried out one last experiment. We carried out a similar light protocol used by Dr. Valon (Fig. 37) when studying the CRY2/mCherry membrane recruitment, which consisted on increasing the exposure time of the light pulses in the following order: 10 ms, 20 ms, 50 ms, 100 ms, 150 ms, 200 ms (Fig. 55).

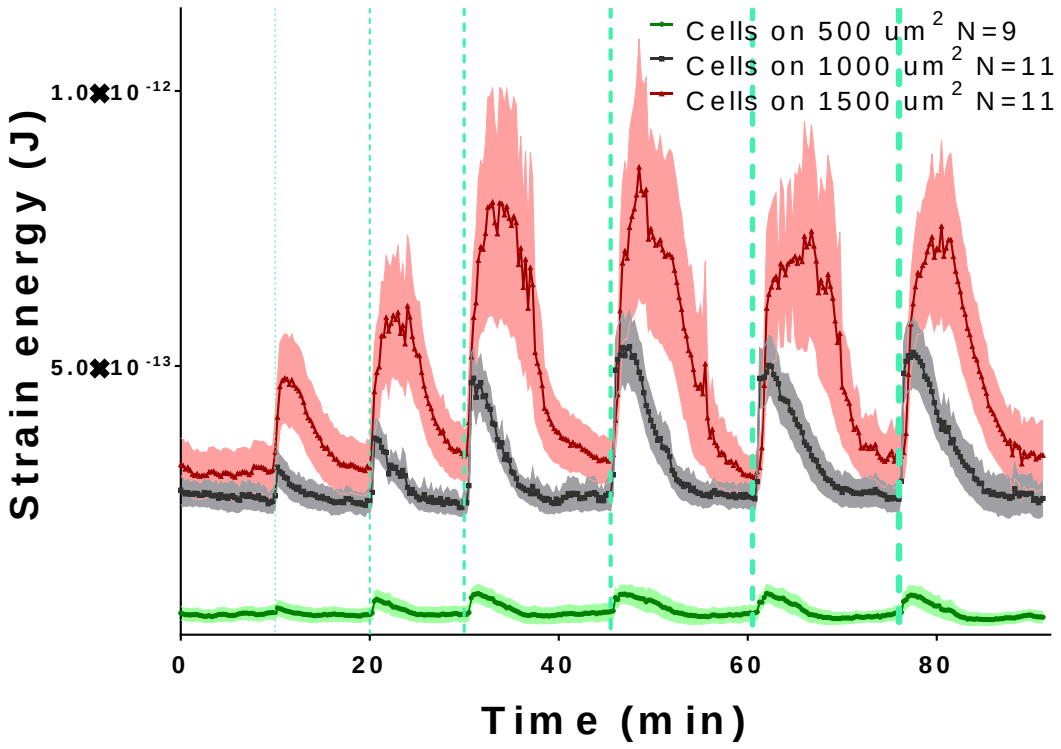

Figure 55 ***Effect of the cellular area on the strain energy level as well as its energy gain and dynamics upon photoactivation of increasing duration.*** *Full lines show mean values, shaded regions correspond to standard error of the mean. Each curve corresponds to an average of 9, 11, and 11 cells for 500 µm², 1000 µm² and 1500 µm² circular adhesive micropatterns, respectively. The activation pulses (represented by light-blue vertical discontinuous lines) were of 10, 20, 50, 100, 150 and 200 ms duration.*

Results obtained from this experience showed that the cell's contractile response reached a saturation point at 100 ms time exposure light pulse. Such behaviour did not follow the same trend reported by Dr. Valon, where the signal of CRY2/mCherry recruitment to the membrane increased all along the protocol. This would imply that no matter the increase of RhoGEF to the membrane, the cell reached its force maximum response after a stimulation of 100 ms of blue light. The saturation was corroborated repeating the activation protocol for cells on the Wheel (Fig. 56). Cells both on Disk and Wheel reached their force saturation point with the same light exposure as in the previous experiment (100 ms), but for the cells on the Wheel pattern the force increase was always lower than that of the ones on the Disk.

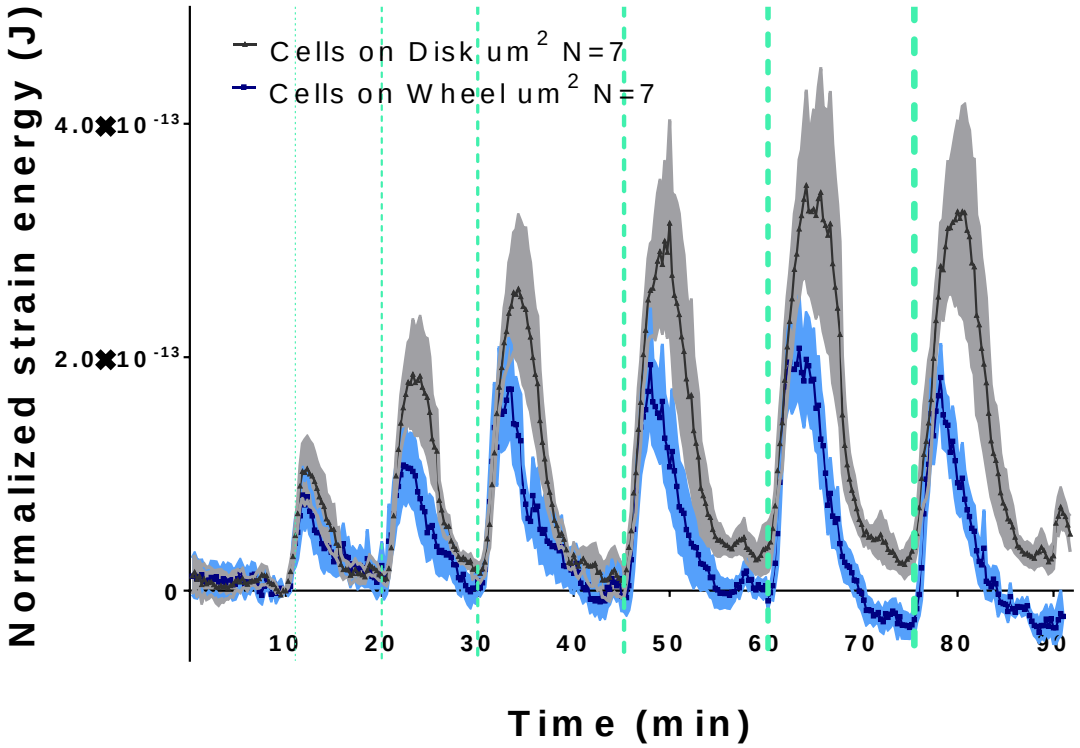

Figure 56 ***Effect of the actin alignment on the normalized energy gain and dynamics upon photoactivation of increasing duration.*** *Full lines show mean values, shaded regions correspond to standard error of the mean. Each curve corresponds to an average of 7 cells both for the Disk and the Wheel micropatterns. The activation pulses (represented by light-blue vertical discontinuous lines) were of 10, 20, 50, 100, 150 and 200 ms duration.*

As already mentioned, an appropriate physical model which allowed capturing the dynamics of the cellular energy based on the geometry and size of the micropatterns, had been obtained by our collaborators in Heidelberg. Comparing the stress peaks measured during the photo-activation protocol for both the Disk and the Wheel, we corroborated the accuracy of the model at reproducing the cellular contractile behaviour. On Figure 57 a fitting of the theoretical model is done over the experimental stress increases obtained after each photo-activation. An increment in cell contractility with augmenting light time exposure can be observed, as well as a clear higher contractile response from cells on Disk over those on Wheel, reaching a maximal stress response of **17.33** kPa and **12.56** kPa for Disk and Wheel, respectively. Both the experimental data and the model showed force saturation after 100 ms light exposure.

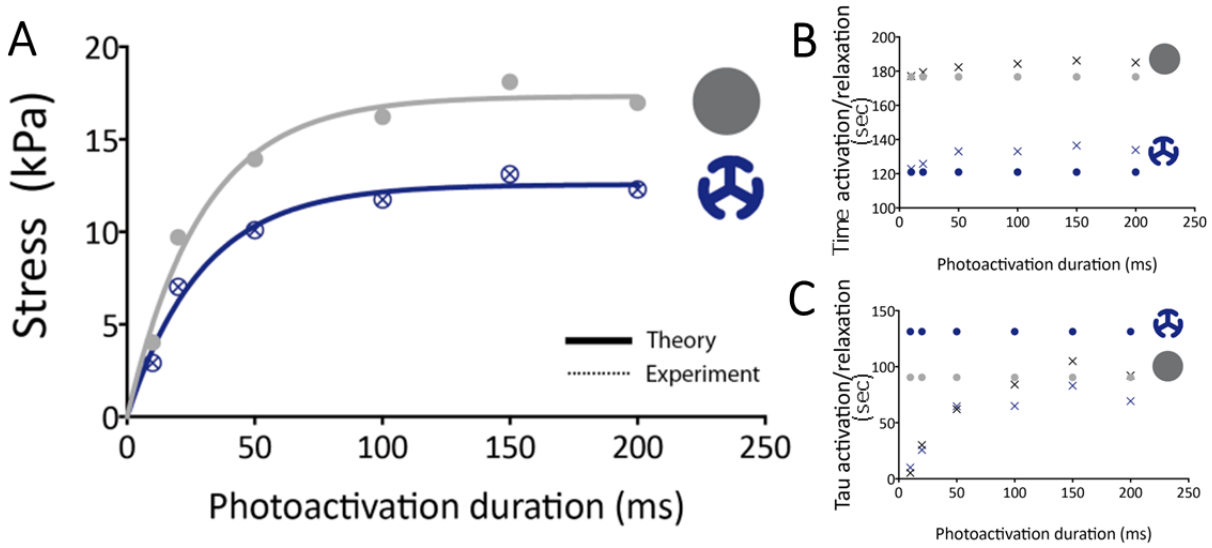

Figure 57 ***Stress dynamics as a function of the photo-activation duration.*** *(A) Stress increase versus photo-activation duration for cells on Disk and Wheel showing a saturation point after 100 ms exposure time. Dots represent experimental values and full lines were obtained with the biophysical model. A higher strain response can also be observed for the cells on the Disk all along the opto-protocol. (B) Stress activation (full dots) and relaxation (crosses) times versus photo-stimulation exposure times. (C) Stress activation (full dots) and relaxation (crosses) constants versus photo-stimulation exposure times. Both activation times and constants are independent of the PA duration. Relaxation times and constant increase in a saturating manner as a function of the PA duration, i.e. a longer PA duration has a longer impact on the contractility of cells. Grey dots and crosses correspond to the Disk pattern, while blue dots and crosses refer to the Wheel pattern.*

Taking advantage of this mathematical model, we studied also the peaks dynamics by obtaining the activation/relaxation constants and real times. Results showed that the activation dynamics are unaffected by photo-activation pulse duration, cells reached their maximum contractile response within the same time window no matter the time exposure. On the other hand, relaxation times increased in a saturating manner as a function of the photo-activation duration, implying that longer light pulses had a longer impact on the contractility of cells and on its return to basal tensional state. Further studies on the actin rheology of the relaxation and possible α-actinin cross-linking variations upon photo-activation could give interesting insights into the difference between activation and relaxation.

The common saturation point discussed earlier would be implying a fascinating fact: the highest contractile point that a cell spread on any of the studied micropatterns could reach upon photo-activation did not depend on its size or its internal actin arrangement. Consequently, the reason for this saturation could be linked to a saturated myosin capacity or a RhoA activity limit. Deeper understanding and characterisation of this force response saturation could be addressed in further research projects.

3.12 Manuscript (unfinished version)

Actin architecture and biochemical activation control single cell tension setpoint

Andersen T[1], Probst D[2], Wang I[1], Moreau P[1], Fitzpatrick V, Boudou T[1], Schwarz U[2]*, Balland M[1]*

[1]Laboratoire Interdisciplinaire de Physique, Grenoble Alpes University, Saint Martin d'Hères, France

[2]Institute for Theoretical Physics and BioQuant, Heidelberg University, Heidelberg, Germany

*Corresponding authors:

Martial Balland, martial.balland@univ-grenoble-alpes.fr

ORCID #: orcid.org/0000-0002-6585-9735

Mailing address: Laboratoire Interdisciplinaire de Physique, UMR 5588, 140 avenue de la physique 38402 Saint Martin d'Hères, France

Ulrich Schwarz, schwarz@thphys.uni-heidelberg.de

ORCID #: orcid.org/0000-0003-1483-640X

Mailing address: Institute for Theoretical Physics, Philosophenweg 19, D-69120 Heidelberg, Germany

Abstract

Cellular decision-making in complex environments depends on both biochemical and mechanical signals. Adherent cells generate mechanical forces to sense the adhesive geometry and rigidity of their environment, with dramatic consequences for cell migration, division, differentiation and fate. Like for many other physiological processes, it has been suggested that cells maintain a characteristic setpoint in tension, so that they can adapt to their mechanical environment (tensional homeostasis). Here we test this hypothesis combining recent advances in traction force microscopy on soft elastic substrates, micropatterning and optogenetics. We find that after transient whole-cell Rho-activation achieved by a Cry2/CBAN-construct, cells return to a constant tension setpoint with near perfect precision. However, we also find that this setpoint is variable, increasing not only with cell spread area, but also with the actin order parameter. Fitting the experimental traction force data to a theoretical model for active contractile systems reveals that force transmission to the environment is reduced when different actin orientations work against each other in the same cell. The peak values for the activation stresses saturate with increasing activation time at a value around 100 ms and are largest for completely polarized cells. Together, our results show that single cells do maintain internal setpoints for tension, which however are constrained by actin architecture and biochemical activation.

Introduction

Living tissues are constantly submitted to mechanical perturbations, arising both from external forces and from internal cell activity. In order to maintain tissue integrity, cell collectives therefore use mechano-chemical circuits to adapt their mechanical state to changes in their environment (Valerie Weaver, Balancing forces, Nature Reviews MCB 2011). Such tensional homeostasis (TH) makes tissue an active material that can keep a desired mechanical function in a robust manner (MacKintosh and Schmidt Active cellular materials 2010; Trepat and Sahai, Nature Physics 2018). TH has first been demonstrated in a quantitative manner by varying the macroscopic stress applied to cell-populated collagen gels (Brown Tensional homeostasis in dermal fibroblasts: mechanical responses to mechanical loading in three-dimensional substrates J Cellular Physiology 1998). It was found that cells dynamically counteracted the effect of externally applied stress, effectively working towards a setpoint of tension. For epithelia it was shown that progression towards a tumour is strongly related to changes in TH, with a central role of the signalling molecule Rho, the master regulator for cell contractility (Weaver 2005, Tensional homeostasis and the malignant phenotype).

Despite the importance of TH on the tissue level, a corresponding understanding on the cell level is still elusive. During recent years, it has been established that cell actively pull on their environment to sense its mechanical properties (review Discher), with dramatic consequences for migration (Isenberg et al, 2009), division (Lafaurie-Janvore et al, 2013) and differentiation (Engler et al, 2006). It also has been shown that cellular force generation is closely related to the organization and regulation of the actin cytoskeleton (Blanchoin review, Koenderink and Paluch COSB review 2018). However, it is not clear if tensional homeostasis on a single cell level corresponds to a well-defined tension setpoint or not. The main obstacle to progress in this direction is the lack of appropriate techniques to dynamically vary the stresses in cells. Traditional approaches in biology use pharmacological or genetic approaches to perturb cell contractility, but these are typically slow and hard to control in a quantitative manner. Direct application of physical force has an immediate effect, but tends to be a strong perturbation to the biological system. Combining micropatterning with an AFM-setup to dynamically measure and control forces, it has been shown that single cell tension evolves towards a plateau, but that this setpoint is variable and depends on the history of mechanical loading (Webster BPH 2014). While cells maintained tension during slow loading, they strongly pulled back during fast loading. In order to quantify TH for single cells in a less intrusive manner, a more flexible and configurable approach is needed to rapidly and dynamically change cell forces. The optimal solution in fact would be a direct manipulation of the regulatory machinery for contractility inside cells. This dynamic control can in fact be achieved with optogenetics (Deisseroth et al, 2011). This technique allows rapid light-mediated protein activation, with the added advantages of low

toxicity and reversibility. Although originally developed for neuroscience, where ion channels or ion transporters are activated by light, during recent years it has been also increasingly applied to the cytoskeleton, where light-sensitive domains are used to effect an allosteric change in a protein of interest (Weitzman & Hahn, 2014; Tischer & Weiner, 2014; De Renzis review Trends in Cell Biology 2016).

Here we combined optogenetics, to induce cell contractility, with traction force microscopy, to measure the strain energy that cells impart to their environment, thus achieving an immediate relation between cell input and output. Moreover, as cell forces are closely related to cell shape, we performed our experiments on micropatterned substrates, to uncouple our findings from cell shape modulation effects. Our experimental data on living cells show that individual cells maintain a constant setpoint of tension, but that it strongly depends on cell size and actin organization. By changing the actin cytoskeleton organization through micropatterning while keeping similar cell envelope and spreading area, we were able to show that actin architecture has a decisive role in determining cellular force production efficiency. As confirmed by a theoretical model for actively contracting thin films with different domains, maximal efficiency is obtained only for completely polarized cells. Force generation is in addition limited by the biochemistry of Rho-activation, as shown here by systematically varying activation time.

Larger cells display a higher strain energy production in response to transient RhoA perturbations

To investigate how cells react to fast transient perturbations, we coupled time resolved force imaging with optogenetic stimulations. Our strategy was to trigger the activation of the small GTPase RhoA, the major regulator of cellular contraction (ref Alan Hall). We used previously described NIH3T3 cells stably expressing a Cry2-CIBN optogenetic probe to dynamically control the localization of ArhGEF11, an upstream regulator of RhoA, by using blue light [Valon et al., 2014]. To limit our measurements from cell shape variability, we used soft micropatterning to restrict cells to predefined areas and shapes (Figure 1a). An established mathematical model that describes the physical core of this situation is the continuum mechanics of a thin contractile film of the same geometry (Figure 1b) (Edwards and Schwarz PRL 2011, Mertz et al. PRL 2012, Oakes Geometry Regulates Traction Stresses in Adherent Cells BPJ 2014). This model describes the cell as a Kelvin-Voigt solid with isotropic active stresses and an elastic foundation. Using traction force microscopy, we first quantified the forces and strain energies exerted by single opto-3T3 fibroblasts spread on disc shaped fibronectin micropatterns printed on soft (5kPa) polyacrylamide hydrogels of increasing areas (500, 1000, 1500 μm^2) (Figure 1a). Cell strain energy increases as a function of cell spreading area (Figure 1c), as previously described by other studies [Tan-Chen PNAS 2003; Reinhart-King-Hammer BiophysJ 2005; Tseng-Balland LabChip 2011, Oakes BiophysJ 2012] and also as predicted by the standard model

(solid line in Figure 1c). The slight differences between experiment and model can be understood from the fact that the actin organization changes in a non-linear fashion with cell size, with actin organization saturating with increased size as measured by the actin order parameter (Figure 1d). Upon photo-activation (100 ms blue light pulse) cell strain energy quickly increased (~2 minutes) before slowly relaxing (6 to 8 minutes) (Figure 1e), in good agreement with earlier reports (Valon BPJ). Most importantly in the context of TH, cell strain energy recovered its original baseline level, confirming the concept of a stable setpoint in tension. We measured an average strain energy baseline of 0.0801 ± 0.0005 pJ, 0.2622 ± 0.0009 pJ and 0.4501 ± 0.0010 pJ on small (500 μm²), medium (1000 μm²) and large (1500 μm²) micropatterns, respectively (Figure 1e), reflecting the higher pre-stress induced by cell spreading area (Figure 1c) and in good agreement with the model predictions. We then quantified the Relative Strain energy Increase upon photoactivation (RSI, maximum peak value minus baseline strain energy). Surprisingly, pre-stressed cells were not limited in their traction efficiency as they were able to generate even higher contractility. The RSI upon a 100 ms blue light stimulation was only 0.0907 ± 0.0173 pJ for cells spread on small micropatterns, but reached 0.3005 ± 0.0627 pJ and 0.4262 ± 0.1150 pJ on medium and large micropatterns, respectively (Fgiure f, error values are expressed as SEM). These results could be reproduced by our model by assuming a double-sigmoidal activation of the active stresses, as suggested by earlier experiments (Valon BPJ). In our simple model, we then also obtained increasing energy gains with increasing cell size. Together, these results validate the concept of TH and show that a simple model can explain the main experimental results. However, Figure 1d also suggests a role of the actin organization that is not reflected by the model. We therefore set out to investigate this point in more detail by using a larger variety of different micropatterns.

Actin polarity determines the efficiency of force production during optogenetic activation

In order to investigate the relationship between the organization of the actin cytoskeleton and efficiency in cellular forces production, we designed a circular micropattern with three branches, hereafter named the “wheel” micropattern (Figure 2a). This micropattern led to a projected cell area similar to its discoidal counterpart while inducing a different organization of the actin cytoskeleton (Figure 2b). Because cells on the disc patterns break the circular symmetry and spontaneously polarize in one direction, the wheel pattern is effectively more isotropic, as it enforces three different domains with pairwise balance each other. In order to adapt the standard model to this actin organization, we divided the computational domain in different parts, each with the main direction of actin orientation determining the direction of the anisotropic stress (Figure 2c). Surprisingly, such a model gives similar strain energies, in very good agreement with the experimental results and in line with the concept of TH. Interestingly, the experiments also revealed a smaller variance on the

wheel pattern. Unexpectedly, however, we measured a different response to blue light stimulation on cells spread on disc versus wheel micropatterns (Figure 2d). The speed of cell contraction was similar on both micropatterns, however, cells on discs, presenting an anisotropic, dipolar actin cytoskeleton, exerted a greater response to photo-activation in terms of force amplitude, with a time to peak of 3.43 ± 0.83 min and a RSI of 0.3536 ± 0.05898 pJ. Cells on wheel patterns, with a more isotropic, tripolar actin organization, responded with a time to peak of 2.71 ± 1.02 min and a RSI of 0.1853 ± 0.02386 pJ. We also verified that the observed responses in terms of force production were not impacted by differences in the fibronectin adhesive area allocated to the cells. To this end we used a ring shaped micropattern that has an adhesive area close to the wheel micropattern and measure both adhesive expression of the cells and the efficiency of their force production. We found no significant differences in the total area occupied by focal adhesion on the three different shapes (see SI). Interestingly the ring shaped micropattern induced an actin organization close to the one observed in the discoidal pattern case. Strikingly the force dynamic response to the optogenetic stimulus was fairly identical for ring and disc patterns demonstrating the main role of the organization of the actin cytoskeleton in the efficiency of force production.

Figure 1: Larger cells display a higher strain energy production in response to transient RhoA perturbations

(a) Disk shaped fibronectin micropatterns on polyacrylamide hydrogels with increasing surface area. The patterns cover an area of 500-1000-1500 um2. (b) Individual actin-labelled cells. (c) Bright-field images merged with respective force maps. They show that NIH 3T3 cells fully spread on all three patterns. (d) Individual stress maps calculated by Fourier Transform Traction Cytometry show that traction forces are localized at cell contour. (e) Static strain energy for cells spread on the three different disk sizes. Using a 1-way ANOVA test, significant difference is found between cells spread on 500 um2 pattern and the other two bigger sizes. (f) Global cellular actin fibre alignment for cells spread on each disk size. This is represented by the actin order parameter. (g) Quantification of the mean strain energy over time for cells on the different disk sizes subjected to one light pulse of 100 ms. (h) Strain energy increase for every activated cell on the three different disk sizes. Calculation is made by subtracting the strain energy value before activation to the highest strain energy value obtained after light activation.

Figure 2 Actin organization regulates the cell's contractile efficiency.

From left to right: 1000 um2 disk shaped and hazard shaped fibronectin micropatterns on polyacrylamide hydrogels with increasing surface area (both patterns cover the same projected area). Colour-coded map given by OrientationJ (plugin for Fiji) showing the angle of oriented features in the image. Individual actin-labelled cells. Bright-field images merged with respective force maps. Individual stress maps calculated by Fourier Transform Traction Cytometry. (b) Static strain energy for cells spread on the 1000 um2 disk and the hazard

shape. Using a 1-way ANOVA test, significant difference is not found between the two cases. (c) Global cellular actin fibre alignment for cells spread on both fibronectin micropatterns. This is represented by the actin order parameter. (d) Normalized quantification of the mean strain energy over time for cells on both shapes subjected to one light pulse of 100 ms. The inset shows a close up of the curve right after photo activation. (e) Strain energy increase for every activated cell on the two different shapes. Calculation is made by subtracting the strain energy value before activation to the highest strain energy value obtained after light activation.

Figure SI Cells with similar actin organization display identical force response

To be written

Materials and methods

TFM gel preparation - MASK METHOD

Description of the procedure based on the work done by Vignaud, Hajer Ennomani, and Théry, 2014 with modifications done at Motiv group.

A photomask (TOPAN), previously rinsed with water and isopropanol, and a glass coverslip (20 mm) are activated together with air plasma (4 minutes) and oxygen plasma (40 seconds). Then a pLL–PEG drop (35 µl) is sandwiched between the chrome side of the mask and the glass coverslip. After 30 min incubation, the glass coverslip is removed and saved for the following step as it is now a passivated surface. The photomask is exposed to deep UV during 3 minutes from the quartz side, burning the pLL–PEG at defined loci with minimum loss of resolution due to diffraction. Then again, a drop (35 µl) of sodium bicarbonate (100 mM) solution of fibronectin (20 ug/ml, Sigma) and Alexa546-conjugated fibrinogen (5 ug/ml, Invitrogen) is sandwiched between the mask and the passivated glass coverslip and incubated for 30 min. For 4.47 kPa hydrogels, a solution containing 12.5% acrylamide (from 40% stock solution) and 7.5% bisacrylamide (from 2% stock solution) was prepared in a 10 mM DPBS solution (pH 7.4). Finally, the polyacrylamide solution is mixed with passivated fluorescent beads (0.2 um, Invitrogen) by sonication before addition of ammonium persulfate (APS) and N,N,N',N'-tetramethylethylenediamine (TEMED). A drop (47 µl) of this solution is sandwiched between the patterned region of the mask and a silanized glass coverslip. After 30 min polymerization, the coverslip with the hydrogel is carefully removed from the mask and stored in DPBS solution at 4 °C. Cells were plated on them the following day.

Cell culture and plating

Stable cell line NIH 3T3 fibroblasts with CIBN-GFP-CAAX and optoGEF-RhoA constructs (kindly provided by L. Valon and M. Copper, Institute Curie, Paris, France) were cultured in Dulbecco's Modified Essential Medium (DMEM) containing 10% foetal bovine serum (FBS) and 0.2% penicillin-streptomycin. Cells were grown in a humidified 5% CO2 incubator at 37ºC. Cells were seeded on patterned substrates at a density of 200.000cells/cm3. All traction force measurements or immunostainings were performed 4 hours after seeding to ensure full spreading of the cells. Leibovitz's L-15 medium, supplemented with 10% FBS and 0.2% penicillin-streptomycin, was used as imaging media for every live imaging experiment.

Live cell imaging and activation

Cell imaging and activation intended for posterior force measurements was carried out using a Nikon Ti-E microscope, Zyla sCMOS camera (Andor, Belfast, UK) and Plan Apo VC 60x/1.40 Oil objective (Nikon). The microscope was equipped with an incubator that maintains the temperature at 37 °C. Global cellular photoactivation was performed using a LED light source (X-Cite/XLED1, Lumen Dynamics, Canada) coupled to a Mosaic digital micromirror device (Andor). Depending on the experiment done, activation pulses were 10-20-50-100-150-200 ms long using an LED at 460 nm with power of 256.7 uW (measured at the back focal plane of the objective).

Cell stainings

For stress fibre labelling, cells were permeabilized and fixed for 10 min with 0.2% W/V Triton X-100 and 4% paraformaldehyde in DPBS buffer to preserve cell shape. Fixed samples were washed with PBS and incubated in blocking buffer for 45 min. Afterwards, cells were stained with phalloidin at 1 mM (Sigma-Aldrich) for 1 hour and finally mounted on glass slides with Mowiol 4-88 (Polysciences, Inc.) and kept at 4ºC overnight.

For live actin measurements, cells were incubated overnight in DMEM medium supplemented with 100 nM SiR-actin (SPIROCHROME) and 10 μM verapamil.

Both live and fixed actin imaging was carried out with a Leica TCS SPE confocal microscope with an HCX PL APO 63x/1.40 oil objective. The microscope was controlled through the Leica Application Suite (LAS) X software. Pictures were then processed using Fiji software.

Actin order parameter analysis

This parameter was obtained with a program that calculates the local orientation in actin images using the structure tensor. The program will first smooth the original image using a Gaussian filter. Then, based on the intensity level, the region in the cell is segmented.

For each pixel in the cell, the structure tensor J (that has 3 elements: J11, J12 and J22) is computed in a local neighbourhood that is also Gaussian. The orientation angle, the coherency and a measure of local gradient (grey level is constant or it changes) are computed from the elements of the structure tensor (λi are the eigenvalues of J):

$$\tan(2\theta)=\frac{2J_{12}}{J_{22}-J_{11}} \qquad coherency=\frac{\sqrt{(J_{22}-J_{11})^2+4J_{12}^2}}{J_{11}+J_{22}}=\frac{\lambda_1-\lambda_2}{\lambda_1+\lambda_2} \qquad gradient=J_{11}+J_{22}=\lambda_1+\lambda_2$$

The average orientation and order parameter S will be computed by averaging over all pixels for which the coherency is above a threshold value, which can be changed.

Average angle: $\theta_m=\langle\theta\rangle_{c>thres}$

Order parameter: $S=\langle\cos(2(\theta-\theta_m))\rangle_{c>thres}$

(S=1 means that the local orientation is parallel to the average orientation, S=0 means that they are orthogonal).

Vinculin staining

After 4 h of culture on the micropatterns, cells were fixed with 3.7% formaldehyde in PBS, permeabilized with 0.2% Triton X-100 in TBS (50 mM Tris-HCl, 0.15 M NaCl, pH 7.4) and blocked with 2% BSA (Sigma Aldrich) in TBS. The samples were then incubated with primary antibodies against vinculin (Sigma Aldrich) and detected with Alexa 488-conjugated, isotype-specific, anti-IgG antibodies (Invitrogen). Actin was labelled with phalloidin-TRITC (Sigma) and nuclei were stained with DAPI (Life Technologies).

Areas of focal adhesions were segmented and measured by using a home-made Image J (National Institutes of Health) routine.

Traction force microscopy

Displacement fields describing the deformation of the polyacrylamide substrate are determined from the analysis of fluorescent beads images before and after removal of the adhering cells with trypsin treatment. The displacement field can be obtained by merging the images of the gel under stress, that means while the cell is alive, and the non-stressed image, which is after the cell has been detached using trypsin. Its calculation is made by a two-step method consisting of particle image velocimetry followed by individual bead tracking (Sabass, 2008, Butler, 2002). Force reconstruction was conducted with the assumption that the substrate is a linear elastic half-space, using Fourier Transform Traction Cytometry (FTTC) with zeroth-order regularization (Sabass 2008). The shear

modulus of the gels used in these experiments was 4,47 kPa. All calculations and image processing were performed in Matlab combining particle image velocimetry and single particle tracking.

Figure 1

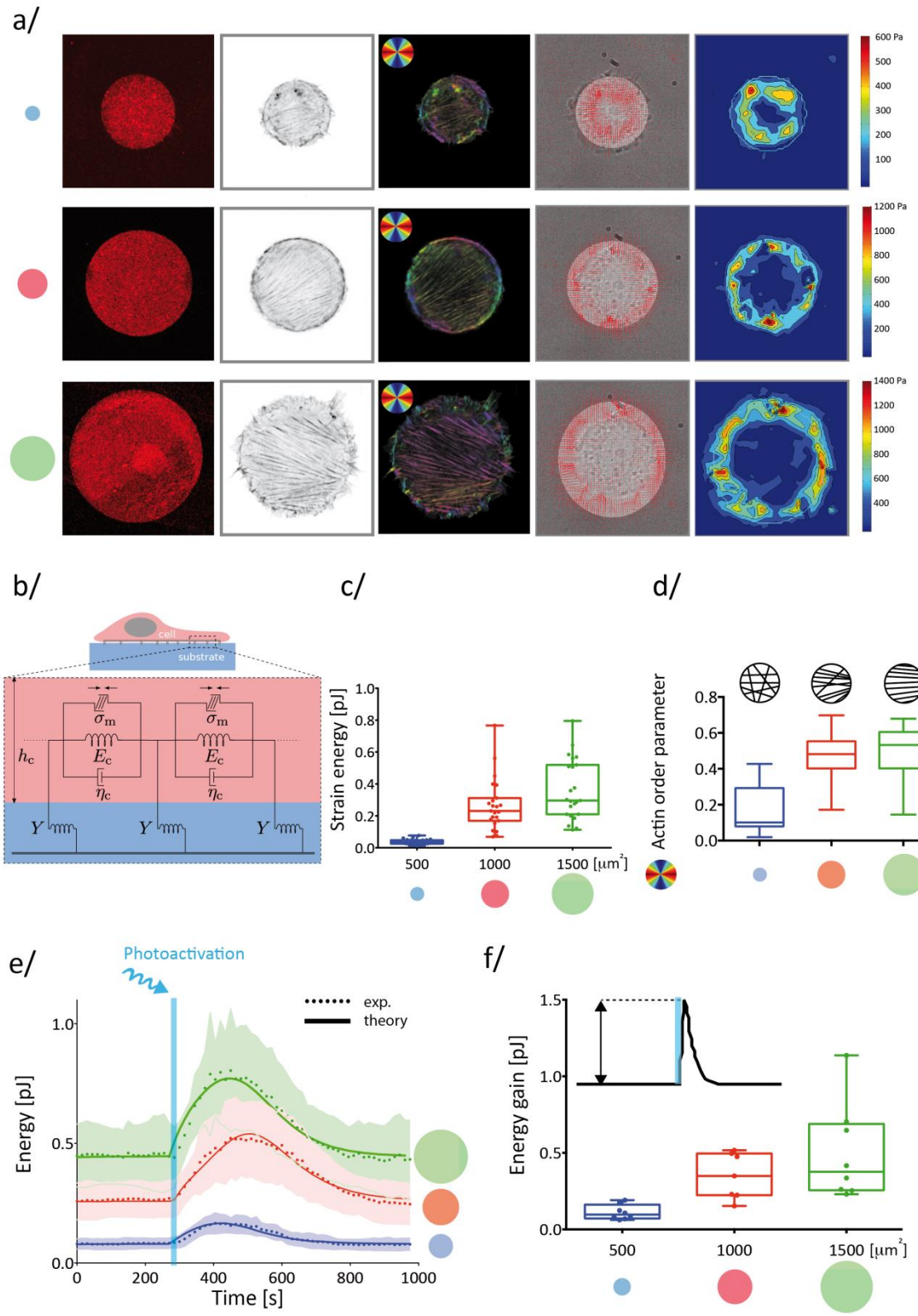
a/
600 Pa
500
400
300
200
100
1200 Pa
1000
800
600
400
200
1400 Pa
1200
1000
800
600
400
b/
cell
substrate
σ_m
E_c
η_c
h_c
Y
c/
Strain energy [pJ]
1.0
0.8
0.6
0.4
0.2
0.0
500
1000
1500 [μm²]
d/
Actin order parameter
0.8
0.6
0.4
0.2
0.0
e/
Photoactivation
exp.
theory
Energy [pJ]
1.0
0.5
0.0
0
200
400
600
800
1000
Time [s]
f/
Energy gain [pJ]
1.5
1.0
0.5
0.0
500
1000
1500 [μm²]

Figure 2

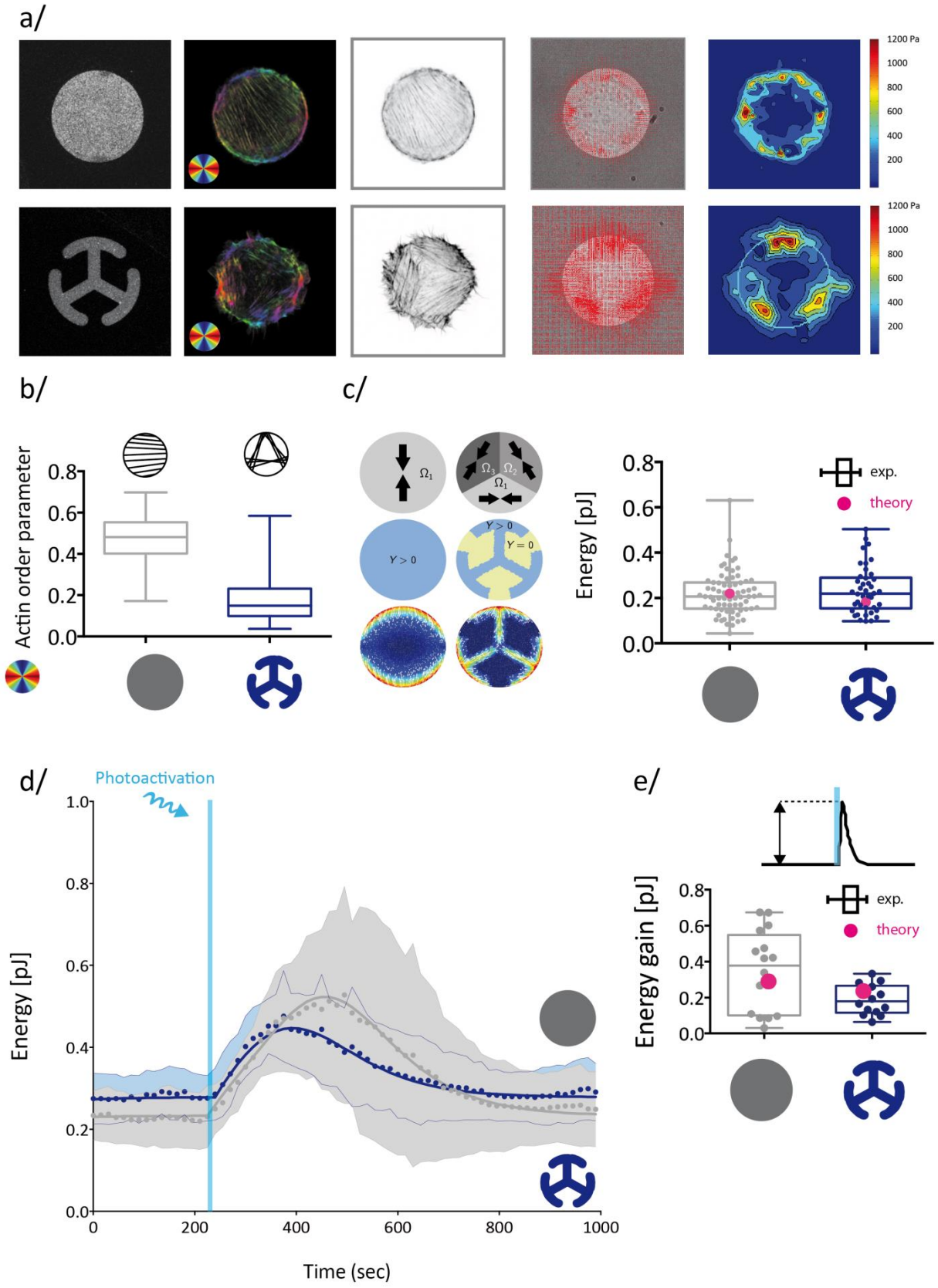
a/
1200 Pa
1000
800
600
400
200
b/
Actin order parameter
0.8
0.6
0.4
0.2
0.0
c/
Ω_1
Ω_3
Ω_2
Ω_1
$Y > 0$
$Y > 0$
$Y = 0$
Energy [pJ]
exp.
theory
d/
Photoactivation
Energy [pJ]
1.0
0.8
0.6
0.4
0.2
0.0
0
200
400
600
800
1000
Time (sec)
e/
Energy gain [pJ]
exp.
theory

Figure 3

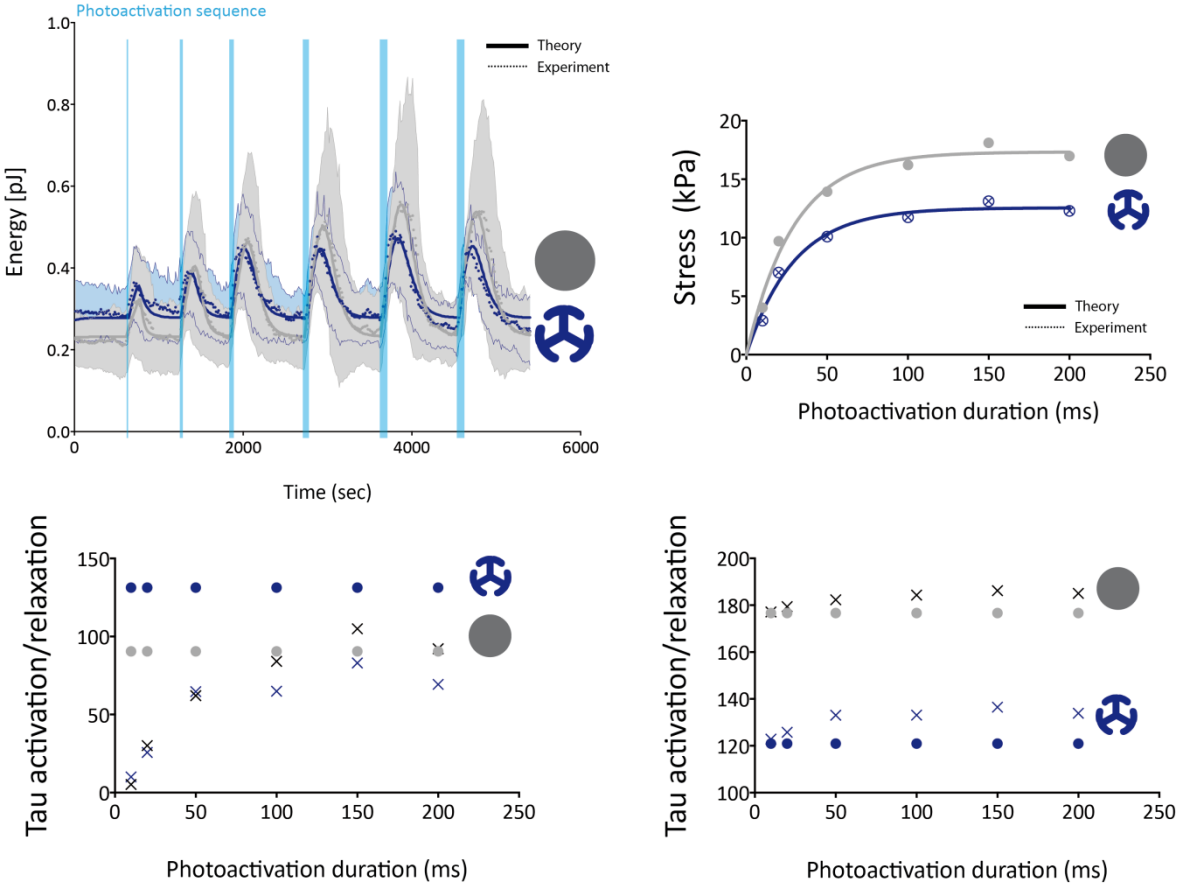
Photoactivation sequence
Theory
Experiment
Energy [pJ]
Time (sec)
Stress (kPa)
Photoactivation duration (ms)
Tau activation/relaxation
Photoactivation duration (ms)
Tau activation/relaxation
Photoactivation duration (ms)

Chapter 4 - Discussion and conclusions

4.1 Discussion

Tensional homeostasis is a fascinating and intriguing concept in the field of mechanobiology that has received increasing attention as its dysregulation has an important contribution to pathological conditions, such as developmental defects, cardiovascular and pulmonary diseases, and cancer [9], [10], [17], [84]. In environments where mechanical modifications and perturbations are common, stresses and strains can accumulate, and lead to tissue deformations that can significantly affect tissue integrity and structures. In consequence, a better understanding of how cell/tissue maintains a stable physiological state against intrinsic and extrinsic mechanical perturbations is of utmost importance.

Although this concept of mechanical integrity preservation is broadly understood and accepted, I would like to draw the discussion towards the fact that being a developing term, the concept of tensional homeostasis is the target of interesting debates both in open discussions and in the bibliography. Idea exchanges with collaborators and colleagues have evidenced the existing dilemma in what is actually meant by single cell tensional homeostasis, if there is such a thing and whether there is a more accurate way of referring to the active process under study.

In the first place a study done by Canovic et al concluded that tensional homeostasis was a multicellular phenomenon and that "it may require a higher level of organization than that of a single cell" [161]. Such a claim introduced controversy in the scientific community as Webster et al and Weng et al, among others, had presented it also as a single cell process in previous publications, the last ones using the term mechanical homeostasis. Considering that Canovic had used endothelial

cells and previously mentioned studies had worked with isolated fibroblasts, further work within the same group led to a recent study by Zollinger and colleagues where different cell types were compared. In their attempt to clear out if tensional homeostasis started at the cellular, multicellular or tissue level they studied the temporal fluctuations of traction forces in isolated and clustered endothelial, fibroblasts and vascular smooth cells. Their conclusion was that the phenomenon of single cell tensional homeostasis does exist, but is cell-type dependent [87].

Other variables have also been shown to impact on the cellular tensional homeostasis. Paszek and collaborators when studying how tissue stiffness could modulate the onset of tumor-malignant behaviour, showed that substrate rigidity impacted significantly on the homeostasis-related cell mechanosensing processes [84]. This dependence with the substrate rigidity was also seen in preliminary results obtained at the end of this project where basal tension levels would vary with different substrate stiffness. Moreover, results presented in the previous chapter showed that such a variation was also happening when increasing cellular sizes, implying that single cell tensional homeostasis is also a size-dependent phenomenon.

A final criticism to this apparently unclear homeostatic concept was done by Webster et al. when studying the tensional steady state of single fibroblasts and their response to perturbations with an elegant approach [86]. Isolating the cells between a micropatterned substrate and an AFM tip they would both measure and modulate forces while also imposing displacements, as mechanical perturbations, to individual contracting cells. Their experiments showed that, after cell displacement perturbation, the cellular contractility did not return to the original basal level but instead reached a new one, increased after a positive strain and reduced after a negative strain. This shifting compensation in the cell contractile state led the authors to redefine the concept of tensional homeostasis with what they decided to call tensional buffering.

Instead of focusing on the details and the parameters of the perturbations chosen for that experiment, which could also give material for discussion, I would like to point out one of the concluding remarks of Webster et al.'s work:

"This behaviour (the non-returning to original steady-state) is in contrast to the ***strict*** definition of tensional homeostasis that predicts a fixed contractile setpoint…"

Such remark puts in evidence how the concept of tensional homeostasis has received different interpretations since it was coined in 1998. At that time, Brown et al presented it as a control mechanism that would, based on the environment, keep a certain level of tension in the cell against external mechanical variations. For some, this certain level has meant a dynamic range and for others a more specific value. Tensional buffering does appear as a more accurate definition, but I would dare to say that although it considers the tensional compensations that the cell presents against perturbations, it disregards the fact that the cell will attempt to go back to the basal state as long as the external environment is still the same. That is what homeostasis is understood as, "an active promotion of equilibrium by biological systems" [162].

My take in this debate is that tensional homeostasis should be regarded as the way that the cells have to adapt their tensional state, within the desired properties, to the mechanical environment by means of feedback loops. It is a description that also tries to embrace Mina Bissell's idea of dynamical reciprocity as it can evolve in the event of permanent external modifications. This definition implies inevitably a more general concept than a fixed setpoint.

As a consequence, such an interpretation could lead to the conclusion that the tensional homeostasis is not a very accurate and scientifically relevant term considering its dependence on so many factors. However, the fact that it might be too

much of a general concept does not prevent possible further characterization and understanding of the mechanisms involved in such process. It is in this light that we aimed at narrowing down the variables to test the dynamics of the homeostatic responses. We probed the contractile reaction of the single fibroblast to photo-perturbations while modifying the cellular size and the internal network arrangement. As a consequence, we were able to 'normalize' the basal level and just interrogate the active process involved in recovering it.

At this point, it is an undeniable fact that every healthy, non-dividing cell has a certain internal tensional equilibrium. From my point of view, and based on what I presented in this work, tensional homeostasis is the correct way to address it. As a future perspective, I would set the focus of the research on the previously mentioned feedback loops, both the positive and the negative ones, and how neighbouring cells impact on them. Most of the work already done has targeted positive feedback loops by imposing 'positive' perturbations, inducing the cell to readjust the system by reducing the momentary tensional increase. Valon et al have recently used an optogenetic construct to downregulate the activity of RhoA [121]. Probing negative feedback loops, as the one just mentioned, might bring exciting insights and better contribute to our understanding of the cellular tensional balance.

4.2 Conclusion

The aim of this thesis project was to delve into the phenomenon of tensional homeostasis in single cells. Derived from the general concept of homeostasis: an elemental adaptive biological process that is of vital importance in maintaining whole-cell/tissue physiology against external perturbations; this tensional by-product is the cellular homeostasis to mechanical perturbations. To study this phenomenon we used an engineered fibroblast cell line carrying a CRY2/CIBN light-gated

dimerizer system coupled to a RhoA activator ARHGEF11. This optogenetic approach allowed us to perturb the global cellular contractile state through the activation of the RhoA signaling cascade with high spatio-temporal resolution. In a reliable and reproducible fashion we were able to study the stress energy increases of the cell to light pulses of varying intensities. The force and contractile readouts were obtained by using a Traction Force Microscopy (TFM), a standard method to study the cellular traction forces produced by stationary or migrating cells on elastic substrates. Finally, in order to constrain the cell so as to avoid migration, analyse contractile responses on different cell sizes and actin network arrangement, and narrow down variables we included the micropatterning technique in our experimental set-up.

All the work done during this project significantly increased my understanding of optogenetic techniques and cellular force measurements, giving me a thorough introduction to the field of mechanobiology. Moreover, on the experimental side, I gained huge expertise in soft substrate engineering and live cell experimentation.

Results obtained all along the thesis taught me many interesting things. Starting from a general point of view, they reinstated the inherent variability of biological systems and the difficulty and complexity of classifying cellular mechanical behaviours within a defined range of values, hence the necessity of a critical spirit at the moment of evaluation.

In more specific project-related terms, results confirmed the existence of a basal contractile state in non-dividing fibroblasts, which was preserved against mechanical perturbations and has been lately referred to as tensional homeostasis. This state was maintained throughout experiments that lasted up to 90 minutes and which involved photo-perturbations of increasing intensities. Moreover, studying cells with different spreading areas showed that this tensional equilibrium still occurred and increasing

the cell size increased its basal value. However, this increase in the internal 'pre-stress' of the cell didn't prevent a proportional stress response against photo-perturbations. This result would imply that the cells spreading area modulates the process of tensional homeostasis. Coupled with this result we also observed a positive correlation between the increase in the actomyosin network alignment and the cell size. Inspired by these findings we aimed at probing the possible link in between the stress fibers alignment and the tensional homeostasis responses to perturbation. To do this, we kept the cell size unchanged in order to keep the same basal tensional state, but modified the global cellular actin arrangement through the design of particular sub-cellular patterning geometries. Results showed a significant decrease in the cellular contractile response to the same perturbation for cells with lower stress fibers alignment. A higher actin alignment translated to a higher force production upon perturbation. This outcome led us to the conclusion that the **arrangement of stress fibers and the actin organization have a strong impact on the dynamic cellular force response.**

A good analogy to illustrate this concept can be made with a tissue that is present in most complex biological systems, the skeletal muscle. The fine alignment between myofibrils bundled in the fibers that make up skeletal muscle is a clear example of efficient force production through high ordered organization. In the same way, a cell with highly aligned stress fibers can exert higher force responses than one where the actomyosin network presents a lower global alignment.

Appendix A - Materials and Methods

Polyacrylamide hydrogel micropatterning -Mask method

Description of the procedure based on the work done by Vignaud, Hajer Ennomani, and Théry, 2014 with modifications done at Motiv group [142].

Coverslip silanization

• This glass treatment is necessary to ensure a good attachment between the PAA gel and the underlying coverslip.

• As silane solutions are toxic, this process should be performed under a chemical hood with appropriate user protection, the silane solution should not leave the hood outside of a hermetically closed container.

• Mix in a 15 ml falcon: 5ml of 100% alcohol, 161ul of 10% acetic acid and 18,5ul bind silane (Plusone Bind-Silane, Silane A-174, M.W. 248.35 g/mol).

• Put 100-200ul of silane solution on each coverslip.

• After 3-4 minutes wipe each coverslip with a kimwipe. (Do not let the coverslip dry before wiping it).

• Leave for 10 minutes to make sure the coverslips are dry and store them at room temperature in a petri dish. Seal the petri dish with parafilm to avoid air dust from getting in.

•This treatment is quite stable over few weeks so you can do many coverslips at the same time to avoid always repeating this fastidious time-consuming process.

pLL–PEG solution preparation

• This solution will be used for the passivation of coverslips before UV exposure and protein coating to avoid unspecific adsorption of protein outside of the exposed area.

• pLL–PEG is usually received as powder and should be stored under protective atmosphere (Argon) if possible, at 20° C. The final concentration we want to achieve is 0.1 mg/ml. Since the powder is usually made of grains that weigh a few mg each, we first produce 1 mg/mL solution that is aliquoted and stored at 20° C. The final solution will be diluted from stock.

• Prepare HEPES 10 mM from powder and milliQ water.

• Equilibrate the pH of the HEPES solution to 7.4 using NaOH.

• Weigh the pLL–PEG and add corresponding HEPES volume to reach a final concentration of 1 mg/mL. Then filter the solution using a syringe and a filter of 0.22 mm mesh size. Aliquot the solution and store at 20° C.

• When needed, thaw an aliquot and dilute it 10 times in HEPES solution to achieve a 0.1 mg/mL pLL–PEG concentration. The pLL–PEG solution should be then stored at 4° C and used within few days.

Preparation of acrylamide solution and polymerization reagent

• Again, as acrylamide is carcinogenic, handle it with care under chemical hood and using proper user protection.

• To know the proportions required for a specific desired final gel rigidity, one can use the table from Tse and Engler (2001) which covers a wide range of rigidities.

• Mix acrylamide and bis-acrylamide solution in PBS to obtain the desired concentration.

• This solution can be stored for a couple of months at 4° C.

• TEMED solution was used as received without further preparation.

• APS solution was prepared from powder in water milliQ at a concentration of 10% w/w and immediately frozen in small 10 mL aliquots and stored at 20° C.

• Since APS is not very stable, one aliquot was used for each experiment and the remaining solution was systematically discarded.

Mask treatment; cleaning and activation

• Dip the mask in a Pyrex with Electroscrub for 5 min rubbing the mask on the chromium side constantly using gloves. This process should be performed under a chemical hood with appropriate user protection.
• After the 5 min, rinse the mask with plenty of deionized water. Dry the mask with nitrogen air gun.
• Rinse both sides of the mask with isopropanol and then dry the liquid carefully using nitrogen gas.
• Use 20mmx20mm coverslips and using the air gun make sure they are dust free before the plasma activation.
• Use megahertz plasma cleaner at 100% power.
• Pre-clean the empty plasma cleaner by running air plasma at 0.2-0.3 mbar pressure during 3 minutes.
• Put the mask (chromium side facing the air) and the coverslips in the plasma cleaner.
• Start pumping out the air in the reactor and wait for the pressure to stabilize at 0.3 mbar.
• Open the air inlet and let plenty of air flow for a minute.
• Pump out the air in the reactor and wait for the pressure to stabilize at 0.3 mbar.
• Run the plasma at 100% power for 4 min.
• Inject plenty of oxygen for a minute.
• Pump out the oxygen in the reactor and wait for the pressure to stabilize at 0.3 mbar.
• Run the plasma at 100% power for 1 min.
• Close the gas inlet, stop pumping, and ventilate the reactor (a filter should be placed on the air inlet to avoid dust intake into the reactor).

pLL–PEG quartz mask coating

• Put one drop of pLL–PEG solution (25 mL/cm2) on the region of interest on the mask. For the case of 20x20mm coverslips you should use 35 µl, and for the 32 mm round coverslips use 70 µl.
• Cover the drop by flipping the activated glass coverslip on it and let it incubate for 30 min.
• Meanwhile, prepare a solution of NaHCO3 pH 8.3. Dissolve 420 mg of sodium bicarbonate in 50 ml of miliQ water using a 50 ml falcon tube.
• At the end of the incubation, lift the coverslips carefully without scratching the coating on the photomask. Leave the coverslips drying face up on a kimwipe. As the coverslips have been coated at the same time we will keep them for the incubation with the ECM protein; they will provide a fully passivized surface that will be used to sandwich the ECM droplet on the activated mask after UV insolation.
• Put the photomask vertically. The solution should run off by itself. Rinse with pll-peg/HEPES and let it dry. Be careful to remember which size has been coated with pLL–PEG to prevent any damage on this side.

Deep UV insolation and protein coating

• At this step, we will burn the passivized surface at specific positions by shining UV light through the chrome photomask from the non-passivized side. The UV light will burn the passivized treatment directly on the mask and this will then allow the adsorption of protein at these specific positions.
• Heat up the UV lamp. This is very important. Power measurements of the lamp have shown that the steady state power is reached after 2–5 min depending on the age of the lamp. We usually let it run for 5 min and then immediately put the sample inside the lamp and start the insolation process. The power measured at steady state was 6 mW/cm2 at a distance of 1 cm from the lamp and a wavelength of 190 nm (you should take care to control the power frequently).

• Flip the mask to have the coated side away from the UV source. You can use small holders on the squares of the mask to prevent scratching of the coating. Expose to UV for 3 min.
• Prepare protein coating solution: we use a solution of 20 mg/ml of fibronectin diluted in sodium bicarbonate 100 mM. A small amount of fluorescently labeled protein could be added in order to see the micropatterns by fluorescence microscopy. Store the solution on ice.
• For the coating solution use 2 µl of fibronectin dilution, 2 µl of fluorescently labeled protein (fibrinogen) and 96 µl of the $NaHCO_3$ solution previously prepared.
• Remove the mask from the UV lamp and set it on a horizontal surface, passivized side now facing up.
• Put a droplet of protein solution (25 ml/cm^2) on the region of interest (35 µl for the case of the 20x20 mm coverslips) and then put the pLL–PEG coated coverslips saved previously on the top, passivized side facing the droplet. Protect from light and let it incubate for 30 min.
• In the meantime, aliquot the desired amount of acrylamide solution and put it to degas in a vacuum bell.
• At the end of the incubation, remove the glass coverslips and discard them. Having the mask horizontally, pour some bicarbonate solution on it to rinse. Afterwards, put the mask vertically and pour some more bicarbonate solution on the coated spots. Let the solution dry by itself.

Transfer on acrylamide gel
• Here we will polymerize the acrylamide gel sandwiched between the patterned photomask and the silanized coverslips. During detachment, the gel will stay attached to the silanized coverslip and the protein from the patterned mask will be transferred to the free surface of the acrylamide gel, resulting in a micropatterned acrylamide surface.
• Set the photomask horizontally with the pattern side facing up. Make sure that you have waited long enough for the solution to dry.
• Collect the acrylamide solution from the vacuum bell and keep the container closed.
• Optional: If you want to add some fluorescent beads in your gel for force measurements, they should be added at this stage (0.4 µl) of the process in the acrylamide solution and the solution should be sonicated for 3 min to destroy any bead aggregates that could have formed during the storage.
• Prepare TEMED and APS and the silanized coverslips. You will add TEMED and APS solution to the acrylamide with the following proportions: 1 ml of TEMED and 1 ml of APS 10% for 165 ml of acrylamide solution. You should proceed as fast as possible in the next steps.
• First, add TEMED to the acrylamide solution, briefly but vigorously mix.
• Second, add APS solution to the acrylamide solution, briefly but vigorously mix.
• Put a drop of 7 ml/cm^2 of the acrylamide polymerization mix on the mask in each patterned area of interest. For the case of the 32 mm diameter round coverslips, you should add 47 µl of the mix.
• Slowly place the silanized coverslip on top while taking care to avoid bubbles.
• Put a cap (to prevent evaporation) and let the gel polymerize for 30 min. Keep the rest of acrylamide in a closed container as a control of gel polymerization.
• Once the polymerization is finished (you should check it by detaching the remaining acrylamide from the tube, it should have the shape of the container and be elastic if you try to pinch it with a pipette tip), cover the coverslips with PBS and let the gel hydrate for 2 min.
• Detach the acrylamide gel by very carefully lifting the silanized coverslip using a razor blade. To do that you should first detach gently all around the coverslip until it comes off by itself. Due to the silanization process, the gel will stay attached to the coverslip. Make sure that the gel is fully immersed during the entire detachment process otherwise you will end up with collapsed micropatterns.
• Rinse the acrylamide gel attached to silanized coverslip (acrylamide coverslips) in PBS several times.
• Control quality with fluorescence microscope if possible.
• Store at 4° C and use within a week.

Mask cleaning

• Start the mask cleaning process while it is still wet with PBS. Do not let it dry otherwise the polyacrylamide will be harder to remove afterwards.
• Use water, soap and a sponge if possible and clean the mask thoroughly. Dry with nitrogen gas gun.
• Rinse both sides with acetone. Dry with nitrogen gas gun.
• Rinse both sides with isopropanol. Dry with nitrogen gas gun.
• Pre-clean the empty plasma cleaner by running air plasma at 0.2-0.3 mbar pressure during 3 minutes.
• Put the mask (chromium side facing the air) in the plasma cleaner.
• Start pumping out the air in the reactor and wait for the pressure to stabilize at 0.3 mbar.
• Open the O_2 inlet and let plenty of oxygen flow for 10 minutes. (Oxygen plasma has a much higher cleaning efficiency than air plasma).
• Pump out the O_2 in the reactor and wait for the pressure to stabilize at 0.3 mbar.
• Run the O_2 plasma at 100% power for 15 min.
• Close the gas inlet, stop pumping, and ventilate the reactor.
• Store the mask in a dust free environment.

Oxygen plasma (Wikipedia)

If the gas used is oxygen, the plasma is an effective, economical, environmentally safe method for critical cleaning. The VUV energy is very effective in the breaking of most organic bonds (i.e., C–H, C–C, C=C, C–O, and C–N) of surface contaminants. This helps to break apart high molecular weight contaminants. A second cleaning action is carried out by the oxygen species created in the plasma (O2+, O2−, O3, O, O+, O−, ionised ozone, metastable excited oxygen, and free electrons). These species react with organic contaminants to form H_2O, CO, CO_2, and lower molecular weight hydrocarbons. These compounds have relatively high vapour pressures and are evacuated from the chamber during processing. The resulting surface is ultra-clean.

Cell culture and plating

Stable cell line NIH 3T3 fibroblasts with CIBN-GFP-CAAX and optoGEF-RhoA constructs (kindly provided by L. Valon and M. Copper, Insitut Curie, Paris, France) were cultured in Dulbecco's Modified Essential Medium (DMEM) containing 10% foetal bovine serum (FBS) and 0.2% penicillin-streptomycin. Cells were grown in a humidified 5% CO_2 incubator at 37ºC. Cells were seeded on patterned substrates at a density of 200.000 cells/cm^3. All traction force measurements or immunostainings were performed 4 hours after seeding to ensure full spreading of the cells. Leibovitz's L-15 medium, supplemented with 10% FBS and 0.2% penicillin-streptomycin, was used as imaging media for every live imaging experiment.

Live cell imaging and activation

Cell imaging and activation intended for posterior force measurements was carried out using a Nikon Ti-E microscope, Zyla sCMOS camera (Andor, Belfast, UK) and Plan Apo VC 60x/1.40 Oil objective (Nikon). The microscope was equipped with an incubator that maintains the temperature at 37 °C. Global cellular photoactivation was performed using a LED light source (X-Cite/XLED1, Lumen Dynamics, Canada) coupled to a Mosaic digital micromirror device (Andor). Depending on the experiment done, activation pulses were 10-20-50-100-150-200 ms long using an LED at 460 nm with power of 256.7 uW (measured at the back focal plane of the objective).

Cell stainings

For stress fibre labelling, cells were permeabilized and fixed for 10 min with 0.2% W/V Triton X-100 and 4% paraformaldehyde in DPBS buffer to preserve cell shape. Fixed samples were washed with PBS and incubated in blocking buffer for 45 min. Afterwards, cells were stained with phalloidin at 1 mM (Sigma-Aldrich) for 1 hour and finally mounted on glass slides with Mowiol 4-88 (Polysciences, Inc.) and kept at 4 ºC overnight.

For live actin measurements, cells were incubated overnight in DMEM medium supplemented with 100 nM SiR-actin (SPIROCHROME) and 10 μM verapamil.

Both live and fixed actin imaging was carried out with a Leica TCS SPE confocal microscope with an HCX PL APO 63x/1.40 oil objective. The microscope was controlled through the Leica Application Suite (LAS) X software. Pictures were then processed using Fiji software.

Actin order parameter analysis

This parameter was obtained with a program that calculates the local orientation in actin images using the structure tensor. The program will first smooth the original image using a Gaussian filter. Then, based on the intensity level, the region in the cell is segmented.

For each pixel in the cell, the structure tensor J (that has 3 elements: J11, J12 and J22) is computed in a local neighbourhood that is also Gaussian. The orientation angle, the coherency and a measure of local gradient (gray level is constant or it changes) are computed from the elements of the structure tensor (λi are the eigenvalues of J):

$$\tan(2\theta)=\frac{2J_{12}}{J_{22}-J_{11}} \qquad coherency=\frac{\sqrt{(J_{22}-J_{11})^2+4J_{12}^2}}{J_{11}+J_{22}}=\frac{\lambda_1-\lambda_2}{\lambda_1+\lambda_2} \qquad gradient=J_{11}+J_{22}=\lambda_1+\lambda_2$$

The average orientation and order parameter S will be computed by averaging over all pixels for which the coherency is above a threshold value, which can be changed.
Average angle: θ m=⟨ θ ⟩c>thres
Order parameter: S=⟨cos(2($\theta - \theta$ m))⟩c>thres

(S=1 means that the local orientation is parallel to the average orientation, S=0 means that they are orthogonal).

Vinculin staining

After 4 h of culture on the micropatterns, cells were fixed with 3.7% formaldehyde in PBS, permeabilized with 0.2% Triton X-100 in TBS (50 mM Tris-HCl, 0.15 M NaCl, pH 7.4) and blocked with 2% BSA (Sigma Aldrich) in TBS. The samples were then incubated with primary antibodies against vinculin (Sigma Aldrich) and detected with Alexa 488-conjugated, isotype-specific, anti-IgG antibodies (Invitrogen). Actin was labeled with phalloidin-TRITC (Sigma) and nuclei were stained with DAPI (Life Technologies).

Areas of focal adhesions were segmented and measured by using a home-made Image J (National Institutes of Health) routine.

Traction force microscopy

Cellular traction force is the physical force exerted by cells on the extracellular matrix. At present, traction force microscopy (TFM) is an efficient and reliable method to determine the cellular traction forces acting on a flat flexible substrate. For that purpose, fluorescent trackers are embedded in the substrate during its fabrication. The key concept of traditional TFM is the acquisition of a pair of ''before kill'' and ''after kill'' microscopy images (hereafter referred to as BK image and AK image, respectively). A BK image is a fluorescence image of the deformation of soft substrates caused by cells, and an AK image is a fluorescence image of non-deformed elastic substrates taken at the same location by detaching the cell through trypsinization. The displacement field can be obtained by merging the images of the gel under stress, that means while the cell is alive, and the non-stressed image, which is after the cell has been detached using trypsin. The composite image reveals the areas in which the cell exerts a force and displaces the beads.

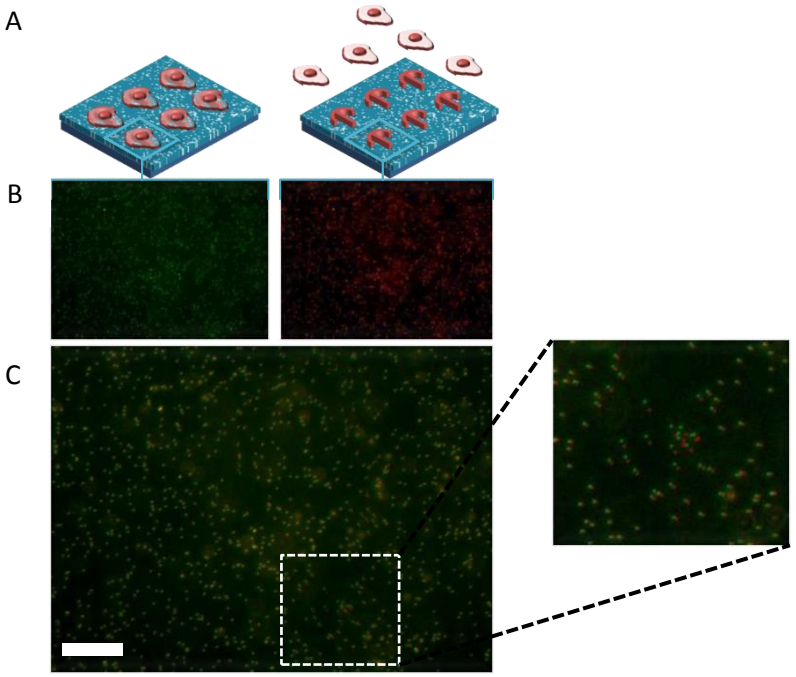

Figure 58 (A) Scheme of cells plated on the gel (left), and cell detached from the gel after trypsination (right). (B) ''before kill'' and ''after kill'' microscopy fluorescence images. (C) Composite image of the BK and AK images, with a close-up clearly showing the displacement of beads as a consequence of the deformation of the gel done by the cell. Scale bar, 15 µm.

For the analysis of the displacement a Matlab program which combines particle image velocimetry and single particle tracking is used. By tracking the movements of the fluorescent trackers, and knowing the mechanical properties of the substrate, one can derive the force field applied on the substrate.

Four hours after plating, the culture medium was discarded, gels where placed on microscope chamber and CO_2 independent medium was added. After placing the chamber on the microscope stage, the gel was manually scanned and each properly spread cell was photographed in brightfield, far red, and mCherry mode. Afterwards, the culture medium was retrieved and 2 ml of trypsin were added. Five minutes later the medium was flushed to remove the cells from their original position and

fluorescent pictures were taken of the coordinates where the cells were. In Figure 59 it can be clearly seen how forces exerted by the cell deform the ECM geometries on which they are plated.

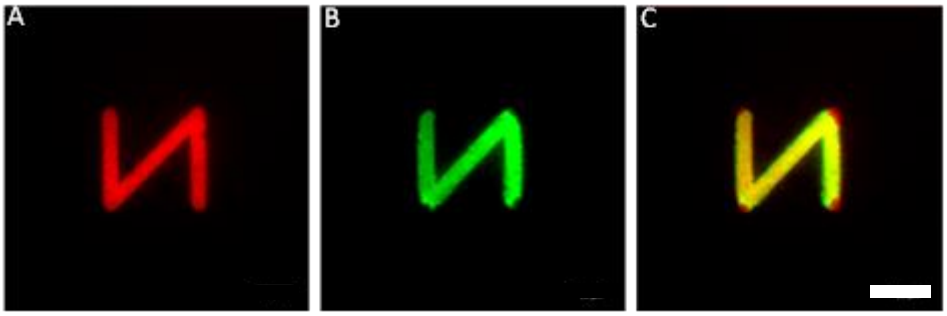

Figure 59 ***Deformation field exerted by the cell on the ECM geometry.*** *(A) [N] shaped isolated micropattern. (B) [N] shaped micropattern being deformed by cell. (C) Composite image with unaffected micropattern in red and plated micropattern in green showing the deformation made by the cell. Scale bar, 15 µm.*

Appendix B – Nuclear mechanosensing

Introduction

This Annex will briefly present an important collaboration done with David Graham from the group of Keith Burridge, University of North Carolina, which led to a publication in the Journal of Cell Biology. This work aimed at better understanding the role of the nucleus in cell migration, polarity and mechanotransduction.

The physical role of the nucleus

As it was mentioned during Chapter 1, the nucleus is amongst the most important elements of the cellular mechanosensing machinery. It not only regulates cellular physical behaviour through gene expression, but it is also physically connected to the actomyosin network and the cytoskeleton through the LINC (Linker of Nucleoskeleton and Cytoskeleton) complex [163], thus playing also a mechanical role in the cellular mechanoresponses (Fig. 60).

Several studies have been carried out to clarify how DNA replication, gene regulation and molecular pathways triggered by the nuclear lamina impact on the cellular mechanotransduction [28], [164]–[166].

However, not much is known when it comes to identifying how important is, for the cell, the nucleus physical presence at the moment of regulating cell polarity, migration and tensional homeostasis. For this reason, the following study focused on studying these processes in the absence of the nucleus. Using enucleated cells and knock-out cell lines, Graham et al. studied the onset of cellular polarization and migration in 1D, 2D and 3D environments and on substrates with varying rigidities.

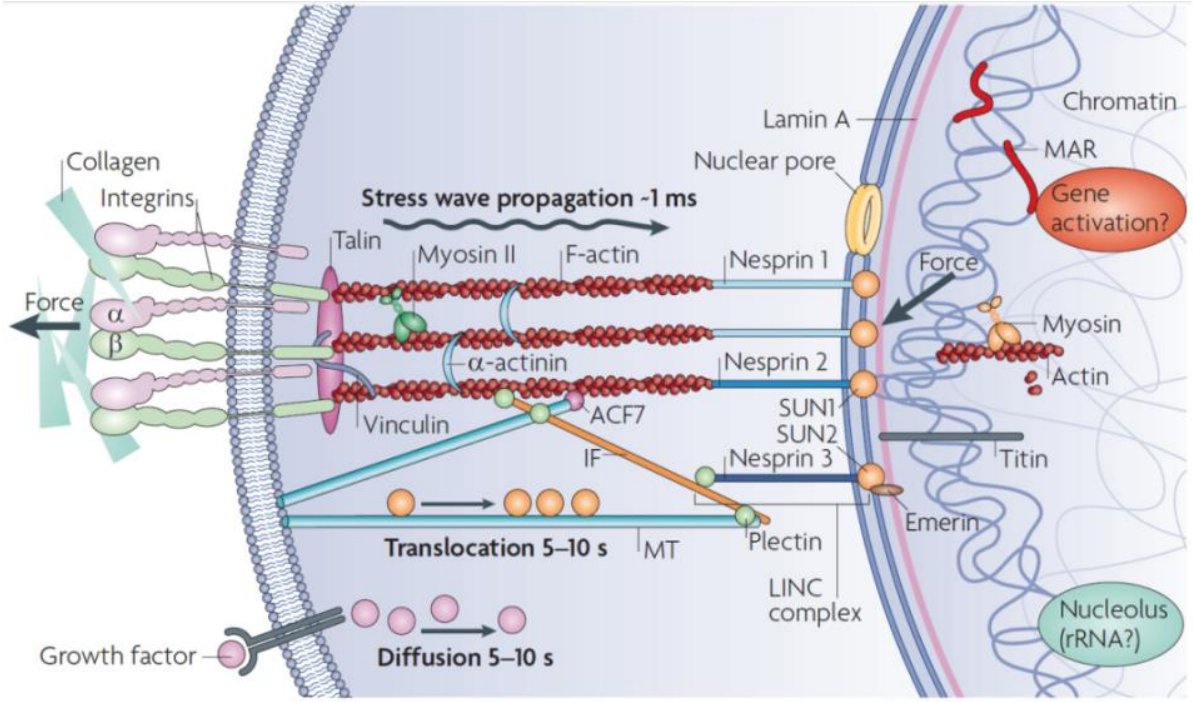

Figure 60 ***The complex machinery that transmits the mechanical perturbations from the environment to the nucleus.*** *External forces are sensed by the integrins at the focal adhesions, information that is then transferred to the actomyosin network that is physically connected to the nucleus LINC complex, which delivers the information to the internal part of the nucleus potentially altering its functions and activating or regulating gene expression. Adapted from* [28].

My contribution to this work consisted mainly on performing image analysis to obtain the cellular force readouts using static force microscopy and providing line micropatterns for 1D migration studies.

Traction force measurements showed that even though mammalian fibroblasts without nucleus (cytoplasts) and cells with nuclear lamina defects were able to exert forces, these were considerably lower than those of intact control cells. Similarly, cytoplasts sensed mechanical cues, such as rigidity variations, but responded in an impaired way. These observations implied that the nucleus plays a fundamental role in the mechanotransduction of the cell. In parallel, results showed that enucleated cells were capable of polarizing and migrating in 1D lines and 2D environments, but not in 3D environments.

Overall, the data obtained suggested that normal cell polarization occurs independently of the nucleus, but the regulation of normal cell contractility and mechanosensing is nucleus dependent.

In the following pages you will find the publication in its published format.

JCB

Article

Enucleated cells reveal differential roles of the nucleus in cell migration, polarity, and mechanotransduction

David M. Graham,[1,2] Tomas Andersen,[5] Lisa Sharek,[1] Gunes Uzer,[4,6] Katheryn Rothenberg,[7] Brenton D. Hoffman,[7] Janet Rubin,[4] Martial Balland,[5] James E. Bear,[1,2] and Keith Burridge[1,2,3]

[1]Department of Cell Biology and Physiology, [2]UNC Lineberger Comprehensive Cancer Center, [3]McAllister Heart Institute, and [4]Department of Medicine, University of North Carolina at Chapel Hill, Chapel Hill, NC
[5]Laboratoire Interdisciplinaire de Physique, Université Grenoble Alpes, Grenoble, France
[6]Department of Mechanical and Biomedical Engineering, Boise State University, Boise, ID
[7]Department of Biomedical Engineering, Duke University, Durham, NC

The nucleus has long been postulated to play a critical physical role during cell polarization and migration, but that role has not been defined or rigorously tested. Here, we enucleated cells to test the physical necessity of the nucleus during cell polarization and directed migration. Using enucleated mammalian cells (cytoplasts), we found that polarity establishment and cell migration in one dimension (1D) and two dimensions (2D) occur without the nucleus. Cytoplasts directionally migrate toward soluble (chemotaxis) and surface-bound (haptotaxis) extracellular cues and migrate collectively in scratch-wound assays. Consistent with previous studies, migration in 3D environments was dependent on the nucleus. In part, this likely reflects the decreased force exerted by cytoplasts on mechanically compliant substrates. This response is mimicked both in cells with nucleocytoskeletal defects and upon inhibition of actomyosin-based contractility. Together, our observations reveal that the nucleus is dispensable for polarization and migration in 1D and 2D but critical for proper cell mechanical responses.

Introduction

The nuclear functions of DNA replication and gene regulation are well known, but the nucleus also plays less understood physical roles where its presence within the cell and connection to the cytoskeleton are thought to be important in cell polarization and cell migration. In both processes, active positioning of the nucleus imparts dynamic structural and functional organization within the cell that ultimately influences cell behavior. Aberrant positioning of the nucleus can lead to developmental defects (Zhang et al., 2009) and impair cellular function (Metzger et al., 2012) and is seen in several human diseases (Gundersen and Worman, 2013). A more recent and equally important physical role of the nucleus has been ascribed to mechanical signaling within the cell. Here, the degree of structural integration of the nucleus within the cell is postulated to be crucial for regulating how cells sense and respond to force (Jaalouk and Lammerding, 2009).

During polarity establishment and cell migration, the nucleus is actively positioned in many cell types. For example, in fibroblasts, rearward nuclear movement allows anterior orientation of the centrosome, promoting anterior–posterior polarity of the cell in 2D (Gomes et al., 2005). In cells migrating in 3D that exhibit unidirectional polarity, the nucleus can be actively repositioned to act as an intracellular piston to facilitate migration (Petrie et al., 2014). Molecular motors, cytoskeletal elements, and cell adhesions are structurally connected within the cytoskeletal system as a whole, and it is thought that each contributes to tensional homeostasis of the cell (DuFort et al., 2011). In light of this, aberrant force transmission between the cytoskeleton and nucleus has been suggested as the underlying cause for defective nuclear positioning (Graham and Burridge, 2016). It is, however, unclear how the position of the nucleus conversely regulates mechanical signaling within the cell to collectively affect these processes. How would removal of the nucleus affect force transmission within the cell?

Recent work has dramatically expanded our understanding of the molecular underpinnings of the mechanical linkages that connect the nucleus to cytoskeletal elements of the cytoplasm. Forces are transmitted through the linker of nucleoskeleton and cytoskeleton (LINC) complex (Crisp et al., 2006), where the inner nuclear membrane proteins Sun1 and Sun2 directly bind with outer nuclear membrane Nesprin proteins in the lumen of the nuclear envelope. Nesprin proteins span the outer nuclear membrane to associate with the cytoskeleton and associated motors, whereas Sun proteins associate with lamin A/C, nuclear pore complexes, and other proteins within the nucleus (Borrego-Pinto et al., 2012). This chain of protein interactions

Correspondence to James E. Bear: jbear@email.unc.edu; Keith Burridge: keith_burridge@med.unc.edu

Supplemental material can be found at:
http://doi.org/10.1083/jcb.201706097

The Rockefeller University Press
J. Cell Biol.
https://doi.org/10.1083/jcb.201706097

allows forces to be exerted on the nucleus and is responsible for rapid strain-stiffening of the nucleus in response to extrinsic force (Guilluy et al., 2014). In addition to applied forces, intrinsic cell-derived forces can transmit through dorsal actin stress fibers to the LINC complex, allowing posterior positioning of the nucleus via actin retrograde flow (Luxton et al., 2010). Because cell-derived forces are highly dependent on the mechanical properties of the microenvironment, the LINC complex likely plays an important role in regulating the response of the cell to environmental rigidity. This was shown for rigidity-dependent nuclear localization of YAP (Elosegui-Artola et al., 2017). Together, these and many other recent studies demonstrate the intricate network of molecular connections that help position the nucleus and make it sensitive to mechanical cues.

Several studies have reported defects in cell polarity, migration, and mechanotransduction upon disruption of nucleoskeletal connections. It is unclear what role the nucleus plays during these processes and how they are affected by nuclear loss as opposed to aberrant nuclear positioning. Cellular enucleation is an older approach that has been used to explore migration in the absence of the nucleus (Goldman et al., 1973; Shaw and Bray, 1977; Euteneuer and Schliwa, 1984, 1992; Verkhovsky et al., 1999). We revisited this technique to study the role of the nucleus in cell polarity and distinct forms of migration (e.g., in 1D, 2D, and 3D) and sought to understand what role the nucleus plays as cells respond to extracellular cues, particularly mechanical cues. Few studies have directly measured the effect of nucleoskeletal disruption on cell behavior in response to mechanical properties of the environment. This is important because the nucleus is integral to cellular responses to force (Wang et al., 2009). In the current study, we have examined how the presence or absence of a nucleus affects cell polarization, cell migration, and mechanical signaling within cells.

Results

Generating cytoplasts

To address the physical role of the nucleus during cell migration, we removed the nucleus from mammalian cells, modifying an older approach (Wigler and Weinstein, 1975) to reproducibly generate high purity cytoplasts (cells without nuclei) from large populations (~2×10^7/gradient). We used both rat embryonic fibroblasts (REF52) and human umbilical vein endothelial cells (HUVECs) to generate cytoplasts. Cells were incubated in the presence of cytochalasin and centrifuged at high speed through a density gradient (Fig. 1 A). This resulted in formation of three distinct strata within the gradient. Fluorescence analysis of fractions from REF52 cells showed that fraction 1 contained mostly cellular debris, fraction 2 contained cytoplasts, and fraction 3 contained nucleoplasts (nuclei surrounded by cytosol and encased in plasma membrane; Fig. 1 B). Similar fractionation strata and composition were observed with HUVECs (Fig. S1 A). Based on morphological observations, enucleation appears to occur through repositioning of the nucleus through the cell body, leading to hyper-elongation of the cell parallel to the direction of the g-force vector (Fig. S1 B). Toward the tail end of the cytoplast (opposite end of nuclear exit), small fragments separate, generating the constituents of fraction 1. Enucleation occurs in the presence of g-force alone, but efficiency is increased with actomyosin destabilization (Fig. S1C). Enucleation of cells expressing nuclear localized-tdTomato led to tdTomato fluorescence in cytoplasts with decreased presence in nucleoplasts (Fig. S1 D). This result is consistent with nuclear envelope rupture (Denais et al., 2016; Raab et al., 2016), which likely occurs during nuclear exit from the cell.

Cytometric profiling of stained fractions with a nuclear fluorescent dye showed 98.7 ± 0.6% purity for REF52 cytoplasts (Fig. 1 C) and 99.1 ± 0.8% purity for HUVEC cytoplasts (Fig. S1 E). Size analysis of REF52 fractions postenucleation revealed relative cell size order as intact > cytoplast > nucleoplast (Fig. S1 F). Volumetric measurements show cytoplasts are ~64% the calculated volume of the cytoplasm of an intact cell (Fig. S1 G), suggesting that ~36% is lost to the nucleoplast and debris fractions. Decreased levels of nuclear proteins within cytoplast fractions along with concomitant increases in levels in nucleoplast fractions were observed by blotting (Fig. 1 D). Similar cell-spreading rates (cytoplast $K_{1/2}$ = 20.6 ± 2.2 min; intact $K_{1/2}$ = 23.0 ± 2.0; $P > 0.05$), including typical radial morphology during spreading, were found between intact cells and cytoplasts (Fig. S1 H).

We analyzed cytoplasts for the presence of nuclear proteins, major organelles, and the cytoskeleton. Cytoplasts were devoid of nuclei and most nuclear-associated proteins (Figs. 1 E and S2 A); contained cytoskeletal networks for filamentous actin, vimentin, and microtubules; and formed vinculin-containing focal adhesions (Fig. 1 F). Cytoplasts retained endoplasmic reticulum, Golgi, mitochondria, and centrosomes (Fig. 1 G). Immunofluorescent staining of nucleoplasts revealed nuclear-associated proteins, organelles, and cytoskeletal systems (Fig. S2 B). We measured cytoplast survival with viability dyes and found REF52 cytoplasts to be stable for 48 h (Fig. 1 H). HUVEC cytoplasts had decreased viability compared with REF52 cells, showing a significant decrease at 6 h with loss of half the population at ~18 h postenucleation (Fig. S2 C). We did not observe obvious decreases in protein levels for Src, nonmuscle myosin IIA, vinculin, and other proteins over 24 h in REF52 cytoplasts (Fig. S2 D). To reduce possible effects attributed to cytoplast deterioration over time, we used REF52 cytoplasts for most experiments, because they exhibited increased survival over HUVEC cytoplasts. These experiments were performed <27 h postenucleation, with most performed <19 h postenucleation. HUVEC cytoplasts were used for shorter experiments (<8 h), with 18-h experiments being the longest. Together, these data demonstrate the ability to generate a high quantity of cytoplasts with high purity.

The nucleus is not required for establishing anterior–posterior polarity

The positions of organelles, including the nucleus and centrosomes, are hallmarks of cell polarity. We assessed polarity establishment in the absence of the nucleus to understand whether the nucleus is necessary for proper localization of centrosomes and the Golgi apparatus. Micropatterns with bilateral, radial, and trilateral symmetries were used (crossbow, circle, and triangle, respectively; Fig. S3 A) to direct organelle positioning with respect to the cell centroid (Fig. S3 B), as performed by others (Théry et al., 2006). We report spatial information for organelle positioning relative to the cell centroid from y-coordinate values, as significant differences from the cell centroid were not found for x-coordinate values for all patterns tested (Fig. S3 C). Centrosomes, which normally position at the cell centroid, were indeed found near the cell centroid for REF52 intact cells and cytoplasts (Figs. 2 A and S3 D). The mean centrosome

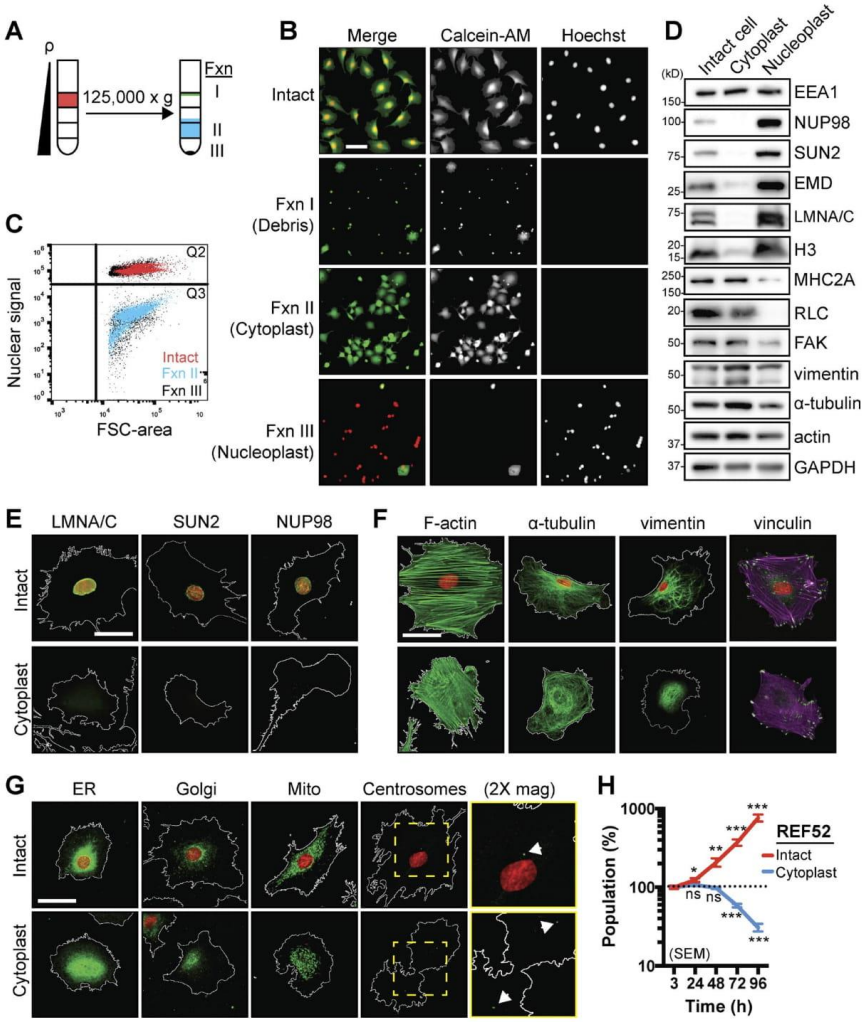

Figure 1. **Cytoplast generation and characterization. (A)** Illustration of enucleation procedure. **(B)** Fluorescence images of plated fractions 2 h after enucleation. **(C)** Cytometric profiles of stained populations with a fluorescent nuclear dye (Vybrant DyeCycle Green). Q2 is region containing positive nuclear staining. Q3 is negative for nuclear staining. **(D)** Western blots of intact cell, cytoplast, and nucleoplast fractions. **(E–G)** Immunofluorescent staining for nuclear proteins (E), cytoskeletal elements (F), and organelles (G). Arrowheads in G mark centrosomes. All nuclei are Hoechst stains and shown in red. Cell outlines are white. **(H)** Cell population as percentage of starting population over time shown as mean ± SEM ($n = 4$ experiments). Student's t test performed between successive time points for either intact cells or cytoplasts. ***, $P < 0.001$; **, $P < 0.01$; *, $P < 0.05$. Bars, 50 µm.

position for intact cells and cytoplasts on crossbows was −1.1 ± 0.4 and −1.2 ± 0.4 µm, respectively, from the cell centroid (Fig. 2 B). Similar to centrosomes, the Golgi positions between the nucleus and the cell leading edge; thus, we measured Golgi positioning on patterns. Consistent with centrosome localization, the Golgi was found near the cell centroid for intact cells and cytoplasts for all patterns tested (Figs. 2 C and S3 E), and the mean Golgi position did not differ between intact cells and cytoplasts (Fig. 2 D). Next, we measured centrosome localization in HUVEC cytoplasts. HUVEC cytoplasts are smaller than REF52 cytoplasts and rarely occupied the full area of the circle micropattern (largest area of the patterns used), preventing us from considering this particular shape. Thus, we used triangle patterns instead. Centrosomes were positioned at the cell centroid for HUVEC intact cells and cytoplasts on crossbow and triangle micropatterns (Fig. 2, E and F). Together, these data

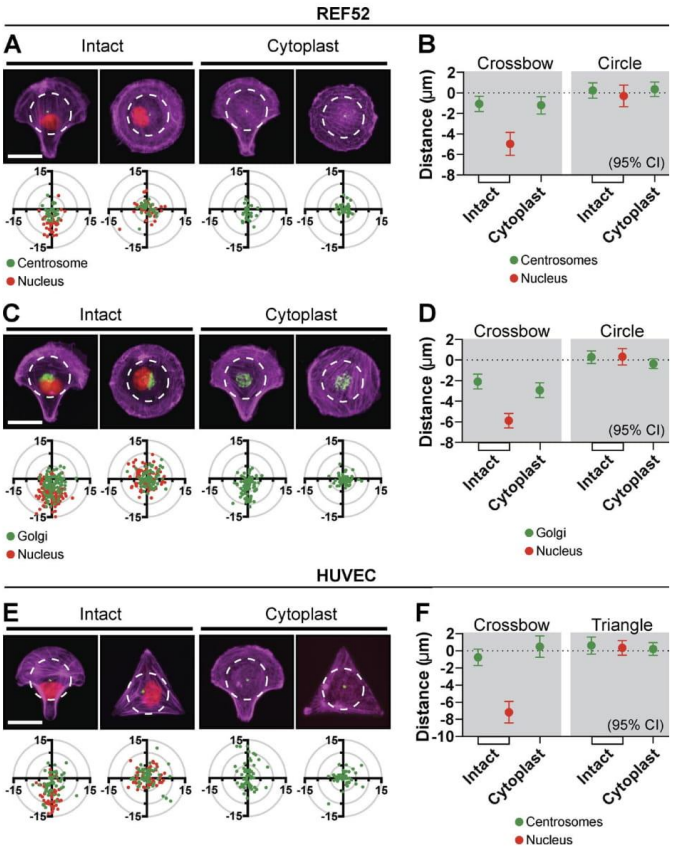

Figure 2. **Cell polarity occurs in the absence of the nucleus. (A)** Images and plots showing localization of centrosomes and nuclei from REF52 intact cells and cytoplasts plated on crossbow (intact cells, *n* = 39; cytoplasts, *n* = 35) and circle (intact cells, *n* = 34; cytoplasts, *n* = 31) patterns. **(B)** Mean y-coordinate distance ± 95% CI of centrosomes for REF52 intact cells and cytoplasts on crossbow and circle patterns. **(C)** Images and plots showing localization of Golgi and nuclei from REF52 cells plated on crossbow (intact cells, *n* = 100; cytoplasts, *n* = 86) and circle (intact cells, *n* = 78; cytoplasts, *n* = 57) patterns. **(D)** Mean y-coordinate distance ± 95% CI of Golgi for REF52 cells on crossbow and circle patterns. **(E)** Images and plots showing localization of centrosomes and nuclei from HUVEC intact cells and cytoplasts plated on crossbow (intact cells, *n* = 52; cytoplasts, *n* = 57) and triangle (intact cells, *n* = 50; cytoplasts, *n* = 49) patterns. **(F)** Mean y-coordinate distance ± 95% CI of centrosomes for HUVECs on crossbow and triangle patterns. All data are from at least three independent experiments. White dashed line circles in A, C, and E show a 30-µm-diameter region of interest. Bars, 25 µm.

demonstrate that normal cell polarization, as indicated by cell morphology and predicted organelle positioning, occurs independently of the nucleus.

The nucleus is not essential for random and directed 2D migration

Cell migration is intrinsically a polarity-driven process (Ridley et al., 2003). Thus, we analyzed 2D random migration in cytoplasts. We found REF52 and HUVEC cytoplasts were migratory, exhibiting anterior–posterior polarity, dynamic lamellipodial extension, and rear retraction (Figs. 3 A and S3 F and Videos 1 and 2). Intact cells displayed a biphasic migration velocity response on increasing fibronectin (FN) concentration, with velocity being slowest on both low (1 µg/ml) and high (≥100 µg/ml) concentrations (Fig. 3, B and C). Unexpectedly, cytoplasts from both REF52 cells and HUVECs did not reveal a biphasic response but instead showed increased migration velocity with increasing FN concentration. We measured the relative amount of FN on glass to determine if concentrations above 100 µg/ml were capable of binding and, as such, sensed by cells. Detectable increases in FN up to at least 400 µg/ml were measured, suggesting that 100 µg/ml is not saturating and that higher concentrations can influence migration behavior (Fig. S3 G). We measured surface expression levels of β1 and β3 integrins in REF52 intact cells and cytoplasts to see whether reduced integrin levels, as a result of enucleation, might explain this response. Using flow cytometry and live-cell labeling with fluorescent-conjugated antibodies, we detected reduced levels of β1 and β3 integrins in cytoplasts as compared with intact cells (Fig. 3 D). However, when normalized to cell size (from flow cytometer forward-scatter metrics), the relative β1 and β3 integrin levels were not different between cytoplasts and intact cells. Furthermore, integrin localization was consistent with adhesion complexes. Lastly, we sought to gauge the effects of cytoplast deterioration on migration velocity, because this would influence migration efficiency over time. We found a decreased rate of −0.12 ± 0.02 µm/h over 24 h for REF52 cytoplasts (Fig. 3 E), demonstrating that cytoplast migration velocity is reduced over time.

Next, we examined directional migration in REF52 cytoplasts to determine what role the nucleus plays as cells respond to guidance cues. We measured directional migration via a microfluidic-based approach, as previously described (Wu et al., 2012). Migration was monitored in gradients of either PDGF (for chemotaxis) or surface-bound FN (for haptotaxis).

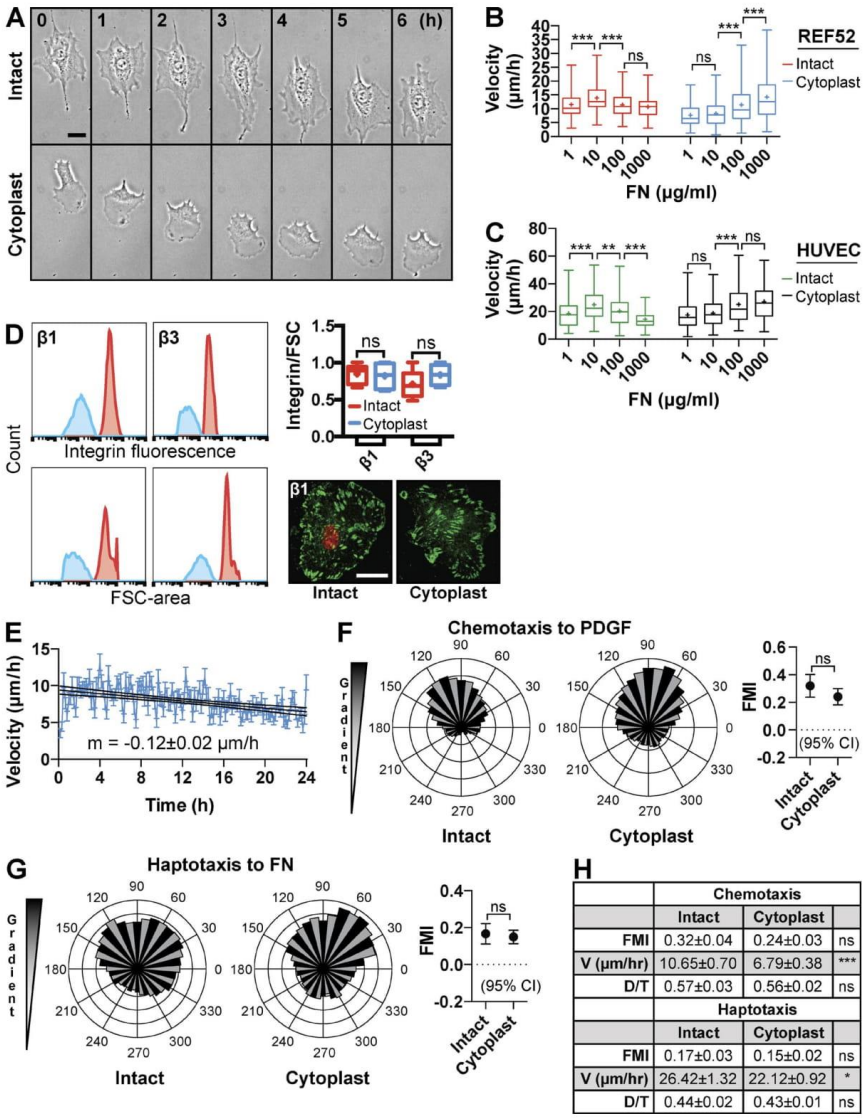

H

	Chemotaxis		
	Intact	Cytoplast	
FMI	0.32±0.04	0.24±0.03	ns
V (μm/hr)	10.65±0.70	6.79±0.38	***
D/T	0.57±0.03	0.56±0.02	ns
	Haptotaxis		
	Intact	Cytoplast	
FMI	0.17±0.03	0.15±0.02	ns
V (μm/hr)	26.42±1.32	22.12±0.92	*
D/T	0.44±0.02	0.43±0.01	ns

Figure 3. **Directed cell migration occurs in the absence of the nucleus. (A)** Stills of a REF52 intact cell and cytoplast migrating. **(B)** REF52 cell velocity on different concentrations of FN. $n \geq 100$ cells per concentration for intact cells and cytoplasts. One-way ANOVA with Tukey's post-hoc test was performed. **(C)** HUVEC cell velocity on different concentrations of FN. $n \geq 90$ cells per concentration for intact cells and cytoplasts. One-way ANOVA with Tukey's post-hoc test performed. **(D)** Histograms (left) from flow cytometry showing β integrin surface expression (top) and forward scatter area (FSC; bottom) for REF52 intact cells and cytoplasts. Graph (top right) of integrin/FSC for β integrins. Images of live-stained REF52 intact cell and cytoplast of equal spread area showing β1 surface staining. Cytometry data from two experiments are shown. **(E)** Mean cell velocity ± SEM over 24 h of cytoplast migration (n = 121 cells; data from two experiments). Linear regression fit to 24-h period ± 95% CI. **(F)** Rose plots (left) for intact cells (n = 169) and cytoplasts (n = 197) migrating in a PDGF gradient. Graph (right) showing mean FMI ± 95% CI. **(G)** Rose plots (left) for intact cells (n = 187) and cytoplasts (n = 199) migrating in a surface-bound FN gradient. Graph (right) showing mean FMI ± 95% CI. **(H)** Table showing FMI, cell velocity and persistence (displacement over total path length [D/T]) values from chemotaxis and haptotaxis experiments. Student's t tests were performed. Unless stated otherwise, all data are from at least three independent experiments. Bars, 25 μm. ***, P < 0.001; **, P < 0.01; *, P < 0.05.

Directional fidelity is shown as forward migration index (FMI), which describes the directional persistence of a cell toward (positive FMI) or away from (negative FMI) an extracellular cue. Cytoplasts showed positive chemotactic (Fig. 3 F) and haptotactic (Fig. 3 G) responses, similar to intact cells (Fig. 3 H). These data demonstrate that the nucleus is dispensable for directional migration in response to PDGF and FN.

The scratch-wound assay (herein referred to as the scratch assay) is widely used to measure collective and polarized migration. Proper nuclear repositioning in cells at the wound margin has been implicated in this migratory response (Gomes et al., 2005; Luxton and Gundersen, 2011). Thus, we assessed the physical necessity of the nucleus in this form of migration. Cytoplast monolayers from REF52 cells were mostly free of nuclei-containing cells (Fig. S4 A); however, purity decreased over time as any intact cells proliferated. We measured the density of nuclei at the end of all scratch experiments (∼16–20 h after scratch) and found nuclear densities of 15.6 ± 0.4 nuclei for intact cells and 1.3 ± 0.1 nuclei for cytoplasts in a 100-μm^2 area. At these densities, effects from intact cells within the cytoplast monolayer are unlikely to affect cytoplast-driven scratch closure. REF52 cytoplasts were capable of scratch closure, which occurred between 4 and 7 h for intact cells and 7 and 16 h for cytoplasts (Fig. 4 A and Video 3). The mean closure time for intact cells was 5.4 h. At this time, cytoplasts closed 80% of the scratch. On average, cytoplasts closed 95.6% of the scratch over 16 h. To reduce scratch closure effects driven by cell proliferation, we inhibited cell division with mitomycin C pretreatment (Fig. 4, B and D). The mean time for cytoplast scratch closure was unchanged from untreated; however, for intact cells, it increased from ∼5 to 8 h. Although the initial rates of scratch closure were similar for both intact cells and cytoplasts, total closure took longer for REF52 cytoplasts (Fig. S4 B). This difference may reflect the slight time-dependent decrease in migration velocity in cytoplasts. Despite this difference, the time to close half of the scratch ($t_{1/2}$) was not different between intact cells and cytoplasts for all treatments tested (Fig. 4 C). HUVEC cytoplasts were also capable of scratch closure (Fig. 4, E and F; and Video 4). A narrower scratch was used for these experiments (Fig. 4 F) to decrease the effects attributed to shorter viability. Similar to REF52 cells, HUVEC cytoplast monolayers were largely devoid of intact cells (Fig. S4 C) and were significantly slower than intact cells at scratch closure (Fig. S4 D). However, these cytoplasts showed nearly identical rates of closure for half of the scratch compared with intact cells (Fig. 4 G). Together, these data demonstrate that the nucleus is not necessary for closure in the scratch assay.

The nucleus is dispensable for migration in 1D, but not 3D, environments

Recent work has shown that the nucleus performs specialized physical functions during 3D migration (Petrie et al., 2014; Denais et al., 2016; Raab et al., 2016). We explored cytoplast migration in collagen gels of two different porosities to gauge cell migration efficacy in environments of different physical constraint and ligand density (Fig. 5 A). Collagen matrices were prepared with different gelation temperatures, producing loose reticular (LR) and highly reticular (HR) matrices, as described elsewhere (Doyle et al., 2015). Cytoplasts migrated slower than intact cells for both LR and HR matrices in both 2D (on top of the gel; Fig. 5 B) and 3D (inside the gel; Fig. 5 C and Video 5). Transitioning from 2D to 3D environments caused a decrease in cell velocity for both intact cells and cytoplasts. Interestingly, cytoplast 3D velocity did not change between LR and HR matrices, whereas intact cell velocity decreased in HR matrices. Moreover, cytoplasts showed a less pronounced uniaxial morphology in 3D than intact cells (Fig. 5 D). Compared with intact cells, which showed a mean accumulated distance over 8 h of 91.4 ± 4.6 µm, cytoplasts were largely immotile, with a mean accumulated distance of 28.0 ± 1.2 µm (Fig. 5 E). The low velocity and low accumulated distance for REF52 cytoplasts were also observed for HUVEC cytoplasts (Fig. 5 F and Video 6). No difference in 3D cell velocity was measured between REF52 and HUVEC cytoplasts (3.0 ± 0.1and 3.3 ± 0.3 µm/h, respectively; $P > 0.05$). This nonmigratory phenotype does not reflect the inability of cytoplasts to signal on collagen, because both phospho-FAK staining and phosphopaxillin staining were evident at focal adhesions when on collagen (Fig. S4 E). Additionally, cytoplasts were able to engage bundled collagen (Video 7) despite showing reduced contraction of collagen gels (Fig. S4 F). Cytoplasts were also able to degrade collagen (Fig. S4 G). We cannot rule out the inability of cytoplasts to polarize in 3D, because a reliable polarity marker for intact cells under these conditions was not found, thus preventing a controlled comparison. Collectively, these data are consistent with the role of the nucleus in facilitating migration in 3D, as previously reported (Petrie et al., 2014).

Next, we explored two mutually nonexclusive explanations for the impaired 3D migration of cytoplasts: (1) migration in 3D environments uniquely requires the physical presence of the nucleus (Petrie et al., 2017) or (2) the low-rigidity collagen matrices differentially affect cytoplasts versus intact cells. The first explanation is difficult to assess and might be addressed with nuclear addback experiments in 3D gels to rescue cytoplast migration in situ or the use of alternative 3D matrices that might confer migration to cytoplasts. Nuclear addback is technically difficult and was not attempted. The use of different matrix materials was not supported, because cytoplasts from primary human fibroblasts were shown to slowly migrate (∼4 µm/h) inside cell-derived matrices (Petrie et al., 2014), closely matching the low cell velocities we observed in collagen. Alternatively, the role of the nucleus in 3D migration could be determined with 1D migration being used as a surrogate for 3D, because these two forms of migration share several principles (Doyle et al., 2009). Thus, we turned to using micropatterned 1D lines (Fig. S4 H), where we found REF52 and HUVEC cytoplasts exhibited a uniaxial morphology and polarity, similar to intact cells. Contrary to our expectations, cytoplasts migrated in 1D (Fig. S4 I and Video 8) with velocities on 5-µm lines of 11.5 ± 0.6 µm/h for REF52 cells and 38.3 ± 1.5 µm/h for HUVECs (Fig. 5, G and H). Cytoplasts were also migratory on lines coated with either FN or collagen (Fig. S4 J). These data demonstrate that the nucleus is dispensable for migration in 1D, but not 3D, environments.

The nucleus regulates cell contractility and the sensitivity of the cell to mechanical cues

The ∼2-mg/ml collagen matrices used for our 3D work have a reported low stiffness, ranging between 0.2 and 0.6 kPa (Mason et al., 2013; Lang et al., 2015). Low matrix stiffness of ∼1 kPa has been reported for 3-mg/ml collagen matrices; this stiffness closely reflects the stiffness sensed at the cellular scale (Doyle et al., 2015). These stiffness values are far less

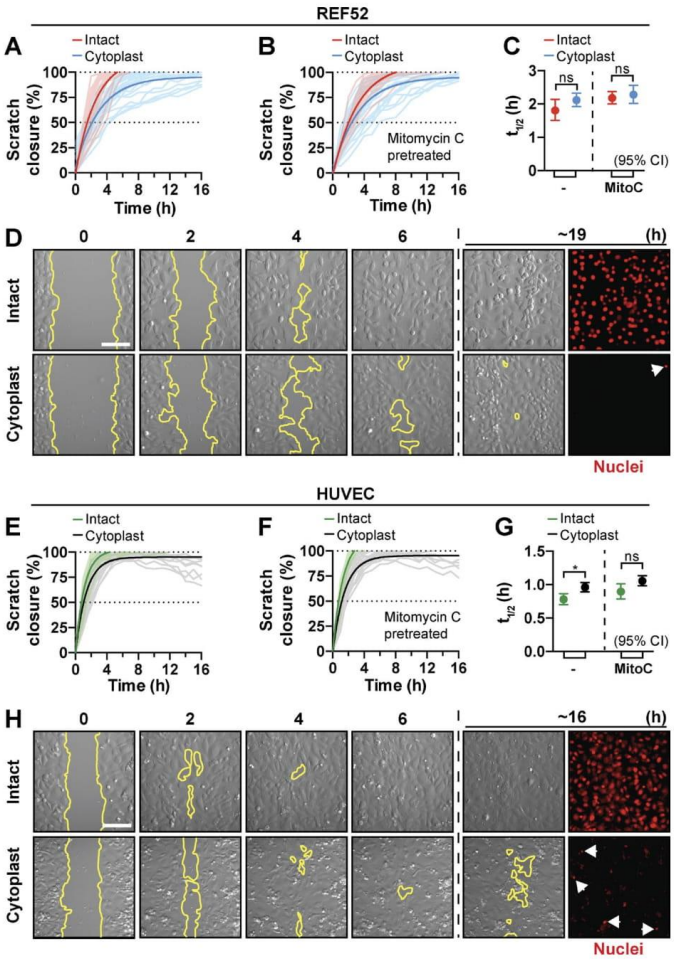

Figure 4. **The nucleus is dispensable for directed migration in the scratch-wound assay.** **(A)** Percent scratch-closure for intact cells (n = 27) and cytoplasts (n = 28). **(B)** Percent scratch-closure for mitomycin C–pretreated intact cells (n = 27) and cytoplasts (n = 22). **(C)** Mean time to close half of the scratch area ($t_{1/2}$ [h]) ± 95% CI. MitoC, mitomycin C. **(D)** Stills from scratch assay of REF52 intact cells (top) and cytoplasts (bottom) from mitomycin C treatment. Open scratch-area outlined in yellow. Arrowheads in D and H indicate nuclei. Data in A–D are from REF52 cells. **(E)** Percent scratch-closure for intact cells (n = 21) and cytoplasts (n = 28). **(F)** Percent scratch-closure for mitomycin C–pretreated intact cells (n = 30) and cytoplasts (n = 23). **(G)** Mean time to close half of the scratch area ($t_{1/2}$ [h]) ± 95%CI. **(H)** Stills from scratch assay of HUVEC intact cells (top) and cytoplasts (bottom) from mitomycin C treatment. Data in E–H are from HUVECs. Open scratch areas are outlined in yellow; arrowheads show nuclei. Note that dead cells also stained with nuclear dye, producing high apparent background. Bars, 100 µm. All scratch-closure graphs were fit with single-phase decay regressions. All data are from at least three independent experiments. Student's t tests were performed. ***, P < 0.001; **, P < 0.01; *, P < 0.05.

than commonly used plastic (E > 10^6 kPa) and glass (E > 50 × 10^6 kPa) substrata for cells and may have an effect on cytoplast migration efficiency. Reliably altering the stiffness of 3D environments in a cell-compatible manner is not trivial, causing concomitant changes to ligand density and pore geometry. Consequently, we tested the effect of microenvironment stiffness on 2D migration by measuring migration in 2D on FN-coated substrata of known stiffness.

Using a range of hydrogels at 0.2, 0.5, 1, 8, 25, and 50 kPa and glass, we found intact cells and cytoplasts showed pronounced, biphasic responses in migration velocity with relation to substrata stiffness (Fig. 6 A). REF52 intact cells showed a peak migration velocity on 8-kPa substrata, whereas cytoplasts showed an unexpected peak migration velocity on 25-kPa substrata. When plotted together, a shift in peak of the biphasic response was evident, with the maximum cytoplast velocity significantly shifted toward stiffer substrata (Fig. 6 B). This trend was not repeated upon inhibition of transcription or translation (Fig. S5 A). These data show cell migration velocity is dependent on substrate stiffness, which is a property observed in other cells (Peyton and Putnam, 2005; Plotnikov et al., 2012; Sunyer et al., 2016). Because mechanosensing depends upon both environmental forces and cell-generated forces (Janmey et al., 2009) and cell-generated forces are largely regulated by actomyosin-based contractility (Pelham and Wang, 1997; Pathak and Kumar, 2012; Raab et al., 2012), we surmised the shift in the optimum stiffness for migration could be a product of reduced whole-cell contractility and a reduction in mechanosensitive signaling on account of loss of the nucleus. For instance, if cell contractility is reduced, then a higher substratum rigidity would be necessary to activate mechanically sensitive pathways that regulate migration. To gain insight into this, we tested baseline mechanosensory responses in REF52 intact cells versus cytoplasts by subjecting them to identical conditions of biaxial

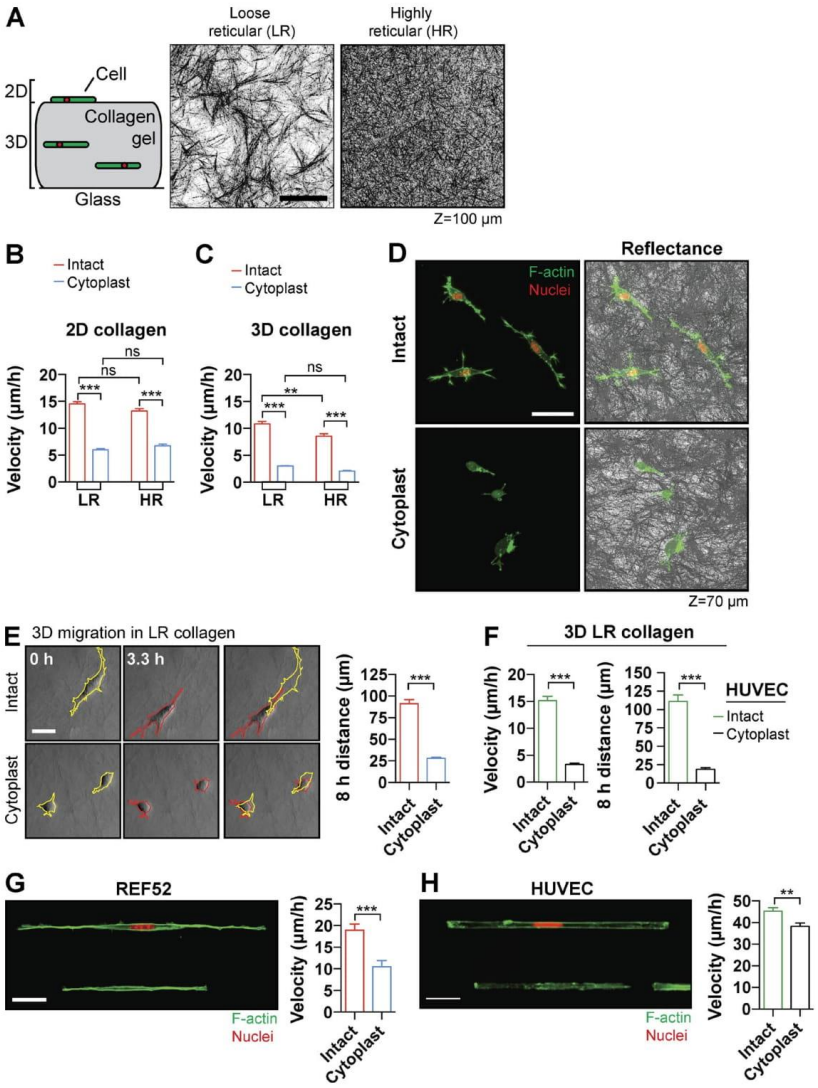

Figure 5. **The nucleus is dispensable for migration in 1D, but not 3D. (A)** Illustration of collagen matrix (left) for measuring 2D and 3D cell migration. Reflectance images (right) from 1.9 mg/ml self-assembled collagen polymerized to form LR or HR matrices, respectively. Bar, 50 µm. Image stack depth is 100 µm. **(B)** Mean 2D cell velocity ± SEM for REF52 cells on top of LR or HR matrices. Intact LR, $n = 184$; cytoplast LR, $n = 169$, intact HR, $n = 62$; cytoplast HR, $n = 52$. **(C)** Mean 3D REF52 cell velocity ± SEM for cells embedded in LR or HR matrices. Intact LR, $n = 136$; cytoplast LR, $n = 111$, intact HR, $n = 50$; cytoplast HR, $n = 54$. **(D)** Images of intact REF52 cells and cytoplasts in 3D LR collagen. Bar, 50 µm. Image stack depth is 70 µm. **(E)** Stills (left) of an intact cell (top) and cytoplasts (bottom) at 0 h (yellow outline) and 3.3 h (red outline). Graph (right) showing accumulated distance ± SEM from continuous 8 h of 3D migration for intact REF52 cells ($n = 71$) and cytoplasts ($n = 64$). **(F)** Graph (left) showing mean 3D cell velocity ± SEM for HUVECs embedded in LR matrix. Intact, $n = 57$; cytoplast, $n = 64$. Graph (right) showing accumulated distance ± SEM from continuous 8 h of 3D migration for intact cells ($n = 35$) and cytoplasts ($n = 41$). **(G)** Images of REF52 cells on 5-µm lines (left) and mean cell velocity ± SEM for 1D migration (right). Intact cells, $n = 110$; cytoplasts, $n = 151$. **(H)** Images of HUVECs on 5-µm lines (left) and mean cell velocity ± SEM for 1D migration (right). Intact cells, $n = 96$; cytoplasts, $n = 108$. Bars: (E, G, and H) 20 µm. All data are from at least three independent experiments. Student's *t* tests were performed. ***, $P < 0.001$; **, $P < 0.01$; *, $P < 0.05$.

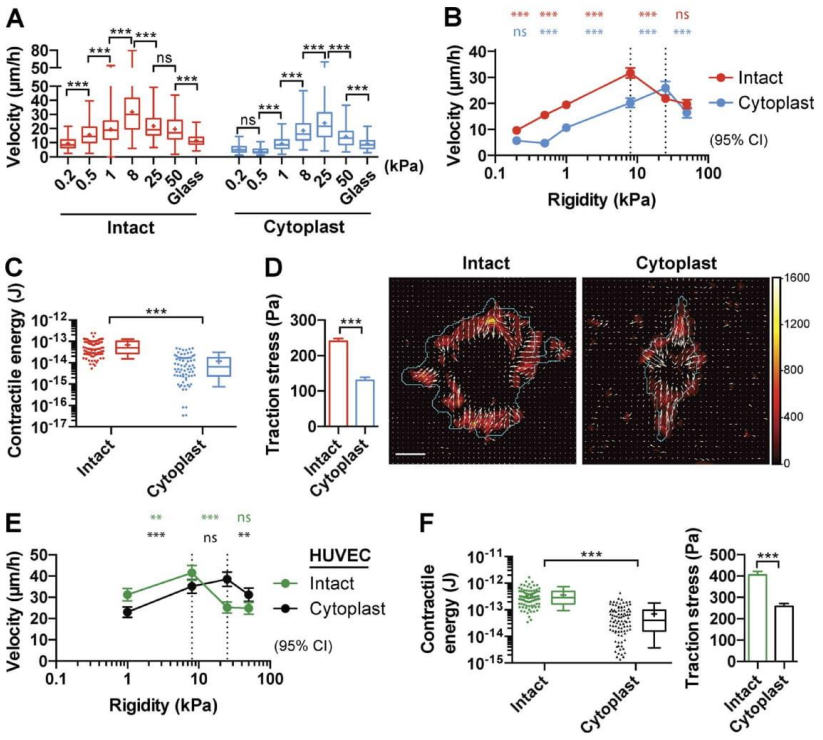

Figure 6. **The nucleus regulates cell contractility and migration in response to substratum rigidity. (A)** REF52 cell velocity on compliant substrata for intact cells ($n \geq 45$/stiffness) and cytoplasts ($n \geq 69$/stiffness). **(B)** Same data in A, showing overlay of cell velocity ± 95% CI on compliant substrata. **(C)** Contractile energy of REF52 intact cells ($n = 98$) and cytoplasts ($n = 72$). **(D)** Graph (left) showing mean traction stress ± SEM for REF52 intact cells and cytoplasts. Representative images (right) of traction stresses. Force vectors (arrows) and cell outlines (cyan) are shown. Bar, 20 µm. Scale is traction stress magnitude (in pascals). **(E)** Cell velocity ± 95% CI on compliant substrata for HUVEC intact cells ($n \geq 72$/stiffness) and cytoplasts ($n \geq 112$/stiffness). **(F)** Contractile energy graph (left) of HUVEC intact cells ($n = 89$) and cytoplasts ($n = 93$). Graph (right) showing mean traction stress ± SEM for HUVEC intact cells and cytoplasts. Dotted lines in B and E show 8 and 25 kPa. All data are from at least three independent experiments. Mann–Whitney *U* tests were performed for all traction force data. One-way ANOVA with Tukey's post-hoc test was performed between stepwise increases in stiffness for A, B, and E. Boxplots in C and F show 10th–90th percentiles. ***, $P < 0.001$; **, $P < 0.01$; *, $P < 0.05$.

cyclic strain. As previously reported, this results in activation of FAK through phosphorylation of Y397 (Li et al., 2001; Uzer et al., 2015). We found increased phospho-FAK levels after strain in both intact cells and cytoplasts. Interestingly, poststrain phospho-FAK levels were lower in cytoplasts than intact cells, suggesting that focal adhesion–based mechanotransduction is less sensitive to force cues in the absence of the nucleus (Fig. S5 B).

We used traction-force microscopy to measure the contractile energy (a whole-cell measure showing the mechanical effort used by the cell in substrate deformation [also known as strain energy]) and traction stress (a per-area-unit measure of the mechanical effort used by the cell in substrate deformation). We found that cytoplasts from REF52 cells had significantly reduced contractile energy and traction stress compared with intact cells (Fig. 6, C and D). This does not appear to be cell specific, because HUVEC cytoplasts also exhibited a similar shift in peak of the biphasic response toward more rigid substrata (Fig. 6 E) and showed decreased contractile energy and traction stress (Figs. 6 F and S5 C). These data, together with the decreased collagen gel contraction by cytoplasts (Fig. S4 F), suggest that the nucleus regulates cell contractility and controls the sensitivity of the cell to mechanical cues.

The LINC complex and lamin A also regulate cell contractility and the sensitivity of the cell to mechanical cues

We sought to understand whether cell contractility and traction stress could be similarly regulated in intact cells with nuclear defects. The LINC complex mediates mechanical coupling between the cytoskeleton and nucleoskeleton via interactions between Nesprin and Sun proteins (Lombardi et al., 2011; Arsenovic et al., 2016). Thus, we codepleted Sun1/Sun2 (siSun1/Sun2) in REF52 cells (Fig. S5 D) to disrupt the LINC complex and subsequently decrease force transduction to the nucleus. Cells treated with a nontargeting siRNA (siCntl) showed a biphasic trend in cell migration velocity across different rigidities, with a peak cell velocity exhibited on 8-kPa substratum (Figs. 7 A and S5 B). In contrast, cells codepleted

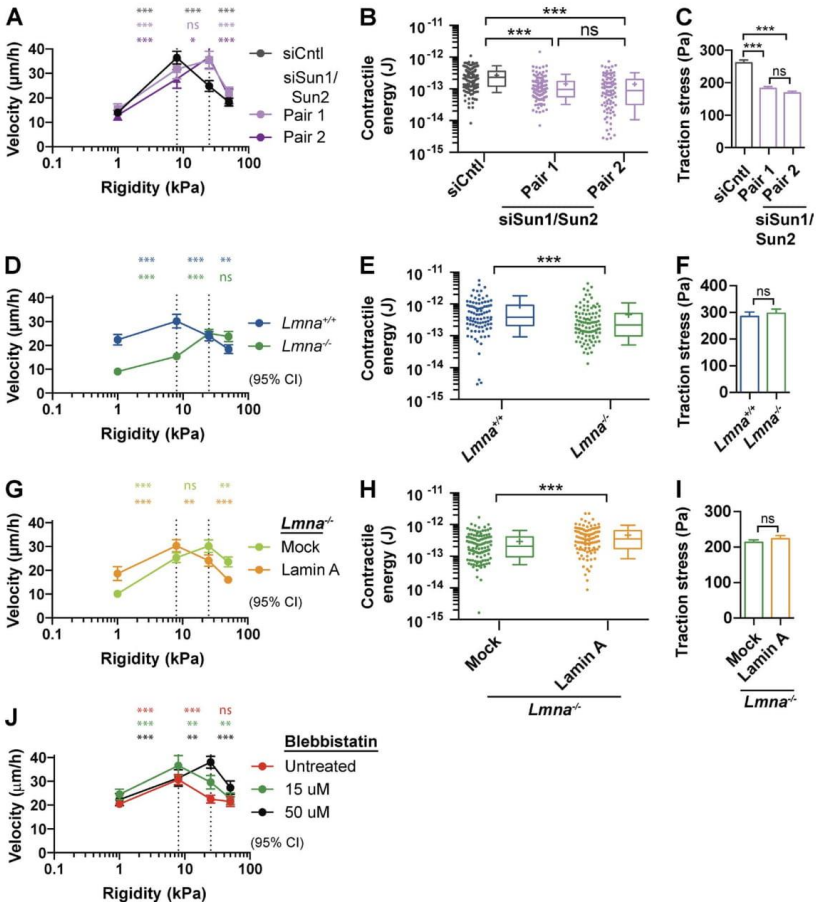

Figure 7. **The LINC complex and lamin A regulate cell contractility and migration in response to substratum rigidity. (A)** Cell velocity ± 95% CI on compliant substrata for REF52 cells treated with siCntl ($n \geq 118$/stiffness), siSun1/Sun2 siRNA pair 1 ($n \geq 71$/stiffness), and siSun1/Sun2 siRNA pair 2 ($n \geq 42$/stiffness). **(B)** Contractile energy of REF52 cells treated with siCntl ($n = 139$), siSun1/Sun2 siRNA pair 1 ($n = 117$), and siSun1/Sun2 siRNA pair 2 ($n = 97$). **(C)** Mean traction stress ± SEM for siCntl and siSun1/Sun2–treated REF52 cells. **(D)** Cell velocity ± 95% CI on compliant substrata for $Lmna^{+/+}$ ($n \geq 79$/stiffness) and $Lmna^{-/-}$ ($n \geq 113$/stiffness) cells. **(E)** Contractile energy of $Lmna^{+/+}$ ($n = 90$) and $Lmna^{-/-}$ ($n = 103$) cells. **(F)** Mean traction stress ± SEM for $Lmna^{+/+}$ and $Lmna^{-/-}$ cells. **(G)** Cell velocity ± 95% CI on compliant substrata for $Lmna^{-/-}$ cells rescued with lamin A ($n \geq 69$/stiffness) or mock ($n \geq 67$/stiffness). **(H)** Contractile energy of $Lmna^{-/-}$ cells rescued with lamin A ($n = 117$) or mock ($n = 106$). **(I)** Mean traction stress ± SEM for $Lmna^{-/-}$ cells rescued with lamin A or mock. **(J)** Cell velocity ± 95% CI on compliant substrata for untreated intact REF52 cells ($n \geq 92$/stiffness) or in the presence of 15 µM ($n \geq 74$/stiffness) or 50 µM ($n \geq 60$/stiffness) bleb. Dotted lines in A, D, G, and J show 8 and 25 kPa. All data are from at least three independent experiments. One-way ANOVA with Tukey's post-hoc test was performed between stepwise increases in stiffness for A, D, G, and J. The Kruskal–Wallis test with Dunn's multiple comparisons was performed for B and C. The Mann–Whitney *U* test was performed for all other traction force data. Boxplots show 10th–90th percentiles. ***, $P < 0.001$; **, $P < 0.01$; *, $P < 0.05$.

of Sun1 and Sun2 showed a shift in peak of the biphasic response toward 8 and 25 kPa. Traction force analysis showed that siSun1/Sun2–treated cells have a lower contractile energy than controls (Fig. 7 B). Moreover, traction stress values were lower in siSun1/Sun2–treated cells than controls (Figs. 7 C and S5 E). These data support the role of the nucleus as a regulator of cell contractility to control the sensitivity of the cell to mechanical cues.

Lamin A/C is an important mechanosensitive nuclear protein (Swift et al., 2013) and is nonessential for LINC complex anchorage (Padmakumar et al., 2005; Crisp et al., 2006; Haque et al., 2006). We measured the mechanoresponses of cells bearing the total loss of this structural nuclear lamina protein. Using $Lmna^{-/-}$ mouse embryonic fibroblasts (MEFs), we found a pronounced shift of the peak migration velocity toward 25- and 50-kPa substrata compared with a peak migration velocity at 8-kPa

substratum for Lmna$^{+/+}$ cells (Fig. 7 D). Consistent with this, traction-force measurements revealed a decreased contractile energy in Lmna$^{-/-}$ cells (Figs. 7 E and S5 F); however, traction stress was not different between Lmna$^{-/-}$ and Lmna$^{+/+}$ MEFs. Using Lmna$^{-/-}$ cells rescued with lamin A only (Fig. S5 G), the peak migration velocity on different rigidities was shifted toward less rigid substrata (peak at 8-kPa substratum) in rescued, but not mock rescued, cells (peak at 8- and 25-kPa substrata; Fig. 7 G). Remarkably, nearly complete restoration of contractile energy was measured in lamin A–rescued cells (Fig. 7 H). Similar to Lmna$^{-/-}$ and Lmna$^{+/+}$ MEFs, however, traction stress was not different between lamin A and mock-rescued Lmna$^{-/-}$ MEFs (Figs. 7 I and S5 H). These data demonstrate a similar nuclear-based modulation of cell migration and contractile energy to that observed in cytoplasts and cells bearing loss of the LINC complex. However, unlike enucleation or depletion of Sun1/Sun2 proteins, the presence of lamin A/C does not affect traction stress.

Lastly, we directly tested the role of cell contractility on regulating migration velocity on different rigidity substrata. Intact REF52 cells were treated with either 15 or 50 µM blebbistatin (bleb) to reduce actomyosin-based contractility while cell migration velocity on different rigidity substrata was measured. Consistent with our earlier measurements, cells showed a shift in peak of the biphasic migration velocity response from 8-kPa substratum, observed in untreated and 15 µM bleb–treated cells, to 25-kPa substratum with 50 µM bleb treatment (Fig. 7 J). The shift in peak migration that was measured upon nuclear loss, loss of connectivity between the cytoskeleton and nucleoskeleton, loss of lamin A/C, and inhibition of actomyosin-based contractility suggests a common pathway that regulates force transduction and cell migration response to environments of different rigidity. These data suggest that the nucleus can regulate the sensitivity of the cell to mechanical cues via modulation of whole cell contractility, a role consistent with the nucleus playing a role in an integrated molecular clutch.

Discussion

Cell biologists have investigated the physical role of the nucleus both in establishing cell polarity and in cell migration for many decades, with a more recent focus on its role in mechanotransduction. Based on our data using both fibroblasts and endothelial cells, we show that the nucleus is not necessary for establishing cell polarity or directional migration but is important for regulating the sensitivity of the cell to mechanical cues. Our data support a working model whereby the nucleus is a critical component of an integrated molecular clutch encompassing focal adhesions, actin stress fibers, and the nucleus.

The nucleus, cell polarity, and 2D cell migration

A relationship between the positions of the centrosome (microtubule-organizing center) and nucleus has long been recognized in many cells (Luxton and Gundersen, 2011). This relationship has been studied extensively, particularly in the context of cells in culture migrating into a scratch wound. For many migrating cells, there is an orientation of the centrosomal–nuclear axis such that the centrosome is located in front of the nucleus and the axis corresponds to the direction of migration. It has been shown that rearward nuclear movement reorients the position of the centrosome and that nuclear repositioning defines cell polarity (Gomes et al., 2005). These and other observations (Lee et al., 2007) have led to the view that the nucleus is critical for anterior–posterior cell polarity. Earlier work, however, suggested the opposite (Chambers and Fell, 1931; Goldstein et al., 1960; Goldman et al., 1973; Piel et al., 2000). We find that centrosome and Golgi localization occur with equal efficiency in the presence or absence of the nucleus, consistent with the notion that the nucleus is not strictly necessary for proper positioning of these organelles.

Similarly, we show that the nucleus is not essential for 2D migration under random and directed conditions. Although cytoplasts migrate more slowly on conventional FN concentrations (10 µg/ml) than control cells, similar migration velocities between cytoplasts and intact cells are found at higher FN concentrations. This suggests that the nucleus is not necessary for migration because changing FN density (which changes adhesion strength) can greatly modulate migration velocity. Given that the establishment of the centrosomal–nuclear axis has been implicated in directed migration, it is striking that cytoplast migration is little affected by the loss of the nucleus. Our directed migration data show cytoplasts chemotax and haptotax at efficiencies similar to intact cells. This indicates that the nucleus is not essential for sensing and responding to these extracellular cues or in establishing and maintaining the polarity required for directional migration. Furthermore, despite showing differences in total scratch closure time, our scratch assay data show similar rates of closure for half the scratch area between cytoplasts and intact cells. Several factors could potentially explain the total scratch closure time lag in cytoplasts, such as time-dependent cytoplast deterioration or decreased FN density from the scratch margin to the scratch center. However, our data indicate that a nucleus is not needed for the polarized positioning of the centrosome and Golgi or for directed cell migration.

Many studies have shown that disruption of proteins that associate the nucleus with the cytoskeleton, such as molecular motors, the LINC complex, and lamins, also cause concomitant defects in cell polarity, cell migration, and cytoskeletal organization (Nery et al., 2008; Roux et al., 2009; Chancellor et al., 2010; Fridolfsson and Starr, 2010; Luxton et al., 2010; Folker et al., 2011; Hale et al., 2011; Lombardi et al., 2011; Stewart et al., 2015). Our results do not contradict these earlier findings but rather indicate that whereas a misconnected or aberrantly positioned nucleus can perturb cell polarity and migration, the complete removal of the nucleus abrogates these defects. Though it is not known how an improperly positioned nucleus hinders cell polarity and migration in all contexts, it most likely involves the role of the nucleus in maintaining cytoskeletal organization and, through this, proper coordination of intra- and intercellular forces. The LINC complex directly mediates force transmission between the nucleus and cytoskeleton (Lombardi et al., 2011; Alam et al., 2015; Stewart et al., 2015; Arsenovic et al., 2016). Aberrant force transmission between the cytoskeleton and the nucleus could differentially affect force-sensitive signaling pathways that regulate polarity establishment and maintenance, as well as cell migration.

The nucleus and 3D cell migration

Although cytoplast migration on 2D surfaces was comparatively normal, it was greatly impaired in 3D collagen gels. At the outset of this study, we were uncertain what effect removing the nucleus would have on a cell's migration in 3D. This is

because the nucleus has been reported to both facilitate and impede migration efficiency in constrained spaces. For example, lobopodial migration is driven by a nuclear-piston mechanism that allows cells to move in 3D (Petrie et al., 2014). It is worth noting that this mechanism of migration does not explain our cytoplast 3D data because the nuclear-piston mechanism was shown in cell-derived matrices and does not operate in collagen matrices. Cytoplasts from that study, however, did show low migration velocity (∼4 µm/h) in cell-derived matrix, consistent with poor migration of cytoplasts in 3D environments.

In addition to the evidence that the nucleus positively contributes to 3D migration, other data suggest that in constrained spaces, the nucleus can limit 3D migration (Wolf et al., 2013). The nucleus can undergo high stress in these environments, leading to nuclear rupture and DNA damage (Denais et al., 2016). Increasing matrix pore size or increasing nuclear plasticity through decreasing levels of lamin A/C have been shown to increase cell migration in constrained spaces (Harada et al., 2014). One would predict that enucleation would increase migration velocity in 3D, based on evidence that a nucleus can restrain migration through narrow 3D matrices. However, we have found the opposite. Because cytoplasts can signal on collagen, exert force on collagen fibers, signal in response to mechanical load on collagen, and degrade and remodel matrix, these factors are unlikely to explain the impaired migration of cytoplasts in 3D.

Why do cytoplasts migrate so poorly in 3D environments? We considered two explanations: dimensionality and the low rigidity of the matrix used in our studies. We observed a general decrease in migration velocity upon changing between 2D and 3D collagen for both intact cells and cytoplasts. Because migration of cells along narrow lines of ECM (1D migration) is thought to be similar to 3D migration (Doyle et al., 2009), we examined how cytoplasts migrate on 1D FN-coated lines. Cytoplasts showed robust migration on these lines. However, these 1D matrix-coated lines were generated on rigid (glass) substrates, similar to the 2D random and directed migration studies described above. Consistent with this idea that rigidity may be critical, cytoplasts exhibit a relatively low migration velocity on the 2D top surface of 3D collagen gels. Ideally, we would have liked to test the role of rigidity in a 3D environment; however, this was technically challenging, because modifying the rigidity of collagen gels usually results either in concomitant changes in ligand density and/or changes in the porosity of the gel, making interpretation of any results ambiguous. Thus, we decided to tackle the rigidity question using 2D hydrogels of varying defined stiffness. Consistent with the idea that substrate stiffness largely accounts for differences between intact cell and cytoplast 3D motility, we observed a shift in the biphasic motility response, with cytoplasts requiring a stiffer substrate to achieve maximum cell velocity.

Impact of the nucleus on the integrated molecular clutch

The velocity of cell migration depends on both the density of the matrix molecules (e.g., FN) on the substrate and the rigidity of this surface. With both increasing matrix density and substratum rigidity, most cells demonstrate a biphasic migration velocity response (Lauffenburger and Horwitz, 1996; Peyton and Putnam, 2005; Pathak and Kumar, 2012). One of the striking results emerging out of our work is that the presence or absence of a nucleus (or connections to the nucleus) affects this response to matrix density and substrate rigidity. Removal of the nucleus shifted the peak velocity to higher matrix densities and higher substrate rigidities. For intact cells, the biphasic velocity response to increasing FN concentrations was generally interpreted as the result of too little adhesion being insufficient to generate optimal traction force, whereas too strong adhesion prevents detachment of adhesions, thereby retarding migration. However, agents that inhibit myosin activity or promote it were previously observed to shift the peak velocity to either faster or slower speeds depending on the FN concentration, indicating that the velocity profile could not be explained based on differences in adhesion strength alone (Gupton and Waterman-Storer, 2006). It was concluded that migration velocity reflects the interplay of many interdependent factors, including adhesion strength, myosin II activity, and actin dynamics (Gupton and Waterman-Storer, 2006). A large body of work has shown that migration velocity depends on nonmuscle myosin II and retrograde actin flow generating traction, as well as on "molecular clutches" (the sites of adhesion involving integrins, often clustered in focal adhesions) transmitting this traction to the substratum (Case and Waterman, 2015). Significantly, the behavior of the molecular clutch is affected by the rigidity of the substratum to which cells are adhering (Chan and Odde, 2008; Bangasser et al., 2017). The clutch properties reflect the number of adhesion molecules engaged, bond strength, and the types of bonds (catch bonds versus slip bonds).

Building on our enucleation results, we postulate that the LINC complex and nuclear lamina serve as a critical part of an extended and integrated molecular clutch that includes focal adhesions, contractile actin stress fibers, and the nucleus (Fig. 8). Actomyosin contractility regulates how cells sense and respond to force. The effect of enucleation on migration velocity was mimicked by inhibiting myosin II activity in intact cells with bleb. Also, consistent with cytoplasts having decreased contractility, they demonstrated reduced collagen gel contraction, decreased contractile energies, and decreased traction stresses. Similar results were obtained when we broke the cytoskeletal connections to the nucleus by disrupting the LINC complex through Sun1/Sun2 depletion. Again, this shifted the peak migration velocity to more rigid substrata and decreased contractile energy and traction stress. This suggests that nucleocytoskeletal connections regulate cell contractility and cell behavior in a manner similar to regulating actomyosin function. Because of the known structural connections between the nucleus and the actin cytoskeleton, a functional interdependence likely exists. Recent efforts have begun to dissect the signaling pathways regulating the LINC complex and actin cytoskeleton, revealing transcription-independent functions that involve regulation of RhoA activity (Thakar et al., 2017). Although our data support a role for nucleoskeletal connections in regulating cell contractility, it will be important in future studies to determine whether other activities such as actin retrograde flow rates and adhesion dynamics are also affected.

It is striking that although only a subset of actin filaments associate with the LINC complex (Khatau et al., 2009; Luxton et al., 2010), perturbing nucleocytoskeletal connections was sufficient to significantly decrease whole-cell contractility and alter mechanosensing. This suggests that LINC complex–associated actin filaments are particularly important in regulating whole-cell tension and cell migration. Consistent with this idea, distinct perinuclear focal adhesions have been reported to exist in several different cell lines, and LINC complex–associated

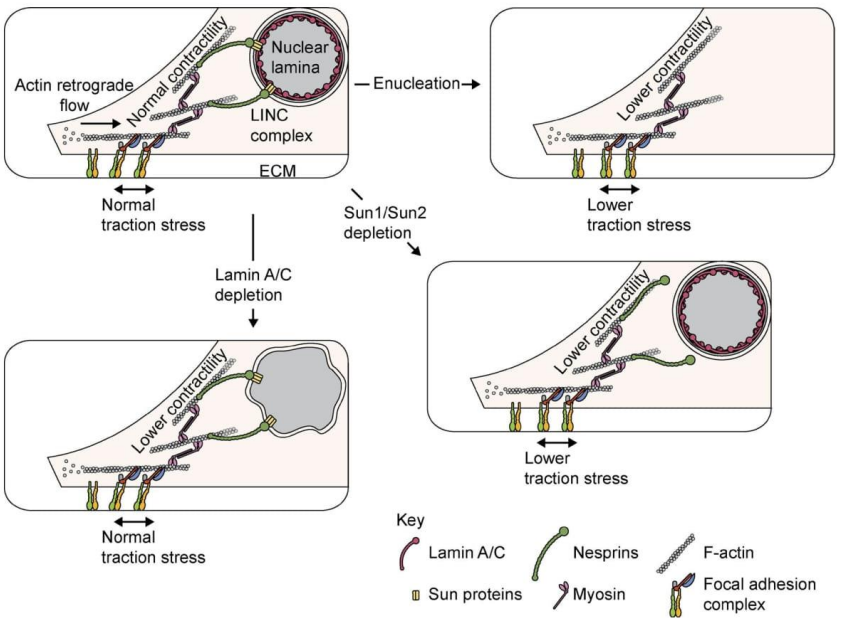

Figure 8. **The nucleus is an integral component of the molecular clutch.** Cartoon showing the nucleus as a structurally integrated, force-sensitive component of the molecular clutch model. The molecular clutch model proposes that ECM-bound integrins indirectly couple to actin retrograde flow and actomyosin contractility via force sensitive proteins (e.g., talin and vinculin) and, once engaged, are capable of bridging force between the extracellular environment and the cytoskeleton. An engaged molecular clutch can exert mechanical force on its environment through focal adhesions, giving rise to normal mechanical effort, as indicated by contractile energy and traction stress. The nucleus, though distal to the focal adhesion, is physically integrated with the cytoskeleton via the LINC complex. Enucleation, disruption of the LINC complex, and loss of lamin A/C caused a decrease in the contractile energy, whereas enucleation and disruption of the LINC complex caused a decrease in traction stress. Collectively, these nuclear defects manifest as lower migration velocity on physiologically normal substrata (~8 kPa) compared with controls. Upon increasing substrata rigidity (8–25 kPa), migration velocity was rescued, suggesting a greater force input was necessary to engage the molecular clutch.

actin filaments have been shown to terminate in focal adhesions that are distinct from the majority (Kim et al., 2012). According to this work, LINC complex–associated focal adhesions are mechanosensitive over a broad range of stiffness (5–500 kPa) as compared with conventional focal adhesions, which are mechanosensitive on only soft substrata (<5 kPa). Collectively, it is possible that nucleocytoskeletal disruption via enucleation or Sun1/Sun2 loss may selectively disrupt a distinct and crucial subset of focal adhesions that disproportionally affect the molecular clutch.

Mutations in nuclear lamins and LINC complex components affect cytoskeletal organization, cell migration, and physical properties of the cells. In particular, previous work with Lmna$^{-/-}$ cells has shown decreases in stress fiber organization, actin dynamics, focal adhesion area, RhoA activity, nuclear stiffness, mechanically induced nuclear signaling, and, more recently, contractility itself (Broers et al., 2004; Lammerding et al., 2006; Hale et al., 2008; Khatau et al., 2009; Ho et al., 2013; van Loosdregt et al., 2017). In our work, we have found that Lmna$^{-/-}$ cells also show a shift in the peak of their migration velocity to higher rigidity substrata. Consistent with these results, they also show decreased contractile energy, but unexpectedly, we did not detect a decrease in traction stress. The reason for this is currently unclear, but one possibility is that this reflects the difference between a soft nucleus that is still attached via the LINC complex to the cytoskeleton as opposed to a disconnected nucleus (Fig. 8). Alternatively, Lmna$^{-/-}$ cells may be affecting other signaling pathways or experimental parameters, such as changes in the polarization of the traction forces, which in turn affect traction stress and cell migration (Jurado et al., 2005; Meili et al., 2010; Bastounis et al., 2014).

One important aspect of our integrated molecular clutch model (Fig. 8) is the bidirectional nature of force in the model. Force on the molecular clutch arises from retrograde actin flow, driving forward protrusion of the leading edge, and also from actomyosin contractility pulling the nucleus and rest of the cell body forward. Myosin-based contractility develops tension between the clutch and the nucleus because of the interconnections between the cytoskeleton and the nuclear envelope mediated by the LINC complex. The tension developed between these two structures (the adhesions and the nucleus) will be diminished externally by decreasing the rigidity of the substratum or internally by enucleation or disrupting the connections to the nucleus. The reduced tension transmitted to the clutch will, in turn, alter the cell's migratory response to both matrix rigidity and matrix density. Depleting lamin A, however, has an intermediate effect, because the nucleus is still connected to the actin cytoskeleton but is less rigid than a nucleus

in which lamin A is present (Haque et al., 2006; Lammerding et al., 2006). Our results highlight the continuing importance of understanding the cytoskeletal–nuclear interconnections and molecular details of the molecular clutch. During the past few years, much has been learned about how tension exerted on the clutch affects the properties and interactions of components mediating adhesion (Elosegui-Artola et al., 2016). Much still remains to be learned about these interactions and also how the signaling events generated by mechanical tension feeds back to impact cell behavior. Ultimately, this information should lead to a better understanding of how cells respond not only to the composition of their environment but also to its physical properties.

Materials and methods

Reagents and materials

Commercial antibodies used for Western blotting and immunohistochemistry were purchased from Cell Signaling Technology (rabbit anti-EEA1, rabbit anti-NUP98, rabbit anti-LMNA/C, mouse anti–histone H3, rabbit anti-MHC2A, rabbit anti-RLC [myosin regulatory light chain], rabbit anti-FAK, rabbit anti-FAK [Y397], rabbit anti-paxillin [Y118], rabbit anti-vinculin, rabbit anti-vimentin, rabbit anti-Src, rabbit anti-AMPKα, and rabbit anti-GAPDH), EMD Millipore (rabbit-anti-Sun1, rabbit anti-Sun2, and mouse anti-actin), Abcam (rabbit anti-emerin), Sigma-Aldrich (mouse anti–α-tubulin and mouse anti–γ-tubulin), BD (mouse anti-GM130), BioLegend (Alexa Fluor 488–conjugated anti–β1 and anti–β3 integrins), and Thermo Fisher Scientific (HRP-conjugated goat anti–mouse and goat anti–rabbit; Alexa Fluor 488, 568, and 633 goat anti–mouse and goat anti–rabbit). Phalloidin (Alexa Fluor 488, 568, 633), ER-Tracker Red (BODIPY), MitoTracker Green FM, CellTracker Green CMFDA, CellTracker Red CMTPX, calcein-AM, Hoechst 33342, Vybrant Dye-Cycle Green nuclear stain, and trypan blue were purchased from Thermo Fisher Scientific. Human FN used to conjugate to Cy5 was purchased from BD. Cy5 conjugation to FN was performed as previously described (Wu et al., 2012). FN used for all other experiments was purified from human plasma, as previously described (Engvall and Ruoslahti, 1977). Rat tail collagen type I was purchased from Advanced BioMatrix. Ficoll-400 was purchased from Fisher (BP525). Polyacrylamide hydrogels were purchased from Matrigen. Mitomycin C, GM6001, actinomycin D, cycloheximide, and SU6656 were purchased from Tocris. Cytochalasin B was purchased from Enzo Life Sciences. Blebbistatin was purchased from Sigma-Aldrich.

Cell culture, expression vectors, and RNAi experiments

REF52 cells were grown in high-glucose DMEM (Invitrogen) containing 10% FBS (Sigma-Aldrich) and 100 U/ml Pen-Strep (Invitrogen). Plasmid transfections were performed with Lipofectamine 2000 reagent (Invitrogen), based on manufacturer's protocol. Stable REF52 lines were generated by transfecting cells with specified constructs and sorting for fluorescence via successive rounds of flow cytometry. These lines include an NLS tdTomato chimera expressing line that was generated with the pQC-NLS-tdTomato construct (courtesy of C. Cepko's laboratory, Harvard Medical School, Boston, MA). A Golgi-EGFP–expressing line was used for all micropattern work and was generated with the pLL-5.5-GIX (Uetrecht and Bear, 2009) construct. This construct encodes a human β-1,4-galactosyltransferase-EGFP chimera. A centrin-EGFP–expressing line was generated with the p3XGFP-centrin construct. HUVECs were purchased from Lonza and cultured in EBM-2 endothelial growth basal medium (EBM-2). All lamin A/C MEF lines, including $Lmna^{+/+}$, $Lmna^{-/-}$, and $Lmna^{-/-}$ rescued with lamin A or mock rescued, were provided by J. Lammerding's laboratory (Cornell University, Ithaca, NY).

RNAi-mediated depletion of Sun1 and Sun2 was performed using siRNA duplexes purchased from Dharmacon. Two separate siRNA pairs were used for Sun1 and Sun2. These were siSun1/Sun2 pair 1: Sun1 (5′-GUAUAUACCAAGACGCCAU-3′), Sun2 (5′-GAGACUUACGAGACGAAGA-3′) and siSun1/Sun2 pair 2: Sun1 (5′-AUGUUGAAUUGGACGGCCA-3′), Sun2 (5′-GCUACAGUGAGGACCGUAU-3′). A nontargeting siRNA (5′-CGAACUCACUGGUCUGACC-3′) was used as a control. Transfection of 50-nM siRNA duplexes was performed with Mirus siQUEST reagent according to the manufacturer. Cells were used for experiments beginning at 48 h after transfection. Validation of RNAi-mediated depletion was monitored after each experiment via Western blot. Quantification of protein knockdown was measured using ImageJ.

Western blotting

Cells were lysed in either radioimmunoprecipitation assay lysis buffer (150 mM NaCl, 50 mM Tris-HCl, 1 mM EDTA, 0.24% sodium deoxycholate, and 1% Igepal, pH 7.5) or 2× Laemmli sample buffer (120 mM Tris-HCL, pH 6.8, 4% SDS, 20% glycerol, and 0.02% bromophenol blue). All lysis buffers contained 100 nM aprotinin, 50 µM leupeptin, 10 µM pepstatin A, and 50 mM sodium orthovanadate. Lysates were run on SDS-PAGE gels and transferred to polyvinylidene fluoride membranes (Immobilon-P; EMD Millipore). Membranes were blocked with either 5% (wt/vol) milk or bovine serum albumin for 1 h at ambient temperature before being incubated with primary antibodies overnight at 4°C. After primary antibody incubation, blots were washed and incubated with HRP-conjugated secondary antibody at ambient temperature for 1 h. Western blots were developed with SuperSignal West Pico or Femto Chemiluminescent Substrate (Thermo Fisher Scientific) and either scanned on a ChemiDoc MP System (Bio-Rad) or developed on film.

Cellular enucleation

Enucleation was performed essentially as described previously (Wigler and Weinstein, 1975), but with modifications. Of note, we observed variation in enucleation efficacy with Ficoll 400 from different commercial sources and even lot numbers. The greatest consistency was observed with Ficoll 400 from Fisher (BP525). Ficoll-400 was dissolved into a 50% (wt/vol) solution in sterile PBS (Ca^{2+}/Mg^{2+} free) through overnight rotation at ambient temperature. The stock was then diluted to 30% (vol/vol) with standard tissue culture media (DMEM containing 10% FBS and 100 U/ml Pen-Strep). The stock Ficoll solution was sterile filtered (0.4 µm) and stored at 4°C. The refractive index of the stock was measured on a refractometer. For the REF52 cell line and cells of similar volume/size (e.g., HUVEC, HeLa), the optimal refractive index of 1.373 produced good purity cytoplasts. Discontinuous iso-osmotic density gradients were poured from freshly prepared stocks of 30%, 20%, 18%, and 15% Ficoll-DMEM containing 10 µg/ml cytochalasin B (dissolved in 100% ethanol) and 0.2% DMSO. Next, 2 ml each of the 30%, 20%, and 18% solutions were layered into a 13.2-ml (14 × 89 mm; Beckman Coulter) cellulose nitrate centrifuge tube, with the greatest density starting at the bottom of the tube. Lastly, 1 ml of the 15% solution was added to the top. The remaining 15% solution was stored at 4°C. Prepared gradients were covered in Parafilm and left to equilibrate overnight in a tissue culture incubator. The SW41 Ti rotor buckets were incubated at 37°C overnight. The next morning, up to 2×10^7 cells per gradient were lifted from tissue culture dishes by either divalent-free PBS containing 5 mM EDTA or 0.05% trypsin-EDTA solution. Cells were pelleted, washed, and resuspended in 1 ml prewarmed 15% Ficoll-DMEM. Resuspended cells were then layered on the top

of the gradient. Lastly, the gradient was topped off with standard tissue culture media, filling the tube to the top, and then loaded into the prewarmed SW41 Ti rotor bucket and incubated in a tissue-culture incubator for 45 min. The gradient was then centrifuged in a Beckman Coulter Optima LE-80K ultracentrifuge at a relative centrifugal force max of 125,000 *g* (27,000 rpm) for 1 h at 30°C and stopped at minimal braking. Fractions were collected from the gradient and washed twice in PBS and twice in DMEM. Cell density and purity were measured on a Cellometer cell counter (Nexcelom) after staining fractions with the Vybrant DyeCycle Green nuclear stain.

Flow cytometry

Cells were suspended in PBS (Ca^{2+}/Mg^{2+} free) containing 0.5% FBS and 5 mM EDTA and stained with Vybrant DyeCycle Green stain at a final concentration of 5 µM for 15 min at 37°C. Samples were then filtered through a 30-µm filter (Sysmex; Partec CellTrics) and placed on ice. Stained populations were individually profiled in a Bio-Rad S3 flow cytometer. For population analyses, ~50,000 cells were profiled per sample. In addition to nuclear dye detection, cytoplasts were also identified from intact cells based on distinct side-scatter profiles. Periodically, this was used to assess cytoplast population purity. FlowJo (v10.1r5) software was used for graphic visualization of population distributions and extraction of statistical values. All fluorescence threshold values were designated based on unlabeled and labeled cells. Values reporting percent enucleation efficiency are based on seven independent enucleation runs.

Surface expression of integrins

Cell surface expression of β1 and β3 integrins was performed by staining adherent cells that had been seeded on 10 µg/ml FN for 3 h under tissue culture conditions. Cells were stained with Alexa Fluor 488–conjugated antibodies against β1 or β3 integrin (BioLegend) for 15 min in serum-containing medium in a tissue-culture incubator per the supplier's recommendation. Cells were trypsinized, pelleted, filtered through a 30-µm filter (Sysmex), and placed on ice before immediately profiling populations in a Bio-Rad S3 flow cytometer. Cytoplasts were initially profiled for purity using the Vybrant DyeCycle Green stain to ensure purity. Median integrin–Alexa 488 fluorescence values for each integrin were divided by the median forward scatter values for each respective population to provide a relative integrin/particle size ratio. Differences in relative integrin levels were not detected between intact cells and cytoplasts when either mean or geometric mean values for integrin–Alexa 488 fluorescence/forward scatter were measured. Values were measured from two independent experiments containing technical duplicates.

Microscopy and image analysis

Immunofluorescent and histochemical cell staining. Cells were fixed with 4% paraformaldehyde in Krebs S-buffer and permeabilized in 0.2% Triton X-100 in PBS for 10 min at room temperature. Cells were blocked for 30 min in PBS containing 5% BSA. Primary antibodies in PBS containing 1% BSA were stained overnight at 4°C followed by extensive washes in PBS. Dyes such as ER-Tracker Red (BODIPY), MitoTracker Green FM, and calcein-AM require living cells for staining and were used per the manufacturer's recommendation. Fluorescent dye–conjugated secondary antibodies were diluted to 1:1,000–1:3,000 in 1% BSA in PBS and applied for 1 h at ambient temperature followed by extensive washes in PBS. For nucleoplast stains, nucleoplasts were seeded onto 20 µg/ml FN–coated glass coverslips and, when appropriate, fixed after 30 min. Glass coverslips coated with poly-L-lysine resulted in higher retention of nucleoplasts. Nucleoplasts were permeabilized and stained as described above. Fluoromount-G (Electron Microscopy Sciences) was used as the mounting medium for fixed cells on coverslips. Fluorescent images were acquired on either a Zeiss Axiovert 200M microscope using 20× or 40× objectives or on an Olympus FV1000 using a 40× objective.

Cell viability

Intact cells and cytoplast populations were stained with 1 µM calcein-AM (to label live cells), 0.2 µg/ml Hoescht 33342, and 0.04% (vol/vol) Trypan blue (to label dead cells) for 10 min in a tissue culture incubator. Dyes were washed out after staining, and images were acquired on an Axiovert 200M microscope with AxioVision software (Zeiss). Calcein-AM and Hoescht 33342 were imaged under fluorescent excitation/emission wavelengths suitable to each fluorophore, whereas trypan blue was imaged via transmitted light. Images were analyzed via automated particle counting with ImageJ software and verified by manual counting of randomly selected images from different time points. Stained populations were used for a single time point and were not restained for later time points. Viability data for intact cells and cytoplasts were derived from at least three independent experiments.

Cell outlines

Cell outlines were generated based on a masked phalloidin channel for all stains except for endoplasmic reticulum and mitochondria for the immunofluorescent and histochemical stains shown in Fig. 1. For endoplasmic reticulum and mitochondria images, cell outlines were manually drawn based on the transmitted light channel. To generate automatically detected outlines based on the phalloidin stain, a binary mask was generated with the phalloidin channel and the binary scale was inverted. Automated edge detection was performed using the "Find Edges" tool in ImageJ. The produced cell outline, designating the cell spread area of a cell, was preserved, whereas automatically outlined debris and background pixels were manually deleted so as to show only cell outlines. The resulting binary outlined channel was inverted, producing a white outline. This channel was then merged with the other stains for that cell. Cell outlines used for scratch assay experiments and matrix remodeling experiments were manually drawn using ImageJ and Adobe Illustrator.

Cell diameter and volume

Cell diameters of live REF52 intact cells and cytoplasts were measured using a Cellometer cell counter (Nexcelom). For volume measurements, cells were suspended in PBS (Ca^{2+}/Mg^{2+} free) and stained with calcein-AM and Hoechst 33342 dyes for 15 min at 37°C. Cells were seeded on glass-bottomed culture dishes that were coated with 0.5% BSA. Cells sedimented to the glass bottom and remained nonadherent. Using an Olympus FV1000 with a 40× objective, confocal fluorescent image stacks were generated for mixed populations of intact cells and cytoplasts. Image stacks were analyzed in ImageJ based on 3D projections of masked calcein-AM and Hoechst 33342 channels. Voxels were measured for each masked image.

Cell spreading

Cell spreading was performed in a 24-well plate coated with 10 µg/ml FN. Cells were lifted and washed twice in serum-free DMEM and seeded at equal number (2,000/well) in serum-free DMEM. The plate was placed in a tissue-culture incubator and fixed with 4% paraformaldehyde at 15-, 30-, 45-, 60-, 120-, and 180-min time points. Immediately after the addition of fixative to wells, Parafilm was used to completely cover fixative-containing wells. This approach prevented volatility-based effects caused by paraformaldehyde on neighboring wells. At the end of the experiment, all cells were permeabilized and stained with phalloidin and Hoechst 33342 dye. Wells were individually

imaged using an Axiovert 200M microscope using a 10× objective. Using ImageJ, images were masked for the phalloidin channel, segmented, and measured for area via automated measuring.

Micropatterning

Micropatterns for shapes (crossbow, circle, triangle) and lines (10 µm wide) were generated using a previously described UV-based photopatterning method (Azioune et al., 2010). (For micropatterning of 5-µm lines, see PNIPAM micropatterning.) In brief, a photomask was designed using AutoCAD (Autodesk) software. Micropatterns used were 50 × 50 µm in size and set 100 µm apart for crossbow, circle, and equilateral triangle shapes. Photolithography was commercially performed (Photo Sciences) on chrome-plated quartz with ±0.25 µm feature tolerance. Round 30-mm glass coverslips (Bioptechs) were cleaned with 70% ethanol and compressed air and plasma cleaned using a PDC-32G Harrick Plasma cleaner for 5 min. Cleaned coverslips were incubated overnight with 0.1 mg/ml poly-L-lysine–grafted polyethylene glycol (Surface Solutions Switzerland) in 15 mM Hepes, pH 7.5, by placing a 150-µl droplet of solution between a coverslip and Parafilm. Coverslips were then washed with deionized water and air dried. Before micropatterning, the photomask was cleaned using 70% ethanol and lint-free wipes (Texwipe). The photomask was placed chrome-side down from the UV source and irradiated in a UVO cleaner (Jelight) for 3 min. A 3-µl drop of deionized water was applied over micropattern region of photomask before loading the poly-L-lysine–grafted polyethylene glycol–coated surface of the coverslip on the photomask. The assembly was placed chrome-side up toward the UV source and irradiated for 3 min in the UVO cleaner. Coverslips were removed, briefly washed with PBS, and coated with 50 µg/ml FN or 250 µg/ml type-I rat tail collagen for 1 h at 37°C. FN-coated micropatterns were used immediately after preparation. Patterns were directly measured using a 40× objective on an Olympus FV1000 confocal microscope after coating with 50 µg/ml Cy5-conjugated FN.

PNIPAM micropatterning

Micropatterned poly(N-isopropylacrylamide) (PNIPAM) coverslips were used to produce 5-µm-wide lines and were produced as previously described (Mandal et al., 2012). In brief, PNIPAM brushes were grafted from glass coverslips and oxidized silicon wafers by surface-initiated atom transfer radical polymerization. *N*-isopropylacrylamide was purified by recrystallization in n-hexane. 3-Aminopropyl-triethoxysilane, triethylamine, $CuCl_2$, 1,1,7,7-pentamethyldiethylenetriamine, and 2-bromo-2-methylpropionyl bromide were used as received. All aqueous solutions were prepared in water. Glass and silicon substrates were cleaned in a 1 M sodium hydroxide aqueous solution for 15 min and rinsed with water. Samples were immersed for 1 min in an aqueous solution of 3-aminopropyl-triethoxysilane. After rinsing with water and drying in a nitrogen stream, samples were immersed for 1 min in a solution of 25 ml dichloromethane containing 1.2 ml triethylamine and 260 ml 2-bromo-2-methylpropionyl bromide, followed by rinsing with dichloromethane, ethanol, and water. This leads to surface immobilization of the atom transfer radical polymerization initiator. A solution of 1 g *N*-isopropylacrylamide, 150 ml 1,1,7,7-pentamethyldiethylenetriamine, and 20 ml water was prepared in a flask and bubbled with argon gas for 30 min before adding 25 mg CuCl. Initiator-grafted samples were immersed in this solution for a prescribed amount of time during which polymerization occurred and finally rinsed with pure water. Dry PNIPAM-bearing coverslips were placed in direct contact with a chromium quartz photomask (Toppan Photomasks). UV irradiation of the surfaces through the photomask was done in a custom-built device housing a set of four low-pressure mercury lamps (NIQ 60/35 XL longlife lamp, ~l–185 and 254 nm, quartz tube, 60 W; Heraeus Noblelight GmbH). Samples were placed at a fixed distance of 9 cm from the UV tubes and irradiated for a prescribed duration between 5 and 10 min. PNIPAM micropatterns were coated with 50 µg/ml FN for all migration work. Line widths were directly measured using a 40× objective on an Olympus FV1000 confocal microscope after coating with 50 µg/ml Cy5–conjugated FN.

Polarity analysis

Cells were plated on micropatterned coverslips and allowed to adhere for 30 min before washing out nonadhered cells. Cells were allowed to spread for up to 3 h in growth media before fixation. REF52 stable lines expressing pLL-5.5-GIX or 3XGFP-centrin were used for Golgi and centrosome detection, respectively. HUVEC cells were stained for centrosomes with an antibody to γ-tubulin. Cells were stained with phalloidin and Hoechst 33342 dyes before mounting on large 75 × 38 × 0.96–1.06 (thick)-mm glass slides (Corning). Cells were imaged using a 20× objective on an Axiovert 200M widefield microscope with the 1.6× optovar in place. Only cells that fully occupied the full area of a pattern were analyzed. Image analysis was performed by measuring the center of mass/centroid for each channel of a single multichannel image, using ImageJ. For both crossbow and triangle patterns, images were rotated to register their orientation. For crossbow patterns, the "bow" portion of the crossbow was perpendicular to the vertical axis of the image frame. For triangle patterns, a vertex was positioned parallel to the vertical axis of the image frame. The resulting x,y-coordinate values for each channel (representing cell area, centrosome or Golgi, and nucleus) were compiled and normalized to the x,y coordinates of the centroid for the cell area. Single component analysis was performed with the normalized x or y coordinates for the centrosome, Golgi, and nucleus for each pattern.

Single-cell tracking

Glass-bottomed culture dishes (Mattek) or polyacrylamide hydrogels (Matrigen) were coated with 10 µg/ml FN (unless stated otherwise) at 37°C for 1 h. Cells were plated and allowed to spread for 3 h. Cells were imaged at 37°C with 5% CO_2 with a 20× objective under 0.5× magnification on an Olympus VivaView FL microscope or under 20× magnification on a Nikon Biostation IM microscope. For cytoplast work, nuclei were stained with the Vybrant DyeCycle Green nuclear stain at the end of experiments to avoid dye-induced toxicity. Single cell tracking was manually performed in ImageJ using the "Manual Tracking" plugin. Cells were tracked based on the approximate centroid location over time. Only single cells were tracked. Cells were no longer tracked after a collision event (with another cell or debris), migration out of the field of view, division, or death. Cells were not retracked if tracking was concluded for any of these reasons. Thus, cell tracks represent individual cells. To obtain velocity and persistence values, raw tracking data were analyzed with the "Chemotaxis Tool" plugin (Ibidi) in ImageJ.

Directional migration assays

Directional migration assays were performed as previously described (Wu et al., 2012). In brief, polydimethylsiloxane (PDMS; Sylgard 184; Dow Corning) microfluidic molds were cast from a custom silicon wafer. The microfluidic device was used to establish a gradient across a defined central chamber that was amenable to both cell migration and live-cell monitoring. For most experiments, intact cells and cytoplasts were plated together. Cells were allowed to spread for 2–3 h prior in the PDMS molds, and experiments were performed for 8–16 h under humidified 5% CO_2 at 37°C. Image acquisition was performed with MetaMorph imaging software (Molecular Devices), with images being acquired every 10 min from multiple stage positions. For chemotaxis, 10 µg/ml FN was used to coat the central chamber. A stable gradient

of PDGF in serum-free DMEM containing 10 µg/ml TRITC-dextran was continuously flowed across this chamber. The PDGF gradient was indirectly imaged based on TRITC-dextran signal. This signal was measured for slope before experiment. Cells were imaged with a 20× objective on an Olympus IX81 microscope. For experiments where intact cells and cytoplasts were coplated, cells were distinguished based on the presence of the nucleus, as determined by differential interference contrast illumination. For haptotaxis, a surface-bound gradient of Cy5-conjugated FN was generated across the central chamber of the PDMS microfluidic mold. The source FN concentration was 400–500 µg/ml. Cells were imaged with a 20× objective under 0.5× magnification on an Olympus VivaView FL microscope at 37°C with 5% CO_2. For experiments where intact cells and cytoplasts were coplated, cells were distinguished based on the presence of the nucleus, as determined by staining at the end of the experiment with Vybrant DyeCycle Green nuclear stain. For all direct migration, single-cell tracking was manually performed in ImageJ using the Manual Tracking plugin. To obtain FMI, persistence, and velocity values, raw tracking data were analyzed with the "Chemotaxis Tool" plugin (Ibidi) in ImageJ. Rose plots were generated using the "secplot" script for MATLAB (http://www.mathworks.com/matlabcentral/fileexchange/14174-secplot).

Scratch assay

Glass-bottomed culture dishes (Mattek) were coated with 10 µg/ml FN for 1 h at 37°C. Cells were densely plated for 2–3 h to establish monolayers. Monolayers were rinsed to remove nonadhered and piled-up cells. For mitomycin C pretreatment, adhered cells were pretreated with 5 µg/ml mitomycin C for 2 h before enucleation. Mitomycin C–treated cells were then plated for 2–3 h before generating a scratch. For experiments with REF52 cells, scratches were made using a P200 pipet tip at a ∼45° angle, resulting in a ∼200-µm-wide scratch. For HUV ECs, scratches were made using a gel loading pipet tip at a ∼45° angle, resulting in a ∼100-µm-wide scratch. Cells were imaged every 10 min for 16 h with a 20× objective under 0.5× magnification on an Olympus VivaView FL microscope. Nuclei were stained with the Vybrant DyeCycle Green nuclear stain at the end of all experiments. Nuclear density was measured for both intact cells and cytoplasts at the end of experiments via sampling three random regions per nuclear image with a 100 µm × 100 µm–square region. These values were then averaged and reported per scratch assay run. Scratch closure was measured for each hour over a 16-h experiment by manually outlining the open cleft area using ImageJ. Scratch closure rates were measured from three or four fields of view per dish. Closure rates were quantified relative to the starting area of the cleft (from $t = 0$). All data were collected from at least three independent experiments.

Collagen matrices

Collagen matrices were formed as described previously (Rommerswinkel et al., 2014). In brief, 50 µl of 10× MEM (Gibco) and 27 µl of 7.5% sodium bicarbonate (Thermo Fisher) were added to 375 µl of 3.3 mg/ml rat tail type-I collagen (Advanced BioMatrix). From this mixture, 115 µl was added to 50 µl of DMEM-10% FBS containing 10^4 cells. The resulting collagen concentration is 1.9 mg/ml. Next, 150 µl of the combined collagen-cell mixture was loaded onto the glass portion of a glass-bottom culture dish (Mattek) and allowed to gel at either 21°C or 37°C for LR or HR matrices, respectively. For 2D migration studies, 50 µl collagen-cell mixture was loaded onto the glass portion of the dish to enable feasible working distance for microscopy. For 21°C gelling, dishes were inverted for the first 10–15 min to avoid cell sedimentation before placing right-side up until complete gelling occurred. Dishes were gently flooded with culture medium after 30 min for 37°C gels and 1 h for 21°C gels, and left to equilibrate for 2–3 h. Cells were imaged every 10 min with a 20× objective under 0.5× magnification on an Olympus VivaView FL microscope. Nuclei were stained with the Vybrant DyeCycle Green nuclear stain at the end of experiments.

Gelatin degradation

Matrix metalloproteinase activity was indirectly assessed via the invadopodia assay, essentially as described elsewhere (Chan et al., 2014). In brief, acid-washed coverslips were coated with 100 µg/ml poly-L-lysine in PBS for 20 min, washed in PBS, incubated with 0.5% glutaraldehyde for 15 min, and then washed in PBS. Coverslips were incubated in a 2 mg/ml final concentration of a 4:1 mixture of porcine gelatin/FITC-conjugated porcine gelatin (Thermo Fisher Scientific) for 1 h at 37°C. Coverslips were quenched with 1% fatty-acid–free BSA for 30 min at 37°C. Cells were incubated on gelatin-coated coverslips for 24 h. As a control, matrix metalloproteinase was inhibited by incubating cells in 10 µM GM6001 over the 24-h incubation. Gelatin degradation was quantified from images acquired using an Axiovert 200M microscope with a 40× objective. Images were analyzed using ImageJ.

Collagen contractility assay

Collagen gels were generated by adding 500 µl of 10× MEM (Gibco), 200 µl culture medium, and 270 µl of 7.5% sodium bicarbonate (Thermo Fisher Scientific) to 3.75 ml of 3.3 mg/ml rat tail type-I collagen (Advanced BioMatrix). From this mixture, 765 µl was added to 1.235 ml culture medium containing 10^6 cells. In a 24-well plate, 400 µl of this mix was added to each well and allowed to gel at 37°C with periodic shaking every 15 min to prevent cell sedimentation. After 1 h, medium was gently added to each well. A P20 pipet tip was used to separate the gel from the well. Samples were placed in an incubator for 24 h before plates were imaged using a desktop scanner (Canon), and images were analyzed using ImageJ. Percent contraction was calculated for each well by measuring the area of the collagen gel and normalizing this value to the area of collagen gels containing no cells. Data were derived from two independent experiments containing technical triplicates.

Biaxial cyclic strain assay

The biaxial strain was performed essentially as described elsewhere (Uzer et al., 2015). In brief, REF52 intact cells and cytoplasts were plated at a density of 30,000 cell/cm^2 per well in six-well BioFlex collagen-I coated plates (BF-3001C; Flexcell). After plating for either 3 or 18 h, cells were subjected to dynamic uniform biaxial cyclic strain at 5% magnitude at 10 cpm for 20 min using the Flexcell FX 5000 under conditions of 37°C and 5% CO_2. Control plates were handled the same but without strain application. Immediately after strain, whole-cell lysates were prepared and probed for phospho-FAK, total FAK, and GAP DH via Western blot analysis. Blots were analyzed using ImageJ. Data were derived from three independent experiments.

Traction-force microscopy

Traction-force work was performed on 8-kPa hydrogels containing 1-µm-diameter fluorescent (580/605–nm) beads (Matrigen). Hydrogels were coated with 20 µg/ml FN before seeding with cells in normal tissue culture conditions. Cells were allowed to spread overnight, and were imaged under 40× magnification using an Olympus VivaView FL microscope. CellTracker Green was added to spread cells (1:5,000), and individual, single cells were randomly selected for imaging. Imaged cells were not in close proximity to other cells so as to eliminate neighbor effects. Cells were imaged using DIC and CellTracker Green fluorescence. Beads were imaged under TRITC excitation/emission wavelengths. Traction force calculations were performed as described previously (Mandal et al., 2014). The contractile energy strictly defines

the total energy Ec transferred from the cell to the elastic distortion of the substrate and is given by

$$Ec = \frac{1}{2}\int \vec{T}(\vec{r}).\vec{u}(\vec{r})dxdy,$$

where T(r) is the traction stress applied by the cell and u(r) is the displacement of a point on the elastic substrate. A Fourier transform traction cytometry algorithm with zero-order regularization was used to calculate cellular traction forces from the measured substrate displacements. Substrate displacements were determined from the images of fluorescent beads embedded inside the gel, first in the presence and then in the absence of adherent cells. To release adhered cells, 1% Triton X-100 prewarmed to 37°C was added to dishes to 0.5% Triton X-100 final volume. After correction for experimental drift, the displacement field was determined in two steps: (1) particle image velocimetry on subimages followed by (2) tracking of individual beads. The final displacement field was obtained by linear interpolation on a regular grid with 0.84-µm spacing. Force reconstruction was conducted under the assumption that the substrate was a linear elastic half-space. All traction force data were derived from at least three independent experiments.

Statistical analysis

All statistical analyses were performed using Prism (GraphPad Software). A linear-regression fit was performed for plot showing cytoplast migration velocity over a 24-h period. Single-phase decay, nonlinear regression analyses were performed for all other line-fit plots. Error bars on bar graphs represent the SEM. Error bars on graphs reporting cell spreading rates, organelle polarity, forward migration indices, scratch assay closure rates, and migration velocity-rigidity rates represent the 95% confidence intervals (CIs). Error bars on boxplots represent the 10th–90th percentiles for data showing 1D line widths and for data showing contractile energy values. An outlier test using the robust regression and outlier removal method with the false discovery rate value (Q) at 1% was performed for data reporting cell diameters and cell velocity. With the exception of the traction force data, statistical significance was measured for all data with the assumption that populations fit a Gaussian distribution. Gaussian-based tests performed were the two-tailed Student's *t* test and the one-way ANOVA with Tukey's post-hoc test. Nonparametric tests performed were the Mann–Whitney *U* test and the Kruskal–Wallis test with Dunn's multiple comparisons. One-way ANOVA with Newman–Keuls post-hoc test was performed for biaxial strain experiments.

Online supplemental material

Fig. S1 shows information relevant to cytoplast generation and characterization and is supplemental to Fig. 1. Fig. S2 shows information relevant to cytoplast generation and characterization and is supplemental to Fig. 1. Fig. S3 shows information relevant to the cell polarity analyses on micropatterns and migration data on FN-coated surfaces and is supplemental to Figs. 2 and 3. Fig. S4 shows information relevant to cytoplast migration in the scratch assay, cytoplast responses on collagen surfaces, and 1D migration data and is supplemental to Figs. 4 and 5. Fig. S5 shows information relevant to the mechanoresponse of intact cells and cytoplasts, as well as cells bearing LINC complex disruption and lamin A/C loss, and is supplemental to Figs. 6 and 7. Video 1 shows random migration of a REF52 intact cell and cytoplast and is related to Fig. 3 A. Video 2 shows random migration of a HUVEC intact cell and cytoplast and is related to Fig. S3 F. Video 3 shows collective migration of REF52 intact cells and cytoplasts in a scratch assay and is related to Fig. 4 D. Video 4 shows collective migration of HUVEC intact cells and cytoplasts in a scratch assay and is related to Fig. 4 H. Video 5 shows 3D migration of REF52 intact cell and cytoplasts in LR collagen and is related to Fig. 5 C. Video 6 shows 3D migration of HUVEC intact cells and a cytoplast in LR collagen and is related to Fig. 5 F. Video 7 shows a REF52 cytoplast engaging and displacing collagen fibers and is related to Figs. 5 C and S4 F. Video 8 shows 1D migration of REF52 intact cells and a cytoplast and is related to Figs. 5 G and S4 I.

Acknowledgments

We thank David Scott for critical discussions, Kellie Beicker and Timothy O'Brien for exploratory efforts, Irina Lebedeva for technical assistance, and members of the Burridge and Bear laboratories for support. We thank Jan Lammerding's laboratory for providing the lamin cell lines. We apologize to all authors whose work could not be cited due to space constraints.

This work was supported by National Institutes of Health grants GM029860 (K. Burridge), GM103723 (K. Burridge), GM111557 (J.E. Bear), AR066616 (J. Rubin), and GM109095 (G. Uzer) and National Science Foundation grant 1454257 (B. Hoffman).

The authors declare no competing financial interests.

Author contributions: D.M. Graham designed and performed most experiments, analyzed data, and prepared the manuscript. T. Andersen and M. Balland analyzed traction-force microscopy images and generated 5-µm-wide 1D lines via the PNIPAM micropatterning technique. L. Sharek provided technical assistance. G. Uzer and J. Rubin performed biaxial strain experiments. K. Rothenberg and B.D. Hoffman provided expertise with the micropatterning technique. J.E. Bear and K. Burridge guided overall experimental design and manuscript preparation and provided funding.

Submitted: 15 June 2017
Revised: 16 November 2017
Accepted: 14 December 2017

References

Alam, S.G., D. Lovett, D.I. Kim, K.J. Roux, R.B. Dickinson, and T.P. Lele. 2015. The nucleus is an intracellular propagator of tensile forces in NIH 3T3 fibroblasts. *J. Cell Sci.* 128:1901–1911. https://doi.org/10.1242/jcs.161703

Arsenovic, P.T., I. Ramachandran, K. Bathula, R. Zhu, J.D. Narang, N.A. Noll, C.A. Lemmon, G.G. Gundersen, and D.E. Conway. 2016. Nesprin-2G, a Component of the Nuclear LINC Complex, Is Subject to Myosin-Dependent Tension. *Biophys. J.* 110:34–43. https://doi.org/10.1016/j.bpj.2015.11.014

Azioune, A., N. Carpi, Q. Tseng, M. Théry, and M. Piel. 2010. Protein micropatterns: A direct printing protocol using deep UVs. *Methods Cell Biol.* 97:133–146. https://doi.org/10.1016/S0091-679X(10)97008-8

Bangasser, B.L., G.A. Shamsan, C.E. Chan, K.N. Opoku, E. Tüzel, B.W. Schlichtmann, J.A. Kasim, B.J. Fuller, B.R. McCullough, S.S. Rosenfeld, and D.J. Odde. 2017. Shifting the optimal stiffness for cell migration. *Nat. Commun.* 8:15313. https://doi.org/10.1038/ncomms15313

Bastounis, E., R. Meili, B. Álvarez-González, J. Francois, J.C. del Álamo, R.A. Firtel, and J.C. Lasheras. 2014. Both contractile axial and lateral traction force dynamics drive amoeboid cell motility. *J. Cell Biol.* 204:1045–1061. https://doi.org/10.1083/jcb.201307106

Borrego-Pinto, J., T. Jegou, D.S. Osorio, F. Auradé, M. Gorjánácz, B. Koch, I.W. Mattaj, and E.R. Gomes. 2012. Samp1 is a component of TAN lines and is required for nuclear movement. *J. Cell Sci.* 125:1099–1105. https://doi.org/10.1242/jcs.087049

Broers, J.L.V., E.A. Peeters, H.J. Kuijpers, J. Endert, C.V. Bouten, C.W. Oomens, F.P. Baaijens, and F.C. Ramaekers. 2004. Decreased mechanical stiffness in LMNA-/- cells is caused by defective nucleo-cytoskeletal integrity: implications for the development of laminopathies. *Hum. Mol. Genet.* 13:2567–2580. https://doi.org/10.1093/hmg/ddh295

Case, L.B., and C.M. Waterman. 2015. Integration of actin dynamics and cell adhesion by a three-dimensional, mechanosensitive molecular clutch. *Nat. Cell Biol.* 17:955–963.

Chambers, R., and H.B. Fell. 1931. Micro-Operations on Cells in Tissue Cultures. *Proc. R. Soc. Lond., B.* 109:380–403. https://doi.org/10.1098/rspb.1931.0090

Chan, C.E., and D.J. Odde. 2008. Traction dynamics of filopodia on compliant substrates. *Science.* 322:1687–1691.

Chan, K.T., S.B. Asokan, S.J. King, T. Bo, E.S. Dubose, W. Liu, M.E. Berginski, J.M. Simon, I.J. Davis, S.M. Gomez, et al. 2014. LKB1 loss in melanoma disrupts directional migration toward extracellular matrix cues. *J. Cell Biol.* 207:299–315. https://doi.org/10.1083/jcb.201404067

Chancellor, T.J., J. Lee, C.K. Thodeti, and T. Lele. 2010. Actomyosin tension exerted on the nucleus through nesprin-1 connections influences endothelial cell adhesion, migration, and cyclic strain-induced reorientation. *Biophys. J.* 99:115–123. https://doi.org/10.1016/j.bpj.2010.04.011

Crisp, M., Q. Liu, K. Roux, J.B. Rattner, C. Shanahan, B. Burke, P.D. Stahl, and D. Hodzic. 2006. Coupling of the nucleus and cytoplasm: role of the LINC complex. *J. Cell Biol.* 172:41–53. https://doi.org/10.1083/jcb.200509124

Denais, C.M., R.M. Gilbert, P. Isermann, A.L. McGregor, M. te Lindert, B. Weigelin, P.M. Davidson, P. Friedl, K. Wolf, and J. Lammerding. 2016. Nuclear envelope rupture and repair during cancer cell migration. *Science.* 352:353–358.

Doyle, A.D., F.W. Wang, K. Matsumoto, and K.M. Yamada. 2009. One-dimensional topography underlies three-dimensional fibrillar cell migration. *J. Cell Biol.* 184:481–490. https://doi.org/10.1083/jcb.200810041

Doyle, A.D., N. Carvajal, A. Jin, K. Matsumoto, and K.M. Yamada. 2015. Local 3D matrix microenvironment regulates cell migration through spatiotemporal dynamics of contractility-dependent adhesions. *Nat. Commun.* 6:8720. https://doi.org/10.1038/ncomms9720

DuFort, C.C., M.J. Paszek, and V.M. Weaver. 2011. Balancing forces: architectural control of mechanotransduction. *Nat. Rev. Mol. Cell Biol.* 12:308–319. https://doi.org/10.1038/nrm3112

Elosegui-Artola, A., R. Oria, Y. Chen, A. Kosmalska, C. Pérez-González, N. Castro, C. Zhu, X. Trepat, and P. Roca-Cusachs. 2016. Mechanical regulation of a molecular clutch defines force transmission and transduction in response to matrix rigidity. *Nat. Cell Biol.* 18:540–548. https://doi.org/10.1038/ncb3336

Elosegui-Artola, A., I. Andreu, A.E.M. Beedle, A. Lezamiz, M. Uroz, A.J. Kosmalska, R. Oria, J.Z. Kechagia, P. Rico-Lastres, A.L. Le Roux, et al. 2017. Force triggers YAP nuclear entry by regulating transport across nuclear pores. *Cell.* 171:1397–1410.e14. https://doi.org/10.1016/j.cell.2017.10.008

Engvall, E., and E. Ruoslahti. 1977. Binding of soluble form of fibroblast surface protein, fibronectin, to collagen. *Int. J. Cancer.* 20:1–5. https://doi.org/10.1002/ijc.2910200102

Euteneuer, U., and M. Schliwa. 1984. Persistent, directional motility of cells and cytoplasmic fragments in the absence of microtubules. *Nature.* 310:58–61. https://doi.org/10.1038/310058a0

Euteneuer, U., and M. Schliwa. 1992. Mechanism of centrosome positioning during the wound response in BSC-1 cells. *J. Cell Biol.* 116:1157–1166. https://doi.org/10.1083/jcb.116.5.1157

Folker, E.S., C. Östlund, G.W.G. Luxton, H.J. Worman, and G.G. Gundersen. 2011. Lamin A variants that cause striated muscle disease are defective in anchoring transmembrane actin-associated nuclear lines for nuclear movement. *Proc. Natl. Acad. Sci. USA.* 108:131–136.

Fridolfsson, H.N., and D.A. Starr. 2010. Kinesin-1 and dynein at the nuclear envelope mediate the bidirectional migrations of nuclei. *J. Cell Biol.* 191:115–128. https://doi.org/10.1083/jcb.201004118

Goldman, R.D., R. Pollack, and N.H. Hopkins. 1973. Preservation of normal behavior by enucleated cells in culture. *Proc. Natl. Acad. Sci. USA.* 70:750–754. https://doi.org/10.1073/pnas.70.3.750

Goldstein, L., R. Cailleau, and T.T. Crocker. 1960. Nuclear-cytoplasmic relationship in human cells in tissue culture. *Exp. Cell Res.* 19:332–342. https://doi.org/10.1016/0014-4827(60)90012-4

Gomes, E.R., S. Jani, and G.G. Gundersen. 2005. Nuclear movement regulated by Cdc42, MRCK, myosin, and actin flow establishes MTOC polarization in migrating cells. *Cell.* 121:451–463. https://doi.org/10.1016/j.cell.2005.02.022

Graham, DM; Burridge. 2016. Mechanotransduction and nuclear function. *Current Opinion in Cell Biology.* 40:98–105. https://doi.org/10.1016/j.ceb.2016.03.006

Guilluy, C., L.D. Osborne, L. Van Landeghem, L. Sharek, R. Superfine, R. Garcia-Mata, and K. Burridge. 2014. Isolated nuclei adapt to force and reveal a mechanotransduction pathway in the nucleus. *Nat. Cell Biol.* 16:376–381. https://doi.org/10.1038/ncb2927

Gundersen, G.G., and H.J. Worman. 2013. Nuclear positioning. *Cell.* 152:1376–1389. https://doi.org/10.1016/j.cell.2013.02.031

Gupton, S.L., and C.M. Waterman-Storer. 2006. Spatiotemporal feedback between actomyosin and focal-adhesion systems optimizes rapid cell migration. *Cell.* 125:1361–1374. https://doi.org/10.1016/j.cell.2006.05.029

Hale, C.M., A.L. Shrestha, S.B. Khatau, P.J. Stewart-Hutchinson, L. Hernandez, C.L. Stewart, D. Hodzic, and D. Wirtz. 2008. Dysfunctional connections between the nucleus and the actin and microtubule networks in laminopathic models. *Biophys. J.* 95:5462–5475. https://doi.org/10.1529/biophysj.108.139428

Hale, C.M., W.-C. Chen, S.B. Khatau, B.R. Daniels, J.S.H. Lee, and D. Wirtz. 2011. SMRT analysis of MTOC and nuclear positioning reveals the role of EB1 and LIC1 in single-cell polarization. *J. Cell Sci.* 124:4267–4285. https://doi.org/10.1242/jcs.091231

Haque, F., D.J. Lloyd, D.T. Smallwood, C.L. Dent, C.M. Shanahan, A.M. Fry, R.C. Trembath, and S. Shackleton. 2006. SUN1 interacts with nuclear lamin A and cytoplasmic nesprins to provide a physical connection between the nuclear lamina and the cytoskeleton. *Mol. Cell. Biol.* 26:3738–3751. https://doi.org/10.1128/MCB.26.10.3738-3751.2006

Harada, T., J. Swift, J. Irianto, J.W. Shin, K.R. Spinler, A. Athirasala, R. Diegmiller, P.C.D.P. Dingal, I.L. Ivanovska, and D.E. Discher. 2014. Nuclear lamin stiffness is a barrier to 3D migration, but softness can limit survival. *J. Cell Biol.* 204:669–682. https://doi.org/10.1083/jcb.201308029

Ho, C.Y., D.E. Jaalouk, M.K. Vartiainen, and J. Lammerding. 2013. Lamin A/C and emerin regulate MKL1-SRF activity by modulating actin dynamics. *Nature.* 497:507–511. https://doi.org/10.1038/nature12105

Jaalouk, D.E., and J. Lammerding. 2009. Mechanotransduction gone awry. *Nat. Rev. Mol. Cell Biol.* 10:63–73. https://doi.org/10.1038/nrm2597

Janmey, P.A., J.P. Winer, M.E. Murray, and Q. Wen. 2009. The hard life of soft cells. *Cell Motil. Cytoskeleton.* 66:597–605. https://doi.org/10.1002/cm.20382

Jurado, C., J.R. Haserick, and J. Lee. 2005. Slipping or gripping? Fluorescent speckle microscopy in fish keratocytes reveals two different mechanisms for generating a retrograde flow of actin. *Mol. Biol. Cell.* 16:507–518. https://doi.org/10.1091/mbc.E04-10-0860

Khatau, S.B., C.M. Hale, P.J. Stewart-Hutchinson, M.S. Patel, C.L. Stewart, P.C. Searson, D. Hodzic, and D. Wirtz. 2009. A perinuclear actin cap regulates nuclear shape. *Proc. Natl. Acad. Sci. USA.* 106:19017–19022. https://doi.org/10.1073/pnas.0908686106

Kim, D.-H., S.B. Khatau, Y. Feng, S. Walcott, S.X. Sun, G.D. Longmore, and D. Wirtz. 2012. Actin cap associated focal adhesions and their distinct role in cellular mechanosensing. *Sci. Rep.* 2:555. https://doi.org/10.1038/srep00555

Lammerding, J., L.G. Fong, J.Y. Ji, K. Reue, C.L. Stewart, S.G. Young, and R.T. Lee. 2006. Lamins A and C but not lamin B1 regulate nuclear mechanics. *J. Biol. Chem.* 281:25768–25780. https://doi.org/10.1074/jbc.M513511200

Lang, N.R., K. Skodzek, S. Hurst, A. Mainka, J. Steinwachs, J. Schneider, K.E. Aifantis, and B. Fabry. 2015. Biphasic response of cell invasion to matrix stiffness in three-dimensional biopolymer networks. *Acta Biomater.* 13:61–67. https://doi.org/10.1016/j.actbio.2014.11.003

Lauffenburger, D.A., and A.F. Horwitz. 1996. Cell migration: a physically integrated molecular process. *Cell.* 84:359–369. https://doi.org/10.1016/S0092-8674(00)81280-5

Lee, J.S.H., C.M. Hale, P. Panorchan, S.B. Khatau, J.P. George, Y. Tseng, C.L. Stewart, D. Hodzic, and D. Wirtz. 2007. Nuclear lamin A/C deficiency induces defects in cell mechanics, polarization, and migration. *Biophys. J.* 93:2542–2552. https://doi.org/10.1529/biophysj.106.102426

Li, W., A. Duzgun, B.E. Sumpio, and M.D. Basson. 2001. Integrin and FAK-mediated MAPK activation is required for cyclic strain mitogenic effects in Caco-2 cells. *Am. J. Physiol. Gastrointest. Liver Physiol.* 280:G75–G87.

Lombardi, M.L., D.E. Jaalouk, C.M. Shanahan, B. Burke, K.J. Roux, and J. Lammerding. 2011. The interaction between nesprins and sun proteins at the nuclear envelope is critical for force transmission between the nucleus and cytoskeleton. *J. Biol. Chem.* 286:26743–26753. https://doi.org/10.1074/jbc.M111.233700

Luxton, G.W., and G.G. Gundersen. 2011. Orientation and function of the nuclear-centrosomal axis during cell migration. *Curr. Opin. Cell Biol.* 23:579–588. https://doi.org/10.1016/j.ceb.2011.08.001

Luxton, G.W.G., E.R. Gomes, E.S. Folker, E. Vintinner, and G.G. Gundersen. 2010. Linear arrays of nuclear envelope proteins harness retrograde actin flow for nuclear movement. *Science.* 329:956–959.

Mandal, K., M. Balland, and L. Bureau. 2012. Thermoresponsive micropatterned substrates for single cell studies. *PLoS One.* 7:e37548. https://doi.org/10.1371/journal.pone.0037548

Mandal, K., I. Wang, E. Vitiello, L.A.C. Orellana, and M. Balland. 2014. Cell dipole behaviour revealed by ECM sub-cellular geometry. *Nat. Commun.* 5:5749. https://doi.org/10.1038/ncomms6749

Mason, B.N., A. Starchenko, R.M. Williams, L.J. Bonassar, and C.A. Reinhart-King. 2013. Tuning three-dimensional collagen matrix stiffness independently of collagen concentration modulates endothelial cell behavior. *Acta Biomater.* 9:4635–4644. https://doi.org/10.1016/j.actbio.2012.08.007

Meili, R., B. Alonso-Latorre, J.C. del Alamo, R.A. Firtel, and J.C. Lasheras. 2010. Myosin II is essential for the spatiotemporal organization of traction forces during cell motility. *Mol. Biol. Cell.* 21:405–417. https://doi.org/10.1091/mbc.E09-08-0703

Metzger, T., V. Gache, M. Xu, B. Cadot, E.S. Folker, B.E. Richardson, E.R. Gomes, and M.K. Baylies. 2012. MAP and kinesin-dependent nuclear positioning is required for skeletal muscle function. *Nature.* 484:120–124. https://doi.org/10.1038/nature10914

Nery, F.C., J. Zeng, B.P. Niland, J. Hewett, J. Farley, D. Irimia, Y. Li, G. Wiche, A. Sonnenberg, and X.O. Breakefield. 2008. TorsinA binds the KASH domain of nesprins and participates in linkage between nuclear envelope and cytoskeleton. *J. Cell Sci.* 121:3476–3486. https://doi.org/10.1242/jcs.029454

Padmakumar, V.C., T. Libotte, W. Lu, H. Zaim, S. Abraham, A.A. Noegel, J. Gotzmann, R. Foisner, and I. Karakesisoglou. 2005. The inner nuclear membrane protein Sun1 mediates the anchorage of Nesprin-2 to the nuclear envelope. *J. Cell Sci.* 118:3419–3430. https://doi.org/10.1242/jcs.02471

Pathak, A., and S. Kumar. 2012. Independent regulation of tumor cell migration by matrix stiffness and confinement. *Proc. Natl. Acad. Sci. USA.* 109:10334–10339. https://doi.org/10.1073/pnas.1118073109

Pelham, R.J. Jr., and Yl. Wang. 1997. Cell locomotion and focal adhesions are regulated by substrate flexibility. *Proc. Natl. Acad. Sci. USA.* 94:13661–13665. https://doi.org/10.1073/pnas.94.25.13661

Petrie, R.J., H. Koo, and K.M. Yamada. 2014. Generation of compartmentalized pressure by a nuclear piston governs cell motility in a 3D matrix. *Science.* 345:1062–1065.

Petrie, R.J., H.M. Harlin, L.I.T. Korsak, and K.M. Yamada. 2017. Activating the nuclear piston mechanism of 3D migration in tumor cells. *J. Cell Biol.* 216:93–100.

Peyton, S.R., and A.J. Putnam. 2005. Extracellular matrix rigidity governs smooth muscle cell motility in a biphasic fashion. *J. Cell. Physiol.* 204:198–209. https://doi.org/10.1002/jcp.20274

Piel, M., P. Meyer, A. Khodjakov, C.L. Rieder, and M. Bornens. 2000. The respective contributions of the mother and daughter centrioles to centrosome activity and behavior in vertebrate cells. *J. Cell Biol.* 149:317–330. https://doi.org/10.1083/jcb.149.2.317

Plotnikov, S.V., A.M. Pasapera, B. Sabass, and C.M. Waterman. 2012. Force fluctuations within focal adhesions mediate ECM-rigidity sensing to guide directed cell migration. *Cell.* 151:1513–1527. https://doi.org/10.1016/j.cell.2012.11.034

Raab, M., J. Swift, P.C.D.P. Dingal, P. Shah, J.-W. Shin, and D.E. Discher. 2012. Crawling from soft to stiff matrix polarizes the cytoskeleton and phosphoregulates myosin-II heavy chain. *J. Cell Biol.* 199:669–683. https://doi.org/10.1083/jcb.201205056

Raab, M., M. Gentili, H. de Belly, H.R. Thiam, P. Vargas, A.J. Jimenez, F. Lautenschlaeger, R. Voituriez, A.M. Lennon-Duménil, N. Manel, and M. Piel. 2016. ESCRT III repairs nuclear envelope ruptures during cell migration to limit DNA damage and cell death. *Science.* 352:359–362.

Ridley, A.J., M.A. Schwartz, K. Burridge, R.A. Firtel, M.H. Ginsberg, G. Borisy, J.T. Parsons, and A.R. Horwitz. 2003. Cell migration: integrating signals from front to back. *Science.* 302:1704–1709. https://doi.org/10.1126/science.1092053

Rommerswinkel, N., B. Niggemann, S. Keil, K.S. Zänker, and T. Dittmar. 2014. Analysis of cell migration within a three-dimensional collagen matrix. *J. Vis. Exp.* 92:e51963.

Roux, K.J., M.L. Crisp, Q. Liu, D. Kim, S. Kozlov, C.L. Stewart, and B. Burke. 2009. Nesprin 4 is an outer nuclear membrane protein that can induce kinesin-mediated cell polarization. *Proc. Natl. Acad. Sci. USA.* 106:2194–2199. https://doi.org/10.1073/pnas.0808602106

Shaw, G., and D. Bray. 1977. Movement and extension of isolated growth cones. *Exp. Cell Res.* 104:55–62. https://doi.org/10.1016/0014-4827(77)90068-4

Stewart, R.M., A.E. Zubek, K.A. Rosowski, S.M. Schreiner, V. Horsley, and M.C. King. 2015. Nuclear-cytoskeletal linkages facilitate cross talk between the nucleus and intercellular adhesions. *J. Cell Biol.* 209:403–418. https://doi.org/10.1083/jcb.201502024

Sunyer, R., V. Conte, J. Escribano, A. Elosegui-Artola, A. Labernadie, L. Valon, D. Navajas, J.M. García-Aznar, J.J. Muñoz, P. Roca-Cusachs, and X. Trepat. 2016. Collective cell durotaxis emerges from long-range intercellular force transmission. *Science.* 353:1157–1161.

Swift, J., I.L. Ivanovska, A. Buxboim, T. Harada, P.C.D.P. Dingal, J. Pinter, J.D. Pajerowski, K.R. Spinler, J.-W. Shin, M. Tewari, et al. 2013. Nuclear lamin-A scales with tissue stiffness and enhances matrix-directed differentiation. *Science.* 341:1240104.

Thakar, K., C.K. May, A. Rogers, and C.W. Carroll. 2017. Opposing roles for distinct LINC complexes in regulation of the small GTPase RhoA. *Mol. Biol. Cell.* 28:182–191.

Théry, M., V. Racine, M. Piel, A. Pépin, A. Dimitrov, Y. Chen, J.-B. Sibarita, and M. Bornens. 2006. Anisotropy of cell adhesive microenvironment governs cell internal organization and orientation of polarity. *Proc. Natl. Acad. Sci. USA.* 103:19771–19776. https://doi.org/10.1073/pnas.0609267103

Uetrecht, A.C., and J.E. Bear. 2009. Golgi polarity does not correlate with speed or persistence of freely migrating fibroblasts. *Eur. J. Cell Biol.* 88:711–717. https://doi.org/10.1016/j.ejcb.2009.08.001

Uzer, G., W.R. Thompson, B. Sen, Z. Xie, S.S. Yen, S. Miller, G. Bas, M. Styner, C.T. Rubin, S. Judex, et al. 2015. Cell mechanosensitivity to extremely low magnitude signals is enabled by a LINCed nucleus. *Stem Cells.* 33:2063–2076.

van Loosdregt, I.A.E.W., M.A.F. Kamps, C.W.J. Oomens, S. Loerakker, J.L.V. Broers, and C.V.C. Bouten. 2017. Lmna knockout mouse embryonic fibroblasts are less contractile than their wild-type counterparts. *Integr. Biol.* 9:709–721.

Verkhovsky, A.B., T.M. Svitkina, and G.G. Borisy. 1999. Self-polarization and directional motility of cytoplasm. *Curr. Biol.* 9:11–20.

Wang, N., J.D. Tytell, and D.E. Ingber. 2009. Mechanotransduction at a distance: mechanically coupling the extracellular matrix with the nucleus. *Nat. Rev. Mol. Cell Biol.* 10:75–82. https://doi.org/10.1038/nrm2594

Wigler, M.H., and I.B. Weinstein. 1975. A preparative method for obtaining enucleated mammalian cells. *Biochem. Biophys. Res. Commun.* 63:669–674. https://doi.org/10.1016/S0006-291X(75)80436-0

Wolf, K., M. Te Lindert, M. Krause, S. Alexander, J. Te Riet, A.L. Willis, R.M. Hoffman, C.G. Figdor, S.J. Weiss, and P. Friedl. 2013. Physical limits of cell migration: control by ECM space and nuclear deformation and tuning by proteolysis and traction force. *J. Cell Biol.* 201:1069–1084. https://doi.org/10.1083/jcb.201210152

Wu, C., S.B. Asokan, M.E. Berginski, E.M. Haynes, N.E. Sharpless, J.D. Griffith, S.M. Gomez, and J.E. Bear. 2012. Arp2/3 is critical for lamellipodia and response to extracellular matrix cues but is dispensable for chemotaxis. *Cell.* 148:973–987. https://doi.org/10.1016/j.cell.2011.12.034

Zhang, X., K. Lei, X. Yuan, X. Wu, Y. Zhuang, T. Xu, R. Xu, and M. Han. 2009. SUN1/2 and Syne/Nesprin-1/2 complexes connect centrosome to the nucleus during neurogenesis and neuronal migration in mice. *Neuron.* 64:173–187. https://doi.org/10.1016/j.neuron.2009.08.018

Appendix C – Biophysical model to predict the experimental data

Theory supplement

Dimitri Probst & Ulrich Schwarz

In the following, we will start with a mathematical description of the model, which aims at reproducing the contractile behavior of the two representative cells. In particular, we will introduce an anisotropic stress tensor to mimic the distribution of SFs on the different FN patterns and incorporate the geometry of the FN pattern into the simulation. Thereafter, we will use the time course of the cellular strain energy to constrain the continuum model. We conclude this section with the comparison of experimental and simulation results and the insights we gain from the model parameters.

1 Two-Dimensional Active Solid and Viscoelastic Models

From the experimental results presented so far, we obtain two indications which allow to find and constrain a physical model. First, we know from the analysis of time-lapse video of the actin-stained cells that the actin architecture is in a steady state and not affected by short PA pulses. Second, the strain energy response upon a single PA pulse shows a rounded off symmetric profile which, after some time span, returns back to the equilibrium energy state the cell adopted before stimulation.

The following one- or two-component rheological models come into question to fulfill the experimental requirements: a solid, a Kelvin-Voigt or a Maxwell model. A pure viscous model is excluded right from the beginning as it will not allow to abide a steady energy state, even in the absence of a PA signal.

We start with the constitutive relation of the two-dimensional active solid model

$$\sigma_{ij} - \sigma_{ij}^{\mathrm{m}} = \lambda \epsilon_{kk} \delta_{ij} + 2\mu \epsilon_{ij} \,, \tag{1}$$

with stress tensor σ_{ij}, linearized strain tensor $\epsilon_{ij} = {}^1\!/_2 \left(\partial_i u_j + \partial_j u_i\right)$ and i^{th} component of the displacement vector u_i. Further, λ and μ denote the two-dimensional Lamé coefficients defined by

$$\lambda = \frac{E_{\mathrm{c}} h_{\mathrm{c}} \nu_{\mathrm{c}}}{1 - \nu_{\mathrm{c}}^2} \,, \tag{2}$$

and

$$\mu = \frac{E_{\mathrm{c}} h_{\mathrm{c}}}{2\left(1 + \nu_{\mathrm{c}}\right)} \,. \tag{3}$$

The parameter σ^{m} denotes the anisotropic motors stress, which consists of two contributions: a constant background stress tensor, which is used to raise the cellular energy to its homeostatic level, and a PA stress tensor, describing the additional time-dependent stress during PA.

The constitutive relations of the active Kelvin-Voigt model and active Maxwell model are, respectively,

$$\sigma_{ij} - \sigma_{ij}^{\mathrm{m}} = \left(1 + \tau_{\mathrm{c}} \frac{\partial}{\partial t}\right) \cdot \left(\lambda \epsilon_{kk} \delta_{ij} + 2\mu \epsilon_{ij}\right) \,, \tag{4}$$

and

$$\frac{\sigma_{ij} - \sigma_{ij}^{\mathrm{m}}}{\tau_{\mathrm{c}}} + \left(\dot{\sigma}_{ij} - \dot{\sigma}_{ij}^{\mathrm{m}}\right) = \frac{\partial}{\partial t}\left(\lambda \epsilon_{kk} \delta_{ij} + 2\mu \epsilon_{ij}\right) , \tag{5}$$

with $\tau_{\mathrm{c}} = {}^{\eta_{\mathrm{c}}}/_{E_{\mathrm{c}}}$ and η_{c} being the material relaxation time and cell viscosity, respectively.

For all models, the force balance equation yields

$$\partial_j \sigma_{ij} = Y\left(\mathbf{x}\right) u_i \,, \tag{6}$$

with Y denoting the spring stiffness density, which can be position-dependent in general. We can calculate Y using

$$Y = \frac{E_{\mathrm{c}} h_{\mathrm{c}}}{l_{\mathrm{p}}^2 \left(1 - \nu_{\mathrm{c}}^2\right)} \,. \tag{7}$$

i with the force penetration length l_{p}, which represents the length scale along which a point force is transmitted in an elastically coupled isotropic medium.

All three models can be solved by means of a FE simulation. In each case, the weak formulation of Equation 6 is

$$\int_{\Omega} \boldsymbol{\sigma} : \left(\nabla \mathbf{v} + \nabla \mathbf{v}^{\mathbf{T}}\right) \mathrm{d}\mathbf{x} + \int_{\Omega} Y \, \mathbf{u}\mathbf{v} \, \mathrm{d}\mathbf{x} = 0 \,, \tag{8}$$

with Ω denoting the area of the viscoelastic disc and $\mathbf{v}$ a test function. We use the FE solver FEniCS to calculate the displacements of the disc (*Alnaes et al.*, 2015). For reasons of stability, we apply the Dirichlet boundary condition $\mathbf{u} = (0, 0)$ at $\mathbf{x} = (0, 0)$.

The strain energy U_{s} invested by the cell is then calculated from the substrate displacements $\mathbf{u}_{\mathrm{s}}$ and traction stresses $\mathbf{T} = Y\mathbf{u} = Y_{\mathrm{s}}\mathbf{u}_{\mathrm{s}}$ via

$$U_{\mathrm{s}} = \frac{1}{2} \int_A \mathbf{T}\mathbf{u}_{\mathrm{s}} \mathrm{d}A = \frac{1}{2} \int_A \frac{Y^2}{Y_{\mathrm{s}}} \mathbf{u}^2 \mathrm{d}A \,. \tag{9}$$

Here, Y_{s} denotes the contribution of the substrate properties to Y. We can estimate Y_{s} via (*Banerjee and Marchetti*, 2012)

$$Y_{\mathrm{s}} = \frac{\pi E_{\mathrm{s}}}{h_{\mathrm{eff}}} \,, \tag{10}$$

with h_{eff} given by

$$h_{\mathrm{eff}}^{-1} = \frac{1}{h_{\mathrm{s}} 2\pi \left(1 + \nu_{\mathrm{s}}\right)} + \frac{1}{L_{\mathrm{c}}} \tag{11}$$

With $E_{\mathrm{s}} = 4.47 \times 10^3 \, {}^{N}/_{\mathrm{m}^2}$, $h_{\mathrm{s}} = 50 \, \mu\mathrm{m}$ and $L_{\mathrm{s}} \approx 40 \, \mu\mathrm{m}$, we have approximately $Y_{\mathrm{s}} = 3.1 \times 10^8 \, {}^{N}/_{\mathrm{m}^3}$.

We can exploit the relation of the strain energy and the cell area to find a way to directly estimate l_{p} from the measurements. Assuming that the elastic disc of radius r_0 is approximately isotropically contractile, we can solve Equation 9 analytically. The radial displacement u_r for this special case yields (*Edwards and Schwarz*, 2011)

$$u_r\left(r\right) = -l_{\mathrm{p}} \frac{\sigma_0 h_{\mathrm{c}}}{\lambda + 2\mu} \cdot \frac{I_1\left(\frac{r}{l_{\mathrm{p}}}\right)}{I_0\left(\frac{r_0}{l_{\mathrm{p}}}\right) - \frac{2\mu}{\lambda + 2\mu} \frac{l_{\mathrm{p}}}{r_0} I_1\left(\frac{r_0}{l_{\mathrm{p}}}\right)} \,, \tag{12}$$

with contractile stress σ_0, disc height h_c and modified Bessel functions of first kind I_0 and I_1. The strain energy then reduces to the integral

$$\begin{aligned} U_\mathrm{s} &= \frac{Y^2}{2Y_\mathrm{s}} \int_0^{2\pi} \mathrm{d}\phi \int_0^{r_0} \mathrm{d}r r u_r^2 \\ &= \frac{\pi}{Y_\mathrm{s}} \cdot \left(\frac{Y l_\mathrm{p} \sigma_0 h_\mathrm{c} \left(1-\nu_\mathrm{c}^2\right)}{E_\mathrm{c} h_\mathrm{c}} \right)^2 \cdot \frac{\int_0^{r_0} \mathrm{d}r r I_1 \left(\frac{r}{l_\mathrm{p}}\right)^2}{\left(I_0\left(\frac{r_0}{l_\mathrm{p}}\right) - (1-\nu_\mathrm{c}) \frac{l_\mathrm{p}}{r_0} I_1\left(\frac{r_0}{l_\mathrm{p}}\right)\right)^2} = \frac{\pi \left(\sigma_0 h_\mathrm{c}\right)^2}{2Y_\mathrm{s}} \zeta\left(\frac{r_0}{l_\mathrm{p}}\right), \end{aligned} \tag{13}$$

using the definition of Y in Equation 7 and

$$\zeta(x) = x^2 \cdot \frac{I_1(x)^2 + \frac{2}{x} I_0(x) I_1(x) - I_0(x)^2}{\left(I_0(x) - (1-\nu_\mathrm{c}) \frac{1}{x} I_1(x)\right)^2}. \tag{14}$$

We can find the two asymptotic trends of the energy by investigating ζ for the two limits $x \ll 1$ and $x \gg 1$. For $x \ll 1$, the modified Bessel functions can be approximated as

$$I_n(x) \xrightarrow[x \ll 1]{} \frac{1}{n!} \left(\frac{x}{2}\right)^n, \tag{15}$$

such that

$$\zeta(x) \xrightarrow[x \ll 1]{} \frac{x^4}{2\left(1+\nu_\mathrm{c}\right)^2} + \mathcal{O}\left(x^5\right), \tag{16}$$

and

$$U_\mathrm{s} \xrightarrow[r_0 \ll l_\mathrm{p}]{} \frac{\pi \left(\sigma_0 h_\mathrm{c}\right)^2}{4Y_\mathrm{s}\left(1+\nu_\mathrm{c}\right)^2} \left(\frac{r_0}{l_\mathrm{p}}\right)^4. \tag{17}$$

For $x \gg 1$, any modified Bessel function converges to

$$I_n(x) \xrightarrow[x \gg 1]{} \frac{\exp x}{\sqrt{2\pi x}}, \tag{18}$$

such that

$$\zeta(x) \xrightarrow[x \gg 1]{} 2x + \mathcal{O}\left(x^2\right), \tag{19}$$

and

$$U_\mathrm{s} \xrightarrow[r_0 \gg l_\mathrm{p}]{} \frac{\pi \left(\sigma_0 h_\mathrm{c}\right)^2}{Y_\mathrm{s}} \cdot \frac{r_0}{l_\mathrm{p}}. \tag{20}$$

Thus, the asymptotic behavior of the strain energy for $r_0 \gg l_\mathrm{p}$ is analogous to those of the total force, of which the latter was demonstrated by *Mertz et al.* (2012). However, for $r_0 \ll l_\mathrm{p}$, the asymptotic behavior of the strain energy and the total force differ. Equation 13 will be used in the next Section 4 to estimate the parameters l_p and $\sigma_\mathrm{bck} h_\mathrm{c}$ from the relation of the cellular strain energy and its spread area.

2 Specification of the Photoactivation Stress Tensor

Both background stress tensor and the PA stress tensor depend on the shape of the FN pattern. Even in the absence of a PA, the orientation of the stress field remains unchanged, such that the

background stress tensor can be assumed to pull in the same direction as the PA stress. We can calculate the anisotropic motor stress tensor σ^{m} directed along an arbitrary angle ϕ with respect to the x-axis via rotation of a stress tensor with its only non-zero component $\sigma_{xx} = \sigma_{\mathrm{bck}} + \sigma_{\mathrm{act}}(t)$. Here, σ_{bck} belongs to the background stress and σ_{act} to the time-dependent PA stress. One has

$$\begin{aligned}\sigma^{\mathrm{m}}(\phi) &= \begin{pmatrix}\cos\phi & -\sin\phi \\ \sin\phi & \cos\phi\end{pmatrix}\begin{pmatrix}\sigma_{\mathrm{bck}}+\sigma_{\mathrm{act}} & 0 \\ 0 & 0\end{pmatrix}\begin{pmatrix}\cos\phi & \sin\phi \\ -\sin\phi & \cos\phi\end{pmatrix} \\ &= (\sigma_{\mathrm{bck}}+\sigma_{\mathrm{act}})\cdot\begin{pmatrix}\cos^2\phi & \frac{1}{2}\sin(2\phi) \\ \frac{1}{2}\sin(2\phi) & \sin^2\phi\end{pmatrix}, \end{aligned} \tag{21}$$

Comparison with the orientation of SFs in cells plated on both patterns lets us assume a motor stress tensor

$$\sigma^{\mathrm{m}}_{\mathrm{FC}} = \begin{pmatrix}0 & 0 \\ 0 & \sigma_{\mathrm{bck}}+\sigma_{\mathrm{act}}\end{pmatrix} \tag{22}$$

in the case of the full circle pattern, as illustrated in Figure 2B (top), and

$$\begin{aligned}\sigma^{\mathrm{m}}_{\Omega 1} &= (\sigma_{\mathrm{bck}}+\sigma_{\mathrm{act}})\cdot\begin{pmatrix}1 & 0 \\ 0 & 0\end{pmatrix}, \\ \sigma^{\mathrm{m}}_{\Omega 2} &= (\sigma_{\mathrm{bck}}+\sigma_{\mathrm{act}})\cdot\begin{pmatrix}\cos^2\left(\frac{2\pi}{3}\right) & \frac{1}{2}\sin\left(\frac{4\pi}{3}\right) \\ \frac{1}{2}\sin\left(\frac{4\pi}{3}\right) & \sin^2\left(\frac{2\pi}{3}\right)\end{pmatrix}, \\ \sigma^{\mathrm{m}}_{\Omega 3} &= (\sigma_{\mathrm{bck}}+\sigma_{\mathrm{act}})\cdot\begin{pmatrix}\cos^2\left(\frac{2\pi}{3}\right) & -\frac{1}{2}\sin\left(\frac{4\pi}{3}\right) \\ -\frac{1}{2}\sin\left(\frac{4\pi}{3}\right) & \sin^2\left(\frac{2\pi}{3}\right)\end{pmatrix}, \end{aligned} \tag{23}$$

for the respective regions Ω_1, Ω_2 and Ω_3 denoted in Figure 2C (top) in the case of the wheel pattern.

We consider three possible models for the time course of the PA stress component σ_{act}, which are depicted in Figure 1A from left to right. The simplest case is the rectangular profile

$$\sigma^{\mathrm{rec}}_{\mathrm{act}}(t) = \begin{cases}\sigma_0 & \text{for } t_0 \le t \le t_{\mathrm{act}} \\ 0 & \text{else}\end{cases}, \tag{24}$$

with peak activation stress σ_0, PA time point t_0 and duration t_{act}. To account for a delayed response of the activation stress, we introduce the exponential profile

$$\sigma^{\mathrm{exp}}_{\mathrm{act}}(t) = \begin{cases}\sigma_0\left(1-\exp\left(-\frac{t-t_0}{\tau_{\mathrm{act}}}\right)\right) & \text{for } t_0 \le t \le t_{\mathrm{act}} \\ \sigma_0\left(1-\exp\left(-\frac{t_{\mathrm{act}}-t_0}{\tau_{\mathrm{act}}}\right)\right)\exp\left(-\frac{t-(t_0+t_{\mathrm{act}})}{\tau_{\mathrm{rel}}}\right) & \text{else}\end{cases}, \tag{25}$$

with stress activation and relaxation times τ_{act} and τ_{rel}. The third stress profile is a double sigmoid function

$$\sigma^{\mathrm{sig}}_{\mathrm{act}}(t) = \frac{\sigma_0}{1+\exp\left(-\frac{t-t_{\mathrm{act}}}{\tau_{\mathrm{act}}}\right)}\cdot\left(1-\frac{1}{1+\exp\left(-\frac{t-t_{\mathrm{rel}}}{\tau_{\mathrm{rel}}}\right)}\right), \tag{26}$$

with the centers of the activating and relaxing sigmoid t_{act} and t_{rel}. Here, the four time time constants allow to combine a discontinuous jump at the ascending edge of the PA stress function and a flat stress plateau, as with the rectangular stress profile, with a damped activation and relaxation, as with the exponential stress profile.

3 Specification of the Shape of the Fibronectin Pattern

For the case of the full circle pattern, we represent the effect of the elastic substrate as well as the elastic contribution of the FAs via springs of constant spring stiffness density Y throughout the entire circle.

For the wheel pattern, we only introduce springs of stiffness density Y at those positions of the circle at which the cell can form connections to the substrate via its FAs, which is exactly the FN coated area. To simulate this fact, we determine the positions $(x,y)_{Y\neq 0}$, at which the stiffness density Y is non-zero, via:

$$
\begin{aligned}
(x,y)_{Y\neq 0} = \Big\{ x,y \,\Big|\, & \Big[R_{\text{in}} \leq \sqrt{x^2+y^2} \leq R \wedge \Big(\frac{\pi}{2} - \frac{\alpha_{\text{out}}}{2} \leq \operatorname{arctan2}(x,y) \leq \frac{\pi}{2} + \frac{\alpha_{\text{out}}}{2} \\
& \qquad \vee\ -\frac{\pi}{6} - \frac{\alpha_{\text{out}}}{2} \leq \operatorname{arctan2}(x,y) \leq -\frac{\pi}{6} + \frac{\alpha_{\text{out}}}{2} \\
& \qquad \vee\ -\frac{5\pi}{6} - \frac{\alpha_{\text{out}}}{2} \leq \operatorname{arctan2}(x,y) \leq -\frac{5\pi}{6} + \frac{\alpha_{\text{out}}}{2} \\
& \qquad \vee\ \pi - \alpha_{\text{overhang}} \leq \operatorname{arctan2}(x,y) \leq \pi \Big) \Big] \vee \\
& \Big[\sqrt{x^2+y^2} \leq R_{\text{in}} \wedge \Big(\Big(-\frac{w}{2} \leq x_1 \leq \frac{w}{2} \wedge y_1 \geq 0 \Big) \\
& \qquad \vee \Big(-\frac{w}{2} \leq x_2 \leq \frac{w}{2} \wedge y_2 \geq 0 \Big) \\
& \qquad \vee \Big(-\frac{w}{2} \leq x_3 \leq \frac{w}{2} \wedge y_3 \geq 0 \Big) \Big) \Big] \Big\},
\end{aligned}
$$

with arm width $w = 5\,\mu\text{m}$, inner radius $R_{\text{in}} = R - w$ and $\alpha_{\text{out}} = \pi/2$. The remaining parameters are

$$
\begin{aligned}
(x_1,y_1) &= (x,\ y) \\
(x_2,y_2) &= \left(x\cdot\cos\left(\frac{2\pi}{3}\right) - y\cdot\sin\left(\frac{2\pi}{3}\right),\ x\cdot\sin\left(\frac{2\pi}{3}\right) + y\cdot\cos\left(\frac{2\pi}{3}\right) \right) \\
(x_3,y_3) &= \left(x\cdot\cos\left(\frac{2\pi}{3}\right) + y\cdot\sin\left(\frac{2\pi}{3}\right),\ -x\cdot\sin\left(\frac{2\pi}{3}\right) + y\cdot\cos\left(\frac{2\pi}{3}\right) \right),
\end{aligned}
$$

and

$$
\alpha_{\text{overhang}} = \frac{5\pi}{6} + \frac{\alpha_{\text{out}}}{2} - \pi \text{ if } \frac{5\pi}{6} + \frac{\alpha_{\text{out}}}{2} > \pi, \text{ otherwise } 0\,. \tag{27}
$$

Equation 27 accounts for the unsteady jump of the $\operatorname{arctan2}$-function at the function values $-\pi$ and π.

4 Simulation Results

We will now start with the selection of an appropriate physical model which allows to capture the dynamics of the cellular energy. Thereafter, we will investigate the effects of the cell area, the shape of the FN pattern or the duration of the PA pulse on the cellular energy level and dynamics. To find the best model fits, we use the conjugate-gradient based parameter optimization method of *Nelder and Mead* (1965).

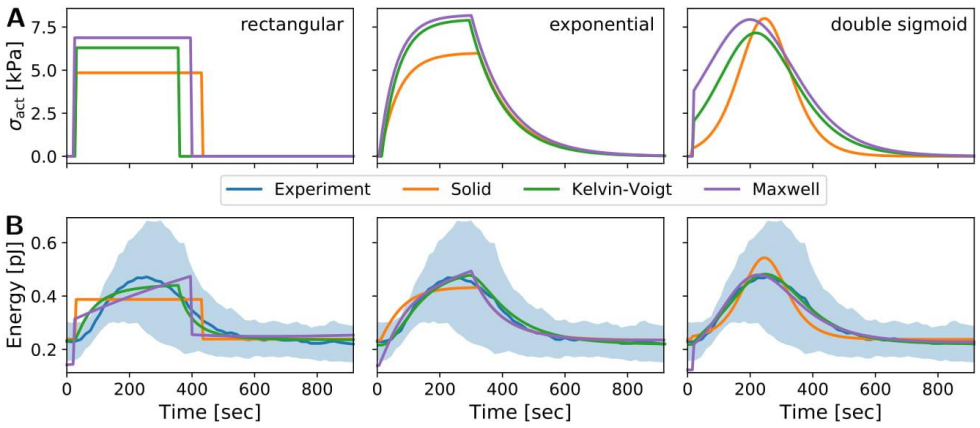

Figure 1: Photoactivation stress profile σ_{act} and the corresponding energy response for the case of a solid, Kelvin-Voigt and Maxwell model. **(A)** Photoactivation stress profiles σ_{act} used to reproduce the experimentally acquired cellular energy response: rectangular, exponential and double sigmoid profile from left to right. Different curves illustrate the optimized stress profiles for the three models. **(B)** Corresponding energy responses for the three different stress profiles and continuum models, illustrated on top of the experimental average. *Shaded regions* denote the standard deviation. A Kelvin-Voigt model with a double sigmoid stress profile fits best to the experimental curve. Corresponding parameter values are listed in Table 0.1.

Model Choice Figure 1A shows the optimized PA stress profiles introduced in Section 2 to reproduce the experimentally acquired cellular strain energy response. The corresponding average experimental energy response and the simulated energy response for the three continuum models upon a single PA pulse of $50\,\mathrm{ms}$ duration are illustrated in Figure 1B.

A rectangular PA stress profile does not provide an adequate description of the cellular dynamics as it introduces discontinuous features in the energy response which are not present in the experimental data. An exponential PA stress profile allows better fits to the experimental data, but can only establish an asymmetric energy response upon PA. The double sigmoid PA stress profile most likely resembles the predominant features of the experimental data.

For the solid model, the double sigmoid fit is inadequate since the stress profile entail a convex course almost over its full range. Due to the model dynamics, the energy profile instantaneously follows the stress profile. The experimental energy profile, however, comprises a lengthy concave course around its peak.

The Maxwell model with double sigmoid PA stress profile can closely capture the dynamics of the cellular contractile energy over the largest part of the time course. However, the ideal parameter values to reproduce the exact energy shape upon a single PA do not allow to keep a constant energy baseline after the PA pulse. This is due to the calculated material relaxation time, which yields $\tau_{\mathrm{c}}^{\mathrm{M}} = \eta_{\mathrm{c}}^{\mathrm{M}}/E_{\mathrm{c}}^{\mathrm{M}} = 147\,\mathrm{s}$ and is an order of magnitude lower than typical relaxation times deduced e.g. by *Oakes et al.* (2017). That is why, in the course of the energy response, which takes about $500\,\mathrm{s} > 3\tau_{\mathrm{c}}^{\mathrm{M}}$, a significant increase of the energy baseline is registered, which is not present in the

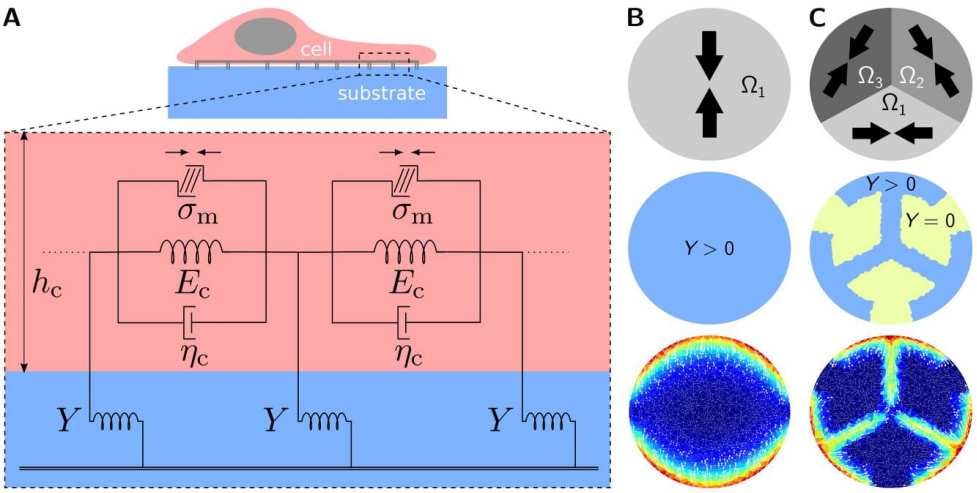

Figure 2: Effective physical representation of the cell and the elastic substrate on different fibronectin patterns and qualitative distribution of simulated traction stresses. **(A)** A Kelvin-Voigt model with active contractility and coupling to an elastic foundation is used to reconstruct the dynamic energy response of cells upon global optogenetic activation (*side view*). **(B-C)** From top to bottom: Principal directions of the stress tensor, distribution of the spring stiffness and a typical qualitative stress map during the simulated photoactivation of circle-patterned and wheel-patterned cells, respectively (*top view*).

experimental curve.

The Kelvin-Voigt model with a characteristic material relaxation time of $\tau_c^{KV} = \eta_c^{KV}/E_c^{KV} = 155\,s$ provides the best fit results. It allows to correct for the shortcomings of the other models. Its parallel arrangement of springs and dashpots makes the material retard any instantaneous signal, such that convex stress profiles appear in a low-pass filtered fashion in the energy response. Further, as a solid model it allows a fast recovery to the energy baseline after optogenetic activation as compared with the Maxwell model.

We will therefore continue with the active Kelvin-Voigt model as a mechanical representation of the cell, as depicted in Figure 2A, and use a double sigmoid PA stress profile σ_{act}^{sig}. In particular, a double sigmoid profile, as illustrated by the green curve in Figure 1A, bears closest analogy to the experimentally acquired time course of the concentration of CRY2/CIBN-dimers upon PA, which was measured by *Valon et al.* (2015): An instantaneous increase on the time scale of $2\,s$ followed by a plateau of tens of seconds duration and a dissociation time of several hundreds of seconds. In general, a double sigmoid shape of the activation function fits better to the Michaelis-Menten kinetics which is a standard model to describe the association and dissociation dynamics of molecules (*Michaelis and Menten*, 1913).

Effect of the Cell Area on its Energy Level and Dynamics To enforce a varying spread area, circular shaped FN micropatterns of area $500\,\mu m^2$, $1000\,\mu m^2$ and $1500\,\mu m^2$ were manufactured. Cells plated on the patterns usually spread until the complete pattern was covered. Only cells which

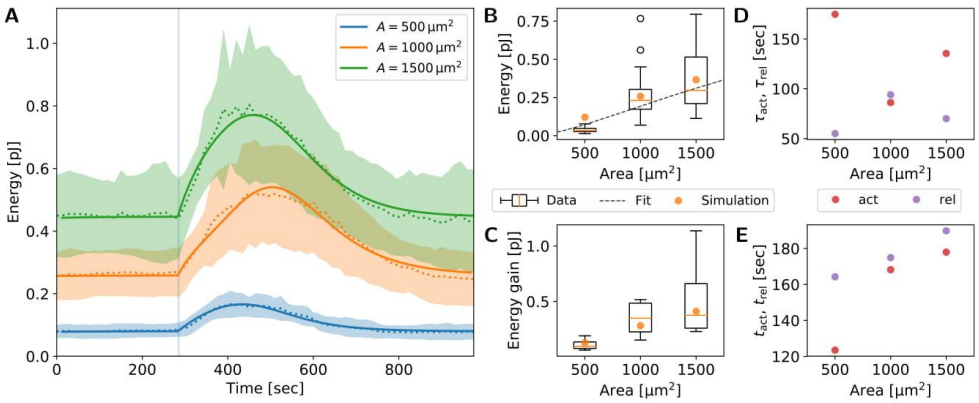

Figure 3: Effect of the cellular area on its energy level as well as its energy gain and dynamics upon photoactivation. **(A)** Time course of the strain energy. *Dotted lines* show mean values, *shaded regions* correspond to standard deviations and *full lines* show model fits. Each curve corresponds to an average of 9, 11 and $11\,\mathrm{cells}$, respectively, which are activated by a pulse of $100\,\mathrm{ms}$ duration. **(B)** Static strain energy level. With increasing spread area, the strain energy increases. *Boxes* denote the statistics of 29, 23 and $23\,\mathrm{cells}$, respectively. The *dashed* line shows the relation for an isotropically contractile disc derived in Equation 13. *Orange* dots show simulation results, with σ_{bck} kept constant for all patterns. **(C)** Strain energy gain upon photoactivation. With increasing spread area, the strain energy increases significantly. *Boxes* denote the statistics of 9, 11 and $11\,\mathrm{cells}$, respectively. *Orange* dots show simulation results, with σ_0 kept constant for all patterns. **(D-E)** PA stress activation and relaxation times τ_{act} and τ_{rel} and centers of the activating and relaxing sigmoid t_{act} and t_{rel}. The sum $\tau_{\mathrm{act}} + \tau_{\mathrm{rel}}$ stays approximately constant for all patterns. The onset t_{act} and offset t_{rel} of the stress plateau increase with the cell area, while the duration of the plateau $t_{\mathrm{rel}} - t_{\mathrm{act}}$ decreases.

fully covered their patterns are considered in the following.

Figure 3A illustrates the average strain energy level as well as the strain energy gain and dynamics as a response to a single PA pulse of $100\,\mathrm{ms}$, both as a function of the cellular spread area. We find that the model dynamics allows to closely reproduce the mean time course of the experimental strain energy upon PA for each cell area.

Before treating the dynamics of the strain energy course in detail, we exploit the positive correlation of the static energy level and the cell area from Figure 3B to estimate the internal stress $\sigma_{\mathrm{bck}} h_{\mathrm{c}}$ and the force penetration length l_{p}. Fitting the analytical expression of an isotropically contracting disc from Equation 13 to the median energy value yields $\sigma_{\mathrm{bck}} h_{\mathrm{c}} = 7.1\,{}^{\mathrm{nN}}/_{\mu\mathrm{m}}$ and $l_{\mathrm{p}} = 10.37\,\mu\mathrm{m}$. If not explicitly stated, we will use the value for l_{p} in the remainder of this chapter. Since we model the cellular contractility via an anisotropic stress tensor which is different from the isotropic one, σ_{bck} and σ_0 are fitted once to the default case of a cell patterned on a FN circle of area $1000\,\mu\mathrm{m}^2$ and left unchanged for the remaining cell areas, if investigating the full data set in Figure 3B and C. Only for the reduced data sets in Figure 3A, we will fit the stresses separately.

From the fit of the energy curve belonging to cells patterned on a FN circle of area $1000\,\mu\mathrm{m}^2$, we

also obtain the stiffness $E_c = 716.0\,\mathrm{Pa}$ and viscosity $\eta_c = 82.94\,\mathrm{kPa}\cdot\mathrm{s}$, if assuming a typical cell height of $h_c = 1\,\mu\mathrm{m}$. These values yield a relaxation time constant $\tau_c = 115.84\,\mathrm{s}$. We will keep these values fixed in the remainder of this chapter.

We find in Figure 3B that, in general, a pure increase of the cell radius, while leaving the background stress σ_{bck} constant, closely reproduces the full data set, which is indicated by the yellow dots. This suggests that SFs generate the same internal stress, independent of their length. In has to be noted that the orange dots represent the energy baseline found in Figure 3A, which only covers a reduced data set. Therefore, simulated energy values appear deviate from the medians of the experimental data, represented by the orange bars.

We find in Figure 3C shows that also the strain energy gain during PA positively scales with the spread area, uncovering a saturation of the energy gain at cell areas larger than $1000\,\mu\mathrm{m}^2$. Simulations with a constant PA stress σ_0 can closely capture this relation, as indicated by the orange dots.

If considering the dynamics of stress generation and dissipation upon PA, we find a negative correlation of the average stress activation and relaxation times τ_{act} and τ_{rel} if varying the cell area, whereas the sum $\tau_{\mathrm{act}} + \tau_{\mathrm{rel}}$ stays approximately constant (see Figure 3D). This suggests that the effect of a single PA pulse on the cellular energy is of equal duration independent of the cell area.

The cell area has, however, a dominant impact on the onset, offset and duration of the stress plateau of the activation function, as illustrated in Figure 3E. With increasing cell area, both on- and offset times t_{act} and t_{rel} increase, while the duration of the stress plateau $t_{\mathrm{rel}} - t_{\mathrm{act}}$ decreases from $40\,\mathrm{s}$ for $500\,\mu\mathrm{m}^2$ area to $10\,\mathrm{s}$ for a cell area larger than $1000\,\mu\mathrm{m}^2$. Thus, for small cells, the saturation of the activating stress starts earlier and takes longer than for larger cells. This indicates that the molecular system evoking the increase of the strain energy upon PA is non-uniformly distributed or activated for a different cell size.

Taken together, the cell area is a major determinant of both the static tensional efficiency of cells and the dynamics of force production.

Effect of the Actin Polarity on the Cellular Energy Level and Dynamics Figure 4 shows the effect of the actin polarity on the energy level as well as the strain energy gain and dynamics upon a single PA pulse of $100\,\mathrm{ms}$ duration. In particular, we compare the contractile dynamics of cells plated on one of the micropatterns. As discussed earlier, the wheel pattern (WP) induces an actin polarity which is different from those induced by the full circle pattern (FCP), while keeping the cell area unchanged.

We find in Figure 4A that the model dynamics closely reproduces the experimental energy curves for both patterns. Figure 4B shows the energy baseline levels of experiment and model calculations required to maintain the energy level. On average, the strain energy level of wheel-patterned cells equals those of circle-patterned cells, although the latter are allowed to adhere to a larger area, due to the designed pattern shape. It has to be noted that this is different for Figure 4A, which, however, only considers a fraction of the full data set. The continuum model with a constant background stress σ_{bck}, which is optimized with respect to the circle-patterned cells, can closely reproduce the median static energy level measured in the experiment.

Although the static energy level of cells on the WP equals those of cells on the FCP, their dynamic strain energy gain in response to a single PA pulse is less effective, as Figure 4C highlights. As

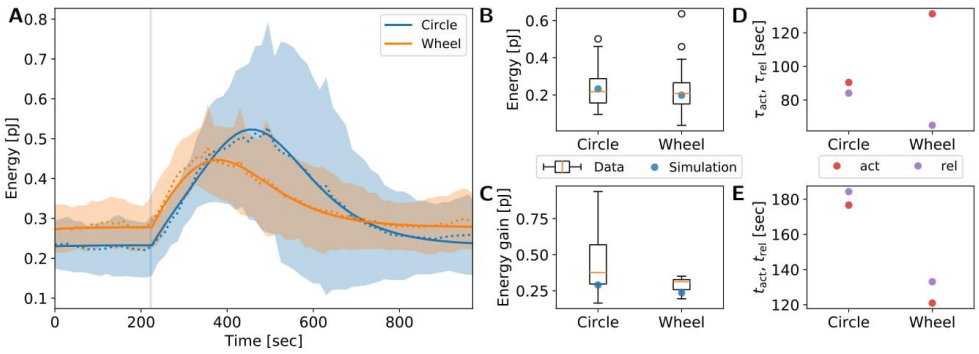

Figure 4: Effect of the FN pattern on the cellular energy level as well as its energy gain and dynamics upon photoactivation. **(A)** Time course of the strain energy. *Dotted lines* show mean values, *shaded regions* correspond to standard deviations and *full lines* show model fits. The curves represent averages of the reduced set of 7 circle-patterned and 5 wheel-patterned cells which are activated by a pulse of $100\,\mathrm{ms}$ duration. **(B)** Static strain energy level. The average energy baselines of circle- and wheel-patterned cells closely resemble. *Boxes* denote the statistics of 40 and $71\,\mathrm{cells}$, respectively. *Blue* dots show simulation results, with σ_{bck} kept constant for both patterns. **(C)** Strain energy gain upon photoactivation. The energy gain of circle-patterned cells is significantly higher than for wheel-patterned cells. *Boxes* denote the statistics of 7 and $5\,\mathrm{cells}$, respectively. *Blue* dots show simulation results, with σ_0 kept constant for both patterns. **(D-E)** PA stress activation and relaxation times τ_{act} and τ_{rel} and centers of the activating and relaxing sigmoid t_{act} and t_{rel}. The sum $\tau_{\mathrm{act}} + \tau_{\mathrm{rel}}$ stays approximately constant for both patterns. Wheel-patterned cells reach their plateau significantly faster, but the duration of the plateau remains unchanged for both patterns.

before, a model with a constant PA stress σ_0 for both patterns closely recovers the experimentally deduced difference.

The experimental ratio of the median strain energy gains between both patterns yields 1.20. From the simulation, we get a ratio of 1.23, which is close to the experimental value. Two aspects can explain the difference in the force production between both patterns, of which both arise from different arrangement of SFs.

On the one hand, SFs in circle-patterned cells usually reveal a parallel alignment across the full diameter of the cell. In the case of wheel-patterned cells, the width of a region of parallelly aligned SFs is only half as large. Assuming a constant SF density and each SF producing the same force, this difference can explain the differing force production for both patterns.

On the other hand, not all SFs in the wheel-patterned cells pull into the same direction. If assuming that each SF produces the same force magnitude F, we can compare the total force $F_{2\mathrm{SF}}$ exerted by two parallel SFs in the case of circle-patterned cells and the total force produced by two SFs from different subregions Ω_n of the wheel-patterned cells (compare Figure 2B-C, top). The magnitude of the sum of two force vectors $\mathbf{F}_1$ and $\mathbf{F}_2$ which originate from the same point and are separated by

an angle α is

$$F_{\mathrm{2SF}} = |\mathbf{F}_1 + \mathbf{F}_2| = \left| \begin{pmatrix} F \\ 0 \end{pmatrix} + \begin{pmatrix} F\cos(\alpha) \\ F\sin(\alpha) \end{pmatrix} \right| = F\sqrt{2\,(1+\cos(\alpha))}\,. \tag{28}$$

For $\alpha = 0°$, which is the situation in circle-patterned cells, we have $F_{\mathrm{2SF}}^{\mathrm{FCP}} = 2F$. For $\alpha = 60°$, i.e. in the case of wheel-patterned cells, we get $F_{\mathrm{2SF}}^{\mathrm{WP}} = \sqrt{3}F$. The ratio of both numbers yields

$$\frac{F_{\mathrm{2SF}}^{\mathrm{FCP}}}{F_{\mathrm{2SF}}^{\mathrm{WP}}} = 1.16\,, \tag{29}$$

which is close to the experimentally and computationally obtained values stated above.

Figures 4D-E show the effect of the actin polarity on the dynamics of stress generation. We find that the stress activation and relaxation times τ_{act} and τ_{rel} for circle-patterned cells resemble each other, while for wheel-patterned cells, the stress activation time is twice as long as the relaxation time. However, in both cases, the sum $\tau_{\mathrm{act}} + \tau_{\mathrm{rel}}$ remains constant, indicating that the duration of the effect of a single PA pulse remains equal, independent of the actin polarity.

Wheel-patterned cells reach their strain energy plateau almost twice as fast than circle-patterned cells, but the duration of the plateau lies in the range of $10\,\mathrm{s}$ for both patterns (see Figure 4E). This suggests that the arrangement of SFs has an impact on the inset of the force saturation in cells, but does not influence the duration of force saturation.

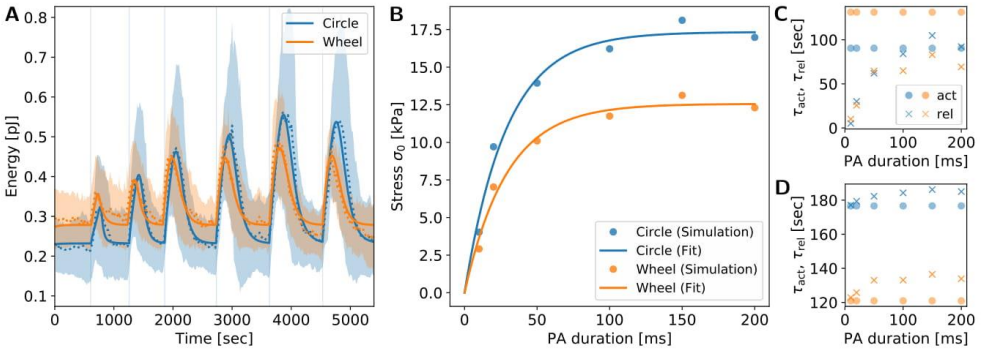

Figure 5: Effect of the PA pulse duration on the cellular energy gain and dynamics. **(A)** Time course of the strain energy. *Dotted lines* show mean values, *shaded regions* correspond to standard deviations and *full lines* show model fits. The curves represent averages of the reduced set of 7 circle-patterned cells and 5 wheel-patterned cells. **(B)** Calculated PA stress σ_0 for the two FN patterns (*dots*) and exponential fit (*lines*). The PA stress σ_0 increases with increasing PA duration and saturates above a PA duration of $29.1\,\mathrm{ms}$ independent of the FN pattern. For the reduced data set in Panel A, circle-patterned cells exert a higher stress than wheel-patterned cells. **(C-D)** PA stress activation and relaxation times τ_{act} and τ_{rel} and centers of the activating and relaxing sigmoid t_{act} and t_{rel}. Both τ_{act} and t_{act} are independent of the PA duration. τ_{rel} and t_{rel} increase in a saturating manner as a function of the PA duration, i.e. a longer PA duration has a longer impact on the contractility of cells. *Blue* dots and crosses correspond to the full circle pattern, while *orange* dots and crosses refer to the wheel pattern.

Overall, actin polarity has hardly an effect on the homeostatic energy level of cells, but is a major determinant of the dynamic force production upon optogenetic regulation.

Effect of the PA Pulse Duration on the Strain Energy Gain and Dynamics Figure 5 demonstrates the impact of the PA pulse duration on the cellular strain energy gain and dynamics. We find in Figure 5A that an active Kelvin-Voigt model with σ_0-dependent stress relaxation time $\tau_{\mathrm{rel}}(\sigma_0)$ a center $t_{\mathrm{rel}}(\sigma_0)$ of the relaxing sigmoid closely resembles the experimental evolution of the cellular energy for both FCP and WP. It has to be noted that, in this paragraph, we fitted σ_{bck} and σ_0 separately for both FN patterns to meet the requirements of the reduced data set presented in Figure 5A. It is, however, expected that for the full data set, which was used to compile the statistics in Figure 4B and C, σ_{bck} and σ_0 will be consistent for both FN patterns.

Figure 5B reveals that an increase of the PA pulse duration leads to an increasing stress response. By fitting an exponentially saturating curve to the calculated stress σ_0 as a function of the PA pulse duration, we obtain a saturation time of $29.1\,\mathrm{ms}$, irrespective of the FN pattern, above which a prolongation of the PA pulse does not evoke an increase of σ_0. For the reduced data set in Figure 5A, we obtain a maximal stress $\sigma_0^{\mathrm{max}} = 17.33\,\mathrm{kPa}$ for cells on the FCP and $\sigma_0^{\mathrm{max}} = 12.56\,\mathrm{kPa}$ for cells on the WP.

Figures 5C-D show that, with increasing PA pulse duration, the stress relaxation time τ_{rel} increases for both FCP and WP proportionally to $\left({}^{\sigma_0}/_{\sigma_0^{\mathrm{max}}}\right)^2$, while the stress activation time τ_{act} remains unaffected. Thus, a prolonged PA pulse has a longer effect on the cellular force production. This is further verified by the rise of t_{rel} proportional to $\left({}^{\sigma_0}/_{\sigma_0^{\mathrm{max}}}\right)^2$, indicating that the plateau of maximal stress lasts longer for longer PA pulses.

Taken together, the duration of the optogenetic activation determines both strength and duration of the cellular energy response, but the energy response saturates in terms of both strength and duration for PA pulses of $29.1\,\mathrm{ms}$ and longer.

Rectangular stress profile	**Solid**	**Kelvin-Voigt**	**Maxwell**
Elastic modulus of the cell E_c	$899.58\,\mathrm{Pa}$	$844.62\,\mathrm{Pa}$	$1165.22\,\mathrm{Pa}$
Viscous modulus of the cell η_c	–	$187.03\,\mathrm{kPa}\cdot\mathrm{s}$	$229.18\,\mathrm{kPa}\cdot\mathrm{s}$
Active stress duration t_{act}	$400.62\,\mathrm{s}$	$326.29\,\mathrm{s}$	$365.03\,\mathrm{s}$
Peak activation stress $\sigma_0^{50\,\mathrm{ms}}$	$4.85\,\mathrm{kPa}$	$6.30\,\mathrm{kPa}$	$6.88\,\mathrm{kPa}$
Exponential stress profile	**Solid**	**Kelvin-Voigt**	**Maxwell**
Elastic modulus of the cell E_c	$845.48\,\mathrm{Pa}$	$796.72\,\mathrm{Pa}$	$861.02\,\mathrm{Pa}$
Viscous modulus of the cell η_c	–	$187.51\,\mathrm{kPa}\cdot\mathrm{s}$	$231.49\,\mathrm{kPa}\cdot\mathrm{s}$
Stress activation time τ_{act}	$61.41\,\mathrm{s}$	$56.37\,\mathrm{s}$	$56.25\,\mathrm{s}$
Stress relaxation time τ_{rel}	$115.16\,\mathrm{s}$	$110.61\,\mathrm{s}$	$118.29\,\mathrm{s}$
Active stress duration t_{act}	$311.59\,\mathrm{s}$	$281.04\,\mathrm{s}$	$290.23\,\mathrm{s}$
Peak activation stress $\sigma_0^{50\,\mathrm{ms}}$	$6.01\,\mathrm{kPa}$	$7.94\,\mathrm{kPa}$	$8.19\,\mathrm{kPa}$
Sigmoid stress profile	**Solid**	**Kelvin-Voigt**	**Maxwell**
Elastic modulus of the cell E_c	$762.52\,\mathrm{Pa}$	$545.92\,\mathrm{Pa}$	$468.83\,\mathrm{Pa}$
Viscous modulus of the cell η_c	–	$84.63\,\mathrm{kPa}\cdot\mathrm{s}$	$68.75\,\mathrm{kPa}\cdot\mathrm{s}$
Stress activation time τ_{act}	$192.45\,\mathrm{s}$	$267.64\,\mathrm{s}$	$348.75\,\mathrm{s}$
Stress relaxation time τ_{rel}	$206.60\,\mathrm{s}$	$340.88\,\mathrm{s}$	$363.36\,\mathrm{s}$
Center of activating sigmoid t_{act}	$215.00\,\mathrm{s}$	$181.64\,\mathrm{s}$	$178.43\,\mathrm{s}$
Center of relaxing sigmoid t_{rel}	$190.49\,\mathrm{s}$	$185.29\,\mathrm{s}$	$174.58\,\mathrm{s}$
Peak activation stress $\sigma_0^{50\,\mathrm{ms}}$	$25.96\,\mathrm{kPa}$	$27.65\,\mathrm{kPa}$	$31.11\,\mathrm{kPa}$
Fixed parameter		**Value**	
Poisson's ratio of the cell ν_c		0.5	
Cell height h_c		$1.0\,\mu\mathrm{m}$	
Cell radius R_c		$17.84\,\mu\mathrm{m}$	
Thickness of the substrate h_s		$50\,\mu\mathrm{m}$	
Poisson's ratio of the substrate ν_s		0.5	
Elastic modulus of the substrate E_s		$4.47\,\mathrm{kPa}$	
Parameter from literature	**Value**		**Reference**
Stiffness of focal adhesion bonds k_a	$2.5\,\mathrm{nN}/\mu\mathrm{m}$		*Balaban et al.* (2001)
Length of sarcomeric sub-unit l_{sarc}	$1\,\mu\mathrm{m}$		*Hu et al.* (2017)
Simulation parameter		**Value**	
Spatial resolution in x-direction Δx		$0.7\,\mu\mathrm{m}$	
Spatial resolution in y-direction Δy		$0.7\,\mu\mathrm{m}$	
Temporal resolution Δt		$15\,\mathrm{s}$	

Table 0.1: Fit and fixed parameters of the strain energy fits from Figures 1.

Bibliography

Alnaes, M., et al., The fenics project version 1.5, *Archive of Numerical Software*, *3*, 9–23, 2015.

Balaban, N. Q., et al., Force and focal adhesion assembly: a close relationship studied using elastic micropatterned substrates, *Nature cell biology*, *3*, 466–472, 2001.

Banerjee, S., and M. Marchetti, Contractile stresses in cohesive cell layers on finite-thickness substrates, *Physical review letters*, *109*, 108,101, 2012.

Edwards, C., and U. Schwarz, Force localization in contracting cell layers, *Physical review letters*, *107*, 128,101, 2011.

Hu, S., et al., Long-range self-organization of cytoskeletal myosin ii filament stacks, *Nature cell biology*, *19*, 133–141, 2017.

Mertz, A. F., et al., Scaling of traction forces with the size of cohesive cell colonies, *Physical review letters*, *108*, 198,101, 2012.

Michaelis, L., and M. L. Menten, Die kinetik der inwertinwirkung, *Biochem.*, pp. 333–369, 1913.

Nelder, J. A., and R. Mead, A simplex method for function minimization, *The computer journal*, *7*, 308–313, 1965.

Oakes, P. W., E. Wagner, C. A. Brand, D. Probst, M. Linke, U. S. Schwarz, M. Glotzer, and M. L. Gardel, Optogenetic control of rhoa reveals zyxin-mediated elasticity of stress fibres, *Nature Communications*, *8*, ncomms15,817, 2017.

Valon, L., F. Etoc, A. Remorino, F. di Pietro, X. Morin, M. Dahan, and M. Coppey, Predictive spatiotemporal manipulation of signaling perturbations using optogenetics, *Biophysical journal*, *109*, 1785–1797, 2015.

Bibliography

[1] I. Pat Williams, KBC Advanced Technologies, "Mechanical integrity." .

[2] and Y. L. W. C. M. Lo, H. B. Wang, M. Dembo, "Cell movement is guided by the rigidity of the substrate, vol. 79, no. 1, pp. 144–152, 2000," *Biophys. J.*, vol. 79, no. 1, pp. 144–152, 2000.

[3] M. L. Gardel, I. C. Schneider, Y. Aratyn-Schaus, and C. M. Waterman, "Mechanical Integration of Actin and Adhesion Dynamics in Cell Migration," *Annu. Rev. Cell Dev. Biol.*, vol. 26, no. 1, pp. 315–333, 2010.

[4] T. Yeung *et al.*, "Effects of substrate stiffness on cell morphology, cytoskeletal structure, and adhesion," *Cell Motil. Cytoskeleton*, vol. 60, no. 1, pp. 24–34, 2005.

[5] K. Franze, "The mechanical control of nervous system development," *Development*, vol. 140, no. 15, pp. 3069–3077, 2013.

[6] T. Iskratsch, H. Wolfenson, and M. P. Sheetz, "Appreciating force and shape-the rise of mechanotransduction in cell biology," *Nat. Rev. Mol. Cell Biol.*, vol. 15, no. 12, pp. 825–833, 2014.

[7] C. C. Dufort, M. J. Paszek, and V. M. Weaver, "Balancing forces: Architectural control of mechanotransduction," *Nat. Rev. Mol. Cell Biol.*, vol. 12, no. 5, pp. 308–319, 2011.

[8] D. E. Jaalouk and J. Lammerding, "Mechanotransduction gone awry," *Nat. Rev. Mol. Cell Biol.*, vol. 10, no. 1, pp. 63–73, 2009.

[9] T. Wyatt, B. Baum, and G. Charras, "A question of time: Tissue adaptation to mechanical forces," *Curr. Opin. Cell Biol.*, vol. 38, pp. 68–73, 2016.

[10] S. Chien, "Mechanotransduction and endothelial cell homeostasis: the wisdom of the cell," *AJP Hear. Circ. Physiol.*, vol. 292, no. 3, pp. H1209–H1224, 2006.

[11] J. M. Barnes, L. Przybyla, and V. M. Weaver, "Tissue mechanics regulate brain development, homeostasis and disease," *J. Cell Sci.*, vol. 130, no. 1, pp. 71–82, 2017.

[12] S. J. Cooper, "From Claude Bernard to Walter Cannon. Emergence of the concept of homeostasis," *Appetite*, vol. 51, no. 3, pp. 419–427, 2008.

[13] K. J. A. Davies, "Adaptive homeostasis," *Mol. Aspects Med.*, vol. 49, pp. 1–7, 2016.

[14] M. J. Bissell, H. G. Hall, and G. Parry, "How does the extracellular matrix direct gene expression?," *J. Theor. Biol.*, vol. 99, no. 1, pp. 31–68, 1982.

[15] G. S. Schultz, J. M. Davidson, R. S. Kirsner, P. Bornstein, and I. M. Herman, "Dynamic reciprocity in the wound microenvironment," *Wound Repair Regen.*, vol. 19, no. 2, pp. 134–148, 2011.

[16] R. A. Brown, R. Prajapati, D. A. McGrouther, I. V. Yannas, and M. Eastwood, "Tensional homeostasis in dermal fibroblasts: Mechanical responses to mechanical loading in three-dimensional substrates," *J. Cell. Physiol.*, vol. 175, no. 3, pp. 323–332, 1998.

[17] J. D. Humphrey, E. R. Dufresne, and M. A. Schwartz, "Mechanotransduction and extracellular matrix homeostasis," *Nat. Rev. Mol. Cell Biol.*, vol. 15, no. 12, pp. 802–812, 2014.

[18] P. Ciarletta, M. Destrade, and A. L. Gower, "On residual stresses and homeostasis: An elastic theory of functional adaptation in living matter," *Sci. Rep.*, vol. 6, no. April, pp. 1–8, 2016.

[19] J. W. Tamkun *et al.*, "Structure of integrin, a glycoprotein involved in the transmembrane linkage between fibronectin and actin," *Cell*, vol. 46, no. 2, pp. 271–282, 1986.

[20] W. Van Dyke and B. Maddow, "Integrin Structure , Activation , and Interactions," pp. 1–15, 1945.

[21] D. Choquet, D. P. Felsenfeld, and M. P. Sheetz, "Extracellular matrix rigidity causes strengthening of integrin- cytoskeleton linkages," *Cell*, vol. 88, no. 1, pp. 39–48, 1997.

[22] W. H. Goldmann, "Mechanotransduction and focal adhesions," *Cell Biol. Int.*, vol. 36, no. 7, pp. 649–652, 2012.

[23] D. E. Leckband and J. de Rooij, "Cadherin Adhesion and Mechanotransduction," *Annu. Rev. Cell Dev. Biol.*, vol. 30, no. 1, pp. 291–315, 2014.

[24] Y. L. Dorland and S. Huveneers, "Cell–cell junctional mechanotransduction in endothelial remodeling," *Cell. Mol. Life Sci.*, vol. 74, no. 2, pp. 279–292, 2016.

[25] P. A. Gottlieb, C. Bae, and F. Sachs, "Gating the mechanical channel Piezo1: A comparison between whole-cell and patch recording," *Channels*, vol. 6, no. 4, pp. 282–289, 2012.
[26] P. Delmas and B. Coste, "XMechano-gated ion channels in sensory systems," *Cell*, vol. 155, no. 2, pp. 278–284, 2013.
[27] G. V. Shivashankar, "Mechanosignaling to the Cell Nucleus and Gene Regulation," *Annu. Rev. Biophys.*, vol. 40, no. 1, pp. 361–378, 2011.
[28] N. Wang, J. D. Tytell, and D. E. Ingber, "Mechanotransduction at a distance: Mechanically coupling the extracellular matrix with the nucleus," *Nat. Rev. Mol. Cell Biol.*, vol. 10, no. 1, pp. 75–82, 2009.
[29] A. P. Navarro, M. A. Collins, and E. S. Folker, "The nucleus is a conserved mechanosensation and mechanoresponse organelle," *Cytoskeleton*, vol. 73, no. 2, pp. 59–67, 2016.
[30] I. Dupin and S. Etienne-Manneville, "Nuclear positioning: Mechanisms and functions," *Int. J. Biochem. Cell Biol.*, vol. 43, no. 12, pp. 1698–1707, 2011.
[31] J. G. Snedeker, "The nuclear envelope as a mechanostat: a central cog in the machinery of cell and tissue regulation?," *Bonekey Rep*, vol. 3, p. 562, 2014.
[32] B. C. Isenberg, P. A. DiMilla, M. Walker, S. Kim, and J. Y. Wong, "Vascular smooth muscle cell durotaxis depends on substrate stiffness gradient strength," *Biophys. J.*, vol. 97, no. 5, pp. 1313–1322, 2009.
[33] J. Lafaurie-Janvore *et al.*, "ESCRT-III assembly and cytokinetic abscission are induced by tension release in the intercellular bridge," *Science (80-.).*, vol. 340, no. 6127, pp. 1625–1629, 2013.
[34] A. J. Engler, S. Sen, H. L. Sweeney, and D. E. Discher, "Matrix Elasticity Directs Stem Cell Lineage Specification," *Cell*, vol. 126, no. 4, pp. 677–689, 2006.
[35] P. W. Oakes, S. Banerjee, M. C. Marchetti, and M. L. Gardel, "Geometry regulates traction stresses in adherent cells," *Biophys. J.*, vol. 107, no. 4, pp. 825–833, 2014.
[36] E. Papusheva and C.-P. Heisenberg, "Spatial organization of adhesion: force-dependent regulation and function in tissue morphogenesis," *EMBO J.*, vol. 29, no. 16, pp. 2753–2768, 2010.
[37] M. Murrell, P. W. Oakes, M. Lenz, and M. L. Gardel, "Forcing cells into shape: The mechanics of actomyosin contractility," *Nat. Rev. Mol. Cell Biol.*, vol. 16, no. 8, pp. 486–498, 2015.
[38] T. Das, K. Safferling, S. Rausch, N. Grabe, H. Boehm, and J. P. Spatz, "A molecular mechanotransduction pathway regulates collective migration of epithelial cells," *Nat. Cell Biol.*, vol. 17, no. 3, pp. 276–287, 2015.
[39] H. Ennomani *et al.*, "Architecture and Connectivity Govern Actin Network Contractility," *Curr. Biol.*, vol. 26, no. 5, pp. 616–626, 2016.
[40] N. C. Gauthier, T. A. Masters, and M. P. Sheetz, "Mechanical feedback between membrane tension and dynamics," *Trends Cell Biol.*, vol. 22, no. 10, pp. 527–535, 2012.
[41] A. Ron *et al.*, "Cell shape information is transduced through tension-independent mechanisms," *Nat. Commun.*, vol. 8, no. 1, 2017.
[42] S. Weng, "PhD Thesis."
[43] P. W. Oakes *et al.*, "Optogenetic control of RhoA reveals zyxin-mediated elasticity of stress fibres," *Nat. Commun.*, vol. 8, 2017.
[44] A. J. Ridley and A. Hall, "Signal transduction pathways regulating Rho-mediated stress fibre formation: requirement for a tyrosine kinase," *Embo J*, vol. 13, no. 11, pp. 2600–2610, 1994.
[45] M. Chrzanowska-Wodnicka and K. Burridge, "Drives the Contractility Formation of Stress Fibers and Focal Adhesions," *J. Cell Biol.*, vol. 133, no. 6, pp. 1403–1415, 1996.
[46] C. B. Khatiwala, P. D. Kim, S. R. Peyton, and A. J. Putnam, "ECM compliance regulates osteogenesis by influencing MAPK signaling downstream of RhoA and ROCK," *J. Bone Miner. Res.*, vol. 24, no. 5, pp. 886–898, 2009.
[47] A. M. Handorf, Y. Zhou, M. A. Halanski, and W. J. Li, "Tissue stiffness dictates development, homeostasis, and disease progression," *Organogenesis*, vol. 11, no. 1, pp. 1–15, 2015.

[48] K. A. Moore *et al.*, "Control of basement membrane remodeling and epithelial branching morphogenesis in embryonic lung by Rho and cytoskeletal tension," *Dev. Dyn.*, vol. 232, no. 2, pp. 268–281, 2005.
[49] A. Mehdizadeh and A. Norouzpour, "New insights in atherosclerosis: Endothelial shear stress as promoter rather than initiator," *Med. Hypotheses*, vol. 73, no. 6, pp. 989–993, 2009.
[50] P. Nigro, J. Abe, and B. C. Berk, "Flow Shear Stress and Atherosclerosis: A Matter of Site Specificity," *Antioxid. Redox Signal.*, vol. 15, no. 5, pp. 1405–1414, 2011.
[51] R. K. Jain, J. D. Martin, and T. Stylianopoulos, "The Role of Mechanical Forces in Tumor Growth and Therapy," *Annu. Rev. Biomed. Eng.*, vol. 16, no. 1, pp. 321–346, 2014.
[52] D. D. Chan *et al.*, "Mechanostasis in apoptosis and medicine," *Prog. Biophys. Mol. Biol.*, vol. 106, no. 3, pp. 517–524, 2011.
[53] F. Grinnell, "Fibroblasts, myofibroblasts, and wound contraction," *J. Cell Biol.*, vol. 124, no. 4, pp. 401–404, 1994.
[54] A. Asnacios and O. Hamant, "The mechanics behind cell polarity," *Trends Cell Biol.*, vol. 22, no. 11, pp. 584–591, 2012.
[55] K. A. Kilian, B. Bugarija, B. T. Lahn, and M. Mrksich, "Geometric cues for directing the differentiation of mesenchymal stem cells," *Proc. Natl. Acad. Sci.*, vol. 107, no. 11, pp. 4872–4877, 2010.
[56] C. M. Nelson, M. M. Vanduijn, J. L. Inman, D. A. Fletcher, and M. J. Bissell, "Tissue Geometry Determines Sites of Mammary Branching Morphogenesis in Organotypic Cultures," pp. 2–5.
[57] M. J. Bissell and D. Radisky, "Putting tumours in context," *Nat. Rev. Cancer*, vol. 1, no. 1, pp. 46–54, 2001.
[58] E. Camand, M. P. Morel, A. Faissner, C. Sotelo, and I. Dusart, "Long-term changes in the molecular composition of the glial scar and progressive increase of serotoninergic fibre sprouting after hemisection of the mouse spinal cord," *Eur. J. Neurosci.*, vol. 20, no. 5, pp. 1161–1176, 2004.
[59] D. T. Butcher, T. Alliston, and V. M. Weaver, "A tense situation: Forcing tumour progression," *Nat. Rev. Cancer*, vol. 9, no. 2, pp. 108–122, 2009.
[60] S. Suresh, "Biomechanics and biophysics of cancer cells," *Acta Mater.*, vol. 55, no. 12, pp. 3989–4014, 2007.
[61] J. S. Allingham, R. Smith, and I. Rayment, "The structural basis of blebbistatin inhibition and specificity for myosin II," *Nat. Struct. Mol. Biol.*, vol. 12, no. 4, pp. 378–379, 2005.
[62] H. Affinity and S. Associated, "Communication," pp. 835–839, 1979.
[63] "No Title."
[64] E. J. Ezratty, M. A. Partridge, and G. G. Gundersen, "Microtubule-induced focal adhesion disassembly is mediated by dynamin and focal adhesion kinase," *Nat. Cell Biol.*, vol. 7, no. 6, pp. 581–590, 2005.
[65] T. Ishizaki *et al.*, "Pharmacological properties of Y-27632, a specific inhibitor of rho-associated kinases.," *Mol. Pharmacol.*, vol. 57, no. 5, pp. 976–983, 2000.
[66] M. Takata *et al.*, "Fasudil, a rho kinase inhibitor, limits motor neuron loss in experimental models of amyotrophic lateral sclerosis," *Br. J. Pharmacol.*, vol. 170, no. 2, pp. 341–351, 2013.
[67] M. Honjo *et al.*, "A myosin light chain kinase inhibitor, ML-9, lowers the intraocular pressure in rabbit eyes," *Exp. Eye Res.*, vol. 75, no. 2, pp. 135–142, 2002.
[68] A. J. Rodriguez, S. M. Shenoy, R. H. Singer, and J. Condeelis, "Visualization of mRNA translation in living cells," *J. Cell Biol.*, vol. 175, no. 1, pp. 67–76, 2006.
[69] C. T. Mierke *et al.*, "Vinculin facilitates cell invasion into three-dimensional collagen matrices," *J. Biol. Chem.*, vol. 285, no. 17, pp. 13121–13130, 2010.
[70] G. Chen, Z. Hou, D. R. Gulbranson, and J. A. Thomson, "Actin-myosin contractility is responsible for the reduced viability of dissociated human embryonic stem cells," *Cell Stem Cell*, vol. 7, no. 2, pp. 240–248, 2010.
[71] G. W. Schmid-Schönbein, K. L. Sung, H. Tözeren, R. Skalak, and S. Chien, "Passive mechanical

properties of human leukocytes," *Biophys. J.*, vol. 36, no. 1, pp. 243–256, 1981.
[72] E. Evans and A. Yeung, "Apparent viscosity and cortical tension of blood granulocytes determined by micropipet aspiration," *Biophys. J.*, vol. 56, no. 1, pp. 151–160, 1989.
[73] W. H. Goldmann, "Mechanical manipulation of animal cells: Cell indentation," *Biotechnol. Lett.*, vol. 22, no. 6, pp. 431–435, 2000.
[74] H. H. H. Vandenburgh, S. Swasdison, and P. Karlisch, "Computer-aided mechanogenesis of skeletal muscle organs from single cells," *FASEB J.*, vol. 5, no. 13, p. 2860, 1991.
[75] P. F. Davies and S. C. Tripathi, "Mechanical stress mechanisms and the cell. An endothelial paradigm," *Circ. Res.*, vol. 72, no. 2, pp. 239–245, 1993.
[76] M. J. Levesque and R. M. Nerem, "The study of rheological effects on vascular endothelial cells in culture," *Biorheology*, vol. 26, no. 2, pp. 345–357, 1989.
[77] S. C. Kuo and M. P. Sheetz, "Force of single kinesin groups measured with optical tweezers," *Science (80-.).*, vol. 260, no. April, pp. 232–234, 1993.
[78] A. R. Bausch, W. Möller, and E. Sackmann, "Measurement of local viscoelasticity and forces in living cells by magnetic tweezers," *Biophys. J.*, vol. 76, no. 1 I, pp. 573–579, 1999.
[79] F. J. Alenghat, B. Fabry, K. Y. Tsai, W. H. Goldmann, and D. E. Ingber, "Analysis of cell mechanics in single vinculin-deficient cells using a magnetic tweezer," *Biochem. Biophys. Res. Commun.*, vol. 277, no. 1, pp. 93–99, 2000.
[80] T. Mizutani, H. Haga, and K. Kawabata, "Cellular stiffness response to external deformation: Tensional homeostasis in a single fibroblast," *Cell Motil. Cytoskeleton*, vol. 59, no. 4, pp. 242–248, 2004.
[81] E. A. Almeida *et al.*, "Matrix survival signaling: from fibronectin via focal adhesion kinase to c-Jun NH(2)-terminal kinase.," *J. Cell Biol.*, vol. 149, no. 3, pp. 741–54, 2000.
[82] K. A. DeMali, K. Wennerberg, and K. Burridge, "Integrin signaling to the actin cytoskeleton," *Curr. Opin. Cell Biol.*, vol. 15, no. 5, pp. 572–582, 2003.
[83] R. Kaunas and S. Deguchi, "Multiple roles for myosin II in tensional homeostasis under mechanical loading," *Cell. Mol. Bioeng.*, vol. 4, no. 2, pp. 182–191, 2011.
[84] M. J. Paszek *et al.*, "Tensional homeostasis and the malignant phenotype," *Cancer Cell*, vol. 8, no. 3, pp. 241–254, 2005.
[85] A. J. Banes *et al.*, "Mechanoreception at the cellular level: the detection, interpretation, and diversity of responses to mechanical signals," *Biochem. Cell Biol.*, vol. 73, no. 7–8, pp. 349–365, 1995.
[86] K. D. Webster, W. P. Ng, and D. A. Fletcher, "Tensional homeostasis in single fibroblasts," *Biophys. J.*, vol. 107, no. 1, pp. 146–155, 2014.
[87] A. J. Zollinger *et al.*, "Dependence of Tensional Homeostasis on Cell Type and on Cell–Cell Interactions," 2018.
[88] S. Weng, Y. Shao, W. Chen, and J. Fu, "Mechanosensitive subcellular rheostasis drives emergent single-cell mechanical homeostasis," *Nat. Mater.*, vol. 15, no. 9, pp. 961–967, 2016.
[89] T. Komatsu, I. Kukelyansky, J. M. McCaffery, T. Ueno, L. C. Varela, and T. Inoue, "Organelle-specific, rapid induction of molecular activities and membrane tethering," *Nat. Methods*, vol. 7, no. 3, pp. 206–208, 2010.
[90] J. E. Toettcher, O. D. Weiner, and W. A. Lim, "Using optogenetics to interrogate the dynamic control of signal transmission by the Ras/Erk module," *Cell*, vol. 155, no. 6, pp. 1422–1434, 2013.
[91] G. Loirand and P. Pacaud, "Small GTPases Involvement of Rho GTPases and their regulators in the pathogenesis of hypertension Involvement of Rho GTPases and their regulators in the pathogenesis of hypertension," no. April, 2017.
[92] J. E. Toettcher, C. A. Voigt, O. D. Weiner, and W. A. Lim, "The promise of optogenetics in cell biology: Interrogating molecular circuits in space and time," *Nat. Methods*, vol. 8, no. 1, pp. 35–38, 2011.
[93] Y. Sano, W. Watanabe, and S. Matsunaga, "Chromophore-assisted laser inactivation - towards a spatiotemporal-functional analysis of proteins, and the ablation of chromatin, organelle and

cell function," *J. Cell Sci.*, vol. 127, no. 8, pp. 1621–1629, 2014.
[94] M. Rauzi, P. Verant, T. Lecuit, and P. F. Lenne, "Nature and anisotropy of cortical forces orienting Drosophila tissue morphogenesis," *Nat. Cell Biol.*, vol. 10, no. 12, pp. 1401–1410, 2008.
[95] S. Sardari, "Study break," *Iran. Biomed.J*, vol. 22, no. 1, pp. 67–68, 2016.
[96] G. Nagel *et al.*, "Channelrhodopsin-1: A light-gated proton channel in green algae," *Science (80-.).*, vol. 296, no. 5577, pp. 2395–2398, 2002.
[97] G. Nagel *et al.*, "Channelrhodopsin-2, a directly light-gated cation-selective membrane channel," *Proc. Natl. Acad. Sci.*, vol. 100, no. 24, pp. 13940–13945, 2003.
[98] E. S. Boyden, F. Zhang, E. Bamberg, G. Nagel, and K. Deisseroth, "Millisecond-timescale, genetically targeted optical control of neural activity," *Nat. Neurosci.*, vol. 8, no. 9, pp. 1263–1268, 2005.
[99] K. Deisseroth, "Controlling the brain with light," *Sci. Am.*, vol. 303, no. 5, pp. 48–55, 2010.
[100] J. E. Toettcher, D. Gong, W. A. Lim, and O. D. Weiner, "Light-based feedback for controlling intracellular signaling dynamics," *Nat. Methods*, vol. 8, no. 10, pp. 837–839, 2011.
[101] D. Tischer and O. D. Weiner, "Illuminating cell signalling with optogenetic tools," *Nat. Rev. Mol. Cell Biol.*, vol. 15, no. 8, pp. 551–558, 2014.
[102] A. Levskaya, O. D. Weiner, W. A. Lim, and C. A. Voigt, "Spatiotemporal Control of Cell Signalling Using A Light- Switchable Protein Interaction," *Nature*, vol. 461, no. 7266, pp. 997–1001, 2009.
[103] M. J. Kennedy, R. M. Hughes, L. A. Peteya, J. W. Schwartz, M. D. Ehlers, and C. L. Tucker, "Rapid blue light induction of protein interaction in living cells," *Nat. Methods*, vol. 7, no. 12, pp. 973–975, 2010.
[104] Y. I. Wu *et al.*, "A genetically encoded photoactivatable Rac controls the motility of living cells," *Nature*, vol. 461, no. 7260, pp. 104–108, 2009.
[105] M. Yazawa, A. M. Sadaghiani, B. Hsueh, and R. E. Dolmetsch, "Induction of protein-protein interactions in live cells using light," *Nat. Biotechnol.*, vol. 27, no. 10, pp. 941–945, 2009.
[106] A. Manuscript, "Biology," vol. 9, no. 4, pp. 379–384, 2012.
[107] B. Kim and M. Z. Lin, "Optobiology: optical control of biological processes via protein engineering," *Biochem. Soc. Trans.*, vol. 41, no. 5, pp. 1183–1188, 2013.
[108] X. X. Zhou, H. K. Chung, A. J. Lam, and M. Z. Lin, "Optical control of protein activity by fluorescent protein domains," *Science (80-.).*, vol. 338, no. 6108, pp. 810–814, 2013.
[109] X. X. Zhou, H. K. Chung, A. J. Lam, and M. Z. Lin, "Optical control of protein activity by fluorescent protein domains," *Science (80-.).*, vol. 338, no. 6108, pp. 810–814, 2012.
[110] B. R. Rost, F. Schneider-Warme, D. Schmitz, and P. Hegemann, "Optogenetic Tools for Subcellular Applications in Neuroscience," *Neuron*, vol. 96, no. 3, pp. 572–603, 2017.
[111] H. Park, S. Lee, and W. Do Heo, "Protein inactivation by optogenetic trapping in living cells," *Methods Mol. Biol.*, vol. 1408, no. 6, pp. 363–376, 2016.
[112] S. Konermann *et al.*, "Optical control of mammalian endogenous transcription and epigenetic states," *Nature*, vol. 500, no. 7463, pp. 472–476, 2013.
[113] X. Wang, X. Chen, and Y. Yang, "Spatiotemporal control of gene expression by a light-switchable transgene system," *Nat. Methods*, vol. 9, no. 3, pp. 266–269, 2012.
[114] E. M. Zhao *et al.*, "Optogenetic regulation of engineered cellular metabolism for microbial chemical production," *Nature*, vol. 555, no. 7698, pp. 683–687, 2018.
[115] C. Janetopoulos and P. Devreotes, "Phosphoinositide signaling plays a key role in cytokinesis," *J. Cell Biol.*, vol. 174, no. 4, pp. 485–490, 2006.
[116] G. Guglielmi, J. D. Barry, W. Huber, and S. De Renzis, "An Optogenetic Method to Modulate Cell Contractility during Tissue Morphogenesis," *Dev. Cell*, vol. 35, no. 5, pp. 646–660, 2015.
[117] M. Raftopoulou and A. Hall, "Cell migration: Rho GTPases lead the way," *Dev. Biol.*, vol. 265, no. 1, pp. 23–32, 2004.
[118] M. V. Rao, P. H. Chu, K. M. Hahn, and R. Zaidel-Bar, "An optogenetic tool for the activation of endogenous diaphanous-related formins induces thickening of stress fibers without an increase

in contractility," *Cytoskeleton*, vol. 70, no. 7, pp. 394–407, 2013.
[119] E. Wagner and M. Glotzer, "Local RhoA activation induces cytokinetic furrows independent of spindle position and cell cycle stage," *J. Cell Biol.*, vol. 213, no. 6, pp. 641–649, 2016.
[120] L. Valon *et al.*, "Predictive Spatiotemporal Manipulation of Signaling Perturbations Using Optogenetics," *Biophys. J.*, vol. 109, no. 9, pp. 1785–1797, 2015.
[121] L. Valon, A. Marï¿½n-Llauradï¿½, T. Wyatt, G. Charras, and X. Trepat, "Optogenetic control of cellular forces and mechanotransduction," *Nat. Commun.*, vol. 8, 2017.
[122] M. Yoshigi, L. M. Hoffman, C. C. Jensen, H. J. Yost, and M. C. Beckerle, "Mechanical force mobilizes zyxin from focal adhesions to actin filaments and regulates cytoskeletal reinforcement," *J. Cell Biol.*, vol. 171, no. 2, pp. 209–215, 2005.
[123] L. Valon, "PhD Thesis."
[124] A. K. Harris, P. Wild, D. Stopak, N. Series, and N. Apr, "Silicone Rubber Substrata : A New Wrinkle in the Study of Cell Locomotion Silicone Rubber Substrata : A New Wrinkle in the Study of Cell Locomotion," vol. 208, no. 4440, pp. 177–179, 2008.
[125] T. Oliver, K. Jacobson, and M. Dembo, "Traction forces in locomoting cells," *Cell Motil. Cytoskeleton*, vol. 31, no. 3, pp. 225–240, 1995.
[126] J. Lee, M. Leonard, T.liver, A. Ishihara, and K. Jacobson, "Traction Forces Generated by Locomting Keratocytes," *J. Cell Biol.*, vol. 127, no. 6, Part 2, pp. 1957–1964, 1994.
[127] G. Bao and S. Suresh, "Cell and molecular mechanics of biological materials," pp. 715–725, 2003.
[128] T. Wakatsuki, M. S. Kolodney, G. I. Zahalak, and E. L. Elson, "Cell mechanics studied by a reconstituted model tissue," *Biophys. J.*, vol. 79, no. 5, pp. 2353–2368, 2000.
[129] K. S. Kolahi *et al.*, "Effect of substrate stiffness on early mouse embryo development," *PLoS One*, vol. 7, no. 7, 2012.
[130] L. D. L. L. P. P. A. M. K. E. M. Lifshitz, "Theory of Elasticity."
[131] M. Dembo and Y. L. Wang, "Stresses at the cell-to-substrate interface during locomotion of fibroblasts," *Biophys. J.*, vol. 76, no. 4, pp. 2307–2316, 1999.
[132] J. P. Butler, I. M. Tolic-Norrelykke, B. Fabry, and J. J. Fredberg, "Traction fields, moments, and strain energy that cells exert on their surroundings," *AJP Cell Physiol.*, vol. 282, no. 3, pp. C595–C605, 2002.
[133] X. Tang, A. Tofangchi, S. V. Anand, and T. A. Saif, "A Novel Cell Traction Force Microscopy to Study Multi-Cellular System," *PLoS Comput. Biol.*, vol. 10, no. 6, 2014.
[134] K. Burton and D. L. Taylor, "Traction forces of cytokinesis measured with optically modified elastic substrata," *Nature*, vol. 385, no. 6615. pp. 450–454, 1997.
[135] M. Dembo and T. Oliver, "Imaging the Traction Stresses Exerted by Locomoting Cells with the Elastic Substratum Method," *Biophys. J.*, vol. 70, no. April 1996, pp. 2008–2022, 1996.
[136] B. Sabass, M. L. Gardel, C. M. Waterman, and U. S. Schwarz, "High resolution traction force microscopy based on experimental and computational advances," *Biophys. J.*, vol. 94, no. 1, pp. 207–220, 2008.
[137] U. S. Schwarz, N. Q. Balaban, D. Riveline, A. Bershadsky, B. Geiger, and S. A. Safran, "Calculation of forces at focal adhesions from elastic substrate data: The effect of localized force and the need for regularization," *Biophys. J.*, vol. 83, no. 3, pp. 1380–1394, 2002.
[138] H. B. Wang, M. Dembo, S. K. Hanks, and Y. Wang, "Focal adhesion kinase is involved in mechanosensing during fibroblast migration.," *Proc. Natl. Acad. Sci. U. S. A.*, vol. 98, no. 20, pp. 11295–300, 2001.
[139] J. H. Wang and B. Li, "The principles and biological applications of cell traction force microscopy," *World*, vol. 29, pp. 449–458, 2010.
[140] K. Mandal and D. D. E. L. U. E, "Contribution des propriétés du micro-environnement sur l ' adhésion cellulaire To cite this version : HAL Id : tel-00870404 Role of ECM Physical Properties on Force Distribution and Cell In- ternal Organization," 2013.
[141] Q. Tseng *et al.*, "A new micropatterning method of soft substrates reveals that different

tumorigenic signals can promote or reduce cell contraction levels," *Lab Chip*, vol. 11, no. 13, p. 2231, 2011.
[142] T. Vignaud, H. Ennomani, and M. Théry, "Polyacrylamide Hydrogel Micropatterning," *Methods Cell Biol.*, vol. 120, pp. 93–116, 2014.
[143] C. S. Chen, J. L. Alonso, E. Ostuni, G. M. Whitesides, and D. E. Ingber, "Cell shape provides global control of focal adhesion assembly," *Biochem. Biophys. Res. Commun.*, vol. 307, no. 2, pp. 355–361, 2003.
[144] R. McBeath, D. M. Pirone, C. M. Nelson, K. Bhadriraju, and C. S. Chen, "Cell shape, cytoskeletal tension, and RhoA regulate stemm cell lineage commitment," *Dev. Cell*, vol. 6, pp. 483–495, 2004.
[145] L. K. Wrobel, T. R. Fray, J. E. Molloy, J. J. Adams, M. P. Armitage, and J. C. Sparrow, "Micropatterning tractional forces in living cells," *Cell Motil. Cytoskeleton*, vol. 52, no. 2, pp. 97–106, 2002.
[146] V. Damljanović, B. C. Lagerholm, and K. Jacobson, "Bulk and micropatterned conjugation of extracellular matrix proteins to characterized polyacrylamide substrates for cell mechanotransduction assays," *Biotechniques*, vol. 39, no. 6, pp. 847–851, 2005.
[147] C. A. Reinhart-King, M. Dembo, and D. A. Hammer, "Endothelial Cell Traction Forces on RGD-Derivatized Polyarylamide Substrata," *Langmuir*, vol. 19, no. 7, pp. 1573–1579, 2003.
[148] J. L. Tan, J. Tien, D. M. Pirone, D. S. Gray, K. Bhadriraju, and C. S. Chen, "Cells lying on a bed of microneedles: An approach to isolate mechanical force," *Proc. Natl. Acad. Sci.*, vol. 100, no. 4, pp. 1484–1489, 2003.
[149] N. Gavara, P. Roca-Cusachs, R. Sunyer, R. Farré, and D. Navajas, "Mapping cell-matrix stresses during stretch reveals inelastic reorganization of the cytoskeleton," *Biophys. J.*, vol. 95, no. 1, pp. 464–471, 2008.
[150] A. D. Rape, W. H. Guo, and Y. L. Wang, "The regulation of traction force in relation to cell shape and focal adhesions," *Biomaterials*, vol. 32, no. 8, pp. 2043–2051, 2011.
[151] K. Mandal, I. Wang, E. Vitiello, L. A. C. Orellana, and M. Balland, "Cell dipole behaviour revealed by ECM sub-cellular geometry," *Nat. Commun.*, vol. 5, 2014.
[152] K. K. PARKER, "Directional control of lamellipodia extension by constraining cell shape and orienting cell tractional forces," *FASEB J.*, vol. 16, no. 10, pp. 1195–1204, 2002.
[153] X. Jiang, D. A. Bruzewicz, A. P. Wong, M. Piel, and G. M. Whitesides, "Directing cell migration with asymmetric micropatterns," *Proc. Natl. Acad. Sci.*, vol. 102, no. 4, pp. 975–978, 2005.
[154] B. Vianay *et al.*, "Variation in traction forces during cell cycle progression," *Biol. Cell*, vol. 110, no. 4, pp. 91–96, 2018.
[155] N. Wang *et al.*, "Mechanical behavior in living cells consistent with the tensegrity model," *Proc. Natl. Acad. Sci.*, vol. 98, no. 14, pp. 7765–7770, 2001.
[156] G. Lukinavičius *et al.*, "Fluorogenic probes for live-cell imaging of the cytoskeleton," *Nat. Methods*, vol. 11, no. 7, pp. 731–733, 2014.
[157] P. J. Albert and U. S. Schwarz, "Dynamics of cell shape and forces on micropatterned substrates predicted by a cellular Potts model," *Biophys. J.*, vol. 106, no. 11, pp. 2340–2352, 2014.
[158] M. Théry, A. Pépin, E. Dressaire, Y. Chen, and M. Bornens, "Cell distribution of stress fibres in response to the geometry of the adhesive environment," *Cell Motil. Cytoskeleton*, vol. 63, no. 6, pp. 341–355, 2006.
[159] E. Kassianidou, C. A. Brand, U. S. Schwarz, and S. Kumar, "Geometry and network connectivity govern the mechanics of stress fibers," *Proc. Natl. Acad. Sci.*, vol. 114, no. 10, pp. 2622–2627, 2017.
[160] K. Burridge and J. R. Feramisco, "Microinjection and localization of a 130K protein in living fibroblasts: a relationship to actin and fibronectin," *Cell*, vol. 19, no. 3, pp. 587–595, 1980.
[161] E. P. Canovic, A. J. Zollinger, S. N. Tam, M. L. Smith, and D. Stamenovi, "Tensional homeostasis in endothelial cells is a multicellular phenomenon," *Am J Physiol Cell Physiol*, vol. 311, pp. 528–535, 2016.

[162] J. D. Humphrey, "Vascular adaptation and mechanical homeostasis at tissue, cellular, and sub-cellular levels," *Cell Biochem. Biophys.*, vol. 50, no. 2, pp. 53–78, 2008.
[163] M. Crisp *et al.*, "Coupling of the nucleus and cytoplasm: Role of the LINC complex," *J. Cell Biol.*, vol. 172, no. 1, pp. 41–53, 2006.
[164] T. Metzger *et al.*, "MAP and kinesin-dependent nuclear positioning is required for skeletal muscle function," *Nature*, vol. 484, no. 7392, pp. 120–124, 2012.
[165] T. P. Driscoll, B. D. Cosgrove, S. J. Heo, Z. E. Shurden, and R. L. Mauck, "Cytoskeletal to Nuclear Strain Transfer Regulates YAP Signaling in Mesenchymal Stem Cells," *Biophys. J.*, vol. 108, no. 12, pp. 2783–2793, 2015.
[166] D. M. Graham and K. Burridge, "Mechanotransduction and nuclear function," *Curr. Opin. Cell Biol.*, vol. 40, pp. 98–105, 2016.